Studies of Beam Impedance with Related Beam Stability and Loss Effects on a High Intensity Proton Synchrotron



D. W. Posthuma de Boer

Trinity College

University of Oxford

A thesis submitted for the degree of

Doctor of Philosophy

Hilary 2026

Acknowledgements

This thesis would not have been possible without contributions from a vast team of people. Amongst them are my supervisors past and present: Dr. Chris Warsop, Prof. Brian Foster, Prof. Adrian Oeftiger and Dr. Ivan Konoplev. Thank you, Brian, for contributing your vast experience and taking the time to review my work. More than once, I have taken solace in the thought that "…if Brian thinks it's alright, then it must be good enough." Thank you, Adrian, it gives me great comfort to have had a leader in the field cast an eye over my work. Thank you, Ivan, for constantly looking for opportunities and pushing me in the early stages of this thesis. Thank you, Chris, for your huge support; for always being generous with your time; for your expert and patient guidance; for your criticism when it was necessary, and for your kindness.

Although not formally a supervisor, I would also like to thank Dr. Rob Williamson for his guidance and contributions. Thank you for giving me a starting point; for your help in acquiring the beam-based experimental data and for your valuable perspectives.

I would like to thank Andy Chamberlain and the staff of the R78 workshop, including Jamie Searis and Lewis Goodenough, who contributed mechanical apparatus for the bench impedance measurements. I would like to thank Oliver Newell, who helped to set up experiments on the RF screens. I would like to thank Ben Orton and Martin Hughes, who helped me perform impedance measurements on the extract kickers in the midst of a global pandemic. I would like to thank Andy Seville for his help to perform the beam-based RCS experiments; the ISIS crew without whom no experiments would have been possible; the accelerator physics team for their inputs and machine physics time and the diagnostics team for keeping the tools working.

I would like to thank the ISIS Neutron and Muon Source and my management, most notably John Thomason, Dean Adams, Tony Kershaw and Alex Pertica, for supporting this work financially, giving me the time to complete it and for your confidence.

Finally, this thesis would have never been finished without the love and support of my wife, Yukino, who has been a source of strength throughout this journey, and to whom I offer my sincere gratitude. Since starting this work, we have had the joy to welcome our son, Louis, into the world and the privilege to spend time with him and watch him grow. Noah will join us in the coming months, and we are excited to share that privilege together with Louis. When I started this work, Yukino and I were both starting something new, and now that we're both at the finishing line, I'm looking forward to whatever comes next.

Abstract

Neutrons have been used to probe the structure of matter for applications as wide-ranging as fundamental magnetism and archaeological investigation, and the particle accelerators which drive short-pulsed neutron scattering facilities are pushing the limits of beam intensity. For future machines to operate safely and effectively, they must rise to the challenge of reducing beam-loss whilst simultaneously increasing intensity.

Whilst beam-loss can be driven by a variety of processes, losses due to coherent transverse beam instabilities are typically expected to worsen as beam intensity increases. One such instability currently limits the operational performance of the ISIS Neutron and Muon Source, and similar instabilities have been observed on at least three other facilities. In order to limit the impact of these instabilities on future machines, it is necessary to understand and mitigate them on those that are currently operating. This thesis will focus on the head-tail instability at ISIS, which was first observed some decades ago but is still not well understood.

Fundamental concepts of beam instabilities will first be reviewed, and then used to identify key requirements for the study. A transverse driving impedance model will be developed, guided by earlier studies to seek-out sources of a low frequency narrowband impedance. Computational tools will be developed to produce this model; taking the form of a new resistive-wall impedance calculation code, and a technique to apply commercial finite-element software to this application.

A new semi-analytical code, based on well established theory, will be developed to compute the properties of beam instabilities. It will be benchmarked against particle tracking simulations and applied to the case of ISIS operating in Rapid Cycling Synchrotron mode and Bunched Storage Ring mode, with the newly developed impedance model. Predictions will be compared with experimental observations, and comments made as to the applicability of this theory to ISIS, despite neglecting space charge.

Conclusions will be drawn on whether the newly developed impedance model can explain the head-tail instability, and observations made in earlier studies. Modifications to key impedance sources will be discussed, with the aim of improving beam stability on ISIS and guiding future equipment designs. Opportunities for future study will also be briefly discussed.

Contents

List of Figures vii

List of Tables xi

1 Introduction 1
- 1.1 Pulsed Neutron Sources . . . 2
  - 1.1.1 Short-Pulse Spallation Neutron Sources . . . 4
  - 1.1.2 Summary of Key Facilities . . . 5
  - 1.1.3 Future Facilities . . . 8
- 1.2 Challenges for Future Short-Pulse Spallation Sources . . . 9
  - 1.2.1 Coherent Transverse Instabilities at Existing Facilities . . . 9
  - 1.2.2 Transverse Instabilities at Future Facilities . . . 10
- 1.3 Thesis Objectives . . . 11

2 The ISIS Neutron and Muon Source 12
- 2.1 Description of the ISIS Accelerator Complex . . . 15
  - 2.1.1 The ISIS Injector . . . 15
  - 2.1.2 The ISIS Synchrotron . . . 16
- 2.2 Operating Modes of ISIS . . . 18
  - 2.2.1 Operational RCS Mode . . . 18
  - 2.2.2 Storage Ring Modes . . . 20
- 2.3 Intensity Limitations of the ISIS Synchrotron . . . 23
  - 2.3.1 The 2 ms Head-Tail Instability . . . 23
  - 2.3.2 Mitigation in RCS Operations . . . 24
  - 2.3.3 Summary of Key Observations . . . 25

3 Wakes and Impedances 27
- 3.1 Fundamental Definitions . . . 29
  - 3.1.1 Wake Functions . . . 29
  - 3.1.2 Transverse (Driving) Wake Force in a Synchrotron . . . 32
  - 3.1.3 Beam Coupling Impedance . . . 34
- 3.2 Transverse Impedance of Common Structures . . . 37
  - 3.2.1 Perfectly Conducting Circular Vacuum Vessel . . . 37
  - 3.2.2 Conductive Circular Vacuum Vessel . . . 39
  - 3.2.3 Transverse Resonator . . . 41
- 3.3 Measurement and Numerical Computation . . . 42
  - 3.3.1 Wire Bench Measurements . . . 42

3.3.2 Finite-Element Tools - CST 49
3.4 Impedance of Multi-Layer Cylindrical Pipes 52
3.4.1 Pipes of Other Geometries 60

4 Transverse Coherent Bunched Beam Instabilities 61
4.1 Theory of Coherent Transverse Instabilities 65
4.1.1 The Linearised Vlasov Equation 66
4.1.2 Interaction Matrix Form 73
4.1.3 Equally Spaced Identical Bunches 74
4.1.4 Low Intensity Limit (Decoupled Azimuthal Modes) 75
4.1.5 Approximate Solutions (PyTMCI) 76
4.2 PyTMCI Benchmarks 76
4.2.1 Example 1 - A Dominant Head-Tail Mode 78
4.2.2 Example 2 - A Higher-Order Radial Mode 80
4.2.3 Example 3 - TMCI 80
4.2.4 Discussion 84

5 Vertical Driving Impedance Model of the ISIS Synchrotron 85
5.1 Introduction 85
5.2 Identification of Key Equipment 86
5.3 RF Screens and Laminated Magnets 87
5.3.1 Material Properties 92
5.3.2 Simplifications to RF Screen and Magnet Model 96
5.3.3 CST Simulations of RF Screens 109
5.3.4 Probe Coil Measurements of RF Screen Impedance 116
5.3.5 RF Screen Impedance Model for the ISIS Synchrotron 126
5.4 RF Cavities 131
5.5 Extraction Kickers 135
5.5.1 Description of Extraction Kicker System 135
5.5.2 Probe Coil Measurements of Extraction Kicker Impedance . . . 137
5.6 Indirect Space Charge 146
5.7 ISIS Vertical Driving Impedance Model 147
5.7.1 Lorentz Beta Dependence 147
5.7.2 Summary of Overall Smooth Focusing Impedance Model 147
5.7.3 Twiss-β_y Weighted Impedance Model 149
5.8 Summary and Conclusion 153

6 Coherent Vertical Instabilities on the ISIS Synchrotron 155
6.1 Introduction 155
6.2 Linearised Vlasov Theory for ISIS 156
6.2.1 Validity of Assumptions 156
6.2.2 Application of the Theory for ISIS 157
6.3 Instabilities in BSRM as a Function of Vertical Tune 159
6.3.1 Experimental Set-up 160

6.3.2 Experimental Results . . . 161
6.3.3 PyTMCI Input Parameters . . . 167
6.3.4 Comparison of PyTMCI and Experimental Results . . . 171
6.3.5 Discussion of BSRM Results . . . 175
6.4 Instabilities in RCS Mode with Fundamental RF . . . 179
6.4.1 Experimental Set-Up . . . 179
6.4.2 Experimental Results . . . 181
6.4.3 PyTMCI Input Parameters . . . 185
6.4.4 Comparison of PyTMCI and Experimental Results . . . 190
6.4.5 PyTMCI Predictions for Higher Intensity . . . 195
6.4.6 Discussion of RCS Results . . . 196
6.5 Summary and Conclusion . . . 199

7 Instability Mitigation on ISIS 200
7.1 Introduction . . . 200
7.2 Impedance Optimisation on ISIS . . . 201
7.3 Impedance Optimisation with Capacitors . . . 201
7.3.1 Experimental Verification . . . 202
7.4 Instability Predictions with Optimised Impedance . . . 203
7.5 Summary and Conclusion . . . 204

8 Conclusion 205
8.1 Summary and Conclusions . . . 205
8.2 Future Work . . . 209

Appendices

A ISIS Design Stage Impedance Reduction 211

B Fourier Conventions 213

C Fourier Conventions for Impedance 216

D Special Hankel Transform 218

E Laguerre Series Coefficients 219

F Eddy Current Conductivity Measurements 220

References 224

List of Figures

1.1 Photograph of the Lady GODIVA pulsed nuclear reactor. 3
1.2 Beam power of several short-pulse spallation neutron sources 4

2.1 Schematic layout of the ISIS Neutron and Muon Source 14
2.2 Superperiod of original ISIS lattice 17
2.3 Main magnetic field of the ISIS RCS with labels 20
2.4 Some ISIS parameters through the RCS acceleration cycle. 21
2.5 Typical RF voltage through an RCS acceleration cycle 21
2.6 Typical beam intensity and loss in ISIS synchrotron 24
2.7 BPM signals of the 2 ms vertical instability on ISIS 24
2.8 BPM difference signal of a vertical instability, published in 1989 24
2.9 Measured betatron tunes throughout the RCS acceleration cycle. 25
2.10 Results from previous instability studies on ISIS 26

3.1 Layout of wake problem, with source and witness charges 30
3.2 Schematic of a circular cross-section conducting pipe 38
3.3 Example approximations to the resistive wall impedance 40
3.4 Example transverse resonator impedance 41
3.5 Schematic of a moving-wire transverse impedance measurement 45
3.6 Schematic of a two-wire transverse impedance measurement 47
3.7 Schematic of a probe-coil transverse impedance measurement 50
3.8 Benchmark of resistive wall impedance computed with CST 51
3.9 Multi-layer cylindrical beam pipe geometry; assumed for RWAL 52
3.10 Benchmark of RWAL with CST and formulas for resistive-wall impedance 59
3.11 Benchmark of RWAL with CST for a multi-layer resistive-wall impedance 59

4.1 Interaction matrix layout for linearised Vlasov equation 74
4.2 PyTMCI benchmark 1, perturbed distribution 79
4.3 Perturbed phase-space distribution for PyTMCI benchmark 1 79
4.4 PyTMCI benchmark 2, perturbed distribution 81
4.5 Perturbed phase-space distribution for PyTMCI benchmark 2 82
4.6 PyTMCI benchmark 3, mode frequencies 83
4.7 PyTMCI benchmark 3, perturbed distribution 83

5.1 ISIS synchrotron layout showing key elements 87

5.2 Typical ISIS RF screen geometry 88
5.3 Schematic of an RF screen assembly, with capacitors indicated. 89
5.4 Schematic showing the mechanical layout for the capacitor connections. 89
5.5 Photo of a singlet RF screen. 89
5.6 Photo of ceramic capacitor holder [186]. 89
5.7 Photograph of RF screen being inserted into its vacuum vessel at ISIS. . 90
5.8 ISIS lattice with alumina vacuum vessels highlighted 91
5.9 Photograph of a probe coil wrapped around a conducting wire. 93
5.10 Impedance versus frequency of a coil around a cylindrical conductor . . 93
5.11 Impedance versus conductivity of a coil around a cylindrical conductor . 93
5.12 Measured conductivity of the RF screen wires 94
5.13 Dielectric loss tangent versus frequency for alumina ceramic 95
5.14 Approximate anhysteretic BH curve for the ISIS steel laminations 95
5.15 Layers of an ISIS RF screen, vacuum vessel and magnet 97
5.16 Geometry of RWAL model to study ceramic impedance 98
5.17 $Z_1^\perp$ computed by RWAL with a lossy ceramic layer 99
5.18 $Z_1^\perp$ computed by RWAL with a shielded lossy ceramic layer 100
5.19 Geometry of annular magnet lamination model 101
5.20 An example laminated magnet CST model 102
5.21 Benchmark of annular lamination model for various crack thicknesses . . 104
5.22 Benchmark of annular lamination model for various inner radii 105
5.23 Benchmark of annular lamination model for various outer radii 106
5.24 Benchmark of annular lamination model for various permeabilities . . . 107
5.25 Estimated transverse impedance of unshielded laminations on ISIS 109
5.26 Capacitor connections on an ISIS RF screen 110
5.27 Geometry of simulated RF screens 111
5.28 $Z_1^\perp$ from CST for RF screens with and without capacitors 114
5.29 $Z_1^\perp$ from CST for RF screens with "lossy metal" and "normal" materials . 115
5.30 Experimental set-up for RF screen impedance measurements 117
5.31 Photograph of singlet RF screen probe coil $Z_1^\perp$ measurements 118
5.32 Measured $Z_1^\perp$ for a singlet RF screen with LCR meter 120
5.33 Imaginary part of measured $Z_1^\perp$ for a singlet RF screen 120
5.34 Verification of measured singlet with VNA set-up 121
5.35 Photograph of dipole RF screen measurements 124
5.36 Real part of the probe coil impedance added by the RF screen 125
5.37 Real part of the probe coil impedance, background subtracted 125
5.38 Overlay of $\mathrm{Re}(Z_1^\perp)$ of each RF screen family as computed by CST. . . . 126
5.39 Simulated $Z_1^\perp$ of a singlet RF screen with series resistors 128
5.40 Resonator parameters of singlet RF screen with series resistors 128
5.41 Simulated $Z_1^\perp$ of a dipole RF screen with series resistors 129
5.42 Resonator parameters of dipole RF screen with series resistors 129
5.43 RF screen resonator quality factor vs. series resistance 129

5.44 Sum of $Z_1^\perp(\omega)$ for simulated RF screens without series resistance 131
5.45 Schematic of an ISIS fundamental RF cavity 132
5.46 Assumed relative permeability of nickel 133
5.47 Material layers of the RF cavity calculation for RWAL 133
5.48 Resistive wall impedance per unit length of an RF cavity 134
5.49 Schematic layout of the ISIS vertical extraction kickers 135
5.50 Photograph of the ISIS extraction kicker vacuum vessel 136
5.51 Simplified ISIS extraction kicker geometry 136
5.52 Schematic of extraction kicker circuit 137
5.53 Photograph of an extraction kicker's terminating resistor 138
5.54 Photograph of an impedance measurement of extraction kicker 139
5.55 Schematic of extraction kicker impedance measurement set-up 139
5.56 $Z_1^\perp(\omega)$ measured in the spare EK1 kicker with open cables 140
5.57 Photograph of TDR measurement of extract kicker cables 141
5.58 TDR measurement of an extract kicker cable 141
5.59 Simulated electric field distribution in the extraction kicker 142
5.60 Circuit diagram used to model the extract kicker and cables 143
5.61 S-parameters predicted by circuit model of kicker and cables 143
5.62 $Z_1^\perp(\omega)$ measured in the spare EK1 kicker with matched cables 143
5.63 Photograph of multi-turn probe coil kicker impedance measurement . . 144
5.64 $Z_1^\perp(\omega)$ of the extraction kicker, measured with three-turn probe 145
5.65 Comparison of various extraction kicker impedance measurements . . . 146
5.66 Real part of the smooth focusing impedance model for $\beta = 1$. 149
5.67 Imaginary part of the smooth focusing impedance model for $\beta = 1$. . . . 150
5.68 Twiss β_y for a single superperiod of the ISIS synchrotron 151
5.69 Real part of the impedance model with Twiss-β_y weighting 152
5.70 Imaginary part of the impedance model with Twiss-β_y weighting 152

6.1 Total RF voltage during BSRM instability experiment 160
6.2 Intensity and BPM signals for various tune settings in BSRM 163
6.3 BPM signals for various tunes showing instability structure in BSRM . . 164
6.4 FFT of BSRM BPM signals, showing baseband frequency region 165
6.5 Coherent oscillation amplitude versus time for different tunes in BSRM . 166
6.6 Growth rates computed for BSRM experiment 167
6.7 Longitudinal distribution for PyTMCI BSRM calculations 168
6.8 Projection of longitudinal distribution for PyTMCI BSRM calculations . 168
6.9 BSRM PyTMCI convergence check, numbers of calculated modes . . . 170
6.10 BSRM PyTMCI convergence check, numbers of RF harmonics 170
6.11 Comparison of growth rates from PyTMCI and experiment in BSRM . 172
6.12 Dipole moment computed by PyTMCI for BSRM experiment 174
6.13 Instability phase-space distribution predicted for BSRM experiment . . . 175
6.14 Measured baseband frequencies in BSRM experiment with impedance . 178
6.15 Fundamental RF cavity gap voltage in RCS experiment 180

6.16 Second harmonic RF cavity gap voltage in RCS experiment 180
6.17 Horizontal and vertical set tunes through the RCS cycle. 180
6.18 BPM signals during RCS experiment 181
6.19 Filtered BPM difference signal during RCS experiment 182
6.20 BPM signal in RCS experiment, showing instability evolution 184
6.21 Line charge density from BPM sum signals, with processed and reconstructed versions 186
6.22 Longitudinal distribution used by PyTMCI for RCS calculations 186
6.23 Kinetic energy and synchrotron tune calculated for RCS experiment . . 187
6.24 Spectrogram of a BPM difference signal during RCS experiment. . . . 188
6.25 Measured vertical tunes versus cycle time for RCS experiment. 188
6.26 RCS PyTMCI convergence check, numbers of calculated modes 190
6.27 RCS PyTMCI convergence check, numbers of RF harmonics 190
6.28 Growth rate predicted by PyTMCI for RCS experiment 191
6.29 Instability phase-space distribution predicted for RCS experiment 192
6.30 Projected instability distribution for RCS experiment 192
6.31 Mean dipole moment per turn, predicted for RCS experiment 192
6.32 Predicted evolution of instability distribution in RCS experiment 194
6.33 Predicted modes for RCS experiment at 2 ms with higher intensity . . . 195
6.34 Measured baseband frequency at different times overlaid with impedance 197

7.1 Measured baseband frequencies during an RCS cycle 201
7.2 Singlet RF screen resonant frequency for different capacitor values . . . 202
7.3 Measured singlet RF screen impedance for different capacitor values . . . 202
7.4 Predicted growth rate for RCS experiment with different capacitor values 203

A.1 Impedance calculation for initial design of ISIS RF screens 212

F.1 Schematic of the wire conductivity measurement geometry. 221
F.2 Real part of the integrand from Equation (F.10). 223
F.3 Benchmark of coil impedance for wire conductivity measurements . . . 223

List of Tables

2.1 Important parameters of the ISIS synchrotron in RCS mode. 15
2.2 Typical values for some parameters throughout the 10 ms acceleration cycle at ISIS. 22

4.1 Parameters used for PyTMCI benchmark example 1. 78
4.2 Parameters used for PyTMCI benchmark example 2. 81
4.3 Parameters used for PyTMCI benchmark example 3. 83

5.1 Properties of first coil. 93
5.2 Properties of second coil. 93
5.3 Parameters used to calculate the impedance of the ISIS magnet laminations. 109
5.4 Dimensions of the simulated RF screens, with parameters as indicated in Figure 5.27. 111
5.5 Simulated RF screen fitted resonator $Z_1^\perp$ parameters. * - It has been assumed that all ten doublet RF screens are identical; mechanical differences of the doublet in the extraction straight are considered negligible. . 113
5.6 Resonator least-squares fit parameters from measurements for a singlet RF screen. 119
5.7 Least-squares fit parameters from measurements for a dipole RF screen. . 125
5.8 Resonator parameters used for ISIS impedance model. * - Assumed . . . 130
5.9 Extraction kicker dimensions, for variables shown in Figure 5.51. 135
5.10 Model extraction kicker resonator impedance parameters. 148
5.11 Weights for $Z_1^\perp$ due to variations in β_y, as defined by Equation (5.13). . . 151

F.1 Parameters used for finite-element benchmark of AC probe coil conductivity measurement technique. 223

Seaward ho! Hang the treasure! It's the glory of the sea that has turned my head.

— R.L. Stevenson, "Treasure Island"

1 Introduction

This thesis is concerned with increasing the scientific output of short-pulse spallation neutron sources. These artificial sources of pulsed neutrons have been used for decades to probe the structure of matter in applications as wide-ranging as fundamental magnetism and archaeological investigation. Today, these facilities are addressing some of society's most pressing issues, such as climate change and antibiotic resistance [1, 2]. They are being used to understand the properties of high-temperature superconductors and advanced steels [3, 4], and to engineer advanced microchips [5].

The neutrons at short-pulse spallation neutron sources are released when intense, short ($\lessapprox 1\,\mu s$) pulses of $\sim 1\,\mathrm{GeV}$ protons collide with a fixed target. These bunches of protons are accumulated and accelerated by high power particle accelerators. A key focus of this thesis will be to overcome an intensity limitation in these machines by partially mitigating a class of beam instability.

At present, there are five major facilities: ISIS (UK), LANSCE (USA), SNS (USA), JSNS (Japan) and CSNS (China). Although these facilities are all unique in some respect, they share the same general layout: a proton synchrotron with a fixed target, neutron moderators and suites of neutron instruments. This similarity makes it possible to address

a general problem, like beam instabilities, by addressing one instance. This thesis will focus on an instability which limits the performance of ISIS. Since beam instabilities can also limit the performance of accelerators for particle and nuclear physics, the solutions developed in this thesis could be applied to those machines too.

This introduction will describe the landscape of short pulse neutron facilities, and their trends. A section on pulsed neutron sources will summarise the historical developments and briefly describe some predecessors to today's short-pulse facilities. The focus will then move to short-pulse sources, and describe their historical developments up to the present, and conclude by looking at proposals for future facilities.

The challenges for these future machines will be discussed in a general way before the primary topic of this thesis is introduced: coherent transverse beam instabilities. Observations of these will be briefly described and it will be concluded that the field can't yet guarantee the beam of a new facility will be stable. This thesis will attempt to address that challenge by focusing on an instability which limits the performance of ISIS. Three objectives will be defined to guide the study and define the structure of the thesis.

1.1 Pulsed Neutron Sources

Now a mainstay of advanced materials science, artificial sources of pulsed, slow neutrons were first produced at the Berkeley radiation lab in 1938, only 6 years after the neutron's discovery. Here, a deuteron beam was accelerated by the 37-inch cyclotron and directed onto a beryllium target, producing fast neutrons which were moderated with paraffin wax. Thermal neutrons were selected by their time-of-flight at a detector [6, 7].

There was great interest in self-sustaining nuclear reactions at this time, and some of the earliest pulsed neutron sources were constructed at Los Alamos National Lab (LANL). In the GODIVA pulsed nuclear reactor shown in Figure 1.1, a fissile sphere was constructed in three sections with a central cavity. A fissile piston could be inserted to temporarily form a critical mass and produce a neutron burst [8, 9].



Figure 1.1: Photograph of the Lady GODIVA pulsed nuclear reactor [10].

These reactors were developed to study the neutron pulses themselves, but demand to use them for irradiation experiments increased [11]. When considering alternative sources of neutrons, Cockcroft noted that electrons from a linear accelerator could also be used to produce neutrons through the (γ, n) reaction [12]. A few years earlier, he had become the first director of the Atomic Energy Research Establishment (AERE) at Harwell, where a 3 MeV electron linac was procured for neutron experiments [13].

Harwell went on to host a number of electron linacs [13], but by the 1970's, an alternative source of neutrons was being considered. Neutron sources based on accelerator-driven nuclear spallation could produce less heat-per-neutron compared to both a reactor and an electron beam, had potentially lower background neutron fluxes compared to a reactor source and could form short intense pulses [14]. A demonstrator machine called ZING-P based in the USA had achieved peak thermal neutron fluxes one order-of-magnitude below a reactor source, but a dedicated facility was expected to exceed those of a reactor. Approval to build several such facilities came in the late 1970's.

1.1.1 Short-Pulse Spallation Neutron Sources

Neutron sources driven by hadron accelerators were first constructed in the mid 1970's, and were based on nuclear spallation from a fixed target. Today, there are several large facilities operating on this principle, and more are planned for the future. These can be divided into continuous and pulsed sources, but this thesis will focus exclusively on machines with short ($\lesssim$ 1 µs) proton pulses, which use synchrotrons to produce their intense beams.

Unlike the high-energy accelerators used in particle physics, the key performance indicator of these machines is beam-power on target; or equivalently beam intensity. Historically, they ran with as little as 1 kW of average beam power, but sources operating today can exceed 1 MW, making them some of the highest power accelerators in operation. This incredible rise in average beam power can be seen in Figure 1.2. Some of these machines and their predecessors will now be summarised.

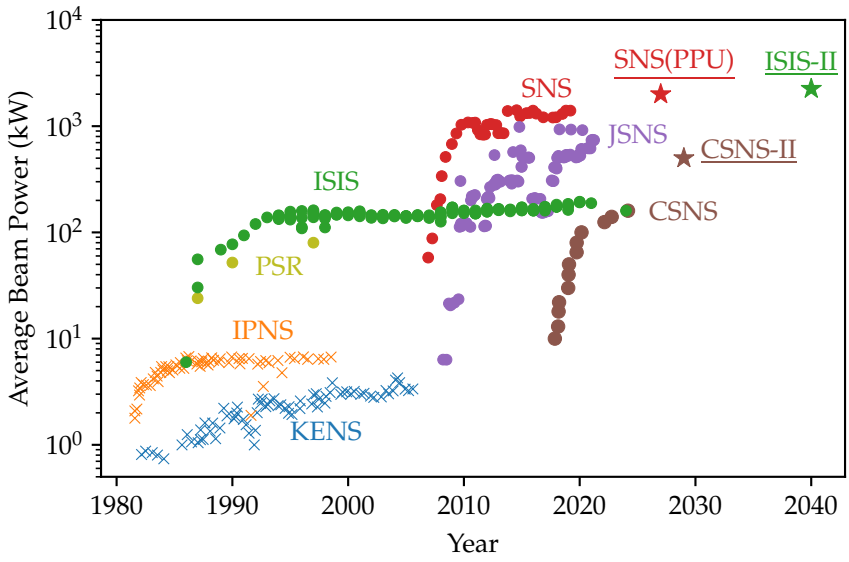


Figure 1.2: Reported beam power of several short-pulse spallation neutron sources, compiled from different sources [15, 16, 17, 18, 19, 20, 21, 22, 23, 24]. Crosses indicate machines that have ceased operations, circles are currently operating and stars are planned facilities.

1.1.2 Summary of Key Facilities

1.1.2.1 ZING-P (1974)

Based at Argonne Laboratory in the USA, ZING-P was the world's first spallation neutron source. It was intended as a prototype for a larger scale facility that was intended to be named "ZING." ZING-P was based on a beamline from the 200 MeV injection booster, "Booster-I", of the Zero Gradient Synchrotron (ZGS). This machine was a 30 Hz, Rapid Cycling Synchrotron (RCS). It began operations in January 1974, having taken three months and $30,000 to complete. It had a water-cooled lead brick target, which was surrounded by two polyethylene moderators and a beryllium reflector. It operated at 10 Hz with an average beam power of 8 W [25].

When Booster-I was replaced by a 500 MeV RCS called "Booster-II", the prototype neutron source was upgraded to ZING-P'. It had a tungsten target with a liquid hydrogen moderator and operated at 30 Hz with an average beam power of 2.4 kW. A user programme was even established, based on the running schedule of the ZGS [25].

Despite the success of this prototype, the original proposal to build ZING was rejected, apparently because its design was too modest [26]. After several changes, a design was eventually approved and the Intense Pulsed Neutron Source (IPNS) project was given the go-ahead in 1978 [1].

1.1.2.2 KENS/ KENS-II (1980)

The KEK Neutron Source and Neutron Scattering Research Facility (KENS), was originally proposed in 1975 as a way to utilise surplus protons from the existing 500 MeV proton booster synchrotron [27]. Approval for the project came in 1977, construction was completed in 1980 [28] and the first practical beams were delivered that same year [29]. After an upgrade to its target systems in 2000, KENS became known as KENS-II which ran until 2006 [15].

[1] ZING was renamed to IPNS because its designers felt an "unpronounceable acronym" would be looked upon more favourably [26].

The facility was commissioned with an average beam power of 1 kW, but by 1998 this had increased to 3 kW [30]. This increase in beam power was achieved, in part, by taking advantage of the charge-exchange injection technique [31], which is still used today at the world's most advanced neutron sources.

KENS ran for more than 25 years and its closure coincided with the construction of a new MW-class neutron source, JSNS, at the Japan Proton Accelerator Research Complex (J-PARC). This facility produced its first neutrons four years after KENS ceased operations, and remains one of the world's most powerful spallation sources [32].

1.1.2.3 IPNS (1981)

The Intense Pulsed Neutron Source (IPNS), was commissioned in 1981. It was based on a 500 MeV proton RCS, with an injection energy of 50 MeV but typically operated with an extraction energy of 450 MeV, giving 7 kW of average beam power. A follow-up machine, IPNS-II would have had a higher average power, but was never constructed [33].

IPNS operated for more than 25 years, but was shut down in 2008 [34], around the same time that the MW-class Spallation Neutron Source (SNS) was coming online. Despite a challenging financial environment, it produced excellent scientific output and continued to operate at the forefront of the field, for example by experimenting with stripping foil materials and investigating alternative accelerator schemes [35, 36].

1.1.2.4 ISIS (1984)

ISIS is the longest serving short-pulsed spallation neutron source in the world, and Europe's first spallation neutron source. Its construction was approved in 1977 and it produced its first neutrons in December 1984 [37, 38]. Its design beam power of 160 kW was a significant increase compared to earlier facilities. The facility was based on an 800 MeV proton RCS, but this energy was not achieved until 1990. Commissioning was initially carried out at 550 MeV then pushed to 750 MeV in 1987, giving an average power of 38 kW [39]. ISIS achieved its design beam power in 1997.

Towards the end of the 1990's, demand for different kinds of neutron experiments motivated the construction of a second target station, TS2. Upon completion in 2008, the facility's nominal beam power for both targets increased to 187 kW [40], but equipment improvements allowed it to operate at 192 kW in the late 2010's. The machine continues to operate today, and has recently celebrated its 40th birthday.

1.1.2.5 LANSCE/ PSR (1985)

The Los Alamos Meson Physics Facility (LAMPF) began operations in 1972. It was based at LANL and was driven by an 800 MeV H^+ and H^- linear accelerator [41]. It was used as a spallation neutron source from around 1977, and delivered neutrons to the Weapons Neutron Research facility, parts of which were later renamed the Los Alamos Neutron Scattering Centre (LANSCE) [42]. LAMPF was renamed to LANSCE in 1995 [43].

Originally, the LAMPF linac had an average design current of 1 mA, but this could only be achieved with a $\sim$ 750 µs long pulse, which is too long for an optimised short-pulsed source. An accumulator ring, the Proton Storage Ring (PSR), was added in 1985 to compress these long pulses to $\sim$ 0.27 µs, making LANSCE a short-pulsed spallation neutron facility with an average beam power of $\sim$ 80 kW. This facility continues to operate today, and the LANSCE Modernisation Project (LAMP) has been initiated to extend operations until at least 2050 [44].

1.1.2.6 SNS (2006)

The decision to construct a new neutron scattering facility in the USA was taken in 1996 as a collaboration between five national laboratories; this included Argonne and LANL which hosted the USA's two existing sources. The Spallation Neutron Source (SNS) came online in 2006 and was producing 1 MW of beam power by the end of 2011, which made it the world's most powerful short-pulsed spallation neutron source. More recently, the facility has operated a user cycle with 1.7 MW [21]. The facility is based on a 1 GeV superconducting linac and an accumulator ring.

1.1.2.7 JSNS (2008)

As the KENS facility came towards the end of its operational life, the Japanese Spallation Neutron Source (JSNS) [45] was being designed. It was based at the J-PARC RCS, with beams extracted to the Materials and Life Science experimental Facility, although the RCS also inject into the 30 GeV main ring for particle physics research. Construction of the facility started in 2001, was completed in 2008 and the facility's first neutrons were produced that same year. JSNS is based on a 400 MeV–3 GeV proton RCS with a design beam-power of 1 MW. The facility currently operates close to its design beam power of 1 MW, although close to 1.5 MW has been demonstrated [17].

1.1.2.8 CSNS (2017)

The Chinese Spallation Neutron Source (CSNS) is currently the world's newest short-pulse spallation neutron source. By choosing to operate with a beam power of 100 kW, CSNS has focused on becoming a reliable user facility with upgrade potential [46]. CSNS is based on an RCS accelerator with an injection energy of 80 MeV and an extraction energy of 1.6 GeV. It came online towards the end of 2017, reached its design power in 2020, operated at 140 kW in 2022 and has demonstrated 170 kW [47].

1.1.3 Future Facilities

Almost every major short-pulsed spallation neutron facility operating today is considering opportunities for upgrades or new facilities: the ISIS-II project is investigating beam powers in the range 1.25 to 2.5 MW [48]; the SNS Proton Power Upgrade (PPU) will eventually increase the operational power of SNS to 2.8 MW [49] with 2.0 MW expected in 2027 [21]; JSNS is exploring opportunities to operate with a 1.5–2.0 MW beam [17]; CSNS-II is expected to increase the operational power of CSNS to 500 kW [50].

Whilst each project may differ, they all share the objective to increase average beam power compared to their respective predecessors. The trend towards higher beam powers, clear in Figure 1.2, is likely to continue as demand for neutron science grows [51].

1.2 Challenges for Future Short-Pulse Spallation Sources

The successful, long-term operation of an accelerator-based facility requires hands-on maintenance of its many complex systems. Radioactive dose rates must allow this to be performed within legal dose limits; and ideally far below them. Increases in intensity must be coupled with relative reductions in beam-losses, so that residual activity is maintained at current levels. Reducing beam-loss is therefore a fundamental challenge to achieve higher intensity beams at future short-pulse spallation neutron sources.

Beam losses are driven by several different processes, and different accelerator configurations can be more or less susceptible to certain effects. Space-charge can drive emittance growth and beam losses, and is particularly important for RCS's due to their lower injection energies. The higher injection energy of an accumulator ring will reduce the effects of space-charge, but can cause beam losses due to uncontrolled stripping of H^- ions [52]. Scattering from stripping foils used in the charge exchange injection process are another significant source of beam loss.

Coherent transverse instabilities are said to occur when a beam oscillates with a growing amplitude in a transverse direction. They can cause beam loss if this amplitude becomes too large. They are caused either by electron clouds or beam-induced electromagnetic wake fields. Instabilities caused by wake fields are the primary focus of this thesis, and their impact on pulsed spallation neutron sources will now be briefly reviewed.

1.2.1 Coherent Transverse Instabilities at Existing Facilities

Whilst designers of the earliest machines made significant effort to avoid instabilities, they were nevertheless observed on all early machines. The instability observed on the PSR was ultimately found to be caused by electron clouds [53], but those on ISIS and IPNS were both thought to be caused by wake fields. The intensity of both IPNS and ISIS have been limited by these instabilities, and this is still the case at ISIS.

More recent facilities drew on past experiences and made extensive use of modern tools to avoid instabilities. For example, SNS, the J-Parc RCS, and CSNS all have TiN coated vacuum vessels [54, 55, 56]. Despite these efforts, coherent instabilities have been observed at both JSNS and CSNS [57, 58], and are thought to be driven by wake fields [59, 60, 58]. SNS has been reported to operate at $> 1\,\mathrm{MW}$ without observing coherent beam instabilities [61], although this would be more challenging to achieve on an RCS, where beams are typically stored for an order of magnitude more time.

To reach their current operational beam powers, ISIS, JSNS and CSNS have adopted sophisticated beam dynamics methods to reduce instability growth rates. At ISIS, it was found that a fast vertical tune ramp and an asymmetric line charge density both reduced the growth rate [62, 63]. JSNS and CSNS both mitigate their instabilities by optimising chromaticity throughout their acceleration cycles [57, 58].

1.2.2 Transverse Instabilities at Future Facilities

Among the five facilities operating today, coherent transverse instabilities on operational beams have been documented in at least four. Wake-driven instabilities are the most prevalent, limiting intensity at ISIS and necessitating active mitigation at JSNS and CSNS, despite design-stage efforts to avoid them. Newer facilities are not immune, with both the oldest and the newest facilities reporting instabilities [64, 57, 58].

If the models of these machines are otherwise complete and accurate, then this would imply that either the theory of these instabilities is not making accurate predictions, or there are major sources of wake fields yet to be mitigated or discovered.

A solution to this will be multi-faceted, but one approach is to understand and mitigate instabilities on existing machines. The lessons learned might be applicable to future facilities, and could provide short-term benefits to existing particle accelerators. Since there is no clear distinction between instabilities observed at older and newer neutron sources, this approach can be applied to any facility operating today. This approach will be adopted here with a focus on ISIS.

1.3 Thesis Objectives

Having adopted the strategy of addressing the coherent instability on ISIS, three objectives are now defined to guide this study.

Since ISIS does not yet have a detailed transverse driving impedance model, the first objective will be to determine the driving impedance contributions of key machine elements. Extensive resources would be required to produce a very general model, so the focus will be on potential drivers of the instability which limits operational performance. This impedance model will be developed in Chapter 5, which will draw on the foundations developed in Chapter 3, where the theory of impedances and wake fields will be reviewed and new tools for computing them introduced.

The second objective is to understand whether the widely accepted theory of coherent transverse instabilities without space charge, can make even partially accurate predictions for the ISIS RCS. The developed impedance model will therefore be used as an input to analytical calculations in Chapter 6, where predictions about transverse coherent instabilities on ISIS will be compared with experimental observations. This will draw on the tools developed in Chapter 4, where the theory of coherent transverse instabilities will be reviewed and new tools for computing them introduced. To ensure that the most accurate predictions are made within the limitations of this analytical approach, a more general theory than previous studies on ISIS will be adopted.

The third objective is to identify methods of improving beam stability on ISIS. If the driver of an instability which limits operational performance is identified, then changes to the relevant equipment should be explored with an aim to reduce the instability growth rate. This will be done in Chapter 7, which will use the conclusions of Chapters 5 and 6.

Perhaps I should not have been a fisherman, he thought. But that was the thing that I was born for.

— E. Hemingway, "The Old Man and the Sea"

2 The ISIS Neutron and Muon Source

In the year that ISIS produced its first neutrons, its design beam power was ~ 23 times higher than the world's next most powerful short-pulse neutron source, IPNS. "They're going to blow us out of the water... It's a heck of a machine," was the way an unnamed American source put it at the time [65]. The proposal to build SNS, which was later renamed ISIS, came in 1976, and followed a detailed consideration of many alternative sources of pulsed neutrons [37]. The decision to build ISIS as a pulsed spallation neutron source followed the decision to discontinue all British high energy physics facilities in favour of its commitment to CERN and other overseas labs, which meant that the NIMROD proton synchrotron was to be decommissioned [66]. As well as producing the highest peak neutron fluxes, cost estimates for a spallation neutron source were lower than those for a dedicated electron linac because infrastructure from NIMROD could be reused [37]. The decision to build ISIS was approved in 1977 and it produced its first neutrons in December 1984.

A schematic of the ISIS facility as it stands today is shown in Figure 2.1. The accelerator complex occupies the top-right of the figure, and is split into a 70 MeV linear accelerator and an 800 MeV RCS. There are two extraction lines from the synchrotron

(EPB1 and EPB2), one directed to the Target Station 1 (TS1) and the other to Target Station 2 (TS2). In its operational configuration, neutrons are produced when proton beams collide with solid tungsten targets situated at the end of these extraction lines. The kinetic energy of these neutrons is initially too high for neutron science applications, so moderators reduce it to thermal levels before the neutrons are transported to suites of instruments which surround the target. During routine operations, this process is repeated at 50 Hz, with four out of five pulses directed to TS1 and one in five to TS2. Muons are produced at an intermediate graphite target in EPB1, around 20 m upstream of the tungsten target. They are used for different kinds of experiments.

As a user facility, ISIS is primarily designed to fulfil the requirements of its users, but it is a versatile machine and can be operated in more than one configuration. The operational configuration where neutrons are produced for users will be referred to as RCS mode, and key parameters for this mode are listed in Table 2.1. As well as RCS mode, the ISIS synchrotron can also be configured to operate as a storage ring, which is referred to as Storage Ring Mode (SRM) or Bunched SRM (BSRM). These configurations are used for accelerator studies, and many parameters from Table 2.1 remain unchanged. The beam remains at its injection energy, the intensity is generally reduced and the beam can either be bunched or coasting depending on the RF settings.

Key elements from the ISIS accelerator complex will now be described, as well as the operational characteristics of key equipment. An overview of how this equipment is used in RCS mode and SRM will then be given. The transverse coherent instability which limits the synchrotron's operational performance will be introduced, and the techniques developed to mitigate it will be described. Finally, efforts to understand the nature of this instability will be discussed with a focus on studies carried out in SRM.

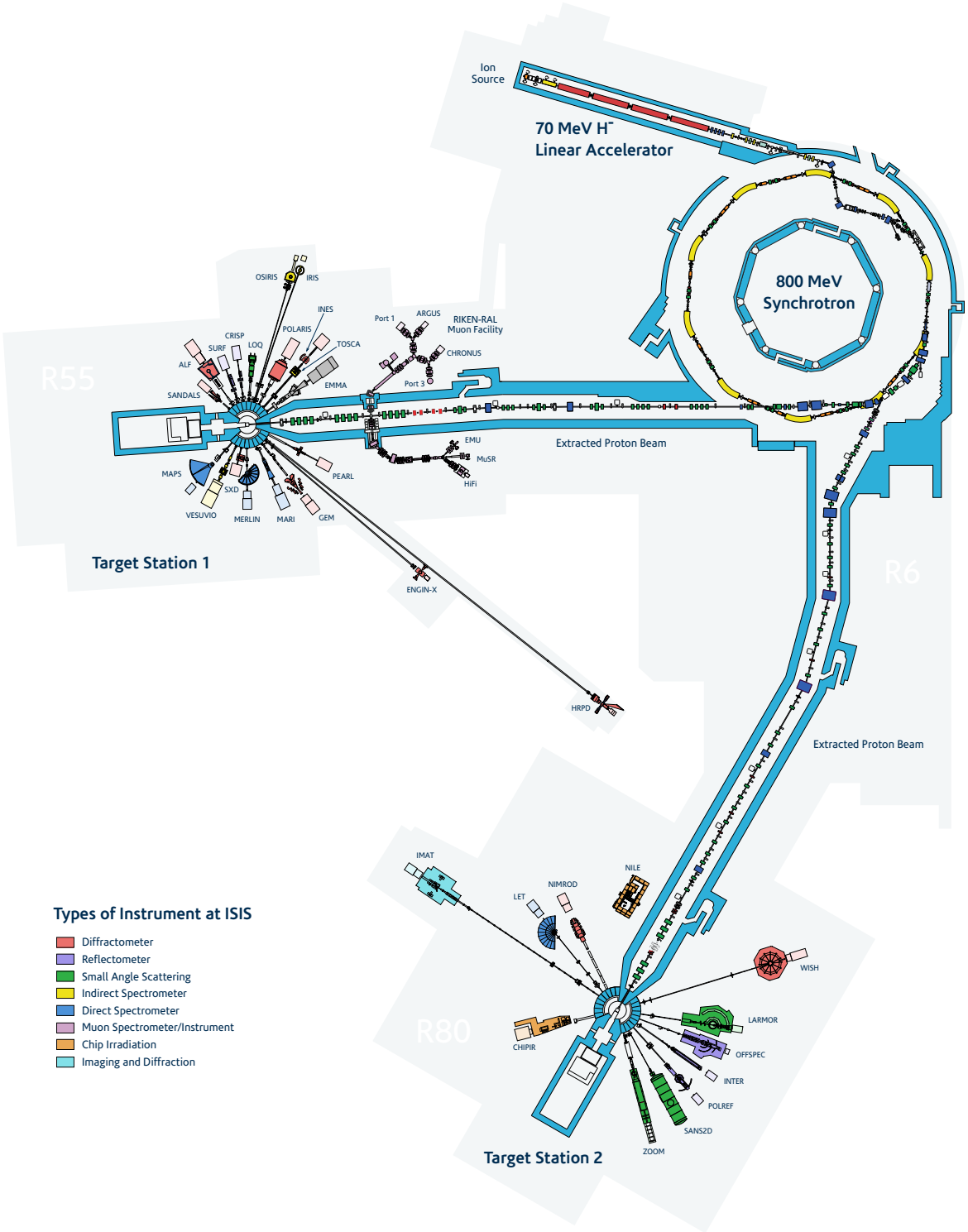


Figure 2.1: Schematic layout of the ISIS Neutron and Muon Source, with the linear accelerator towards the top, 800 MeV proton RCS and two extracted proton beamlines (EPB1 and EPB2) connecting the RCS to the target stations. Neutron instruments surround each of the two target stations. The intermediate target and muon instruments are towards the end of EPB1 [67].

Table 2.1: Important parameters of the ISIS synchrotron in RCS mode.

Parameter	Symbol	Value
Injection Kinetic Energy		70 MeV
Extraction Kinetic Energy		800 MeV
Circumference	C	163.36 m [68]
Number of Superperiods		10
Dipole Bend Radius		7 m
Nominal Protons Per Bunch	N	1.5×10^{13}
Number of Bunches	M	2
Repetition Rate		50 Hz
Transition Gamma	γ_{Tr}	5.034
Nominal Tunes	$Q_{\mathrm{H}}, Q_{\mathrm{V}}$	4.31, 3.83
Chromaticity	ξ_x, ξ_y	−1.1, −1.1 [69]
Number of Fundamental Cavities		6
Number of Second Harmonic Cavities		4

2.1 Description of the ISIS Accelerator Complex

2.1.1 The ISIS Injector

The ISIS injector consists of: a Penning type H^- ion source; a Low Energy Beam Transport (LEBT) line; a radio frequency quadrupole (RFQ); a four-tank Alvarez style drift-tube linac and a High Energy Drift Space (HEDS) which transports the accelerated beam to the synchrotron. These elements occupy the uppermost part of Figure 2.1, and span up to the point where the injector meets the synchrotron.

The Penning type ion source, produces a 50 mA beam of 35 keV H^- ions [70]. These are extracted in unbunched pulses of between 200 and 240 µs, and then guided with solenoid magnets through the LEBT to the RFQ. This accelerates the beam to 0.67 MeV and focuses it transversely, whilst its 202.5 MHz operating frequency forms the beam into bunches with a ~ 5 ns spacing [71]. These bunches then pass directly into the linear accelerator.

The linear accelerator is approximately $40\,\mathrm{m}$ long. It is divided into four Alvarez style drift-tube tanks which also operate at $202.5\,\mathrm{MHz}$ to match the bunch structure coming from the RFQ. These tanks produce a $\sim 70\,\mathrm{MeV}$, $\sim 25\,\mathrm{mA}$ H^- beam at the output [72], which passes into the HEDS. This consists of focusing and bending magnets, a debuncher cavity, a pulsed vertical sweeper magnet and several diagnostic devices. As shown in Figure 2.1, the HEDS passes over the top of the synchrotron and connects to it from the inside radius.

2.1.2 The ISIS Synchrotron

The synchrotron is composed of ten superperiods, as shown in Figure 2.1, conventionally labelled SP0 to SP9. SP0 is dedicated to injection, and contains the apparatus for the stripping foil and injection bump magnets. SP1, which is immediately adjacent to SP0, is dedicated to extraction, and contains the extraction kickers and septum magnet; it also houses the machine's graphite collimators. The other superperiods house radio-frequency (RF) cavities and a range of diagnostic systems.

Each superperiod is made up of a combined function dipole (BD), a doublet quadrupole (QF, QD) and a singlet quadrupole (QC) as shown in Figure 2.2. These elements are referred to as the "main magnets" because in RCS mode they operate as part of a single $50\,\mathrm{Hz}$ resonant circuit with a DC offset, which fixes the facility's repetition rate [68, 73]. Even when operating as a storage ring, it is customary to talk about timing in terms of a reference phase of this sinusoidal magnetic field; this will be explained in more detail in Section 2.2.1.

In addition to these main magnetic fields, ISIS uses around forty correction magnets to optimise the closed orbit and betatron tune throughout the acceleration cycles. Each correction magnet has its own programmable power supply, and can be independently configured. The correction ("trim") quadrupoles are labelled as QTD and QTF in Figure 2.2, and can be used to control the betatron tune. The other correction magnets are primarily for horizontal and vertical steering, and are distributed around the ring.

Space was reserved for higher-order magnets (OC), as well as in some less regular locations that aren't shown. Two sets of four octupoles were installed to suppress transverse instabilities [68, 74]. These were not used operationally and many of them have been removed from the synchrotron; the remaining magnets are not routinely powered. Two sets of three sextupoles were also installed to correct sextupole field errors [75], but weren't used operationally either. Many of these were removed, and the remaining magnets are not routinely powered so the machine operates at its natural chromaticity. The opportunity to use these magnets is now being investigated again [76].

The vacuum vessels inside these fast cycling magnets are constructed from alumina ceramic with an internal conducting RF screen. These ceramic chambers occupy more than 50 % of the ISIS circumference, and were adopted to prevent the Eddy currents which would flow in a conducting chamber. These currents would otherwise cause excessive heating and a reduced field quality [77].

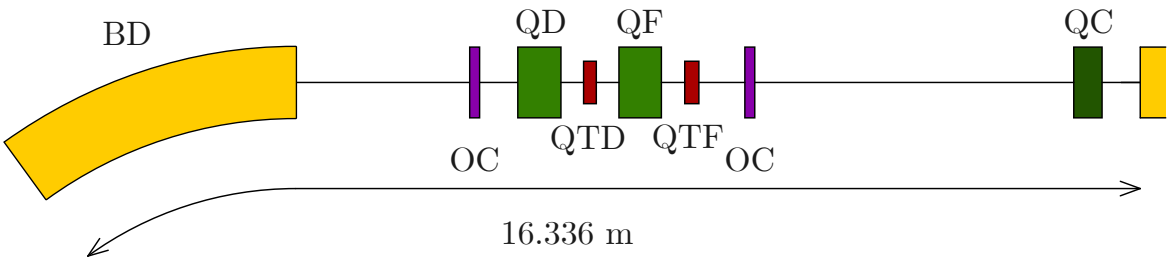


Figure 2.2: Magnets within a superperiod of the originally proposed ISIS lattice [68]. BD is a combined function dipole, QD and QF form the doublet quadrupoles and QC is the singlet quadrupole. QT are trim quadrupoles and OC are for higher order magnets.

The H^- beam from the HEDS is injected into the synchrotron on a bumped orbit, where a carbon stripper foil removes electrons with ~ 98 % efficiency to produce a proton beam [78, 79, 80]. It takes ≈ 135 revolutions of the synchrotron to accumulate the ≈ 200 µs injected pulse, so the injected and recirculating beams are combined in this process. After the beam has been accumulated, the injection bump is removed to shift the trajectory away from the foil.

Acceleration and bunching in the synchrotron are achieved with six fundamental RF cavities which operate with harmonic number $h = 2$ ($f_{RF} = hf_{rev}$). They are a ferrite-loaded shorted coax construction [81], and each one has two accelerating gaps. Four second harmonic cavities ($h = 4$) were added to increase the bunching factor and improve the trapping efficiency [82]. A programmable delay between the fundamental and second harmonic cavities is used to optimise the beam's longitudinal distribution. To accommodate the large revolution frequency swing required for operational RCS mode (0.67 MHz to 1.54 MHz), the resonant frequencies can be controlled with a bias current, which adjusts the permeability of the cavities' ferrite through its hysteresis curve.

In addition to magnets and RF cavities, the ISIS synchrotron contains a large number of diagnostic systems [83]. These measure beam properties and allow the various magnets and cavities to be optimised; they also provide key inputs to machine protection systems and feedback loops. Key diagnostics that will be used in this thesis include: beam intensity monitors, which measure the average current; beam position monitors (BPMs), which measure the average transverse offset and beam loss monitors (BLMs), which detect secondary particles produced when the primary beam collides with the vacuum system.

2.2 Operating Modes of ISIS

2.2.1 Operational RCS Mode

This mode is used for routine operation of the ISIS facility, where neutrons and muons are produced from its targets. Whilst in this mode, users are often able to perform experiments at the instruments which surround the targets. Beam power on target is a key performance indicator in this mode, so ISIS is made to operate with the highest intensity possible without causing excessive beam loss.

In this mode, the main magnets operate as part of a single resonant circuit with a DC offset. The magnetic field of the main dipoles is shown in Figure 2.3, and given by

$$B(t) = B_{\mathrm{DC}} - B_{\mathrm{AC}} \cos\left(2\pi f_{\mathrm{rep}} t\right), \tag{2.1}$$

where $f_{\mathrm{rep}} = 50\,\mathrm{Hz}$ is the repetition rate, $B_{\mathrm{DC}} = 0.4365\,\mathrm{T}$ and $B_{\mathrm{AC}} = 0.2605\,\mathrm{T}$. The minimum of this sinusoidal field is said to occur at the RCS cycle time of $0\,\mathrm{ms}$, and it is customary to refer to times relative to this; even in SRM when there is no AC field. For example, the HEDS H^- beam is usually injected into the synchrotron around $-0.4\,\mathrm{ms}$, and injection is normally completed by around $-0.2\,\mathrm{ms}$.

Space-charge forces are considerable at injection, with peak incoherent tune spreads of ~ 0.5 [69]. Transverse phase space painting is used reduce the impact of space charge by controlling the transverse emittance of the accumulated beam. In the vertical plane, this is achieved by the vertical sweeper magnet at the end of the HEDS, which adjusts the beam's vertical position at the foil. Horizontally, painting is achieved by the shifting dispersive orbit in the synchrotron due to the falling magnetic field; see Figure 2.3.

During injection, the amplitude of the RF cavity gap voltages are maintained below $\approx 1\,\mathrm{kV}$-per-gap, or $< 8\,\%$ of values used later the RCS cycle. This has the effect that the accumulated beam is almost coasting, but it is captured by rapidly increasing the RF cavity gap voltages. This process is referred to as "trapping", and whilst non-adiabatic, it is $\sim 97\,\%$ efficient and typically completed by $\sim 1\,\mathrm{ms}$ as indicated in Figure 2.3.

Acceleration in the synchrotron takes place on the rising part of main magnet's sinusoidal field, and therefore takes $10\,\mathrm{ms}$ to complete. To maintain a closed orbit, the RF cavity resonant frequencies and gap voltages are synchronised with the main magnetic field, and can be derived as shown in Figure 2.4; some numeric quantities are also listed in Table 2.2. A typical plot of one-turn-voltage throughout the $10\,\mathrm{ms}$ acceleration cycle is also shown in Figure 2.5, which is a sum of all the gap voltages for each harmonic.

Once the beam has reached its final energy, an extraction trigger is generated by the neutron instruments which begins the extraction process. Three vertical kicker magnets in SP1 are synchronised for their fields to rise inside the ~ 200 ns gap between proton bunches, and remain energised until both bunches have been kicked. The deflected bunches enter the extraction aperture of a septum magnet and are then transported to their designated target station.

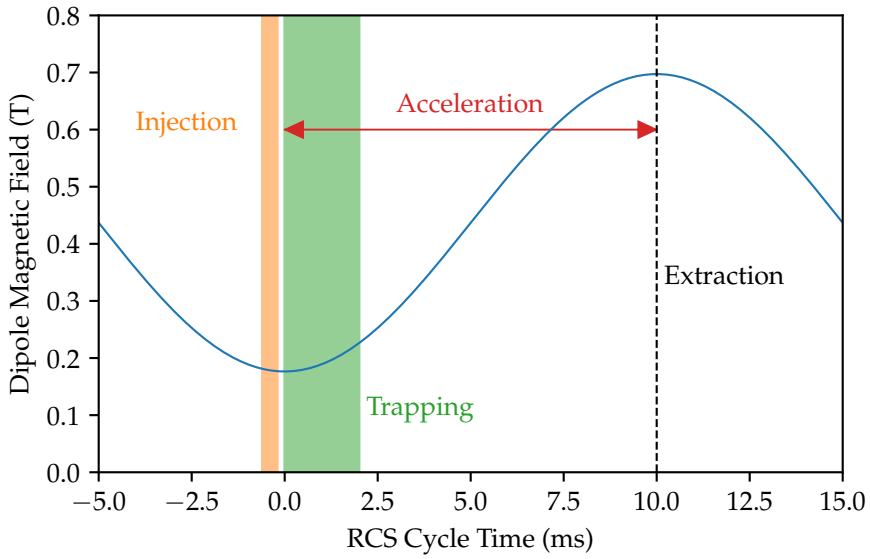


Figure 2.3: Dipole magnetic field throughout the RCS cycle, adapted from [80]. Injection is labelled between −0.4 and −0.2 ms, trapping from 0 to 2 ms, acceleration between 0 and 10 ms and extraction at the end of the RCS cycle.

2.2.2 Storage Ring Modes

To facilitate studies of the ISIS machine, the synchrotron can be configured to operate as a storage ring with the beam at the injection energy. This removes the complication of sweeping revolution frequencies, and can simplify the analysis of beam behaviour. For example, previous studies have used SRM and BSRM mode to investigate the transverse impedance of ISIS and bunched beam instabilities [84, 80].

To operate the synchrotron as a storage ring, the main magnet is driven with a DC current and ramping currents on the correction magnets are usually replaced by DC

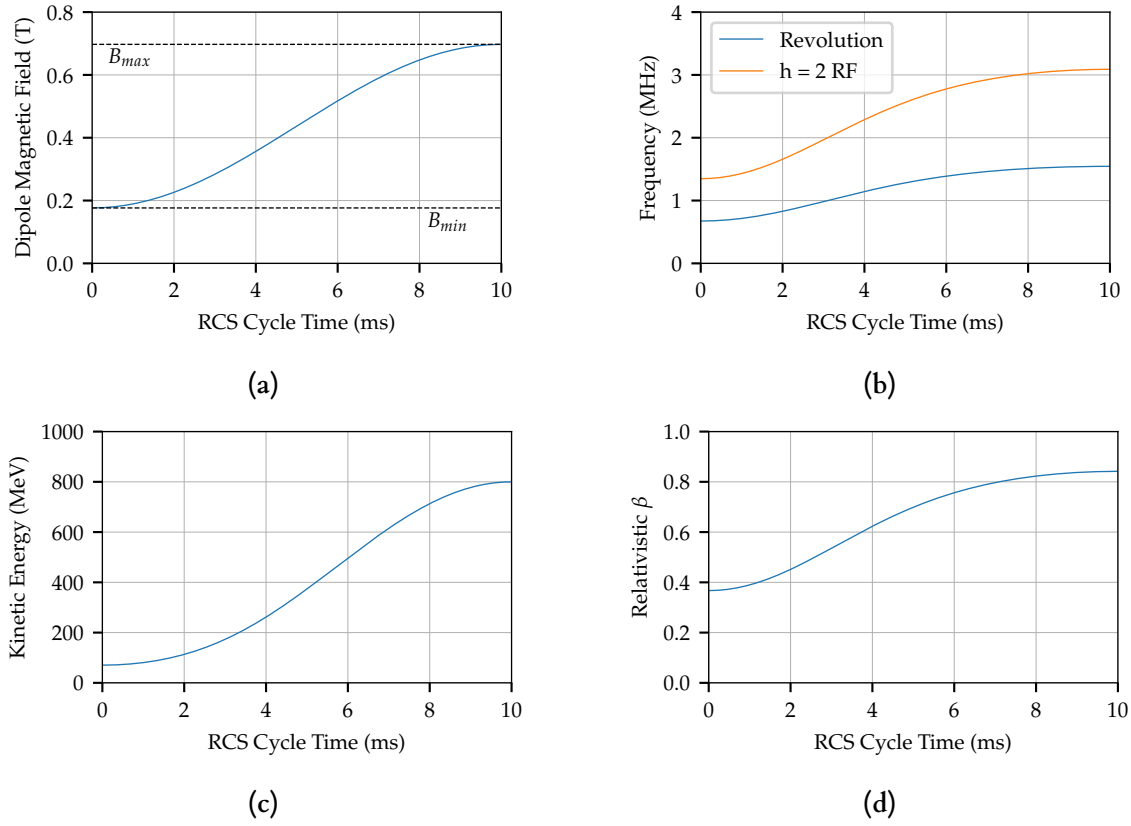


Figure 2.4: Beam and synchrotron parameters throughout the RCS acceleration cycle.

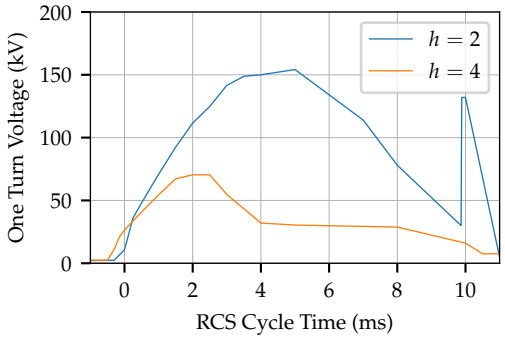


Figure 2.5: A typical one turn voltage of the fundamental and second harmonic cavities through the RCS acceleration cycle. This is from the sum from all RF cavities.

values after injection. Closed orbits can be adjusted with the steering magnets, whilst the trim quadrupoles can be used to control the betatron tune. When operating in this configuration, the beam is not extracted, and 100 % beam loss occurs in the synchrotron

Table 2.2: Typical values for some parameters throughout the 10 ms acceleration cycle at ISIS.

RCS Cycle Time (ms)	Rev. Frequency (MHz)	Kinetic Energy (MeV)	β
0	0.674	70.4	0.367
1	0.715	80.6	0.390
2	0.828	113.2	0.451
3	0.983	173.1	0.536
4	1.144	261.6	0.623
5	1.283	373.6	0.699
6	1.388	496.7	0.757
7	1.463	615.1	0.797
8	1.510	713.1	0.823
9	1.536	777.5	0.837
10	1.545	800.0	0.842

hall. To limit equipment activation, beam intensity is typically reduced to between ~ 10 and 20 % of operational intensity, and the machine's repetition rate is reduced to ~ 1 Hz.

In SRM, a coasting beam is accumulated and stored. All RF cavities have a demand gap voltage of 0 V and have their resonant frequencies set off-tune to limit self-bunching of the coasting beam. SRM beams cannot be stored for significantly longer than 10 ms, not least because they are driven onto the foil by the injection bump magnets at 50 Hz. It is therefore assumed that an injected pulse is completely lost before the next pulse arrives.

In the case of BSRM, all but one of the fundamental RF cavities and all the second-harmonic RF cavities are configured to be off-tune and set to have a demand gap voltage of 0 V. The remaining fundamental RF cavity is configured with $h = 2$, so that two bunches are formed, and the demand gap voltage can be varied whilst the beam is stored.

2.3 Intensity Limitations of the ISIS Synchrotron

A typical measurement of average beam loss around the synchrotron ("BLM Sum Loss") in an operational RCS cycle is shown in Figure 2.6. The causes of this beam loss can be attributed to processes known to take place at particular times. Before $0\,\mathrm{ms}$, beam losses are primarily caused by foil scattering; between 0 and $2\,\mathrm{ms}$ they are mainly attributed to longitudinal trapping and space-charge effects; beam losses between 2 and $\sim 3\,\mathrm{ms}$ are mostly attributed to a head-tail instability [80].

Observations of this instability will now be described, as well as the measures taken to suppress it during routine operations. Key results from a recent measurement campaign will also be summarised [80].

2.3.1 The 2 ms Head-Tail Instability

The basic nature of this coherent, vertical instability can be understood from Figure 2.7, which shows the difference signal of a beam position monitor overlaid for several turns. The fact that this distribution has been measured by a vertical beam position monitor verifies that this is a vertical coherent instability. Its distribution along the bunch has one low-amplitude node towards the centre, which is characteristic of an $l = 1$ head-tail mode. The scope trace in Figure 2.8, published in 1988, shows a similar distribution.

The position monitor signal shown in Figure 2.7 was recorded after second harmonic cavities had been added to the RCS mid-2000's [82], so only fundamental cavities were installed when the earlier figure was acquired. Although there is no generally accepted theory for coherent instabilities in the presence of second harmonic cavities, the similarity of the observed distribution, its rapid growth rate and its appearance at the same time through the RCS cycle, have led to the assumption that the instability observed today shares a common cause with the one observed during the commissioning of ISIS.

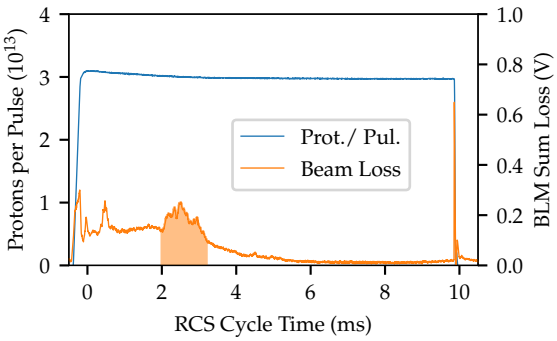


Figure 2.6: Typical plots of beam intensity and sum beam-loss at ISIS, through a 10 ms RCS cycle [85, 80]. Highlighted region is associated with coherent instability.

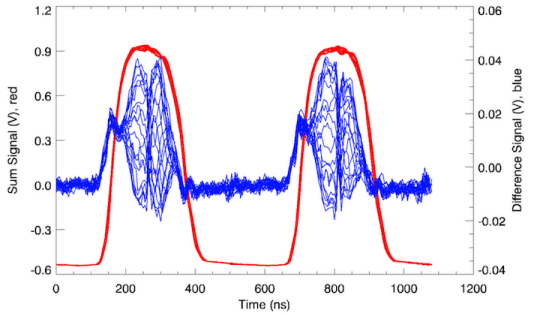


Figure 2.7: Sum (red) and difference (blue) signals from a vertical BPM with each line taken during a single turn, starting from around 2.6 ms into the RCS cycle [80]. The oscillation is superimposed on a closed-orbit offset.

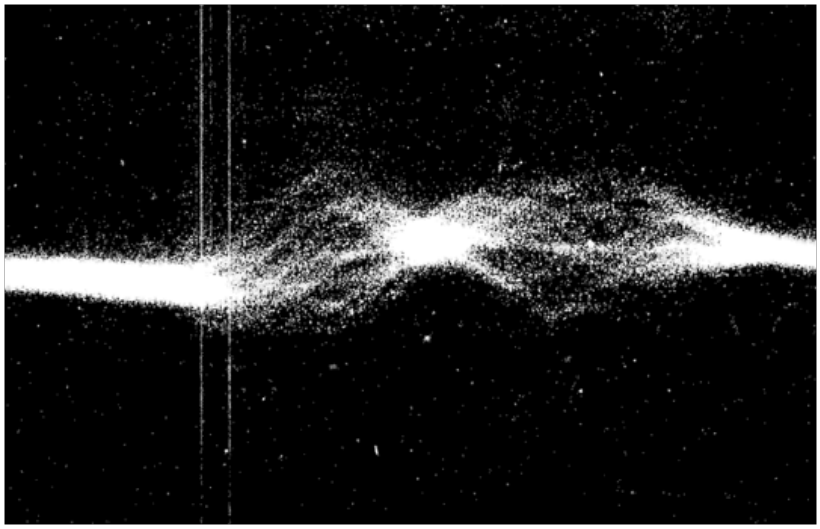


Figure 2.8: Scope capture of vertical dipole moment along a bunch, with each line being from a single revolution [39].

2.3.2 Mitigation in RCS Operations

The instability at 2 ms was observed before ISIS reached its design beam power [39], so techniques to limit the beam loss it caused were developed. The vertical tune had been set high at injection to limit the impact of direct space-charge, but it was found that head-tail losses could be significantly reduced by rapidly ramping the vertical tune from ~ 3.83 to 3.72 at 2 ms [86]. Figure 2.9 shows recent measurements of coherent tune.

Ramping the vertical tune with the trim quadrupoles is still the primary mitigation technique used today, but as the beam's intensity increased, additional mitigation strategies became necessary. It was found that the growth rate could be further reduced by generating an asymmetric line-charge density with the second-harmonic RF cavities [63, 69], which is now done routinely. Beam loss reduction has been demonstrated with an experimental damping system [87], but an operational version has not yet been commissioned.

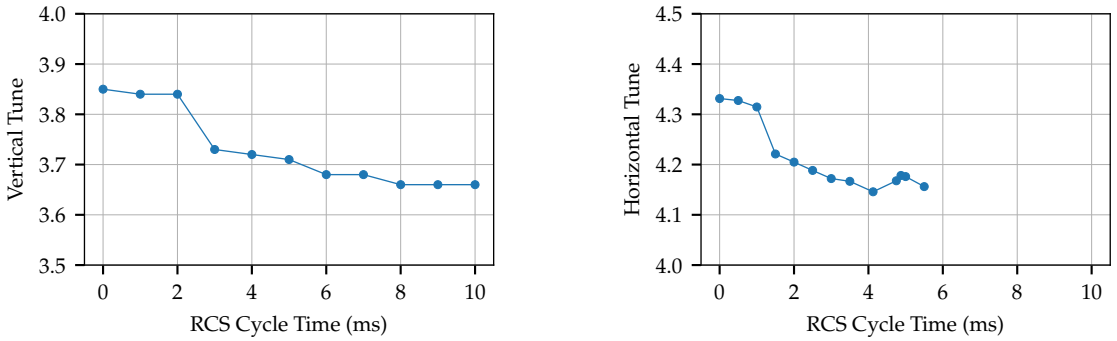


Figure 2.9: Typical values of (a) vertical and (b) horizontal measured tune throughout the RCS acceleration cycle [85].

2.3.3 Summary of Key Observations

Instabilities of the kind observed at 2 ms are ordinarily driven by beam-generated wake fields, and are therefore caused by some equipment installed in the ISIS RCS. The observation that the instability grew more quickly as the tune approached an integer, and the fact that key equipment had been designed to prevent instabilities (see Appendix A), led early investigations to conclude that it was caused by the resistive vacuum vessels and RF screens. This conclusion was reiterated by more recent investigations [88].

On the basis of this conclusion, and accepting some simplifying assumptions to head-tail theory, it was predicted that head-tail modes with $|l| = 2$ and 3 should have the fastest growth rates, but the single node observed in Figure 2.7 is consistent with an

$|l| = 1$ instability. Furthermore, characteristic growth times were predicted to be on the order of ms, but measured values of 200 to 600 µs are typical [88, 64, 80]. These discrepancies remain unexplained and have motivated an alternative formulation of coherent transverse instability theory [86], and more recently, an extensive measurement campaign to rigorously characterise the instability [80].

In the course of this campaign, it was found that in BSRM the growth rate rose as the tune approached an integer, but fell again before reaching it, as shown in Figure 2.10 [84]. Experiments performed in SRM with a coasting beam reproduced this, indicating a resonator impedance at ~ 85 kHz, with a magnitude on the order of $1\,\mathrm{M\Omega\,m^{-1}}$, which is also shown in Figure 2.10 [80]. To put this into perspective, coherent instabilities on the JParc RCS are driven by impedances on the order of $10\,\mathrm{k\Omega\,m^{-1}}$ [60]. Whilst the resonant frequency of the identified narrowband impedance means it is unlikely to cause the 2 ms instability, its large magnitude and low frequency stand out and will guide this study. The equipment responsible for this large resonator impedance has not yet been identified.

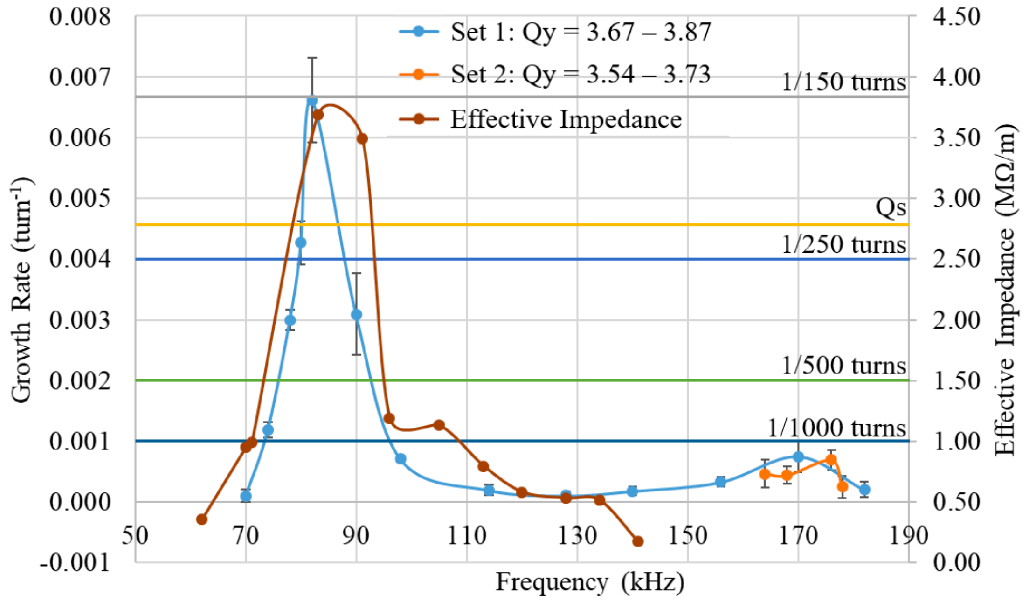


Figure 2.10: Growth rate of bunched beam instabilities observed in BSRM as a function of baseband betatron sideband frequency, overlaid with the measured effective impedance [80].

Yet high over the city our line of yellow windows must have contributed their share of human secrecy to the casual watcher in the darkening streets, and I was him too, looking up and wondering. I was within and without, simultaneously enchanted and repelled by the inexhaustible variety of life.

— F. Scott Fitzgerald, "The Great Gatsby"

3 Wakes and Impedances

Coherent instabilities of the kind seen on ISIS are commonly caused by a beam's electromagnetic interaction with its surroundings. As the beam traverses a structure, it induces charges and currents, whose fields act back on the beam and can cause a transverse oscillation with growing amplitude. The distribution of those fields determine their impact on beam stability, which will be discussed in Chapter 4.

Rather than specifying the electromagnetic field as a function of space and time, which can be challenging, it is more common to specify derived quantities such as the "wake function" or the "impedance". The wake function characterises the impulse on a point particle in the time domain, while the impedance is derived from the Fourier transform of the wake function [89].

Before these derived quantities were widely adopted, studies of beam instabilities often included detailed derivations of electromagnetic fields [90]. At the same time, instabilities were often categorised by the fields which caused them, for example the "resistive-wall" and "beam-cavity" instabilities. In the field of high-energy, high-intensity particle accelerators, the wake and impedance concepts largely decoupled the topics of beam instabilities and the fields that caused them.

The coupling impedance concept was adopted by the field of coherent instabilities in high-energy, high-intensity particle accelerators by V.G. Vaccaro [91]. It was first used in the context of longitudinal effects, where the impedance has a direct connection to circuit theory. With the observation of coherent transverse instabilities in both electron and proton accelerators [92, 93, 94, 95], a transverse counterpart was introduced. Early references credit the definition of the transverse beam coupling impedance to H.G. Hereward [96, 97].

From around the same time, some authors focused primarily on the study of beam instabilities, with comparatively little reference to the fields that drove them [98]. For these authors, it became more common to categorise instabilities based on a beam's behaviour, such as the "head-tail", "coupled-bunch" and "mode-coupling" instabilities. The properties of these instabilities could be computed with wake functions or impedances, and a qualitative description could be made from the general properties of these quantities, such as whether the impedance could be described as a narrow peak (narrowband) or a wide distribution (broadband) [89].

At the same time, some authors focused primarily on deriving wake functions and impedances for ever more complex systems. For example multi-layer cylindrical vacuum vessels [99], perfectly conducting vacuum vessels of arbitrary cross-sections [100, 101], kicker magnets [102, 103, 104, 105], laminated magnet structures [106, 107], to name but a few studies. Numerical tools were developed whose main outputs were impedances or wakes and not field maps [108, 109, 110, 111, 112]. Experimental methods of evaluating impedances in the lab was another distinct area of research [113, 114, 102, 115], as well as beam-based measurements [116].

Today, the concept of a beam coupling impedance remains fundamental to the study of coherent instabilities. Tools for studying beam stability often require an impedance or a wake function as an input [117, 118, 119, 120, 121, 122]. The definition of these concepts has not fundamentally changed since their early inception, although their application to hadron machines has demanded that the $\beta = 1$ assumption be reconsidered.

Without this assumption, it was found that incoherent impedances can be significant even for cylindrical structures [101, 123], and it has become common to distinguish between a driving and a detuning transverse impedance [124, 125]. In some machine elements it has been found that the latter of these is required to explain bench impedance measurements [126, 127]. New results for analytical wakes and impedances are still published [128, 129], new codes for computing them are being written [64, 130], and new experimental techniques for characterising them are still under development [131]. As future machines continue to push the limits of beam intensity, the field of beam coupling impedances can only become more critical.

3.1 Fundamental Definitions

3.1.1 Wake Functions

Wake functions characterise the average force a source charge exerts on a witness charge. To describe this scenario, an absolute Cartesian coordinate system, (x, y, s), is defined as shown in Figure 3.1, where the two charges are also indicated. The source charge, q_1, has coordinates (x_1, y_1, s_1) where $s_1 = vt$, and witness, q_2, has coordinates (x_2, y_2, s_2). Both source and witness charges are assumed to have a velocity vector $\vec{v} = \beta c\vec{\mathbf{s}}$ where a bold vector is a unit vector, and q_2 is separated from q_1 along the s-axis by the distance constant $z = s_2 - s_1$. The witness charge passes any given longitudinal position at a time $-\frac{z}{\beta c}$ after q_1 has passed it.

In the ultra-relativistic limit, as $v \to c$, causality dictates that the electromagnetic field of the source charge cannot extend in front of it, so the resulting fields are termed "wake fields" and can only exist for $s < s_1$. A force is then only exerted on a trailing witness charge with $z < 0$, that arrives at any given longitudinal coordinate after q_1 has passed it. Outside the ultra-relativistic limit, wake fields will also exist ahead of the source particle.

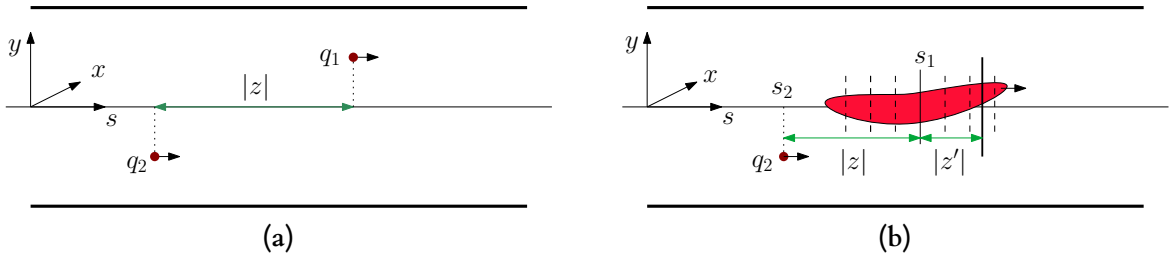


Figure 3.1: Layout of (a) source and witness charges and (b) source bunch and witness charge.

The force on q_2 due to a wake field at s is given by the field at the position s some time after q_1 has passed that location

$$\vec{F}(s) = q_2 \left[\vec{E}\left(x, y, s; t - \frac{z}{v}\right) + \vec{v} \times \vec{B}\left(x, y, s; t - \frac{z}{v}\right) \right]_{\substack{x=x_2 \\ y=y_2}} . \tag{3.1}$$

Notice that if $z < 0$, the field is evaluated at s, some time after the source particle has passed that position. The wake function is defined to characterise the average force on the witness particle as it traverses the region between $s = \pm L/2$,

$$\vec{W}(z) = \frac{-1}{q_1 q_2} \left[\int_{s=-L/2}^{L/2} \vec{F}\left(x, y, s; t - \frac{z}{v}\right) \mathrm{d}s \right]_{\substack{x=x_2 \\ y=y_2}} \tag{3.2}$$

$$= \frac{-1}{q_1} \left[\int_{s=-L/2}^{L/2} \vec{E}\left(x, y, s; t - \frac{z}{v}\right) + \vec{v} \times \vec{B}\left(x, y, s; t - \frac{z}{v}\right) \mathrm{d}s \right]_{\substack{x=x_2 \\ y=y_2}} , \tag{3.3}$$

where the EM fields are understood to be generated by the source particle at (x_1, y_1, s_1). The minus sign is included by convention so that in the longitudinal direction, a positive wake implies energy loss. This can be expressed in terms of the average force on q_2

$$\frac{1}{L}\vec{W}(z) = \frac{-1}{q_1 q_2} \left[\frac{1}{L} \int_{s=-L/2}^{L/2} \vec{F}\left(x, y, s; t - \frac{z}{v}\right) \mathrm{d}s \right]_{\substack{x=x_2 \\ y=y_2}} \tag{3.4}$$

$$= \frac{-1}{q_1 q_2} \left\langle \vec{F} \right\rangle . \tag{3.5}$$

Wake functions can be used to compute the average force on a witness particle due to a source bunch of particles with a finite extent, see Figure 3.1. s_1 will now become the coordinate of a synchronous particle and $e\lambda(z)$ is the charge distribution defined with respect to the position of this synchronous particle. Considering that each infinitesimal

slice of the bunch produces a wake, we can substitute $q_1 \to e\lambda(z')\mathrm{d}z'$. The wake must now be evaluated not at z, which separates the witness charge from the synchronous particle, but $z - z'$, the distance which separates the witness charge from the infinitesimal slice being considered. The average force on q_2 is the integral over source slices

$$\left\langle \vec{F} \right\rangle = -\frac{q_2 e}{L} \int_{z'=-\infty}^{\infty} \lambda(z') \vec{W}(z - z')\, \mathrm{d}z', \tag{3.6}$$

which is a convolution; wake functions thus resemble a Green's function. Here $\lambda(z')$ is defined such that $\int_{z'=-\infty}^{\infty} \lambda(z')\, \mathrm{d}z' = N$, the net number of charges per-bunch, or protons-per-bunch for a proton beam.

Since longitudinal and transverse beam dynamics are often considered to be decoupled, it is common to define wakes in terms of their impulses in these separate planes. In general, the longitudinal wake function depends on x_1, y_1, x_2 and y_2, but the source and witness particles are often assumed to have coordinates $x_1 = x_2 = y_1 = y_2 = 0$. The "longitudinal wake function" is then defined as

$$W^{\parallel}(z) = -\frac{1}{q_1} \left[\int_{s=-L/2}^{L/2} E_s \left(x, y, s; t - \frac{z}{v} \right) \mathrm{d}s \right]_{\substack{x=x_2=0 \\ y=y_2=0 \\ x_1=0 \\ y_1=0}}. \tag{3.7}$$

In the transverse direction, it is common to consider vertical and horizontal wakes separately, and only terms linear in the offset of source or witness particles. These are known respectively as the driving and detuning wake functions. The vertical driving wake is defined as

$$W_1^{y,\mathrm{driving}}(z) = \frac{1}{d_1} \left[W(z) \right]_{\substack{x=x_2=0 \\ y=y_2=0 \\ x_1=0 \\ y_1=d_1}}, \tag{3.8}$$

$$\approx -\frac{1}{d_1 q_1} \left[\int_{s=-L/2}^{L/2} E_y \left(x, y, s; t - \frac{z}{v} \right) + v B_x \left(x, y, s; t - \frac{z}{v} \right) \mathrm{d}s \right]_{\substack{x=x_2=0 \\ y=y_2=0 \\ x_1=0 \\ y_1=d_1}}, \tag{3.9}$$

where $v \gg v_x$ has been assumed. The driving wake is described as "coherent", because for small offsets it does not depend on the witness particle's transverse position.

Detuning wakes impart an impulse whose magnitude is linear with respect to x_2 or y_2, and are sometimes referred to as quadrupolar in analogy to quadrupole magnets which share this characteristic [101, 124, 125, 132]. The vertical detuning wake is defined as

$$W_1^{y,\text{detuning}}(z) = \frac{-1}{q_1 d_2}\left[\int_{s=-L/2}^{L/2} E_y\left(x,y,s;t-\frac{z}{v}\right) + vB_x\left(x,y,s;t-\frac{z}{v}\right)\,\mathrm{d}s\right]_{\substack{x=x_2=0\\ y=y_2=d_2\\ x_1=0\\ y_1=0}}. \quad (3.10)$$

To understand the impact of wake fields on ISIS to first-order, the longitudinal, transverse driving, transverse detuning and skew wakes must be fully characterised. Such a detailed description is beyond the scope of this thesis, whose primary objective is to identify the cause of the 2 ms vertical instability on ISIS. As a low-β machine, with approximately rectangular cross-section vacuum vessels [1], the detuning impedance on ISIS is not expected to be negligible. This will affect the beam's coherent oscillation frequencies and would only drive instabilities with particular betatron tune settings, so a driving impedance is ultimately expected to be the source of the instability.

Driving wakes and impedances will therefore be the primary focus of this work, and for notational convenience, $W_1^{y,\text{driving}}(z)$ will be denoted as $W_1^{\perp}(z)$. Dependence on other coordinates will not usually be specified because they are either implied, or are not consequential to the arguments being made. References to a "transverse" wake or impedance are to be interpreted as meaning the driving components.

3.1.2 Transverse (Driving) Wake Force in a Synchrotron

Convolution integrals similar to Equation (3.6) can be used to compute the average driving wake force due a bunch rather than a point particle. In that case, the longitudinal distribution of a beam and its transverse offset must be considered. s_1 will now become the coordinate of a synchronous particle and $e\lambda(z)$ is the charge distribution defined with respect to this synchronous particle's position. Considering that each infinitesimal slice of the bunch produces a transverse wake, we can substitute $d_1\mathrm{d}q_1 \rightarrow eD(z',s)\lambda(z')\mathrm{d}z'$,

[1] The vacuum vessels will be described in more detail in Chapter 5.

where $D(z', s)$ is the average offset of the longitudinal slice at z' and $s = \beta ct$. The explicit dependence on s is to allow the offset to vary with time. The convolution integral for the vertical driving force becomes

$$\langle F_y \rangle = -\frac{q_2 e}{L} \int_{z'=-\infty}^{\infty} \lambda(z') D(z', s) W_1^{\perp}(z - z') \, \mathrm{d}z', \tag{3.11}$$

which expresses the average force on a witness particle as it traverses a wake field.

In principle, a beam's trajectory should be computed by tracking particles through the wake field of every component sequentially, but for circular machines, it has been found that it is usually sufficient to sum the wakes of all sources in the ring and apply an impulse once per revolution [89]. The average force during the first revolution of a circular accelerator is

$$\langle F_y \rangle = -\frac{q_2 e}{\beta c T_0} \int_{z'=-\infty}^{\infty} \lambda(z') D(z', s) W_1^{\perp}(z - z') \, \mathrm{d}z', \tag{3.12}$$

where $W_1^{\perp}(z)$ is from here considered to be the sum of wake functions over a single revolution and T_0 is the revolution period.

A wake field's amplitude will attenuate with time as its energy is converted to heat. The time scales required for significant attenuation can be longer than the revolution time of a circular accelerator; for example resonant modes in a cavity can be particularly long-lived. In this case, the wake seen by a witness particle on the n^{th} turn includes a contribution from previous turns. To compute the force on a witness particle due to earlier passes of a machine, we consider the witness particle to have an s_2 that is one full revolution behind the source so its value of $|z|$ is larger by one circumference. The average force on turn n is then the sum of contributions from the current turn and all previous turns. Performing this summation and exchanging the sum and integral order gives

$$\langle F_y \rangle = -\frac{q_2 e}{\beta c T_0} \int_{z'=-\infty}^{\infty} \sum_{p=n}^{\infty} D(z', s - p\beta c T_0) \lambda(z') W_1^{\perp}(z - z' - p\beta c T_0) \, \mathrm{d}z'. \tag{3.13}$$

In the ultra-relativistic limit $W_1^\perp(z > 0) = 0$ because a particle's EM field does not extend ahead of it, so the range of this summation can be extended to $n \to -\infty$; the wake force from future revolutions can be neglected. The EM fields of a non-ultra-relativistic particle will extend ahead of it, but it is still expected to be a reasonable approximation for a machine whose circumference is much larger than its beam pipe aperture, because the EM fields will fall off rapidly after a distance comparable to the beam pipe aperture [133]. It is therefore assumed that future revolutions can be included, giving

$$\left\langle F_y \right\rangle = -\frac{q_2 e}{\beta c T_0} \int_{z'=-\infty}^{\infty} \sum_{p=-\infty}^{\infty} D(z', s - p\beta c T_0)\lambda(z') W_1^\perp(z - z' - p\beta c T_0)\, \mathrm{d}z'. \tag{3.14}$$

Equivalent versions of this well-known formula can be found in textbooks on the subject of beam stability, for example Equation (6.172) of [89].

3.1.3 Beam Coupling Impedance

The fact that the average force can be expressed as a convolution raises the possibility that one might take advantage of Fourier techniques. Whilst it would be possible to formulate the theory of beam stability in terms of the Fourier transform of the transverse wake, it is more common to introduce the "transverse beam coupling impedance," [89]

$$Z_1^\perp(\omega) = \frac{i}{\beta c} \int_{z=-\infty}^{+\infty} W_1^\perp(z) e^{-i\omega \frac{z}{\beta c}}\, \mathrm{d}z \tag{3.15}$$

$$= \frac{i}{\beta c} \hat{W}_1^\perp(\omega). \tag{3.16}$$

This "hat" definition of the Fourier transform differs slightly from the common time-frequency convention, so Appendix B provides some additional information.

By taking the Fourier transform of Equation (3.14) with the hat definition, the average force can be written in terms of the impedance rather than the wake function

$$\begin{aligned}\left\langle \hat{F}_y \right\rangle (\omega, s) &= -\frac{q_2 e}{\beta c T_0} \sum_{p=-\infty}^{\infty} \int_{z=-\infty}^{\infty} \left[\int_{z'=-\infty}^{\infty} D(z', s - p\beta c T_0) \lambda(z') W_1(z - z' - p\beta c T_0) \, \mathrm{d}z' \right] e^{-i\omega \frac{z}{\beta c}} \, \mathrm{d}z, \\ &= -\frac{q_2 e}{\beta c T_0} \sum_{p=-\infty}^{\infty} \int_{z'=-\infty}^{\infty} D(z', s - p\beta c T_0) \lambda(z') \, \mathrm{d}z' \int_{z=-\infty}^{\infty} W_1(z - z' - p\beta c T_0) e^{-i\omega \frac{z}{\beta c}} \, \mathrm{d}z, \\ &= -\frac{q_2 e}{\beta c T_0} \sum_{p=-\infty}^{\infty} e^{-i\omega p T_0} \hat{W}_1(\omega) \int_{z'=-\infty}^{\infty} \lambda(z') D(z', s - p\beta c T_0) e^{-i\omega \frac{z'}{\beta c}} \, \mathrm{d}z',\end{aligned}$$

where the shift theorem has been used. Assuming now that $D(z', s)$ has harmonic time-dependence with the conventions used in [89], so that it describes a coherent oscillation at the frequency Ω,

$$D(z', s) = D_0 D_1(z') e^{-i\Omega \frac{s}{\beta c}}, \tag{3.17}$$

where D_0 is a constant and $D_1(z')$ describes the longitudinal distribution of the average transverse offset. The average force can then be written more conveniently by making the substitution

$$\begin{aligned}\lambda(z') D(z', s - p\beta c T_0) &= \lambda(z') D_0 D_1(z') e^{-i\Omega \frac{s - p\beta c T_0}{\beta c}} &(3.18)\\ &= D_0 \lambda_1(z') e^{-i\Omega \frac{s}{\beta c}} e^{i\Omega p T_0}, &(3.19)\end{aligned}$$

where $\lambda_1(z') = \lambda(z') D_1(z')$ can be interpreted as describing the longitudinal distribution of the beam's dipole moment. The expression for the frequency-domain force becomes

$$\left\langle \hat{F}_y \right\rangle (\omega, s) = -\frac{D_0 q_2 e}{\beta c T_0} e^{-i\Omega \frac{s}{\beta c}} \sum_{p=-\infty}^{\infty} e^{i\Omega p T_0} e^{-i\omega p T_0} \hat{W}_1(\omega) \hat{\lambda}_1(\omega).$$

Substituting the definition of the transverse impedance gives

$$\left\langle \hat{F}_y \right\rangle (\omega, s) = i \frac{D_0 q_2 e}{T_0} e^{-i\Omega \frac{s}{\beta c}} \sum_{p=-\infty}^{\infty} e^{-ipT_0(\omega - \Omega)} \hat{\lambda}_1(\omega) Z_1^{\perp}(\omega), \tag{3.20}$$

and substituting the Poisson summation formula from Appendix B, gives

$$\left\langle \hat{F}_y \right\rangle (\omega, s) = i\frac{D_0 q_2 e}{T_0} e^{-i\Omega\frac{s}{\beta c}} \frac{2\pi\beta c}{C} \sum_{p=-\infty}^{\infty} \delta\left(\omega - \Omega - \frac{2\pi\beta c}{C}p\right) \hat{\lambda}_1(\omega) Z_1^{\perp}(\omega), \tag{3.21}$$

where $C = \beta c T_0$ is the machine's circumference. Now performing an inverse transform to obtain the time-domain force

$$\left\langle F_y \right\rangle (z, s) = i\frac{D_0 q_2 e}{T_0} e^{-i\Omega\frac{s}{\beta c}} \frac{2\pi}{T_0} \sum_{p=-\infty}^{\infty} \frac{1}{2\pi\beta c} \int_{\omega=-\infty}^{\infty} \delta\left(\omega - \Omega - \frac{2\pi}{T_0}p\right) \hat{\lambda}_1(\omega) Z_1^{\perp}(\omega) e^{i\omega\frac{z}{\beta c}} \, \mathrm{d}\omega, \tag{3.22}$$

$$= i\frac{D_0 q_2 e}{\beta c T_0^2} e^{-i\Omega\frac{s}{\beta c}} \sum_{p} \hat{\lambda}_1(p\omega_0 + \Omega) Z_1^{\perp}(p\omega_0 + \Omega) e^{i(p\omega_0+\Omega)\frac{z}{\beta c}}, \tag{3.23}$$

where $\omega_0 = 2\pi\frac{\beta c}{C}$. Then by defining

$$\omega' = \Omega + p\omega_0, \tag{3.24}$$

and setting $q_2 = +e$, the force formula can be written as

$$\left\langle F_y \right\rangle (z, s) = i\frac{D_0 e^2}{\beta c T_0^2} e^{-i\Omega\frac{s}{\beta c}} \sum_{p=-\infty}^{\infty} \hat{\lambda}_1(\omega') Z_1^{\perp}(\omega') e^{i\omega'\frac{z}{\beta c}}, \tag{3.25}$$

which is the equivalent of Equation (6.173) in [89]. The average transverse force on a witness particle due to a bunch can therefore be computed from the wake function or the transverse impedance, which is derived from the Fourier transform of the wake function.

There are several reasons to express the force in terms of the impedance. Firstly because it can be easier to derive expressions for the impedance than for the wake function. Perhaps most importantly, it introduces the intuitive notion that the force due to a particular dipole distribution is related to the overlap between $\hat{\lambda}_1(\omega')$ and $Z_1^{\perp}(\omega')$. If these two quantities do not overlap, for example because impedances are only significant at very high frequencies, then the beam will not "see" them. If we can make some reasonable estimates for $\hat{\lambda}_1(\omega')$ and Ω, then we can both make qualitative predictions and understand beam stability from the general properties of an impedance. These matters will be reviewed in Chapter 4.

3.2 Transverse Impedance of Common Structures

The transverse beam coupling impedance has been a focus of high-intensity research since at least the 1970's, so formulas for the impedance of common structures have been available for several decades [102]. Such formulas will be used extensively in this thesis, so some common impedances will now be stated without derivation.

Since a wake function is by definition real, the real part of its Fourier transform is an even function and the imaginary part is an odd function [134]. These relationships are reversed for the transverse impedance, because it is defined in Equation (3.16) as a Fourier transform with a coefficient of i, giving

$$\mathrm{Re}\left(Z_1^{\perp}(-\omega)\right) = -\,\mathrm{Re}\left(Z_1^{\perp}(\omega)\right) \tag{3.26}$$

$$\mathrm{Im}\left(Z_1^{\perp}(-\omega)\right) = +\,\mathrm{Im}\left(Z_1^{\perp}(\omega)\right). \tag{3.27}$$

Impedances are therefore often quoted for only positive ω.

3.2.1 Perfectly Conducting Circular Vacuum Vessel

Circular cross-section conducting pipes such as the one shown in Figure 3.2, often make up the vacuum systems of particle accelerators. If the beam were contained inside a circular cross-section vacuum-vessel made from a perfect electrical conductor, then surface charges and currents would ensure that the beam's EM fields did not penetrate the vessel's surface.

In this scenario, the beam experiences its own repulsive space-charge self-field, which is considered beyond the scope of this thesis, and an image-charge field from the surface charges and currents. These images are responsible for the "indirect space-charge impedance" per unit length, defined as

$$\frac{1}{L}Z_1^{\perp}(\omega) = -i\frac{\mu_0 c I_1^2\left(\frac{\omega a}{\beta\gamma c}\right)}{\beta\gamma^2\pi a^2}\frac{K_1\left(\frac{\omega b}{\beta\gamma c}\right)}{I_1\left(\frac{\omega b}{\beta\gamma c}\right)}, \tag{3.28}$$

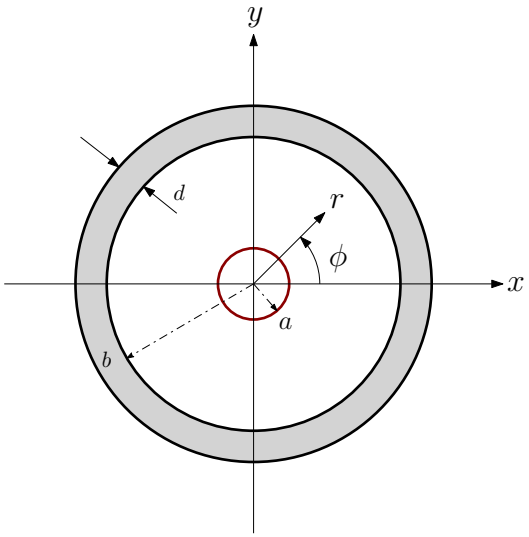


Figure 3.2: Geometry of a circular cross-section conducting pipe, with inner radius b and thickness d. The source distribution is taken as a ring of charge of radius a, which will be justified in Section 3.4. Cartesian and polar coordinates are also indicated.

where b is the pipe's inner radius and I_1 and K_1 are first order modified Bessel functions of the first and second kinds. a is the offset of a point charge, or equivalently a ring of charge with a radius of a and a $\cos(\theta)$ charge distribution, which will be introduced in Section 3.4 [135, 89]. This formula is also known as the indirect space-charge impedance for a pipe of circular cross-section.

It is usually a good approximation that $\frac{\omega a}{\beta\gamma c} \ll 1$, so that $I_1\left(\frac{\omega a}{\beta\gamma c}\right) \approx \frac{\omega a}{2\beta\gamma c}$ [136], giving

$$\frac{1}{L}Z_1^{\perp}(\omega) \approx -i\frac{\mu_0\omega^2}{4\pi c\beta^3\gamma^4}\frac{K_1\left(\frac{\omega b}{\beta\gamma c}\right)}{I_1\left(\frac{\omega b}{\beta\gamma c}\right)}, \tag{3.29}$$

which is the form that will be used in the following chapters.

The indirect space-charge impedance is somewhat unlike other impedances because of its dependence on a, and because it tends to zero in the limit $\beta \to 1$. It is a purely imaginary impedance, and for low-β machines, it can dominate other sources.

3.2.2 Conductive Circular Vacuum Vessel

If the pipe shown in Figure 3.2 were made from a good conductor with conductivity σ, then the indirect space-charge impedance appears in addition to a resistive-wall impedance [135]. If the skin-depth in the pipe,

$$\delta(\omega) = \sqrt{\frac{2}{\omega\mu\sigma}}, \tag{3.30}$$

is small compared to its thickness d, then beam-induced fields won't penetrate the pipe and $d \to \infty$ can be assumed. In this frequency range, and assuming $\delta \ll b$, the "thick-wall" approximation is valid, and the transverse impedance per unit length is [135]

$$\frac{1}{L}Z_1^{\perp}(\omega) = \frac{\mu_0 \beta c \delta}{2\pi b^3}(1-i)\,. \tag{3.31}$$

This is not valid as $\omega \to 0$, because the skin depth will become large compared to d and b. In that limit the real and imaginary parts of Equation (3.31) tend to infinity. It also becomes invalid at very high frequencies which will be discussed in Section 3.4.

Simple formulas for a pipe whose thickness is small compared to the skin depth can be derived from first principles, but an approach using an equivalent circuit and assuming $\beta = 1$ gives an intuitive interpretation of the low-frequency impedance [137]. In this frequency range, the resistive-wall impedance is given by

$$\frac{1}{L}Z_1^{\perp}(\omega) = -\frac{2c}{\omega b^2}\frac{i\omega\frac{L_p}{2\pi}R_p}{R_p - i\omega\frac{L_p}{2\pi}}. \tag{3.32}$$

where

$$L_p = \frac{\mu_0}{2}, \tag{3.33}$$

is referred to as the "bypass inductance" per-unit-length, and at low frequencies

$$R_p = \frac{\rho}{2\pi b d} \tag{3.34}$$

is the chamber's resistance per-unit-length, where $\rho = 1/\sigma$ is the material's resistivity. This "thin-wall" formula is expected to be valid in the limit $\omega \to 0$, where it tends to an imaginary constant.

Intuitively this description can be understood in terms of currents in the vacuum vessel taking the path of least resistance through a parallel combination of a resistor and an inductor. Properties of the resistive path are controlled by the geometry and material properties of the vacuum vessel, whilst the inductance is the same for all circular cross-section vessels. At very low frequencies, the inductor will become the lowest impedance path, and at high frequencies the resistive path will be preferred, so the real part of the impedance becomes non-zero.

Examples of the thin and thick resistive wall impedances are shown in Figure 3.3 for a pipe of finite thickness. Below the frequency where $\delta = d$, the impedance is described by the thin-wall approximation. In this region, the real part of the impedance increases with frequency from 0 at $\omega = 0$ to a maximum when $\delta = \sqrt{bd}$, then falls with $1/\omega$ in the "Sacherer" region. At intermediate frequencies above the frequency where $\delta = d$, the impedance is described by the thick-wall approximation and the real and imaginary parts both follow $1/\sqrt{\omega}$ [138]. The high frequency region where the thick-wall approximation becomes invalid is not shown here, but will be described in Section 3.4.

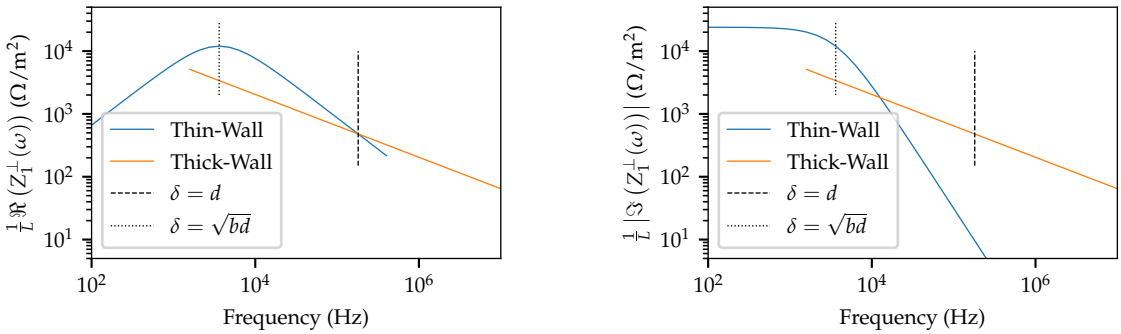


Figure 3.3: Real (a) and absolute imaginary (b) parts of the thin and thick resistive-wall impedances for a $\beta = 1$ beam in a 1 mm thick stainless-steel pipe, with an inner radius of 5 cm. The frequency at which the skin-depth is equal to the pipe thickness is indicated.

3.2.3 Transverse Resonator

The resistive-wall impedance is broadband, and therefore differs significantly in its behaviour from a resonant structure such as a kicker magnet or an RF cavity. In these structures the impedance is expected to be significant close to the resonant frequency and negligible at other frequencies. Such impedances are termed narrowband impedances, where the real part of the impedance resembles a peak at the resonant frequency.

For such impedances, the ideal transverse resonator model is useful, and is defined as

$$Z_1^\perp(\omega) = \frac{\omega_r}{\omega} \frac{R_\perp}{1 + iQ_r \left(\frac{\omega_r}{\omega} - \frac{\omega}{\omega_r} \right)}, \tag{3.35}$$

where ω_r is the resonant angular frequency, $R_\perp$ is the transverse shunt impedance in units of $\Omega\,\mathrm{m}^{-1}$ and Q_r is the quality factor [139]. Some example resonator impedances are shown in Figure 3.4.

The resonator impedance will be used extensively in the following chapters. The definition of Equation (3.35) has no explicit dependence on β, which is absorbed into $R_\perp$. Unless stated explicitly, $\beta = 1$ should be assumed when resonator parameters are quoted, and for the resonators discussed in this thesis the dependence can be added by multiplying $Z_1^\perp$ by β.

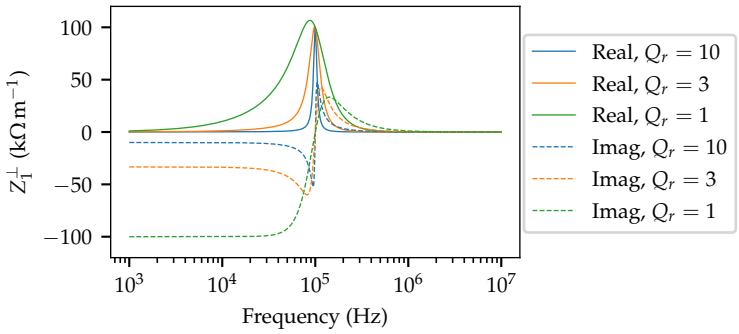


Figure 3.4: Transverse resonator impedance defined in Equation (3.35), with $R_\perp = 100\,\mathrm{k}\Omega\,\mathrm{m}^{-1}$, $\frac{\omega_r}{2\pi} = 100\,\mathrm{k}\Omega$ and several different values of Q_r.

3.3 Measurement and Numerical Computation

This section will introduce techniques of finding $Z_1^\perp$ experimentally and numerically. It will make use of the time-frequency Fourier transform, which is defined here as

$$\mathcal{F}\left(f(t)\right) = \tilde{f}(\omega) = \int_{-\infty}^{\infty} f(t) e^{-i\omega t}\, \mathrm{d}t, \tag{3.36}$$

and its inverse as

$$\mathcal{F}^{-1}\left(\tilde{f}(\omega)\right) = f(t) = \frac{1}{2\pi}\int_{-\infty}^{\infty} \tilde{f}(\omega) e^{i\omega t}\, \mathrm{d}\omega. \tag{3.37}$$

With this convention and the definition of the impedance in terms of a wake function given by Equation (3.16), the horizontal driving impedance can be found in terms of the Fourier transformed EM fields with

$$Z_1^\perp(\omega) = \frac{-i}{q_1 d_1}\left[\int_{s=-L/2}^{L/2}\left(\tilde{E}_x^*(x,y,s;\omega) - v\tilde{B}_y^*(x,y,s;\omega)\right) e^{-i\omega\frac{s}{v}}\, \mathrm{d}s\right]_{\substack{x=x_2=0\\ y=y_2=0\\ x_1=d_1\\ y_1=0}}, \tag{3.38}$$

where a complex conjugate is indicated by an asterisk. This equation is derived in Appendix C, and uses Fourier conventions [89] that differ from some sources [135].

3.3.1 Wire Bench Measurements

Maxwell's equations in Cartesian coordinates include

$$\frac{\partial E_x}{\partial s} - \frac{\partial E_s}{\partial x} = -\frac{\partial B_y}{\partial t}, \tag{3.39}$$

and taking the Fourier transform of this gives

$$\frac{\partial \tilde{E}_x}{\partial s} - \frac{\partial \tilde{E}_s}{\partial x} = -i\omega\tilde{B}_y. \tag{3.40}$$

Substituting the definition for $\tilde{B}_y$ into Equation (3.38) gives

$$Z_1^{\perp}(\omega) = \frac{-i}{q_1 d_1}\left[\int_{s=-L/2}^{L/2}\left(\tilde{E}_x^*(x,y,s;\omega) - v\tilde{B}_y^*(x,y,s;\omega)\right)e^{-i\omega\frac{s}{v}}\,\mathrm{d}s\right]_{\substack{x=x_2=0\\y=y_2=0\\x_1=d_1\\y_2=0}}, \tag{3.41}$$

$$= \frac{-i}{q_1 d_1}\left[\int_{s=-L/2}^{L/2}\left(\tilde{E}_x^* + i\frac{v}{\omega}\left[\frac{\partial\tilde{E}_x^*}{\partial s} - \frac{\partial\tilde{E}_s^*}{\partial x}\right]\right)e^{-i\omega\frac{s}{v}}\,\mathrm{d}s\right]_{\substack{x=x_2=0\\y=y_2=0\\x_1=d_1\\y_1=0}}, \tag{3.42}$$

$$= \frac{-i}{q_1 d_1}\int_{s=-L/2}^{L/2}\left(\tilde{E}_x^* + i\frac{v}{\omega}\frac{\partial\tilde{E}_x^*}{\partial s}\right)e^{-i\omega\frac{s}{v}}\,\mathrm{d}s - \frac{v}{\omega q_1 d_1}\int_{s=-L/2}^{L/2}\frac{\partial\tilde{E}_s^*}{\partial x}e^{-i\omega\frac{s}{v}}\,\mathrm{d}s. \tag{3.43}$$

Only fields which are $\propto e^{-i\omega\frac{s}{v}}$ propagate with the beam and contribute to the average force [108, 124], so the first integral is zero, leaving

$$Z_1^{\perp}(\omega) = -\frac{v}{\omega q_1 d_1}\int_{s=-L/2}^{L/2}\frac{\partial\tilde{E}_s^*}{\partial x}e^{-i\omega\frac{s}{v}}\,\mathrm{d}s \tag{3.44}$$

$$= \frac{v}{\omega d_1}\left[-\frac{1}{q_1}\frac{\partial}{\partial x}\int_{s=-L/2}^{L/2}\tilde{E}_s^*(x,y,s;\omega)e^{-i\omega\frac{s}{v}}\,\mathrm{d}s\right]_{\substack{x=x_2=0\\y=y_2=0\\x_1=d_1\\y_1=0}} \tag{3.45}$$

$$= \frac{v}{\omega d_1}\left[\frac{\partial Z^{\parallel}}{\partial x}\right]_{\substack{x=x_2=0\\y=y_2=0\\x_1=d_1\\y_1=0}}. \tag{3.46}$$

This is the basis of lab-based measurements of $Z_1^{\perp}$ and is related to the Panofsky-Wenzel theorem [140]. It connects the transverse impedance with the longitudinal impedance for a beam with a transverse offset. The longitudinal impedance can be measured by stretching a wire through a structure [113], so it follows that the transverse impedance can be found by estimates of this partial derivative. Perhaps the most intuitive application of this formula is the moving-wire method.

3.3.1.1 Moving-Wire Method

In a moving-wire measurement, a single wire is stretched through the Device-Under-Test (DUT) and its longitudinal impedance measured with different transverse offsets. For structures whose detuning impedance is zero, the transverse impedance can be

obtained from the gradient of the longitudinal impedance with transverse offsets, as per Equation (3.46); for small transverse offsets it can be estimated from the fitting coefficient of a parabola. Unfortunately, since the wire's transverse offset effectively sets the transverse offset of both the source and witness particles, this method returns a sum or difference of the driving and detuning impedances [126, 141, 142, 143]. One method of distinguishing these two components is to use the two-wire method, which will be described in the next section.

In the moving-wire method, the longitudinal impedance is obtained from the input impedance of the coaxial transmission line formed in the experiment, which are typically measured with a Vector Network Analyser (VNA). A typical experimental set-up is indicated in Figure 3.5, which shows the coaxial wire passing through the structure being measured with a transverse offset. Matching circuits convert the characteristic impedance of the connecting cables to that of the coaxial line formed in the experiment to prevent reflections at the transitions. Measurements in the REF configuration allow effects of the matching circuits and other equipment to be subtracted [142].

Several different formulas exist to calculate the impedance contributed by the DUT from scattering parameters measured by the VNA. If the length of the DUT is small compared to the wavelength of the excitation, then a "lumped" approximation can be made, which assumes the impedance is infinitely short. In this case the Hahn-Pedersen formula

$$Z^{\parallel} = 2Z_0 \frac{s_{21}^{\mathrm{REF}} - s_{21}^{\mathrm{DUT}}}{s_{21}^{\mathrm{DUT}}} \tag{3.47}$$

can be used [114], where s_{ij} is a scattering parameter made in either the REF or DUT configurations shown in Figure 3.5 [144]. When the DUT is not short compared to the wavelength, the impedance is more appropriately described by the improved impedance formula for distributed impedances [145]

$$Z^{\parallel} = -Z_0 \ln\left(\frac{s_{21}^{\mathrm{DUT}}}{s_{21}^{\mathrm{REF}}}\right)\left(1 + \frac{\ln\left(s_{21}^{\mathrm{DUT}}\right)}{\ln\left(s_{21}^{\mathrm{REF}}\right)}\right). \tag{3.48}$$

The Walling log-formula is another commonly used expression [146, 114]

$$Z^{\parallel} = -2Z_0 \ln\left(\frac{s_{21}^{\mathrm{DUT}}}{s_{21}^{\mathrm{REF}}}\right), \tag{3.49}$$

which is primarily for distributed impedances, but provided $Z^{\parallel} \ll Z_0$, and no strong resonances are present, then it is also approximately true for lumped impedances.

Regardless of the formula being used, it is challenging to measure the impedance accurately with these transmission-line techniques. The difference between s_{21}^{DUT} and s_{21}^{REF} is often small, particularly at low frequencies, and since the impedance is determined by the difference between these quantities, seemingly small systematic errors can be significant. Suggestions for making accurate measurements include minimal movements of any connecting cables [146].

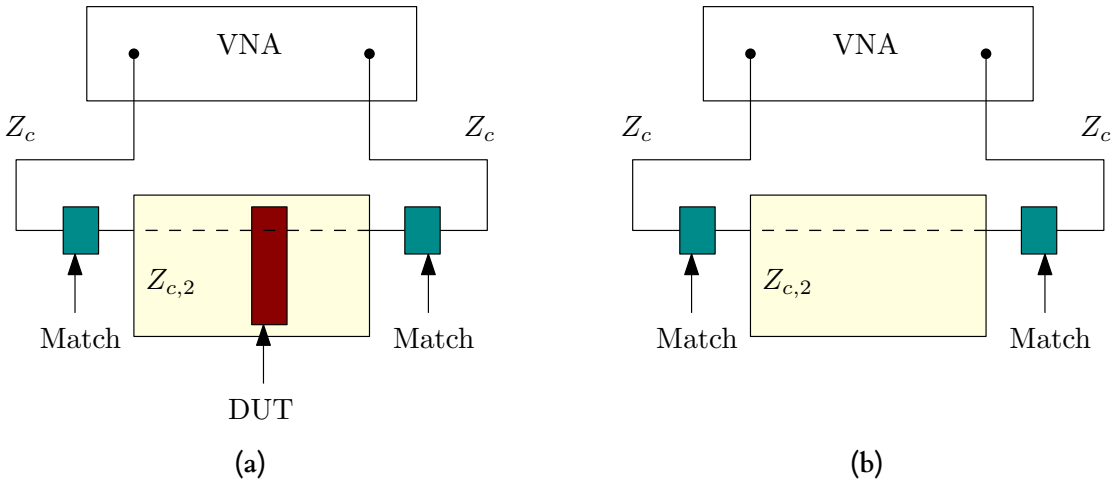


Figure 3.5: Schematic of a moving-wire transverse impedance measurement in the DUT (a) and REF (b) configurations. The same measurement chamber is used in both configurations, and the DUT is either included in the set-up or not. Matching on either side of the measurement chamber is to suppress reflections at the interface between the $Z_c = 50\,\Omega$ characteristic impedance in the cables and $Z_{c,2}$ of the measurement chamber.

3.3.1.2 Two-Wire Method

The detuning impedance is defined for a source distribution on-axis, it is generated by the monopole part of the source beam [132]. If a source distribution could be identified with the same dipole term as a single offset charge, but without a monopole term, then the fields associated with the detuning impedances would not be generated, but a witness particle would experience the same driving impedance.

One such source distribution consists of two charges with opposite polarity moving at the same velocity, spaced equidistantly from the origin along one transverse axis. In the static $\beta = 0$ case, this source distribution consists of two charges $\pm q$ offset from the origin by $\pm\Delta/2$. Since these lie along the same transverse axis, the charge density can be written as $\rho_q(x, y, s) = \delta(y)\delta(s)\sigma_Q(x)$, giving multipole moments [147]

$$M_m = \int_{-\infty}^{\infty} \sigma_Q(x) x^m \, \mathrm{d}x, \tag{3.50}$$

which gives $2q\left(\frac{\Delta}{2}\right)^m$ for $m = 1, 3, 5...$ and 0 otherwise. This source distribution therefore has no monopole moment, but a dipole moment $q\Delta$ which is equal to that of a single charge with offset $x = \Delta$. A wire arrangement that approximates this source would produce no detuning wake, and any measured transverse impedance would be dominated by the driving component.

To produce such a source term in a bench setup, two wires can be stretched through a structure separated from the central axis by $\pm\Delta/2$ along one transverse direction. The two wires must be driven with an odd differential TEM mode [144], so that currents and voltages on the two wires propagate in anti-phase. $Z_1^\perp$ can be obtained by approximating the partial derivative in Equation (3.46) with

$$\frac{\partial Z^\parallel}{\partial x} \approx \frac{Z^\parallel(x = \Delta/2) - Z^\parallel(x = -\Delta/2)}{\Delta} = \frac{2Z^\parallel(x = \Delta/2)}{\Delta} = \frac{Z^\parallel_{\mathrm{odd}}}{\Delta},$$

which gives

$$Z_1^\perp(\omega) = \frac{v}{\omega\Delta^2} Z^\parallel_{\mathrm{odd}}. \tag{3.51}$$

As in the moving-wire method, $Z^{\parallel}_{\text{odd}}$ is typically measured with a VNA, and the impedance of a reference measurement must be subtracted to find the impedance added by the DUT. A typical experimental set-up is indicated in Figure 3.6, which shows the odd TEM-mode being driven by a 180° hybrid splitter; in principle a 4-port VNA could also be used. As with the moving-wire method, the matching circuits convert the characteristic impedance of the transmission line cables, which are typically 50 Ω, to the characteristic impedance of the odd mode of the two-wire transmission line.

As with the moving-wire experiment, the input impedance of the transmission line must be estimated with either the lumped, distributed or log formulas. Just as with the moving-wire method, this will include contributions from the connecting cables, the matching sections and the properties of the transmission line itself. $Z^{\parallel}_{\text{odd}}$ added by the DUT is often measured by subtracting the impedance of the two-wire line with the DUT from a reference configuration (REF), which will include contributions from all equipment except the DUT.

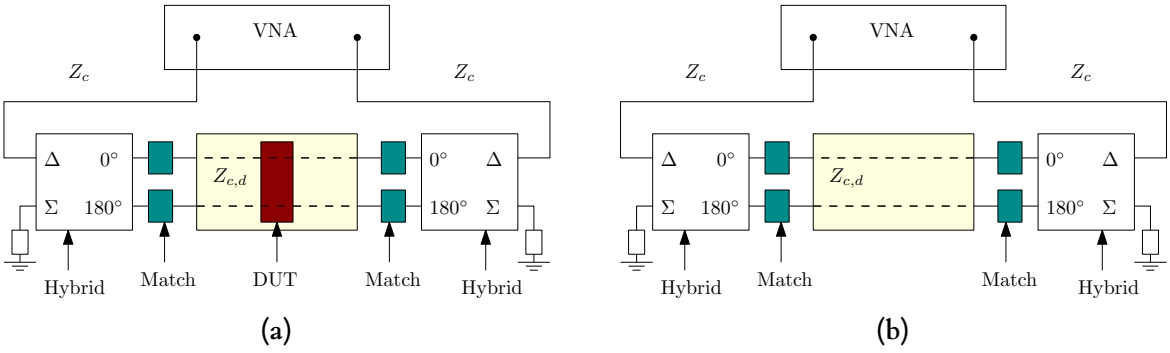


Figure 3.6: Schematic of DUT (a) and REF (b) configurations of a two-wire bench impedance measurement. The output of a VNA is passed into a 180 deg-hybrid splitter, which outputs two components that are out-of-phase. These are passed into matching circuits, which match the $Z_c = 50\,\Omega$ output to half of the differential-mode characteristic impedance of the two-wire line inside the test chamber. The same process on the output of the chamber reverses this process, so that a single-ended signal is returned to the VNA.

3.3.1.3 Probe-Coil Method

Equation (3.51) was also introduced to measure the transverse impedance by rectangular loop of wire [102], referred to here as a probe-coil. In this measurement, the device under test is excited by the dipole current formed by the probe-coil but without an in-phase charge distribution. $Z^{\parallel}_{\text{odd}}$ is then interpreted as the impedance added to the probe coil by the DUT with a suitable reference subtracted. Despite the source not being a perfect representation of a beam [109], the probe-coil method is particularly advantageous at low frequencies, where obtaining accurate results with transmission-line techniques can be practically challenging [148].

An experimental set-up for a probe-coil measurement is shown schematically in Figure 3.7. VNA's are often substituted with LCR meters to measure the probe coil's impedance at low frequencies. This set-up is simplified compared to the transmission-line methods because at low frequencies, most common structures can be considered as lumped impedances. If a VNA is used, then the lumped impedance can be obtained from the s_{11} parameter with

$$Z_{\text{lumped}} = Z_0 \frac{1 + s_{11}}{1 - s_{11}}, \tag{3.52}$$

which is measured for the REF and DUT configurations. The transverse impedance can then be found with

$$Z_1^{\perp}(\omega) = \frac{v}{\omega \Delta^2} \left(Z^{\text{DUT}}_{\text{lumped}} - Z^{\text{REF}}_{\text{lumped}} \right), \tag{3.53}$$

where $Z^{\text{DUT}}_{\text{lumped}}$ and $Z^{\text{REF}}_{\text{lumped}}$ are the lumped impedances of the probe-coil in the DUT and REF configurations.

The probe-coil method is typically only used to measure $\text{Re}\,(Z_1^{\perp})$ because a large magnetic image term is added to the measured imaginary impedance. This image term is not present with a reference configuration in free space, and so is not subtracted from the DUT impedance. Reference measurements can be specifically designed to include the image term, but this requires additional equipment, for example a vacuum vessel

constructed from a very good conductor [115]. This term has been identified on several occasions [149, 115, 103], and appears because the EM fields of a probe coil do not match exactly those of a $\beta = 1$ beam.

In the kHz frequency range, the difference between the probe-coil's resistance in the REF and DUT configurations is typically small, so systematic errors can dominate a measurement. If the transverse impedance from Figure 3.3 was measured with a probe coil, the difference in the resistance at $10\,\mathrm{kHz}$ for a $1\,\mathrm{cm}$-wide coil in a $1\,\mathrm{m}$ long pipe would be $\approx 0.2\,\mathrm{m\Omega}$. Such small changes can be caused by temperature variations or changes to electrical contacts when moving between REF and DUT configurations [146].

These fractional errors can be reduced with additional turns of the probe coil [115], which increases the measured impedance by a factor of N_t^2 for a probe-coil of N_t turns. Equation (3.53) must then be modified, so that

$$Z_1^{\perp}(\omega) = \frac{v}{\omega N_t^2 \Delta^2}\left(Z_{\mathrm{lumped}}^{\mathrm{DUT}} - Z_{\mathrm{lumped}}^{\mathrm{REF}}\right). \tag{3.54}$$

The upper frequency range of the probe-coil method is limited by the coil's resonant frequency, which will reduce as more turns are added.

Despite some of its shortcomings, the probe-coil method is still widely used because of its effectiveness at low frequencies. It remains an important benchmark for numerical simulations and for identifying impedances on structures that are challenging to simulate. The general technique also forms the basis of a numerical method that will be described in Section 3.3.2 [64, 60, 148].

3.3.2 Finite-Element Tools - CST

The CST wakefield solver is a widely used tool to evaluate impedances and wakes. It does this by tracking a beam through a structure in the time domain, calculating the EM fields and then integrating these fields along a designated path to approximate the wake function. The impedance is then found from a numerical Fourier transform of the computed wake. Its frequency resolution is determined by the maximum simulated

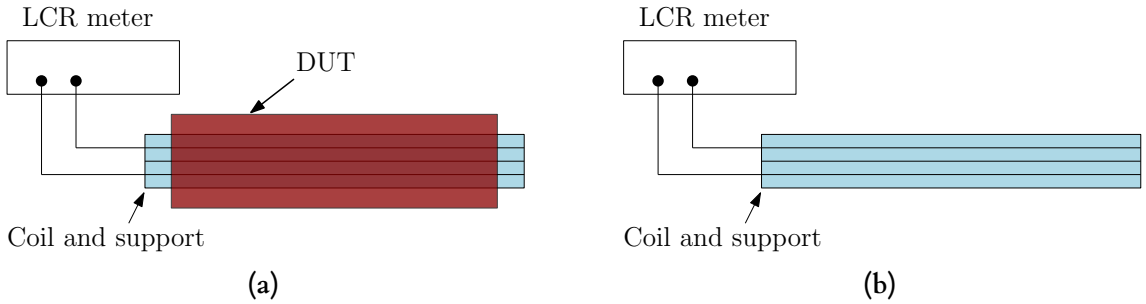


Figure 3.7: Schematic of DUT (a) and REF (b) configurations of a probe-coil bench impedance measurement. In both cases the coil's impedance is measured with an LCR-meter, and no matching is required. The probe coil is shown as being mounted on an electrically insulating support, which will not disturb the magnetic fields associated with the dipole-current.

distance behind a bunch. Improving resolution requires longer simulation times [149], which can become prohibitive on standard hardware, and numerical errors can occur.

Some of these issues can be addressed with numerical tools that operate in the frequency domain [150, 109], however these do not yet have some of the advanced features required for a practical simulation of all types of equipment. Analytical tools which calculate $Z_1^\perp$ in the frequency domain have been developed for structures with particular geometries, but they are more limited in the complexity of the equipment they can model; one such tool will be described in more detail in Section 3.4.

To address some of these issues, a method of computing $Z_1^\perp(\omega)$ has been developed that uses the low-frequency solver in CST, which operates in the frequency domain. In this technique a rectangular current loop is generated inside a finite-element model of the DUT, which mimics the probe-coil experimental set-up described in Section 3.3.1.3. The impedance seen by the current loop can be extracted from the simulation and substituted into Equation (3.53).

Since the simulated current loop has no resistive losses, a reference simulation is not required to compute $\mathrm{Re}\,(Z_1^\perp(\omega))$; the real part of impedance from a REF simulation would be zero. As with the experimental set-up, the imaginary part of the impedance includes a contribution from the magnetic image impedance, which can be removed with a dedicated reference simulation [115]. Since the magnetic image can dominate

the imaginary part of the impedance and depends on the surface current distribution, changes to the model's mesh between REF and DUT simulations can cause large systematic errors. The mesh should ideally be kept identical in the two simulations.

An example simulation has been carried out to demonstrate computing the resistive-wall impedance with this technique. Figure 3.8 shows $\frac{1}{L}Z_1^\perp$ for a 2 mm thick, stainless-steel pipe with an inner radius of 50 mm. It is overlaid with the thin and thick-wall formulas introduced in Section 3.2. Good agreement between CST and the approximate formulas is seen at low frequencies, whilst errors at higher frequencies are likely due to imperfect meshing of the current-carrying region of the pipe's inner surface.

High-frequency accuracy could be improved by adopting a surface-impedance approximation, but this must be valid for both the REF and DUT simulations to avoid changes to the model's mesh. A broadband characterisation therefore requires several simulations.

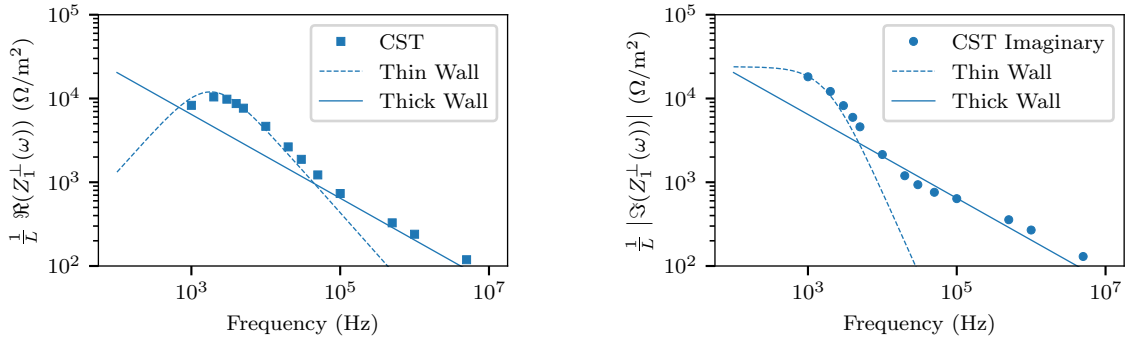


Figure 3.8: Real (a) and absolute value of the imaginary (b) parts of the $\beta = 1$ transverse impedance per unit length, of a 2 mm thick, circular cross-section, stainless-steel pipe with an inner radius of 50 mm, computed by CST. Thick and thin-wall approximations as defined by Equations (3.32) and (3.31) are overlaid.

3.4 Impedance of Multi-Layer Cylindrical Pipes

Resistive Wall for Arbitrary Layers (RWAL) is a new code to compute the transverse impedance of multi-layer cylindrical structures, such as that shown in Figure 3.9. It solves a set of linear field-matching equations in the frequency domain using a python-based computer algebra system [151] and Cramer's rule to obtain a formula for the impedance. Computation time limits the number of material layers that can be solved to five (seven regions in total), but general solutions for a given number of layers are computed once saved to disk. Numerical evaluation uses arbitrary precision floating-point numbers [152]. The result is a code that is fast and works on many operating systems.

When the analytical method that underpins RWAL was originally introduced [99], the resulting codes LAWAT and LAWAL, were used for decades before an updated version was released [153]. Just a few years later, the limitation on number-of-layers was overcome by expressing the final matrix as a product of several 4x4 matrices [123]. The original analytical technique has been extended to include anisotropic material properties [128], and non-cylindrical pipes [112, 154].

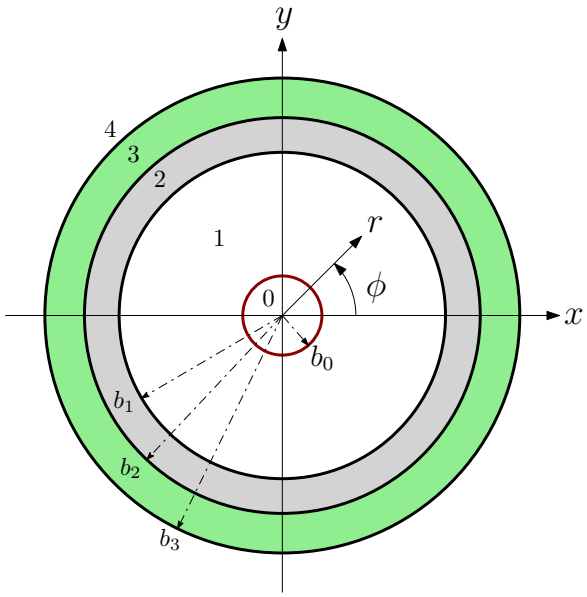


Figure 3.9: Multi-layer cylindrical beam-pipe, with ring-beam of radius b_0.

The source particle has a charge q_1 and travels parallel to the axis of a multi-layer cylindrical cross-section vessel with a velocity $\vec{v} = v\vec{\mathbf{s}}$, and an offset from the central axis by $d_1\vec{\mathbf{x}}$. The charge density of this particle can be expressed in polar coordinates as

$$\rho_q(t) = \frac{q_1}{d_1}\delta(r - d_1)\delta_p(\phi)\delta(s - vt), \tag{3.55}$$

where $\delta_p(\phi) = \sum_{n=-\infty}^{\infty}\delta(\phi - 2\pi n)$ is a 2π-periodic Dirac delta function.

From the time-frequency Fourier definitions in Equations (3.36) and (3.37), the frequency domain representation of this source is

$$\tilde{\rho}_q(\omega) = \frac{q_1}{d_1 v}\delta(r - d_1)\delta_p(\phi)e^{-i\omega\frac{s}{v}}. \tag{3.56}$$

By expanding $\delta_p(\phi)$ as a Fourier series this can be expressed as

$$\tilde{\rho}_q(\omega) = \sum_{m=0}^{\infty}\frac{Q_m}{(1+\delta_{m0})\pi d_1^{m+1}v}\delta(r - d_1)\cos(m\phi)e^{-i\omega\frac{s}{v}}, \tag{3.57}$$

where $Q_m = q_1 d_1^m$ is the m^{th} multipole moment, δ_{m0} is 1 if $m = 0$ and 0 otherwise. The Fourier transform of the current density is equal to $\tilde{\rho}_q(\omega)v\vec{\mathbf{s}}$, and can be expressed as a surface current in the $\vec{\mathbf{s}}$ direction,

$$\tilde{\kappa}_s = \sum_{m=0}^{\infty}\frac{Q_m}{(1+\delta_{m0})\pi d_1^{m+1}}\cos(m\phi)e^{-i\omega\frac{s}{v}}. \tag{3.58}$$

Each term in the summation is an infinitesimal ring of current with radius d_1, and different azimuthal dependence. Rather than considering the source particle as being point-like, it can instead be considered to be a sum of charge rings. These act as the source of the wake fields, which must now be computed.

If these charge-rings move inside a pipe with cylindrical cross-section, then the geometry of the source and interfaces can be understood to be a set of concentric cylinders, as shown in Figure 3.9. Each annular region is given an index 1 to P and the innermost circular region has the index 0. The region with an index n has an outer radius b_n, and the outermost region has $b_P \to \infty$; the particle's offset, $d_1 = b_0$ has been renamed to match this convention.

Regions $n = 0, 1$ are assumed to be free space, and the material layers with $n \geq 2$ are filled with linear, isotropic materials with a complex permeability

$$\mu_n = \mu_0(\mu_n' - i\mu_n''), \tag{3.59}$$

a complex permittivity with conductor losses

$$\varepsilon_{c,n} = \varepsilon_n - i\frac{\sigma_n}{\omega}, \tag{3.60}$$

and complex permittivity with dielectric loss

$$\varepsilon_n = \varepsilon_0 \left(\varepsilon_n' - i\varepsilon_n''\right), \tag{3.61}$$

where ε_0 and μ_0 are respectively the permittivity and permeability of free space [144]. The imaginary parts of these quantities are responsible for losses, and their sign is a convention defined based on the time-frequency Fourier definitions. It is assumed that the current density is given by

$$\vec{J} = \sigma\vec{E} + \rho_q\vec{v}, \tag{3.62}$$

and that $\vec{v} = v\vec{\mathbf{s}}$.

Maxwell's equations in the region n can be written out in cylindrical polar coordinates component-by-component as

$$\frac{1}{r}\frac{\partial \tilde{E}_{r,n}}{\partial r} + \frac{1}{r}\frac{\partial \tilde{E}_{\phi,n}}{\partial \phi} - ik\tilde{E}_{s,n} = \frac{1}{\varepsilon}\tilde{\rho}_q, \tag{3.63}$$

$$\frac{1}{r}\frac{\partial \tilde{E}_{s,n}}{\partial \phi} + ik\tilde{E}_{\phi,n} = -i\omega\tilde{B}_{r,n}, \tag{3.64}$$

$$-ik\tilde{E}_{r,n} - \frac{\partial \tilde{E}_{s,n}}{\partial r} = -i\omega\tilde{B}_{\phi,n}, \tag{3.65}$$

$$\frac{1}{r}\frac{\partial}{\partial r}\left(r\tilde{E}_{\phi,n}\right) - \frac{1}{r}\frac{\partial \tilde{E}_{r,n}}{\partial \phi} = -i\omega\tilde{B}_{s,n}, \tag{3.66}$$

$$\frac{1}{r}\frac{\partial \tilde{B}_{r,n}}{\partial r} + \frac{1}{r}\frac{\partial \tilde{B}_{\phi,n}}{\partial \phi} - ik\tilde{B}_{s,n} = 0, \tag{3.67}$$

$$\frac{1}{r}\frac{\partial \tilde{H}_{s,n}}{\partial \phi} + ik\tilde{H}_{\phi,n} = i\omega\varepsilon_{c,n}\tilde{E}_{r,n}, \tag{3.68}$$

$$-ik\tilde{H}_{r,n} - \frac{\partial \tilde{H}_{s,n}}{\partial r} = i\omega\varepsilon_{c,n}\tilde{E}_{\phi,n}, \tag{3.69}$$

$$\frac{1}{r}\frac{\partial}{\partial r}\left(r\tilde{H}_{\phi,n}\right) - \frac{1}{r}\frac{\partial \tilde{H}_{r,n}}{\partial \phi} = \tilde{\rho}_q v + i\omega\varepsilon_{c,n}\tilde{E}_{s,n}. \tag{3.70}$$

Time derivatives have been substituted with $\frac{\partial}{\partial t} \rightarrow i\omega$ from the derivative theorem of Fourier transforms [134]. Derivatives with respect to s have been substituted with $\frac{\partial}{\partial s} \rightarrow -i\frac{\omega}{v} = -ik$ because it can be seen from Equation (3.38), that any field components which do not have an $e^{-i\omega s/v}$ dependence will not contribute to the impedance; the witness particle is only affected by synchronous field components [124].

These can be manipulated to produce the electric wave equation

$$\frac{1}{r}\frac{\partial}{\partial r}\left(r\frac{\partial \tilde{E}_{s,n}}{\partial r}\right) + \frac{1}{r^2}\frac{\partial \tilde{E}_{s,n}}{\partial \phi} - (k^2 - \omega^2\mu_n\varepsilon_{c,n})\tilde{E}_{s,n} = 0, \tag{3.71}$$

and an equivalent magnetic equation. General solutions in a region n can be found by separating variables then imposing azimuthal periodicity to obtain

$$\tilde{E}_{s,n}(r,\phi,s,\omega) = \sum_{m=0}^{\infty}\left[A'_n I_m(\chi_n r) + B'_n K_m(\chi_n r)\right]\left[A''_n\cos(m\phi) + B''_n\sin(m\phi)\right]e^{-i\omega\frac{s}{v}}, \tag{3.72}$$

$$\tilde{H}_{s,n}(r,\phi,s,\omega) = \sum_{m=0}^{\infty}\left[D'_n I_m(\chi_n r) + F'_n K_m(\chi_n r)\right]\left[D''_n\cos(m\phi) + F''_n\sin(m\phi)\right]e^{-i\omega\frac{s}{v}}, \tag{3.73}$$

where

$$\chi_n^2 = k^2 - \omega^2 \varepsilon_{c,n} \mu_n, \tag{3.74}$$

is the radial propagation factor and I_m, K_m are modified Bessel functions of the first and second kinds, and order m. With $(P+1)$ regions, there are $4(P+1)$ unknowns and P boundaries. If $\tilde{E}_s$, $\tilde{E}_\phi$, $\tilde{H}_s$ and $\tilde{H}_\phi$ are matched at all these boundaries, then there will be a total of $4P$ equations, so four additional equations must be found for a unique solution. The innermost region $(n = 0)$ contains the origin where $K_m(\chi_0 r) \to \infty$ unless $B_0 = F_0 = 0$. In the outermost region, $I_m(\chi_P r) \to \infty$ unless $A_P = D_P = 0$, leaving a total of $4P$ unknowns.

As surface normal vectors at every interface are $\hat{r}$, the matching conditions are

$$\tilde{E}_{s,n+1}(r = b_n) - \tilde{E}_{s,n}(r = b_n) = 0, \tag{3.75}$$

$$\tilde{H}_{s,n+1}(r = b_n) - \tilde{H}_{s,n}(r = b_n) = 0, \tag{3.76}$$

$$\tilde{E}_{\phi,n+1}(r = b_n) - \tilde{E}_{\phi,n}(r = b_n) = 0. \tag{3.77}$$

Multiplying both sides of these conditions by $\cos(m'\phi)$, integrating over ϕ from 0 to 2π and utilising the orthogonality of sine and cosine functions reveals that fields associated with different values of m can be matched separately. A similar matching condition usually applies for $\tilde{H}_\phi$, but not at the innermost boundary where there is a surface current $\tilde{\kappa}_s$

$$\tilde{H}_{\phi,1}(r = b_n) - \tilde{H}_{\phi,0}(r = b_n) = \begin{cases} \tilde{\kappa}_s, & \text{if n = 0} \\ 0, & \text{otherwise} \end{cases}. \tag{3.78}$$

Applying the same orthogonality argument reveals that the m^{th} term in the summations of $\tilde{H}_\phi$ are determined by the m^{th} term in the surface current summation. It follows that all fields can be decomposed into components associated with the m^{th} term in Equation (3.58). Provided the interfaces between regions have azimuthal symmetry, fields with different values of m do not couple [89]; this would not be the case for other geometries.

Inspection then reveals that of these components, $\tilde{E}_s^{(m)}$, $\tilde{E}_r^{(m)}$, $\tilde{H}_\phi^{(m)}$ are $\propto \cos(m\phi)$ and $\tilde{H}_s^{(m)}$, $\tilde{H}_r^{(m)}$ and $\tilde{E}_\phi^{(m)}$ are $\propto \sin(m\phi)$. The longitudinal field components associated with the m^{th} multipole can be written as

$$\tilde{E}_{s,n}^{(m)}(r,\phi,s,\omega) = [A_n I_m(\chi_n r) + B_n K_m(\chi_n r)]\cos(m\phi)e^{-i\omega\frac{s}{v}}, \tag{3.79}$$

$$\tilde{H}_{s,n}^{(m)}(r,\phi,s,\omega) = [D_n I_m(\chi_n r) + F_n K_m(\chi_n r)]\sin(m\phi)e^{-i\omega\frac{s}{v}}. \tag{3.80}$$

If the outermost region is considered to be filled with a perfect electrical conductor (PEC) or a perfect magnetic conductor (PMC), then fields inside those regions are not considered, which reduces the number of regions to solve for by one, the total number of unknowns by two, and the number of matching equations by four; two additional equations are required. These can be obtained by noting that electric fields parallel to a PEC surface are required to vanish at the surface giving, $\tilde{E}_{s,P-1}(r = b_{P-1}) = \tilde{E}_{\phi,P-1}(r = b_{P-1}) = 0$, and H fields parallel to the surface of a PMC are required to vanish giving, $\tilde{H}_{s,P-1}(r = b_{P-1}) = \tilde{H}_{\phi,P-1}(r = b_{P-1}) = 0$.

The impedance was given in terms of these fields by Equation (3.38), which is for a point source. Since the dipole moment of the source particle is provided by the $m = 1$, $\cos(\phi)$ charge ring from Equation (3.58), only this term needs to be considered for the transverse driving impedance. Rewriting this equation in terms of a $\cos(\phi)$ charge-ring gives the transverse impedance over a length L as

$$Z_1^{\perp}(\omega) = -\frac{L}{k\pi d_1^2 q_1}\left[\int_0^{2\pi} \tilde{E}_{s,0}^{*,(m=1)}(r,\phi,s;\omega)\cos(\phi)e^{-i\omega\frac{s}{v}}\,\mathrm{d}\phi\right]_{r=d_1}, \tag{3.81}$$

which can be found from the electric field in the $n = 0$ region [135].

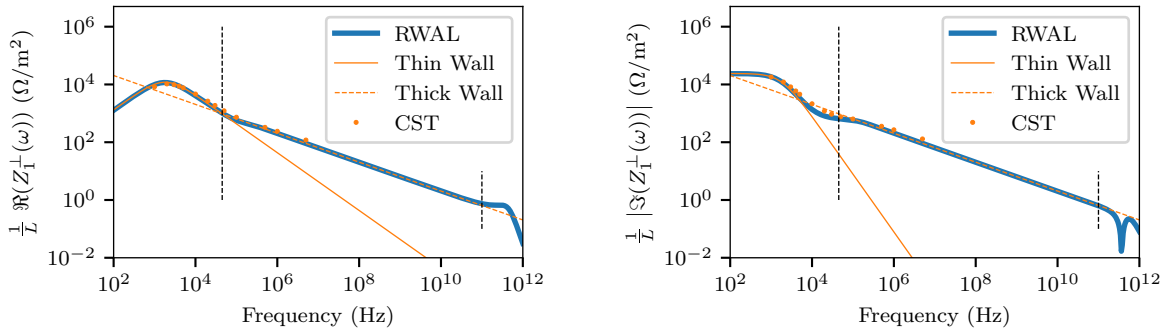
For a given number of regions, RWAL uses a computer algebra system to build up a matrix of matching coefficients [151]. In principle the fields could be computed in all of the annular regions, but the impedance depends only on fields in the beam region, and it is computationally easier to solve for only one region. RWAL therefore uses Cramer's rule to solve for the unknown coefficient in the beam-region and then finds a general expression for the transverse impedance. Finding this general expression for 2

or 3 material layers (4 or 5 regions) typically takes a few minutes on standard hardware, but 4 or 5 material layers can take several hours; a larger number of material layers has not been attempted. These expressions are saved to disk as plain text files, and can be reloaded without having to repeat the solution process. Direct and indirect space-charge impedances are included in the saved solutions of $Z_1^{\perp}$, [135], but are then optionally subtracted. Frequency-dependent material properties can be defined by specifying them as functions of the frequency variable, and lossy materials can be included by specifying their complex material properties [144].

The outputs of RWAL can be compared with the thick and thin-wall impedances given in Section 3.2. This requires two material layers composed of the metal vacuum chamber surrounded by free-space. Figure 3.10 shows an example of an impedance computed by RWAL for a $2\,\mathrm{mm}$-thick stainless steel pipe. Results using the CST low-frequency method described in Section 3.3.2 are overlaid.

Below $\sim 45\,\mathrm{kHz}$ the skin-depth in the pipe is greater than its thickness, and the thin-wall approximation is valid. Above this frequency the skin-depth is smaller than the pipe's thickness and the thick-wall approximation is valid until $\sim 100\,\mathrm{GHz}$. Above this frequency, the real part of the impedance drops rapidly, and the imaginary part changes sign (Figure 3.10 shows the absolute value), which is associated with resonant behaviour between a beam and a propagating waveguide mode [155, 156]. In this frequency range, the material's conductivity should be modified to account for high-frequency effects, but as this thesis is primarily concerned with frequencies in the $100\,\mathrm{kHz}$ - $10\,\mathrm{MHz}$ range, such effects will not be considered.

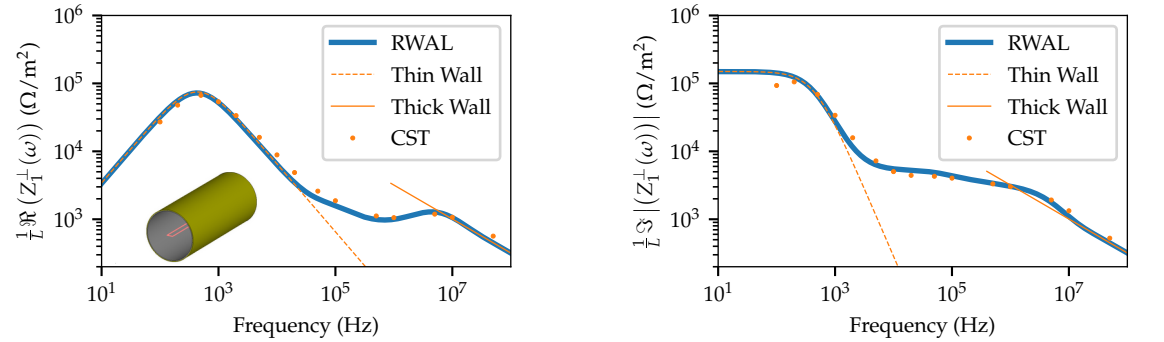
Both RWAL and CST are not limited to single-layer conducting pipes. Figure 3.11 shows a pipe in free space, with a $0.5\,\mathrm{mm}$ thick, copper coating surrounding the outside of a $0.2\,\mathrm{mm}$ thick stainless-steel pipe with an inner radius of $20\,\mathrm{mm}$ (3 material layers, 5 regions). Above $\sim 10\,\mathrm{MHz}$ the innermost stainless layer shields the outer layers, so that the impedance is well approximated by a thick-wall impedance for stainless steel. Below $\sim 10\,\mathrm{kHz}$, the skin depth in the innermost layer is twenty-times its thickness, so that



(a) (b)

Figure 3.10: Real (a) and absolute imaginary (b) parts of the resistive-wall impedance per unit length, for a $\beta \approx 1$ beam inside a a 50 mm radius, stainless steel ($\sigma = 1.4 \times 10^6\,\mathrm{S\,m^{-1}}$) pipe with a thickness of 2 mm. Thin and thick-wall impedance approximations are overlaid, as well as CST results computed by the low-frequency method. The vertical dashed line close to 45 kHz indicates where pipe's skin-depth equals its thickness. The high-frequency vertical dashed line indicates 100 GHz, where the thick-wall approximation breaks down.

it does not effectively shield the outer copper layer. The impedance in this frequency range resembles a thin-wall type impedance, with properties dominated by the copper layer. Both of these approximations are overlaid.



(a) (b)

Figure 3.11: Real (a) and absolute imaginary (b) parts of the driving resistive-wall impedance for a 20 mm diameter, 0.2 mm thick, stainless-steel pipe with conductivity of $1.4 \times 10^6\,\mathrm{S\,m^{-1}}$, a 0.5 mm thick outside copper coating with conductivity of $5.8 \times 10^7\,\mathrm{S\,m^{-1}}$, surrounded by free-space. Results are shown from RWAL and a low-frequency CST simulation. Thin-wall approximations are shown using properties of the copper layer, and the thick-wall approximation uses stainless-steel properties. A screenshot of the CST model is shown in the inset to (a).

3.4.1 Pipes of Other Geometries

RWAL only solves for circular cross-section, cylindrical pipes, and the analytical approach has been extended to other geometries such as multi-layer flat [112], and elliptical [154] pipes. Before these developments, it was shown that for ultra-relativistic beams travelling in conducting pipes, the driving impedance for a rectangular or elliptical beam pipe is equal to that of a circular pipe multiplied by a constant that depends on the geometry [100]. This was extended to include more general geometries [101], and the constants became known as "Yokoya form-factors".

Despite being derived for good conductors, Yokoya form-factors [101] have been applied to materials outside this category, such as ferrite. It has been found that this can lead to significant errors [104], suggesting that care must be taken when applying Yokoya factors outside the regime in which they were derived. It has been found that even for good conductors, Yokoya factors become frequency dependent for non-ultra-relativistic beams [157]. This same study has verified that for elliptical chambers, Yokoya factors remain a good approximation even for non-relativistic beams provided

$$\frac{\omega}{\beta^2\gamma c} \ll 1, \tag{3.82}$$

limiting the applicable frequency range; significant errors were observed from $\frac{\omega}{\beta^2\gamma c} \approx 10$.

Based on this observation, the Yokoya form-factors will be assumed to be a good approximation for ISIS at injection below $\approx$ 70 MHz. Since this is more than 100× the revolution frequency at injection, it is concluded that Yokoya form-factors can be assumed to be valid for all conducting vacuum vessels at ISIS.

And as I sat there listening to that sound of the night which bop has come to represent for all of us, I thought of my friends from one end of the country to the other and how they were really all in the same vast backyard doing something so frantic and rushing about.

— J. Kerouac, "On the Road"

4

Transverse Coherent Bunched Beam Instabilities

The wake fields introduced in Chapter 3 can cause a beam to oscillate in the transverse plane. If the amplitude of this oscillation grows with time, then the beam is said to be unstable. Equation (3.11) shows that for a given wake function, the average force on a witness particle is linearly proportional to the charge of the source particle, so the growth-rate of an instability will depend on the beam's intensity. More intense beams tend to be less stable, although this is not always the case.

Instabilities were only observed when technology enabled sufficiently intense beams to be produced [92, 93, 158]. The foundations of a theoretical framework followed shortly after the first observation[159], and was based on a coasting beam with a coherent transverse offset and a wake force generated by a resistive vacuum vessel. In this theory, the average wake force associated with a rectangular vacuum vessel was computed and linearised with respect to the beam's transverse offset, then substituted as a perturbing term into the Vlasov equation. This analysis demonstrated that under certain conditions, the amplitude of an oscillation could grow exponentially.

Despite the successes of this approach, the majority of high-intensity particle accelerators use bunched rather than coasting beams, so a new treatment was developed to address the problem of *bunches* performing rigid transverse oscillations [160]. This method expressed the average force due to wake fields as a driving term in the harmonic oscillator equation, with the undriven oscillator describing betatron oscillations within the main focusing fields. Coherent oscillations were considered as perturbations on this motion, and the rate of amplitude growth was computed from the eigenvalues of a set of coupled equations.

It was later realised that treating bunches as rigid oscillators neglected the impact of synchrotron oscillations, which provided a "feedback" mechanism whereby the force on a particle could depend on its own transverse offset some time earlier, even for single-turn wakes [161, 162, 163]. It also neglected the crucial role of chromaticity in producing a betatron phase advance between the head and tail of a bunch. This "head-tail" effect was first developed using the harmonic oscillator approach, with several macro particles per bunch to allow for internal degrees of freedom. It was qualitatively understood by considering a wake generated by the head of a bunch disturbing the tail, and then synchrotron motion exchanging the head and tail particles.

An approach to studying the head-tail effect based on the Vlasov equation was ultimately developed [98], which considered internal degrees of freedom within a bunch, synchrotron motion and chromaticity. It decomposed the perturbed distribution into an infinite series of modes in longitudinal phase space, and although the theory was general enough to accommodate the effects of mode coupling and quite general beam distributions, initial work focused on a simplified version.

Neglecting coupling between some classes of modes leads to matrix equations which can be used to compute the complex mode frequencies, Ω [89]

$$0 = \det\left[\left(\frac{\Omega - \omega_\beta}{\omega_s} - l\right) - \underline{M}\right],$$
$$M_{kk'} = A\sum_{p=-\infty}^{\infty} Z_1^\perp(\omega')g_{lk}(\omega' - \omega_\xi)g_{lk'}(\omega' - \omega_\xi),$$

where A is a constant, $\underline{M}$ is an interaction matrix and the functions $g_{lk}(\omega)$ are related to the spectrum of the perturbed distribution and must be found for a particular unperturbed distribution. In this form, the eigen-quantities must be found numerically, but a further approximation can be made by considering only elements on the main diagonal of the interaction matrix. The resulting equations are often put into the form [138]

$$\Omega^{(l,n)} - \omega_\beta - l\omega_s = B\frac{\sum_{p=-\infty}^{\infty} Z_1^\perp(\omega')h_{l,n}(\omega' - \omega_\xi)}{\sum_{p=-\infty}^{\infty} h_{l,n}(\omega' - \omega_\xi)} = BZ_1^{\perp,\text{eff}},$$

where B is a constant, $h_{l,n}(\omega) = \left|\hat{\lambda}_1^{(l,n)}(\omega)\right|^2$ is the energy spectrum of the perturbed longitudinal distribution, $\lambda_1^{(l,n)}(z)$, for the azimuthal mode l and radial mode n and $Z_1^{\perp,\text{eff}}$ is the "effective impedance." The mode numbers characterise the dipole moment distribution in longitudinal phase space using polar coordinates.

This form requires $h_{l,n}$ to be known for a particular unperturbed distribution, and whilst it has been found for some, the equations can be further simplified by considering the "sinusoidal modes" [98], where only $n = 0$ is considered and it is assumed that

$$\lambda_1^{(l,0)}(z) \approx \begin{cases} \cos\left((l+1)\pi\frac{z}{2\hat{z}}\right) & l = 0, 2, ...\text{and } |z| < \hat{z}, \\ \sin\left((l+1)\pi\frac{z}{2\hat{z}}\right) & l = 1, 3, ...\text{and } |z| < \hat{z}, \\ 0 & |z| > \hat{z}, \end{cases}$$

where $\hat{z}$ is half the total bunch length of a water-bag distribution. This gave a simple form of $h_{l,0}(\omega)$, which could then be used to write down closed-form formulas [164].

This form has shown good general agreement with experiments [165] and the closed form formulas it produces have given an intuitive understanding of how instabilities, impedances and chromaticity are related. In short, instabilities can develop if there are

frequencies where the impedance and a mode's energy spectra, shifted by chromaticity, are both non-zero. The nature of any overlap between these quantities determines the resulting dynamics. The real part of the impedance primarily determines an instability's growth rate, whilst the imaginary part determines mode frequency shifts [89].

Sacherer's work was a significant milestone in the development of instability theory. The formulas he derived for decoupled instability growth rates are still in use [166] and the general theory has formed the basis of many future developments. A more general application of the theory was developed [167] that included both azimuthal mode coupling and more general distributions, and continues to be used in recent applications [120, 118, 168, 119]. The general formalism has also been the foundation of studies into Landau damping [169], dual-harmonic RF systems [170], the impact of externally applied noise forces [171], efforts to incorporate amplitude-dependent tunes [172] and direct space-charge [173, 174, 175, 176, 177, 178, 179].

On ISIS, the simplified theory was applied to make predictions for the head-tail instability described in Chapter 2, but discrepancies with experiment were identified [86, 88, 80]. It was predicted that azimuthal modes ± 2 or ± 3 would grow faster than mode ± 1, but the observed distribution is more consistent with mode ± 1 [86]. Furthermore, instability growth rates are observed to be on the order of $0.1\,\mathrm{ms}$, whilst predictions assuming a resistive-wall impedance are on the order of some ms [88, 64].

To understand the source of this instability and verify that the theoretical model makes at least partially accurate predictions for ISIS, the more general form of Sacherer's theory will be presented and applied [167]. This still contains a number of simplifying assumptions, and neglects the impact of space-charge. Despite this, the widespread acceptance of the theory suggests that it may retain some predictive power for ISIS. By using the general theory, the number of simplifications can be minimised and predictions will be the best that analytical techniques can offer. This theory is based on solutions to the linearised Vlasov equation, which will now be derived, and a new code to find numerical solutions, PyTMCI will be introduced.

4.1 Theory of Coherent Transverse Instabilities

The Vlasov equation describes the evolution of a distribution function ψ for a system with the Hamiltonian H. It can be expressed as

$$\frac{\partial \psi}{\partial s} = [H, \psi], \tag{4.1}$$

where the Poisson brackets imply a summation over the pairs of canonical coordinates for a single particle. The most general application would include 3 pairs of coordinates: horizontal, vertical and longitudinal. In this analysis the transverse planes are considered decoupled so the summation is performed for the vertical (y, p_y) and longitudinal (z, δ) coordinates, where y and z are vertical and longitudinal displacement from the synchronous particle, p_y is the transverse momentum divided by the longitudinal momentum and δ is the fractional momentum offset from the synchronous particle.

Wake effects will be considered to be a perturbation on a machine's primary magnetic focusing fields, so the Hamiltonian will be defined as

$$H(y, p_y, z, \delta) = H_0(y, p_y, z, \delta) + \epsilon H_1(y, p_y, z, \delta), \tag{4.2}$$

where H_0 and ϵH_1 are the unperturbed and perturbed Hamiltoninans. Similarly, the beam's distribution will be assumed to evolve as a perturbation on a wake-free, unperturbed distribution

$$\psi(y, p_y, z, \delta) = \psi_0(y, p_y, z, \delta) + \epsilon \psi_1(y, p_y, z, \delta), \tag{4.3}$$

where ψ_0 and $\epsilon\psi_1$ are the unperturbed and perturbed distributions. ϵ is a small parameter in both of these definitions.

In what follows a linearised form of this problem will be formulated by neglecting higher order terms of ϵ. Solutions will then be sought by arranging the various quantities into an "interaction matrix", whose eigenvalues contain a growth rate associated with the perturbed distribution. To evaluate the entries of this matrix, an oscillation

frequency associated with the perturbed distribution will be assumed to be similar to the low intensity limit. After briefly considering the impact of beams composed of many identical bunches, a new code, PyTMCI, will be introduced to calculate numerical solutions for growth rates and instability distributions.

4.1.1 The Linearised Vlasov Equation

The Vlasov equation can then be expressed as

$$\begin{aligned}\frac{\partial \psi}{\partial s} &= [H, \psi] = [H_0 + \epsilon H_1, \psi_0 + \epsilon\psi_1]\,, \\ &= [H_0, \psi_0 + \epsilon\psi_1] + [\epsilon H_1, \psi_0 + \epsilon\psi_1]\,, \\ &= [H_0, \psi_0] + [H_0, \epsilon\psi_1] + [\epsilon H_1, \psi_0] + [\epsilon H_1, \epsilon\psi_1]\,.\end{aligned}$$

The unperturbed distribution will follow

$$\frac{\partial \psi_0}{\partial s} = [H_0, \psi_0]\,, \tag{4.4}$$

so cancelling these terms gives

$$\epsilon\frac{\partial \psi_1}{\partial s} = [H_0, \epsilon\psi_1] + [\epsilon H_1, \psi_0] + [\epsilon H_1, \epsilon\psi_1]\,. \tag{4.5}$$

It can be seen that the final term is $\propto \epsilon^2$, so this term will be neglected, leaving

$$\epsilon\frac{\partial \psi_1}{\partial s} = [H_0, \epsilon\psi_1] + [\epsilon H_1, \psi_0] \tag{4.6}$$

$$\begin{aligned}&= \frac{\partial H_0}{\partial y}\frac{\partial \epsilon\psi_1}{\partial p_y} - \frac{\partial H_0}{\partial p_y}\frac{\partial \epsilon\psi_1}{\partial y} + \frac{\partial \epsilon H_1}{\partial y}\frac{\partial \psi_0}{\partial p_y} - \frac{\partial \epsilon H_1}{\partial p_y}\frac{\partial \psi_0}{\partial y} \\ &\quad + \frac{\partial H_0}{\partial z}\frac{\partial \epsilon\psi_1}{\partial \delta} - \frac{\partial H_0}{\partial \delta}\frac{\partial \epsilon\psi_1}{\partial z} + \frac{\partial \epsilon H_1}{\partial z}\frac{\partial \psi_0}{\partial \delta} - \frac{\partial \epsilon H_1}{\partial \delta}\frac{\partial \psi_0}{\partial z}.\end{aligned} \tag{4.7}$$

Up to this point, no details of the specific system have been used, but a solution will require knowledge of H_0, ϵH_1 and ψ_0.

The unperturbed Hamiltonian, H_0, will be assumed to describe oscillations in the longitudinal and transverse planes. In the longitudinal direction, a particle will perform linear synchrotron oscillations, which are generally caused by the focusing effect of

RF cavities. In the transverse direction, a particle will perform betatron oscillations about a closed orbit, which are caused by the focusing magnetic fields of the accelerator; in a synchrotron these are mainly provided by quadrupole magnets [180]. These too will be considered to be linear, so the unperturbed Hamiltonian can therefore be written directly as

$$H_0(y, p_y, z, \delta) = \frac{1}{2}\left(\frac{\omega_\beta}{\beta c}\right)^2 y^2 + \frac{1}{2}p_y^2 - \frac{1}{2\eta}\left(\frac{\omega_s}{\beta c}\right)^2 z^2 - \frac{\eta}{2}\delta^2, \tag{4.8}$$

where η is the momentum slip factor defined as

$$\eta = \frac{1}{\gamma_{\mathrm{Tr}}^2} - \frac{1}{\gamma^2}, \tag{4.9}$$

and γ_{Tr} is the transition gamma. Equation (4.8) is the Hamiltoninan for a harmonic oscillator in two decoupled directions.

The wake force will change the beam's transverse momentum, so if there were only a wake force without an external guiding field the momentum would follow

$$\frac{\mathrm{d}p_y}{\mathrm{d}s} = \frac{1}{\beta c}\frac{\mathrm{d}p_y}{\mathrm{d}t} = \frac{1}{\beta^2 E_{\mathrm{t}}}F_y, \tag{4.10}$$

where $E_{\mathrm{t}} = \gamma mc^2$ is the total energy and F_y is the force experienced by the particle; it has been assumed that the longitudinal velocity is much larger than the transverse. Since F_y is independent of y, it can be seem from Hamilton's canonical equations in the absence of an external focusing field

$$\frac{\mathrm{d}p_y}{\mathrm{d}s} = -\epsilon\frac{\partial H_1}{\partial y}, \tag{4.11}$$

that the perturbed Hamiltonian must be

$$\epsilon H_1 = -\frac{y}{\beta^2 E_{\mathrm{t}}}F_y. \tag{4.12}$$

This is independent of δ and p_y, so $\frac{\partial H_1}{\partial \delta} = \frac{\partial H_1}{\partial p_y} = 0$ can be substituted leaving

$$\begin{aligned}\epsilon\frac{\partial \psi_1}{\partial s} = {} & \frac{\partial H_0}{\partial y}\frac{\partial \epsilon\psi_1}{\partial p_y} - \frac{\partial H_0}{\partial p_y}\frac{\partial \epsilon\psi_1}{\partial y} + \frac{\partial \epsilon H_1}{\partial y}\frac{\partial \psi_0}{\partial p_y} \\ & + \frac{\partial H_0}{\partial z}\frac{\partial \epsilon\psi_1}{\partial \delta} - \frac{\partial H_0}{\partial \delta}\frac{\partial \epsilon\psi_1}{\partial z} + \frac{\partial \epsilon H_1}{\partial z}\frac{\partial \psi_0}{\partial \delta}.\end{aligned} \tag{4.13}$$

Substituting the perturbed Hamiltonian and partial derivatives of the unperturbed Hamiltonian

$$\epsilon\frac{\partial\psi_1}{\partial s} = \left(\frac{\omega_\beta}{\beta c}\right)^2 y\frac{\partial\epsilon\psi_1}{\partial p_y} - p_y\frac{\partial\epsilon\psi_1}{\partial y} - \frac{1}{\beta^2 E_\mathrm{t}}F_y\frac{\partial\psi_0}{\partial p_y} - \frac{1}{\eta}\left(\frac{\omega_s}{\beta c}\right)^2 z\frac{\partial\epsilon\psi_1}{\partial\delta} + \eta\delta\frac{\partial\epsilon\psi_1}{\partial z} - \frac{y}{\beta^2 E_\mathrm{t}}\frac{\partial F_y}{\partial z}\frac{\partial\psi_0}{\partial\delta}. \tag{4.14}$$

Following published methods [89], polar coordinates will be introduced for both the longitudinal and transverse planes with the definitions

$$y = q\cos(\theta), \tag{4.15}$$

$$p_y = -\frac{\omega_\beta}{\beta c}q\sin(\theta), \tag{4.16}$$

$$z = r\cos(\phi), \tag{4.17}$$

$$\delta = \frac{\omega_s}{\eta\beta c}r\sin(\phi), \tag{4.18}$$

which will be substituted into the Vlasov equation. Chromaticity, which describes the betatron tune of off-momentum particles, plays an important role in the theory of instabilities, and is included here by making the substitution $\omega_\beta \rightarrow \omega_\beta(1+\xi\delta)$ where ξ is the normalised chromaticity; the term this would contribute to $\frac{\partial H_0}{\partial\delta}$ is neglected so that the longitudinal motion is unaffected by the transverse amplitude [89]. After making this substitution and assuming $\frac{\partial\psi_0}{\partial\theta} = \frac{\partial\psi_0}{\partial\phi} = 0$, the equation becomes

$$\frac{\partial\epsilon\psi_1}{\partial s} = -\frac{\omega_\beta(1+\xi\delta)}{\beta c}\frac{\partial\epsilon\psi_1}{\partial\theta} - \frac{\omega_s}{\beta c}\frac{\partial\epsilon\psi_1}{\partial\phi} + \frac{F_y}{\beta^2 E_\mathrm{t}}\frac{\beta c}{\omega_\beta}\sin(\theta)\frac{\partial\psi_0}{\partial q} - \frac{q}{\beta^2 E_\mathrm{t}}\frac{\partial F_y}{\partial z}\frac{\eta v}{\omega_s}\sin(\phi)\cos(\theta)\frac{\partial\psi_0}{\partial r}. \tag{4.19}$$

Attention is now turned to the distribution functions. The unperturbed distribution has already been assumed to have no θ or ϕ dependence, but now it is further assumed that chromaticity does not affect the transverse distribution, so the unperturbed distribution can be expressed as a separated product

$$\psi_0 = f_0(q)g_0(r), \tag{4.20}$$

where f_0 and g_0 are the unperturbed transverse and longitudinal distributions. A form is assumed for the perturbed distribution

$$\epsilon\psi_1 = f_1(q,\theta,s)g_1(r,\phi), \tag{4.21}$$

where f_1 and g_1 are the transverse and longitudinal distributions. Explicit s dependence has been assigned to f_1, because the instabilities being investigated are coherent transverse oscillations with an amplitude that changes with time.

Since the motion of interest is a coherent dipole oscillation, the transverse perturbed distribution is assumed to be the unperturbed distribution, but offset by a distance from the origin and rotating around it in the same direction as the unperturbed betatron motion. Using the second term in the Taylor expansion of $f_0(y-\Delta,p_y)$, then substituting $\Delta = D_0 e^{\mathrm{Im}\{\Omega\}\frac{s}{\beta c}}$ gives an expression for the transverse dependence of the perturbed distribution

$$f_1(q,\theta,s) = -D_0\frac{\partial f_0}{\partial q}e^{i\left(\theta-\Omega\frac{s}{\beta c}\right)}. \tag{4.22}$$

The real part of Ω sets the frequency of the oscillation, or the time-period for a full rotation in the transverse phase-space and the imaginary part describes a growing or damping of the offset from the origin. Substituting this into Equation (4.20) and collecting terms, then following the usual approach of deriving the Sacherer integral equation [89] and substituting $\sin(\theta) \rightarrow \frac{1}{2i}e^{i\theta}$ and $\cos(\theta) \rightarrow \frac{1}{2}e^{i\theta}$ gives

$$\begin{aligned}\left[i\frac{\Omega}{\beta c}g_1 - ig_1\frac{\omega_\beta(1+\xi\delta)}{\beta c} - \frac{\omega_s}{\beta c}\frac{\partial g_1}{\partial\phi}\right]\left(D_0\frac{\partial f_0}{\partial q}\right)e^{-i\Omega\frac{s}{v}}\\ = -i\frac{F_y}{2\beta^2E_\mathrm{t}}\frac{\beta c}{\omega_\beta}g_0(r)\frac{\partial f_0}{\partial q} - \frac{q}{2\beta^2E_\mathrm{t}}\frac{\partial F_y}{\partial z}\frac{\eta v}{\omega_s}\sin(\phi)f_0\frac{\partial g_0}{\partial r}.\end{aligned} \tag{4.23}$$

The perturbed longitudinal distribution is now expanded as a Fourier series in ϕ,

$$g_1(r,\phi) = e^{i\frac{\xi\omega_\beta}{\eta\beta c}z}\sum_{l=-\infty}^{\infty}R_l(r)e^{il\phi}, \tag{4.24}$$

$$\frac{\partial g_1}{\partial\phi} = -i\frac{\xi\omega_\beta}{\eta\beta c}e^{i\frac{\xi\omega_\beta}{\eta\beta c}z}r\sin(\phi)\sum_l R_l(r)e^{il\phi} + e^{i\frac{\xi\omega_\beta}{\eta\beta c}z}\sum_l ilR_l(r)e^{il\phi}. \tag{4.25}$$

After substituting this into Equation (4.23) and some algebra, it is found that

$$\sum_{l''=-\infty}^{\infty} R_{l''}(r)\left[\frac{\Omega}{\beta c}-\frac{\omega_\beta}{\beta c}-l''\frac{\omega_s}{\beta c}\right]\left(D_0\frac{\partial f_0}{\partial q}\right)e^{-i\Omega\frac{s}{\beta c}}e^{i\frac{\xi\omega_\beta}{\eta\beta c}z}e^{il''\phi} = -\frac{F_y}{2\beta^2E_\mathrm{t}}\frac{\beta c}{\omega_\beta}g_0(r)\frac{\partial f_0}{\partial q}+i\frac{q}{2\beta^2E_\mathrm{t}}\frac{\partial F_y}{\partial z}\frac{\eta\beta c}{\omega_s}\sin(\phi)f_0\frac{\partial g_0}{\partial r}. \tag{4.26}$$

The force and its derivative are then substituted from Equation (3.25), and $D_0e^{-i\Omega\frac{s}{v}}$ cancelled. The summation on the left hand side is removed by multiplying both sides by $e^{-il\phi}$ and integrating from 0 to 2π. The third Bessel function identity in Table (6.1) of [89] is substituted, as well as

$$\hat{\lambda}_1(\omega) = \int_{z=-\infty}^{+\infty}\int_{\delta=-\infty}^{\infty} g_1(r,\phi)\,\mathrm{d}\delta e^{-i\omega\frac{z}{\beta c}}\,\mathrm{d}z \tag{4.27}$$

$$= 2\pi\frac{\omega_s}{\eta\beta c}\sum_{l'=-\infty}^{\infty} i^{-l'}\int_{r=0}^{\infty} R_{l'}(r)J_{l'}\left(\frac{\omega}{\beta c}r-\frac{\xi\omega_\beta}{\eta\beta c}r\right)r\,\mathrm{d}r, \tag{4.28}$$

where the area element $\mathrm{d}\delta\,\mathrm{d}z=\frac{\omega_s}{\eta\beta c}r\mathrm{d}r\mathrm{d}\phi$ has been used. Equation (4.26) becomes

$$\begin{aligned}\left[\Omega-\omega_\beta-l\omega_s\right]\left(\frac{\partial f_0}{\partial q}\right)R_l(r) = -i\frac{\pi e^2}{\beta^2\gamma m_0c^2T_0^2}\frac{\omega_s}{\eta\beta c}\sum_{l'=-\infty}^{\infty} i^{l-l'}\sum_{p=-\infty}^{\infty} Z_1^\perp(\omega')\\ \left[\int_{r'=0}^{\infty} R_{l'}(r')J_{l'}\left(\frac{\omega'-\omega_\xi}{\beta c}r'\right)r'\,\mathrm{d}r'\right]\\ \left[\frac{\beta c}{\omega_\beta}g_0(r)\frac{\partial f_0}{\partial q}J_l\left(\frac{\omega'-\omega_\xi}{\beta c}r\right)-\frac{\omega'}{\beta c}\frac{\eta\beta c}{\omega_s}qf_0\frac{\partial g_0}{\partial r}\frac{l}{\frac{\omega'}{\beta c}r-\frac{\xi\omega_\beta}{\eta\beta c}r}J_l\left(\frac{\omega'-\omega_\xi}{\beta c}r\right)\right],\end{aligned} \tag{4.29}$$

with

$$\omega' = p\omega_0+\Omega \qquad\qquad p\in\mathbb{Z}. \tag{4.30}$$

4.1.1.1 Series Expansion of Longitudinal Distribution

The unperturbed longitudinal distribution and the radial part of the perturbed distribution are expanded with a basis of generalised Laguerre polynomials [167], which were chosen because of their orthogonality on the interval $[0, \infty)$ and because certain integrals involving them have been tabulated. The substitutions made are

$$R_l(r) = a^{|l|} r^{|l|} e^{-ar^2} \sum_{n'=0}^{\infty} \alpha_{ln'} L_{n'}^{(|l|)}(ar^2), \tag{4.31}$$

$$g_0(r) = \frac{N\eta\beta c}{2\pi\omega_s} e^{-ar^2} \sum_{k=0}^{\infty} G_k L_k^{(0)}(ar^2), \tag{4.32}$$

where a is a free constant parameter. Equation (4.31) is substituted into Equation (4.29), both sides multiplied by $r^{|l|} L_n^{(l)}(ar^2)$ and integrated over ar^2 from 0 to ∞. Equation (4.32) is also substituted, as well as

$$\frac{\partial g_0}{\partial r} = -\frac{N\eta\beta c}{2\pi\omega_s} 2are^{-ar^2} \left(\sum_{k=0}^{\infty} G_k L_{k-1}^{(1)}(ar^2) + \sum_{k=0}^{\infty} G_k L_k^{(0)}(ar^2) \right), \tag{4.33}$$

which has used the identity $L_k^{(\alpha)'}(x) = -L_{k-1}^{(\alpha+1)}(x)$ and symmetry properties of Bessel functions [181]. Equation (4.29) then takes the form

$$\begin{aligned} &\left[\Omega - \omega_\beta - l\omega_s\right] \left(\frac{\partial f_0}{\partial q}\right) \alpha_{ln} \frac{\Gamma(|l| + n + 1)}{n!} = -i \frac{Nr_0 c}{2\beta\gamma\omega_\beta T_0^2} \sum_{l'=-\infty}^{\infty} i^{l-l'} \sum_{p=-\infty}^{\infty} Z_1^{\perp}(\omega') \\ &\left[\int_{r'=0}^{\infty} R_{l'}(r') J_{l'} \left(\frac{\omega' - \omega_\xi}{\beta c} r' \right) r' \, \mathrm{d}r' \right] \\ &\sum_{k=0}^{\infty} G_k \left[\frac{\partial f_0}{\partial q} I_{lnk}^{(1)}(\omega' - \omega_\xi) + 2aqf_0 \frac{\eta\omega'\omega_\beta l}{\omega_s(\omega' - \omega_\xi)} \left(I_{lnk}^{(2)}(\omega' - \omega_\xi) + I_{lnk}^{(1)}(\omega' - \omega_\xi) \right) \right], \end{aligned} \tag{4.34}$$

with the definitions [182]

$$\begin{aligned} I_{lnk}^{(1)}\left(\omega' - \omega_\xi\right) &= 2a(\mathrm{sgn}(\omega' - \omega_\xi)\mathrm{sgn}(l))^{|l|} \int_{r=0}^{\infty} r^{|l|+1} e^{-ar^2} L_n^{(|l|)}(ar^2) L_k^{(0)}(ar^2) J_{|l|} \left(\frac{|\omega' - \omega_\xi|}{\beta c} r \right) \mathrm{d}r \\ &= (\mathrm{sgn}(\omega' - \omega_\xi)\mathrm{sgn}(l))^{|l|} (-1)^{n+k} \left(\frac{|\omega' - \omega_\xi|}{2a\beta c} \right)^{|l|} \exp\left(-\frac{|\omega' - \omega_\xi|^2}{4a\beta^2 c^2} \right) \\ &\quad L_n^{(-n+k)} \left(\frac{|\omega' - \omega_\xi|^2}{4a\beta^2 c^2} \right) L_k^{(|l|+n-k)} \left(\frac{|\omega' - \omega_\xi|^2}{4a\beta^2 c^2} \right), \end{aligned} \tag{4.35}$$

and (see Appendix D)

$$I^{(2)}_{lnk}(\omega'-\omega_\xi) = 2a\int_{r=0}^{\infty} r^{|l|+1}e^{-ar^2}L_n^{(|l|)}(ar^2)L_{k-1}^{(1)}(ar^2)J_l\left(\frac{\omega'-\omega_\xi}{\beta c}r\right)\mathrm{d}r$$
$$= (\mathrm{sgn}(\omega'-\omega_\xi)\mathrm{sgn}(l))^{|l|}\left(\frac{|\omega'-\omega_\xi|}{2a\beta c}\right)^{|l|}\exp\left(-\frac{|\omega'-\omega_\xi|^2}{4a\beta^2c^2}\right)$$
$$\sum_{r_1=0}^{k-1}(-1)^{n+r_1}L_n^{(-n+r_1)}\left(\frac{|\omega'-\omega_\xi|^2}{4a\beta^2c^2}\right)L_{r_1}^{(|l|+n-r_1)}\left(\frac{|\omega'-\omega_\xi|^2}{4a\beta^2c^2}\right). \quad (4.36)$$

After substituting for the remaining $R_{l'}(r')$ in Equation (4.34), defining $x^2 = ar'^2$ and using the tabulated result [181, eqn.7.421-6]

$$\int_0^\infty x^{\nu+1}e^{-x^2}L_n^\nu(x^2)J_\nu(xy)\,\mathrm{d}x = \frac{1}{2n!}\left(\frac{y}{2}\right)^{2n+\nu}e^{-y^2/4}, \quad (4.37)$$

it is found that

$$\left[\Omega-\omega_\beta-l\omega_s\right]\left(\frac{\partial f_0}{\partial q}\right)\alpha_{ln}\frac{\Gamma(|l|+n+1)}{n!} =$$
$$-i\frac{Nr_0c}{2\beta\gamma\omega_\beta T_0^2}\sum_{l'=-\infty}^{\infty}i^{l-l'}\sum_{p=-\infty}^{\infty}Z_1^\perp(\omega')\sum_{n'=0}^{\infty}\alpha_{l'n'}Q_{l'n'}(\omega'-\omega_\xi) \quad (4.38)$$
$$\sum_{k=0}^{\infty}G_k\left[\frac{\partial f_0}{\partial q}I^{(1)}_{lnk}(\omega'-\omega_\xi)+2aqf_0\frac{\eta\omega'\omega_\beta l}{\omega_s(\omega'-\omega_\xi)}\left(I^{(2)}_{lnk}(\omega'-\omega_\xi)+I^{(1)}_{lnk}(\omega'-\omega_\xi)\right)\right],$$

with

$$Q_{l'n'}(\omega'-\omega) = a^{|l'|/2-1}\mathrm{sgn}(l')^{|l'|}\frac{1}{2n'!}\left(\frac{\omega'-\omega_\xi}{2\sqrt{a}\beta c}\right)^{2n'+|l'|}e^{-\frac{\left(\omega'-\omega_\xi\right)^2}{4a\beta^2c^2}}. \quad (4.39)$$

The coefficients, G_k, are found from the Laguerre series expansion of $g_0(r)$, as described in Appendix E.

4.1.1.2 Assuming a Transverse Gaussian Distribution

Substituting a transverse Gaussian distribution

$$f_0(q) = Ae^{-\frac{q^2}{2\sigma_y^2}}, \quad (4.40)$$
$$\frac{\mathrm{d}f_0}{\mathrm{d}q} = -\frac{q}{\sigma_y^2}f_0(q), \quad (4.41)$$

into Equation (4.38), cancelling qf_0 and then multiplying both sides by σ_y^2 gives

$$\begin{aligned}\left[\Omega - \omega_\beta - l\omega_s\right]\alpha_{ln}\frac{\Gamma(|l|+n+1)}{n!} = \\ -i\frac{Nr_0c}{2\beta\gamma\omega_\beta T_0^2}\sum_{l'=-\infty}^{\infty} i^{l-l'}\sum_{p=-\infty}^{\infty} Z_1^\perp(\omega')\sum_{n'=0}^{\infty}\alpha_{l'n'}Q_{l'n'}(\omega'-\omega_\xi) \\ \sum_{k=0}^{\infty} G_k\left[I_{lnk}^{(1)}(\omega'-\omega_\xi) - 2a\sigma_y^2\frac{\eta\omega'\omega_\beta l}{\omega_s(\omega'-\omega_\xi)}\left(I_{lnk}^{(2)}(\omega'-\omega_\xi) + I_{lnk}^{(1)}(\omega'-\omega_\xi)\right)\right].\end{aligned} \tag{4.42}$$

The term $\propto \sigma_y^2$ is usually neglected on the basis that provided σ_y is not too large and $\omega' \neq \omega_\xi$, it is small compared to the other term.

4.1.2 Interaction Matrix Form

Ω and α_{ln}, should be found from the eigenvalues and vectors of an interaction matrix. This is formed by rearranging Equation (4.42) into the form

$$\begin{aligned}\left[\frac{\Omega-\omega_\beta}{\omega_s}\right]\alpha_{ln} =& l\alpha_{ln} - i\frac{n!}{\Gamma(|l|+n+1)}\frac{Nr_0c}{2\beta\gamma\omega_\beta\omega_s T_0^2}\sum_{l'=-\infty}^{\infty} i^{l-l'}\sum_{p=-\infty}^{\infty} Z_1^\perp(\omega') \\ &\sum_{n'=0}^{\infty}\alpha_{l'n'}Q_{l'n'}(\omega'-\omega_\xi) \\ &\sum_{k=0}^{\infty} G_k\left[I_{lnk}^{(1)}(\omega'-\omega_\xi) - 2a\sigma_y^2\frac{\eta\omega'\omega_\beta l}{\omega_s(\omega'-\omega_\xi)}\left(I_{lnk}^{(2)}(\omega'-\omega_\xi) + I_{lnk}^{(1)}(\omega'-\omega_\xi)\right)\right].\end{aligned} \tag{4.43}$$

This can be expressed more succinctly as a matrix equation

$$\left[\frac{\Omega-\omega_\beta}{\omega_s}\right]\begin{pmatrix}\cdots\\ \alpha_{0,0}\\ \alpha_{1,0}\\ \alpha_{2,2}\\ \cdots\end{pmatrix} = \underline{M}\begin{pmatrix}\cdots\\ \alpha_{0,0}\\ \alpha_{1,0}\\ \alpha_{2,2}\\ \cdots\end{pmatrix} \tag{4.44}$$

where $\underline{M}$ is the interaction matrix, with elements defined as

$$\begin{aligned}M_{lnl'n'} = l\delta_{nn'}\delta_{ll'} - i\frac{n!}{\Gamma(|l|+n+1)}\frac{Nr_0c}{2\beta\gamma\omega_\beta\omega_s T_0^2}i^{l-l'}\sum_{p=-\infty}^{\infty} Z_1^\perp(\omega')Q_{l'n'}(\omega'-\omega_\xi) \\ \sum_{k=0}^{\infty} G_k\left[I_{lnk}^{(1)}(\omega'-\omega_\xi) - 2a\sigma_y^2\frac{\eta\omega'\omega_\beta l}{\omega_s(\omega'-\omega_\xi)}\left(I_{lnk}^{(2)}(\omega'-\omega_\xi) + I_{lnk}^{(1)}(\omega'-\omega_\xi)\right)\right],\end{aligned} \tag{4.45}$$

and the matrix structure shown in Figure 4.1.

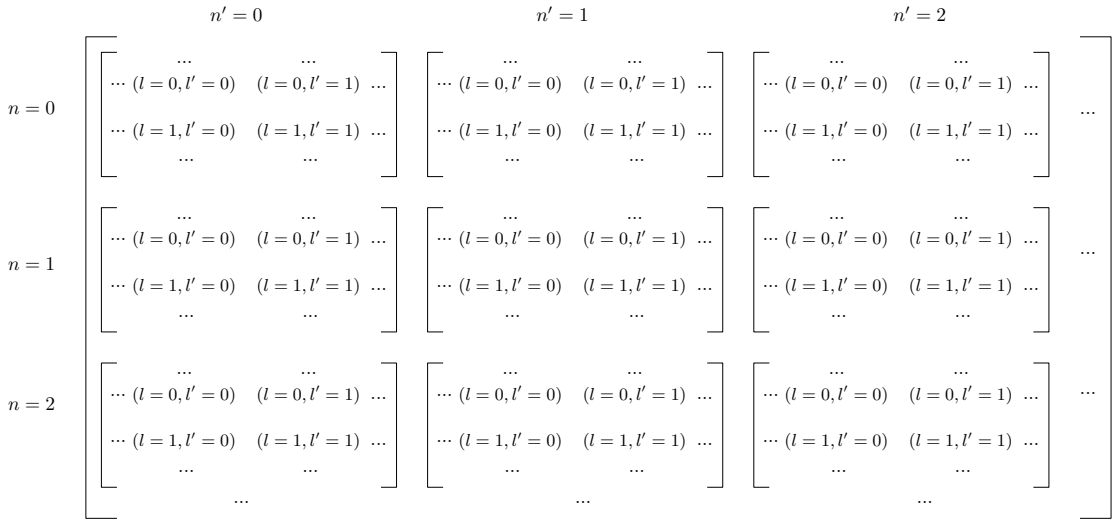


Figure 4.1: Shows dependence of the matrix $\underline{M}$ on l, l', n and n' for one possible structure.

4.1.3 Equally Spaced Identical Bunches

Equation (4.45) was derived for a single bunch, but can be modified to account for multiple bunches by introducing additional terms to the wake force in Equation (3.14). These additional terms contain the same wake function, but evaluated at a distance z which is only a fraction of the machine circumference.

It is found that the bunches oscillate with a collective multi-bunch mode μ_b, which can take an integer value between 0 and $M - 1$, where M is the number of bunches [89]. The Vlasov equation takes the form of Equation (4.42), but with the substitution

$$\sum_{p=-\infty}^{\infty} ()_{\omega'=p\omega_0+\Omega} \rightarrow M \sum_{p=-\infty}^{\infty} ()_{\omega'=pM\omega_0+\mu_b\omega_0+\Omega} \,. \tag{4.46}$$

4.1.4 Low Intensity Limit (Decoupled Azimuthal Modes)

The matrix elements of Equation (4.45) have several functions that need to be evaluated at ω', as defined in Equation (4.30), which depends on the unknown quantity Ω. In the low N limit, or the case where $Z_1^\perp = 0$, this dependence is removed and the interaction matrix elements become

$$M_{lnl'n'} = l\delta_{nn'}\delta_{ll'}, \tag{4.47}$$

which produces a diagonal matrix with eigenvalues

$$\Omega^{(l,n)} = \omega_\beta + l\omega_s, \tag{4.48}$$

and eigenvectors with only a single non-zero term for each value of n. It follows that in the limit of small N or a weak wake force, the different azimuthal modes of instability have properties that are independent of each other, the azimuthal modes are therefore described as decoupled [89].

In this regime, only a single term contributes to the Fourier series expansion of $g_1(r,\phi)$. For a dominant azimuthal mode number l, the perturbed distribution will then have the form

$$-D_0\frac{\partial f_0}{\partial q}R_l(r)e^{i\left(\theta+l\phi-\Omega\frac{s}{\beta c}\right)}e^{i\frac{\xi\omega_\beta}{\eta\beta c}z}. \tag{4.49}$$

For the case that $\xi = 0$, it can be seen that the projection of this onto the (r,ϕ) plane is $\propto e^{i\left(l\phi-\Omega\frac{s}{\beta c}\right)}$, which, for $l \neq 0$, describes a rotation. If $\xi \neq 0$, then this rotation gains an additional term describing a travelling wave in the z-direction, and for $l = 0$ this will be the only travelling wave. For a beam below transition ($\eta < 0$) with $\xi < 0$, this will appear to travel from the tail to the head of the bunch. If $l \neq 0$, then the combination of these two travelling waves will distort the rotational dynamics.

4.1.5 Approximate Solutions (PyTMCI)

PyTMCI [119] is a new code to evaluate the transverse stability of a bunched beam by evaluating the eigenvalues and vectors of the interaction matrix in Equation (4.44). A number of assumptions and approximations must first be made to find the eigenquantities of this infinite matrix.

To evaluate the matrix elements of Equation (4.45), PyTMCI uses the well-known perturbation technique [89] on the low-intensity limit. In this approach, Equation (4.48) is substituted for Ω on the RHS of Equation (4.45), and the eigenvectors and eigenvalues of the resulting matrix found numerically. Since it is usually the case that $\omega_\beta \gg \omega_s$, PyTMCI also has the option to make the substitution $\Omega^{(l)} \approx \omega_\beta$, which speeds up computation by introducing certain symmetries to the interaction matrix.

In principle this matrix has infinite dimensions, so it must be truncated in both the azimuthal and radial indices l and n for a numerical solution. Convergence of the eigenvalues and vectors must be verified by manually increasing the maximum value of l and n. The infinite summations over p and k must also be truncated and convergence verified, or coefficients above a certain index verified as being sufficiently small.

The term $\propto \sigma_y^2$ will be neglected, which is justified on ISIS because the experiments described in Chapter 2 indicated the presence of a large amplitude, low-frequency narrowband impedance. The dominant terms in the impedance summation are therefore expected to occur at the lowest frequency betatron sidebands, where $\omega' \neq \omega_\xi$ and this term is expected to be negligible.

4.2 PyTMCI Benchmarks

With these modifications, PyTMCI can obtain eigenvalues and vectors of the interaction matrix. The eigenvalues can be rearranged to obtain a mode's frequency $\mathrm{Re}\,(\Omega)$ and its growth rate

$$\tau^{-1} = \mathrm{Im}\,(\Omega)\,. \tag{4.50}$$

A positive growth rate indicates an unstable mode with an exponentially growing coherent offset, whilst a negative growth rate indicates that a mode is stable. In this thesis, the quantity of interest is usually the growth rate of the most unstable mode because this can limit the time a beam can be stored. To verify that PyTMCI makes accurate predictions for this quantity, its outputs will be benchmarked against results from the particle tracking code PyHEADTAIL [122] for some example problems.

Perfect agreement between PyTMCI and PyHEADTAIL is not expected for several reasons. Firstly, because the quantities of interest will depend on the initial coordinates of the macroparticles in PyHEADTAIL, which are randomly generated to match the given distribution. The finite number of these macroparticles will cause results to exhibit Schottky noise [183], so that in principle an average of many initial distributions should be used. PyHEADTAIL will also more accurately simulate the non-linear regions of the longitudinal phase-space and the associated synchrotron tune spread, since PyTMCI assumes linear synchrotron motion without tune spread.

Given these differences, differences on the order of 10 % for the characteristic growth time, τ, of the most unstable mode will be considered a successful benchmark. Convergence of PyTMCI results will therefore not be verified in this section, and instead a maximum of 20 azimuthal modes and 10 radial modes will be used, which are the current limit of PyTMCI. Similarly, unless stated otherwise, PyHEADTAIL results will be taken from a single simulation with 100,000 macroparticles.

The perturbed longitudinal distribution, $g_1(r, \phi)$ onto the z-axis, is also of interest and can be found from the eigenvectors of the most unstable mode with Equations (4.24) and (4.31). The projection of $g_1(r, \phi)e^{-i\Omega \frac{s}{\beta c}}$ is proportional to the beam's transverse dipole moment, and its distribution can be compared with the beam position monitor signals such as the one shown in Figure 2.8. The distributions computed by PyTMCI and PyHEADTAIL will also be compared.

4.2.1 Example 1 – A Dominant Head-Tail Mode

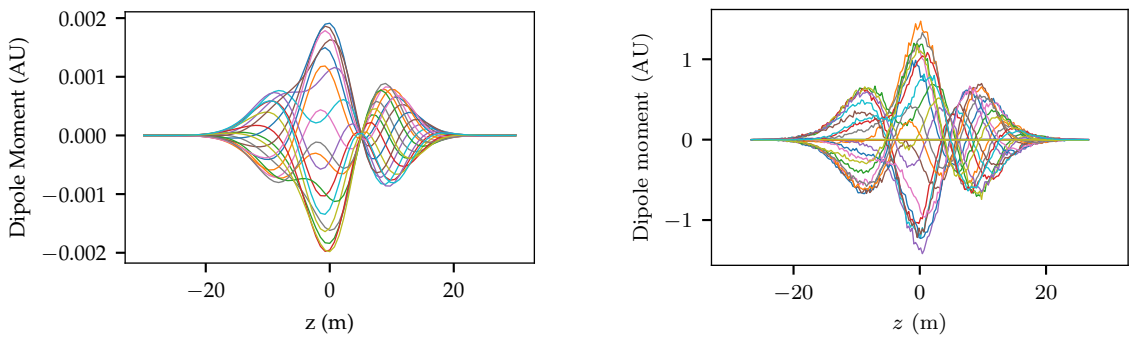
The first example demonstrates an unstable head-tail mode with a single dominant azimuthal component and the lowest-order radial component. The accelerator parameters used for this example are listed in Table 4.1, and the impedance was defined as a single resonator defined by Equation (3.35) with $f_r = 5\,\mathrm{MHz}$, $R_\perp = 1\,\mathrm{M\Omega\,m^{-1}}$ and $Q_r = 3$.

For these parameters, PyTMCI predicts $\tau = 136\,\mu\mathrm{s}$ whilst PyHEADTAIL predicts $124\,\mu\mathrm{s}$. The projection of the perturbed distributions are shown in Figure 4.2. The growth rates differ by only $\approx 10\,\%$, which is considered a good level of agreement. The longitudinal distribution of the dipole moment also appears qualitatively similar, with a high-amplitude oscillation around $z \approx 0$ and two smaller oscillations around $z \approx \pm 10$. There is one clear node on the right hand side of the projected distribution, but the asymmetry indicates that some mode coupling has occurred. The azimuthal mode number can be identified from the eigenvalue, which is computed to be -2.01 by PyTMCI and -1.9 by PyHEADTAIL, and the projected distribution still visibly resembles an azimuthal mode $l = \pm 2$ instability.

The perturbed longitudinal distribution, $g_1(r, \phi)$, computed by PyTMCI is shown in Figure 4.3 for a number of phases. The motion of the transverse dipole moment is seen to resemble a distorted rotation in the longitudinal phase space. This matches the description of a single decoupled azimuthal mode dominating the distribution when $l \neq 0$, as described in Section 4.1.4. As explained in that Section, the distortion arises because $\xi \neq 0$, so the distribution includes a travelling wave component in the z and ϕ directions.

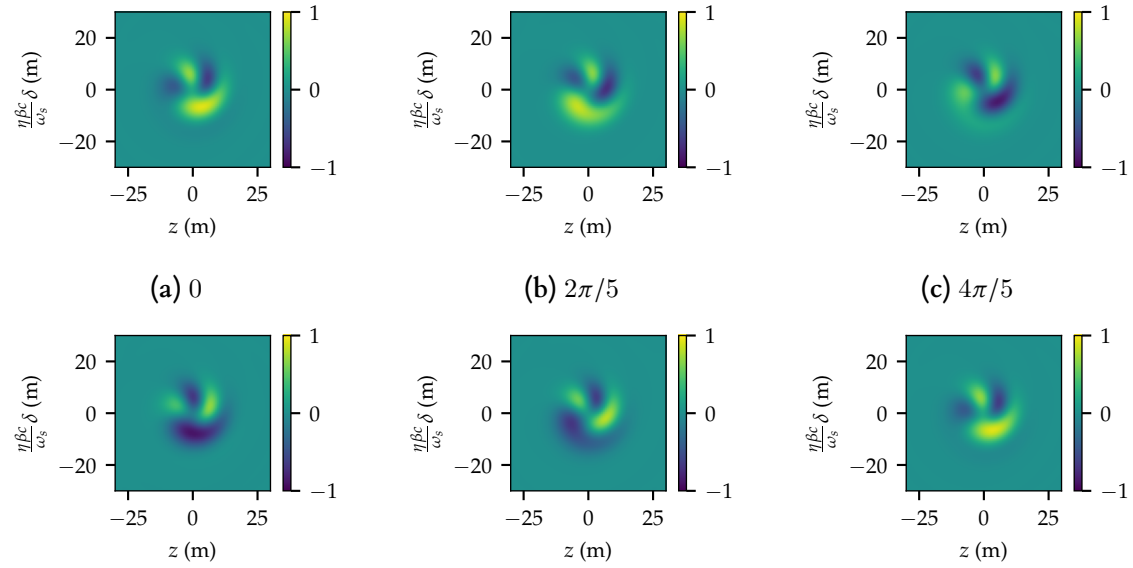
Table 4.1: Parameters used for PyTMCI benchmark example 1.

Parameter	Value	Parameter	Value
Circumference	$163.3\,\mathrm{m}$	Transition γ	5.034
Particle Type	proton	Betatron Tune	3.83
Relativistic β	0.65	Synchrotron Tune	0.008
Number of Bunches	1	Chromaticity	-0.5
Particles per bunch	2×10^{13}		



(a) (b)

Figure 4.2: Perturbed distribution $g_1(r, \phi)$ of PyTMCI benchmark example 1, projected onto the z axis for several consecutive turns. Each line is one revolution and colours help to distinguish different turns. Distributions were computed by PyTMCI (a) and PyHEADTAIL (b).



(a) 0 (b) $2\pi/5$ (c) $4\pi/5$

(d) $6\pi/5$ (e) $8\pi/5$ (f) 2π

Figure 4.3: Longitudinal phase-space distribution, $g_1(r, \phi)$, for the unperturbed distribution computed by PyTMCI for benchmark example 1. From left-to-right, top-to-bottom plots show an advancing phase as indicated by captions. Colours indicate a quantity proportional to the vertical dipole moment in arbitrary units.

4.2.2 Example 2 - A Higher-Order Radial Mode

In the last example, the distribution in Figure 4.2 resembled an azimuthal mode ±2 head-tail instability with the lowest order radial mode. It is not generally true that the azimuthal mode number will correspond to the number of nodes, because higher-order radial modes can cause additional high-amplitude regions that should appear on either side of the projection. The number of nodes is therefore given by $|l| + 2\kappa$, where κ is a positive integer [117]. In this example, an azimuthal mode zero instability will be demonstrated with two nodes in its projected distribution, indicating that a higher-order radial mode is dominant.

The accelerator parameters used for this example are listed in Table 4.2, and the impedance was defined as a single resonator defined by Equation (3.35) with $f_r = 115\,\mathrm{kHz}$, $R_\perp = 1\,\mathrm{M\Omega\,m^{-1}}$ and $Q_r = 3$.

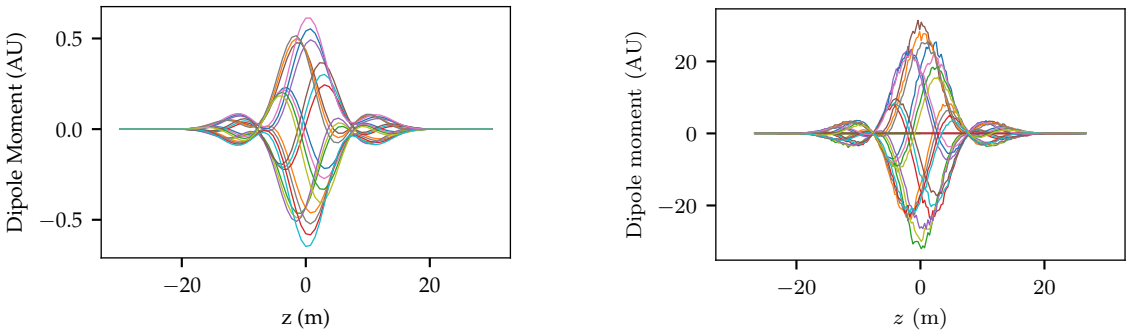
For these parameters, PyTMCI predicts a characteristic growth time of $99\,\mu\mathrm{s}$ whilst PyHEADTAIL predicts $115\,\mu\mathrm{s}$. The projection of the perturbed distributions are shown in Figure 4.4. The growth rates differ by only $\approx 15\,\%$, which is considered a good level of agreement. The longitudinal distributions are qualitatively similar, with a high-amplitude oscillation around $z \approx 0$ and two smaller oscillations around $z \approx \pm 10$. Whilst this instability resembles an azimuthal mode $l = 2$ instability, PyTMCI gives $(\Omega - \omega_\beta)/\omega_s = 0.009$ and PyHEADTAIL gives 0.011, indicating $l = 0$ is dominant. This can also be seen from Figure 4.5, which shows $g_1(r, \phi)$ computed by PyTMCI. The distribution does not evolve as a rotation, but as a wave travelling from the tail to the head as would be expected for an $l = 0$ instability.

4.2.3 Example 3 - TMCI

The last two examples demonstrated head-tail type instabilities with a single dominant azimuthal mode. In this example, the input parameters listed in Table 4.3 and resonator impedance parameters ($f_r = 5\,\mathrm{MHz}$, $R_\perp = 1\,\mathrm{M\Omega\,m^{-1}}$ and $Q_r = 3$) have been identified so

Table 4.2: Parameters used for PyTMCI benchmark example 2.

Parameter	Value	Parameter	Value
Circumference	163.3 m	Transition γ	5.034
Particle Type	proton	Betatron Tune	3.83
Relativistic β	0.37	Synchrotron Tune	0.0195
Number of Bunches	1	Chromaticity	-1.4
Particles per bunch	2×10^{13}		

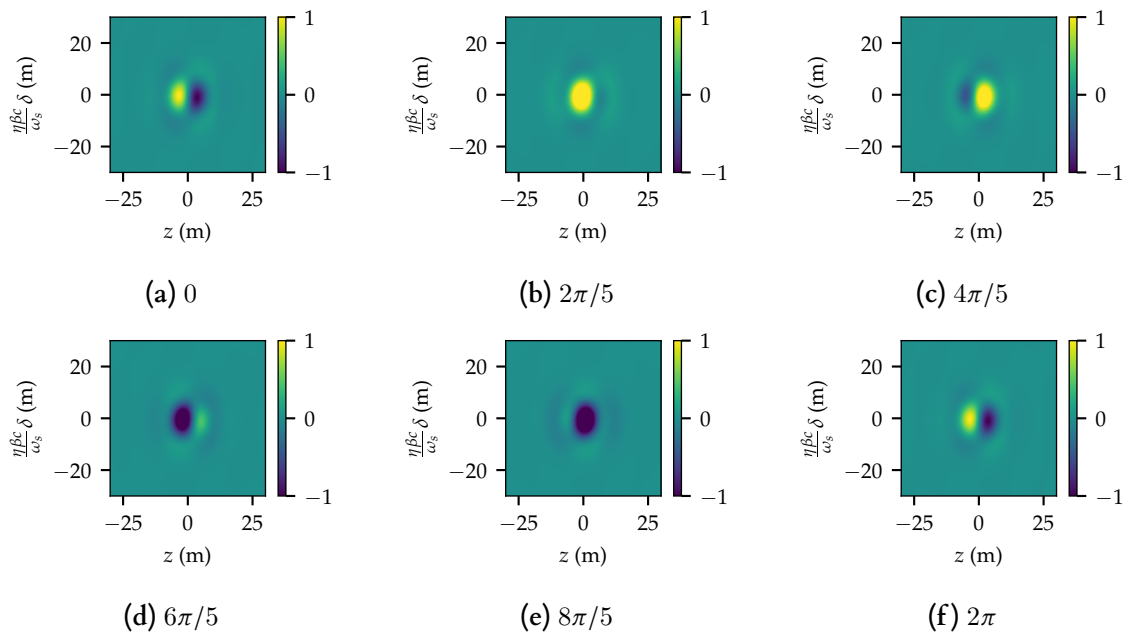


(a) (b)

Figure 4.4: Perturbed distribution $g_1(r, \phi)$ of PyTMCI benchmark example 2, projected onto the z axis for several consecutive turns. Each line is one revolution and colours help to distinguish different turns. Distributions were computed by PyTMCI (a) and PyHEADTAIL (b).

as to induce azimuthal mode coupling. Growth rates and projected distributions will be compared, but to verify that mode coupling is taking place, the mode frequencies will be found for many values of N, the number of protons per bunch. For a TMCI, two mode frequencies will be observed to become degenerate.

Mode frequencies can be found from the eigenvalues output by PyTMCI, but for PyHEADTAIL they must be identified from the spectra of the beam's dipole moment over time. It can be difficult to identify mode frequencies in this way, because the most unstable mode can dominate the spectrum and small peaks can be obscured by noise. Spectra will therefore be obtained by averaging the periodograms of several repeat PyHEADTAIL simulations, which is a common technique in the analysis of Schottky signals [183].



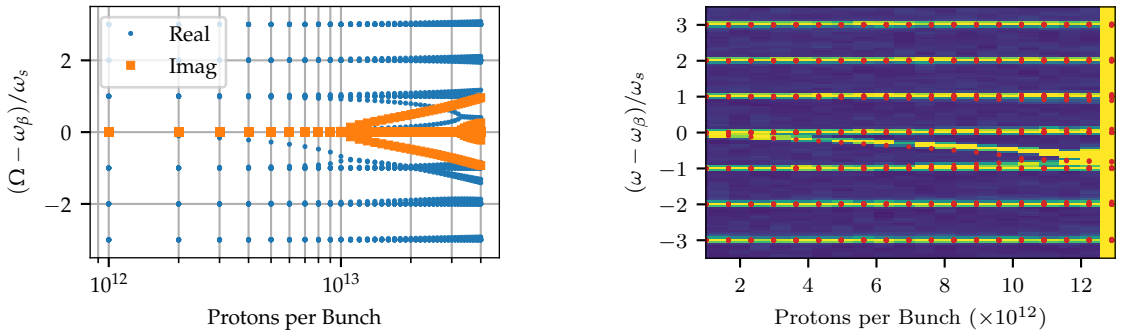
(a) 0 (b) $2\pi/5$ (c) $4\pi/5$

(d) $6\pi/5$ (e) $8\pi/5$ (f) 2π

Figure 4.5: Longitudinal phase-space distribution, $g_1(r, \phi)$, for the unperturbed distribution computed by PyTMCI for benchmark example 2. From left-to-right, top-to-bottom plots show an advancing phase as indicated by captions. Colours indicate a quantity proportional to the vertical dipole moment in arbitrary units.

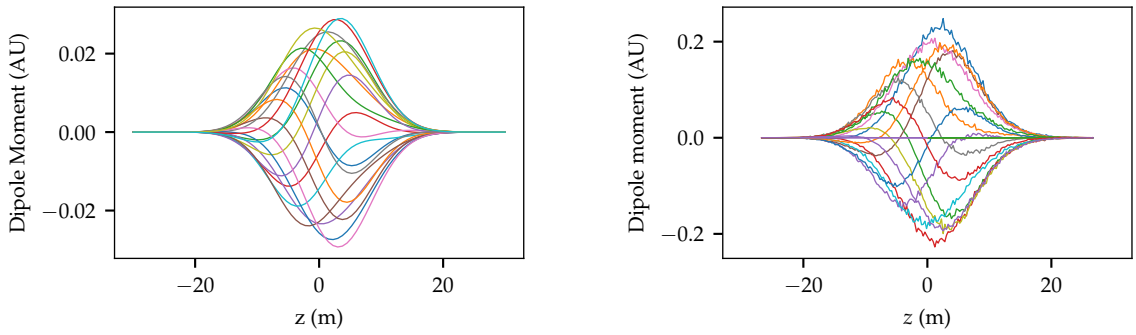
Figure 4.6 shows an amplitude spectrum of the dipole moment computed by PyHEADTAIL, with PyTMCI mode frequencies overlaid. It can be seen that the frequency associated with an azimuthal mode $l = 0$ falls towards the $l = -1$ frequency as N is increased. The two mode frequencies become degenerate between $N = 1.0$ and 1.2×10^{13}, indicating a TMCI will occur above this threshold. The growth rate increases rapidly around this value, which can be seen from the thickening of the spectral line and from the large imaginary part of Ω in the PyTMCI results. These observations confirm that the instability is a TMCI.

To compare growth rates and distributions, a value of N above the TMCI threshold was chosen and is listed with other parameters in Table 4.3. For these, PyTMCI predicts a growth time of $64.1\,\mu s$ whilst PyHEADTAIL predicts $62.2\,\mu s$. These differ by $\approx 3\,\%$, which is considered to be excellent agreement. The distributions shown in Figure 4.7 also appear qualitatively similar, having a single large-amplitude region close to $z = 0$.



(a) (b)

Figure 4.6: Normalised instability mode frequencies computed by PyTMCI (a) and PyHEADTAIL (b). In (b) the red dots are overlaid mode frequencies computed by PyTMCI and the other colours indicate spectral amplitude. Both PyTMCI and PyHEADTAIl predict that mode $l = 0$ and -1 become degenerate around $N = 1 \times 10^{13}$ protons. In (a) it can be seen that the growth rate increases rapidly for higher values.



(a) (b)

Figure 4.7: Perturbed distribution $g_1(r, \phi)$ of PyTMCI benchmark example 3, projected onto the z axis for several consecutive turns. Each line is one revolution and colours help to distinguish different turns. Distributions were computed by PyTMCI (a) and PyHEADTAIL (b).

Table 4.3: Parameters used for PyTMCI benchmark example 3.

Parameter	Value	Parameter	Value
Circumference	163.3 m	Transition γ	5.034
Particle Type	proton	Betatron Tune	3.83
Relativistic β	0.65	Synchrotron Tune	0.0081
Number of Bunches	1	Chromaticity	0.0
Particles per bunch	1.3×10^{13}		

4.2.4 Discussion

PyTMCI has been benchmarked against the PyHEADTAIL particle tracking code for three sets of example inputs, demonstrating both head-tail instabilities and a TMCI. In all cases, growth rates were consistent within $15\,\%$, which is well within the order-of-magnitude agreement that was sought. In all cases, the projected distributions were also qualitatively similar. In the last example, mode frequencies were compared for many values of N, and the same shifting of mode frequencies was observed from both codes.

It is therefore concluded, for the purpose of this thesis, that PyTMCI produces accurate numerical outputs that can be trusted to within an order of magnitude. It is understood that its predictions are made within the limits of a simplified analytical framework that neglects potentially important factors, such as direct space-charge; the justification for these simplifications were given in the introduction of this chapter.

PyTMCI will now be used extensively in Chapter 6, where instabilities observed at the ISIS proton synchrotron will be investigated.

There, in the middle of the broad, bright high-road - there, as if it had that moment sprung out of the earth or dropped from the heaven - stood the figure of a solitary woman, dressed from head to foot in white…

— W. Collins, "The Woman in White"

5 Vertical Driving Impedance Model of the ISIS Synchrotron

5.1 Introduction

Chapter 3 introduced the concept of beam coupling impedances. The transverse wake associated with a source particle having an offset defined the driving impedance, and the wake associated with an offset witness particle defined the detuning impedance. The longitudinal impedance was defined from the longitudinal wake associated with on-axis source and witness particles. A full dynamical description of a beam's behaviour, made within the constraints of the model's assumptions, would at least require all of these impedances to be known. However, the starting point for this thesis is that there have been no detailed, systematic studies of ISIS beam impedances. It is beyond the scope of this work to produce a full description of all impedances, so priorities will first be identified. After estimating the impedance contributions of key equipment, the model will be finalised by considering the effects of Lorentz β and Twiss β_y.

5.2 Identification of Key Equipment

The observation of a coherent vertical instability with a fast growth rate implies the presence of a large, unknown vertical driving impedance. Whilst the detuning impedance cannot be neglected in general, it acts incoherently and so in most operational scenarios it won't cause a coherent instability on its own. Since the observed vertical instability causes significant beam-loss and limits operational intensity, an impedance model which includes the driving impedance associated with this instability, and identifies its source, is one of the primary goals of this thesis. Therefore, only vertical driving impedances which could plausibly be responsible for this instability will be investigated. The observation that instability growth rates peak close to an integer tune for both bunched and coasting beams further restricts the impedances of interest to those of the low-frequency narrowband type [80].

The overall vertical driving impedance model will therefore consist of a broadband wall impedance and several resonators. These will be contributed by key pieces of equipment, as indicated in Figure 5.1. Key contributors to the wall impedance will include the magnet RF screens, which occupy around $55\,\%$ of the circumference, and the RF cavities, which occupy around $15\,\%$. Other elements occupy much smaller fractions of the circumference, and so their wall impedance contributions will not be considered directly. This includes the graphite collectors, because they occupy $\lessapprox 2\,\%$ of the machine circumference and aren't expected to resonate at low frequencies. ISIS contains two types of vertical kicker magnet: the extraction kickers and the Q-kicker. The Q-kickers are used for tune measurements, and have matched terminations on both ends of the kicker circuit and so will not be considered here. The three extraction kickers are longer than the Q-kickers and are shorted on one side, so these will be investigated. Resonances on the RF screens, which are capacitively coupled at one end, will also be considered.

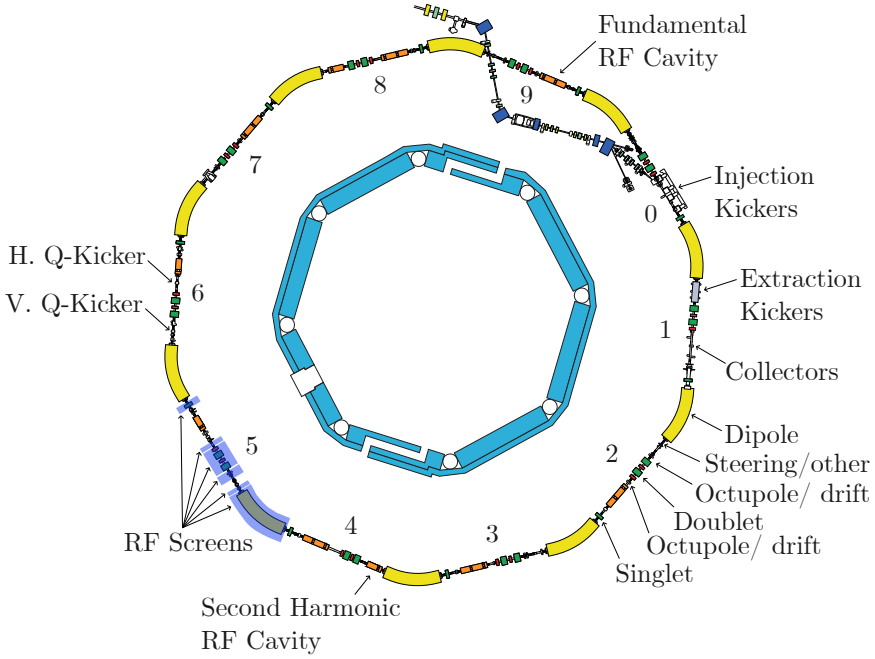


Figure 5.1: ISIS Synchrotron layout [67] with key elements labelled. RF-screen locations are indicated for one superperiod, and superperiod numbers are shown.

5.3 RF Screens and Laminated Magnets

The vacuum vessels inside all AC magnets at ISIS are constructed from alumina ceramic with specially designed conducting RF screens. These assemblies were designed to mitigate the eddy current effects that would occur if a standard stainless-steel vessel were used. In total, they account for more than 50% of the ISIS circumference, which can be seen in Figure 5.1. The RF screens are constructed from a series of 2.3 mm diameter, stainless-steel wires and side-plates in the case of dipole magnets. Whilst their exact construction varies between magnets, some typical cross-sectional geometries are shown in Figure 5.2. Along the magnet's length, the wires sit inside macor ceramic spacers which are typically spaced by some 10's of cm.

The wires and side-plates which make up the RF screens prevent the beam's electromagnetic field from extending to the magnet pole faces, or ideally the alumina ceramic; equivalently they help to shield the beam from the undesirable RF properties of the

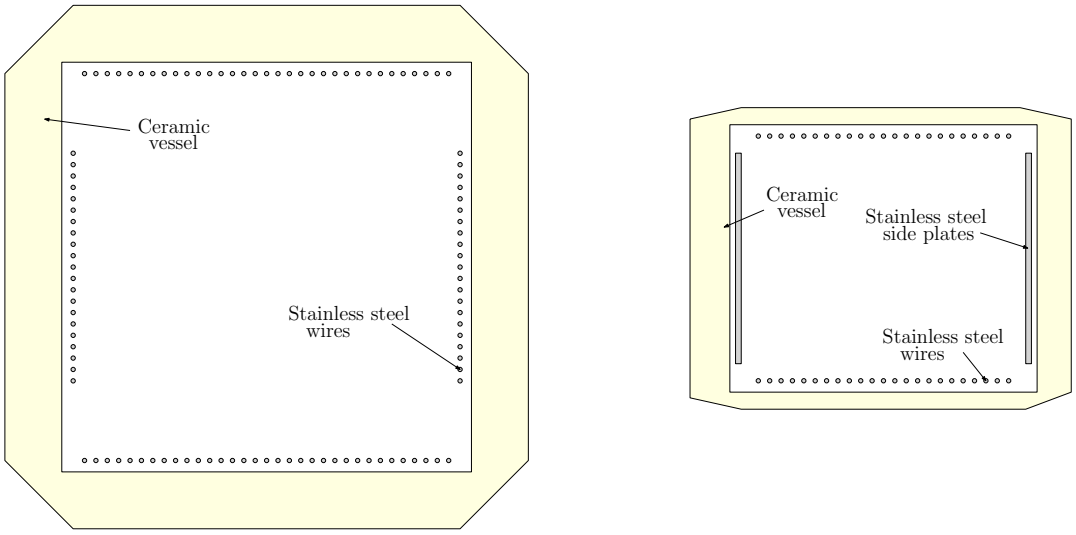


Figure 5.2: Schematic cross-section of a typical RF screen for (a) quadrupoles, steering and higher order magnets (b) dipoles. For illustration purposes only.

vacuum vessel and surrounding equipment [184]. Currents and charges induced by the beams electromagnetic field should ideally be contained in the screens, so that the total current enclosed by a loop surrounding the conductor's cross-section is ideally zero.

Significant power would also be deposited in these wire assemblies if Eddy currents were able to flow unimpeded. This is prevented by capacitors which isolate each wire or side plate. The overall layout of these capacitor connections are indicated in Figure 5.3. With typical capacitances of $0.1\,\mu\text{F}$, an Eddy current loop would see impedance magnitudes of $\sim 64\,\text{k}\Omega$, whilst a $100\,\text{kHz}$ beam-induced current sees only $\sim 16\,\Omega$ per wire. For many years, the capacitors have been considered to be short circuits and neglected from investigations of the coupling impedance of wire cages [135, 185].

The physical mechanism used to achieve these capacitive connections is shown in Figure 5.4, and Figure 5.5 shows a photograph of the aperture of a singlet quadrupole's vacuum vessel and its RF screen. The wires which compose the screens are bent by $90°$ at one end and held in position by a series of macor ceramic spacers. Connections to the wires are made via a pair of RF finger strips, which are secured to opposite sides of

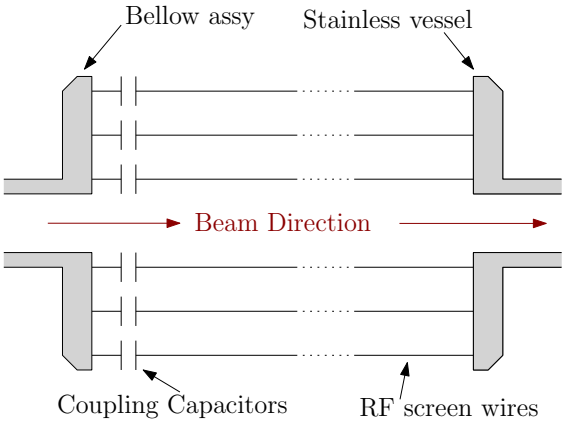


Figure 5.3: Schematic of an RF screen assembly, with capacitors indicated.

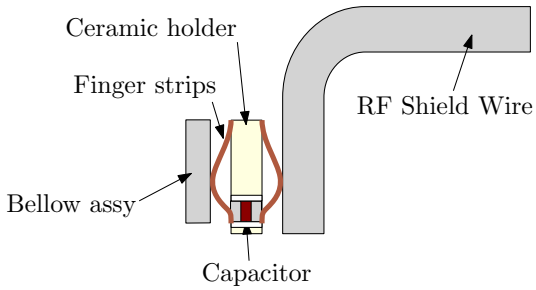


Figure 5.4: Schematic showing the mechanical layout for the capacitor connections.

a ceramic holder. On one side of the ceramic holder, the finger strips are isolated from one another, and each one is compressed against a single upturned wire. On the other side of the ceramic holder, all finger strips are shorted together and compressed against the conducting vacuum vessel. Coupling capacitors sit in slots within the ceramic holder and connect the two compressed finger strips. A photograph of a ceramic holder and several capacitors is shown in Figure 5.6.

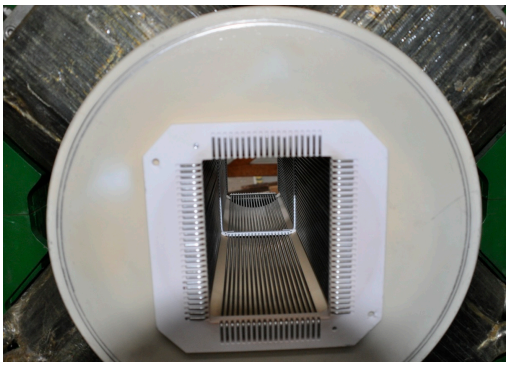


Figure 5.5: Photo of a singlet RF screen.

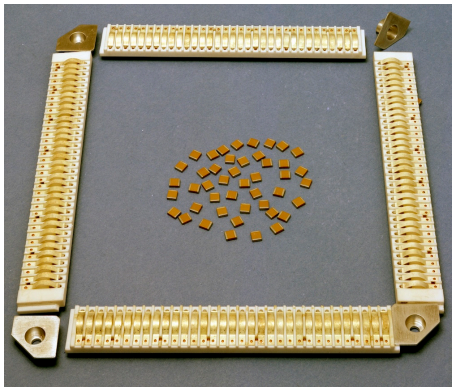


Figure 5.6: Photo of ceramic capacitor holder [186].

The RF screens sit within alumina ceramic vacuum vessels, which form part of the ISIS vacuum system [187, 188]. These are manufactured in lengths of $\sim 0.3\,\mathrm{m}$, and connected by glass joints which are fused in an oven [77]. Each ceramic vacuum vessel

is inserted into the aperture of its magnet, and the RF screen then inserted into the ceramic chamber. Figure 5.7 shows an RF screen being inserted into the vacuum vessel of a doublet quadrupole. These vessels sit inside the laminated steel magnet yokes, which are considered sufficiently thick to form the final electromagnetic boundaries.

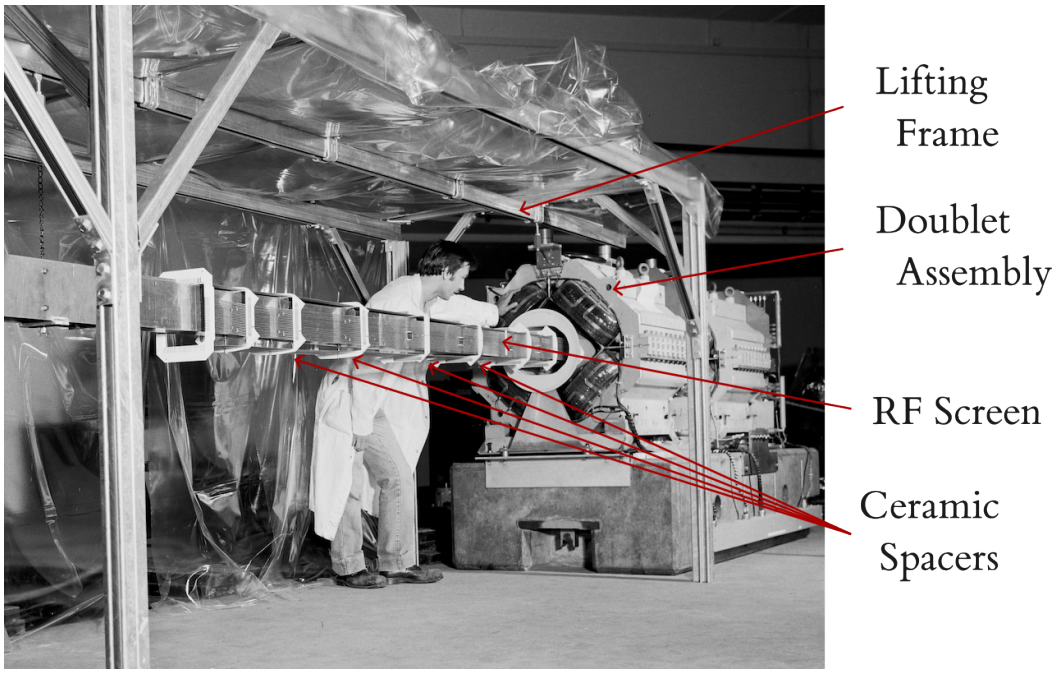


Figure 5.7: Photograph of an RF screen being inserted into the alumina ceramic vacuum vessel of a quadrupole doublet [186] with added labels. The wires are held inside the ceramic spacers which appear white. The screen is suspended from a specially designed lifting frame.

An engineering schematic of all ten ISIS superperiods is shown in Figure 5.8, where space occupied by RF screens has been highlighted with green lines; the red lines indicate the capacitive connections and the pink lines indicate capacitive connections that have been assumed from drawings where equipment changes have been made. The numbers in this figure refer to "Module numbers", with the dipoles being Module 1 at the beginning and end of each SP, the doublets being Modules 11 and 61 and the singlets being Module 30. Modules 9/ 10 and 13 are up or downstream of the doublet in most SPs and contain corrector or higher order magnets. Several other pieces of equipment are described in Chapter 2.

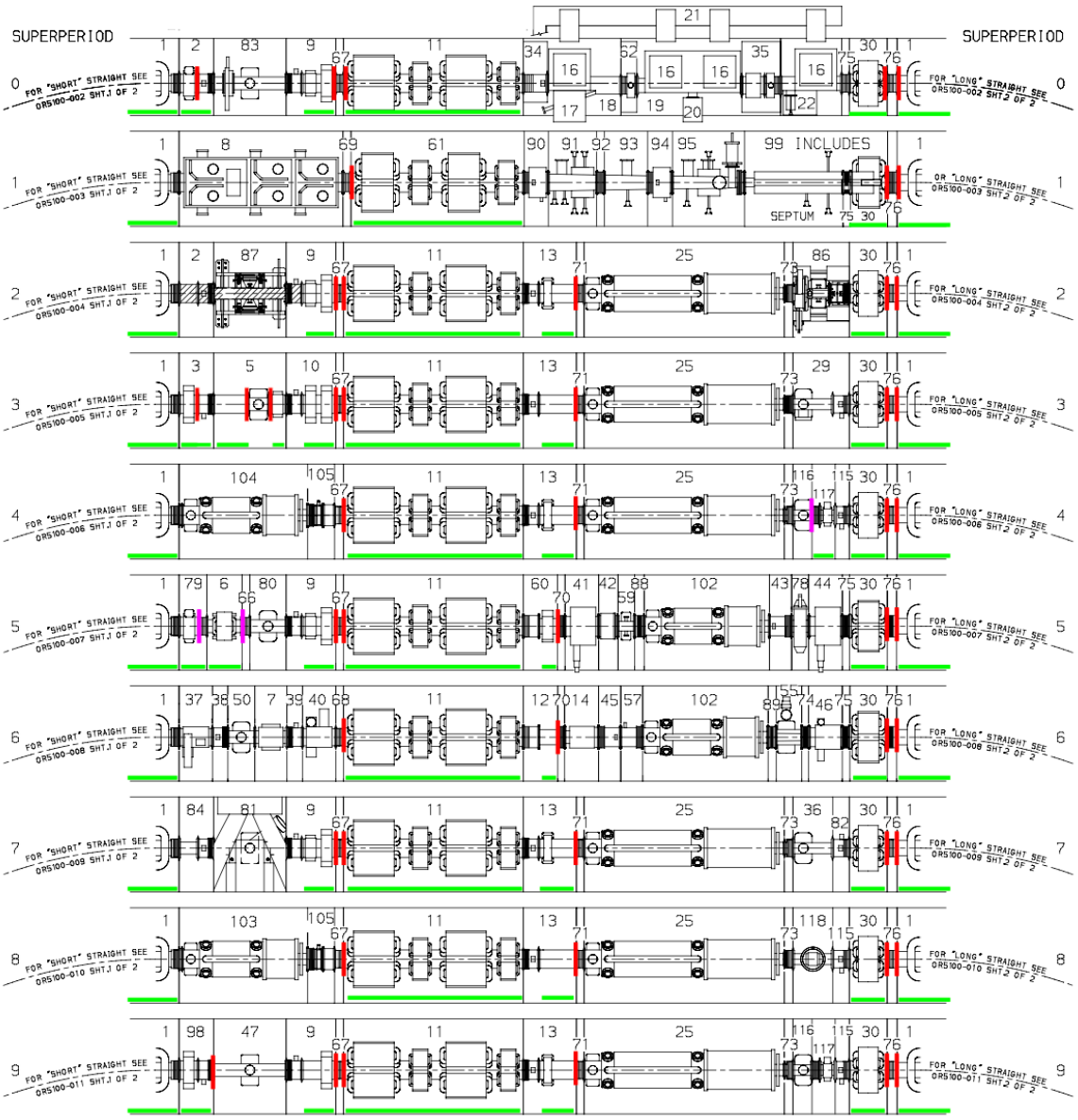


Figure 5.8: Engineering drawing of the ISIS superperiods [189] with added highlighting. Green lines show areas with space for magnets and have alumina vacuum vessels. Red lines show areas with capacitive RF connections and pink lines show where capacitive RF connections are expected.

5.3.1 Material Properties

5.3.1.1 RF Screen Wire Conductivity

Equation (3.31) gives the transverse impedance of a thick cylindrical conducting pipe. It indicates that in addition to the RF screen geometry, at least the electrical conductivity and magnetic permeability of the RF screen wires are required to estimate $Z_1^{\perp}$. Wires which make up the RF screens are constructed from 310-stainless-steel, which is generally recommended for applications demanding low permeabilities. For this reason, the magnetic permeability will be assumed to be 1.

The conductivity of an RF screen wire has been measured because of the wide variation of published values. With a wire diameter of $2.3\,\mathrm{mm}$, the DC resistance of a $30\,\mathrm{cm}$ sample was less than $0.1\,\Omega$ as measured by a standard lab multimeter. Since samples with different cross-sectional dimensions were not available, it was decided that standard DC methods of measuring conductivity would not be adequate. Instead, the Eddy current method outlined in Appendix F was adopted. This involved measuring the impedance of a probe coil wrapped around an RF screen wire.

Two probe coils were constructed with properties listed in Tables 5.1 and 5.2; two coils were used to highlight systematic errors associated with the coil geometry. A photograph of an example probe coil is shown in Figure 5.9. The frequency range of between 50 and $250\,\mathrm{kHz}$ was chosen, because with typical conductivities [190] and the parameters listed in Table 5.2, the resistance in this range is predicted to increase monotonically with conductivity so that unique solutions are expected for a given resistance. This is clear in Figures 5.10 and 5.11, which shows a $400\,\mathrm{kHz}$ drive frequency having two solutions in the conductivity range between 1×10^5 and $3 \times 10^6\,\mathrm{S\,m^{-1}}$.

The measurement is performed in two stages: the first stage measures the coil's resistance in free space without a sample wire; the second measures the probe coil's resistance with the sample wire along its axis. Both measurements were performed using an LCR meter. The coil's resistance is unchanged in the second experiment, but

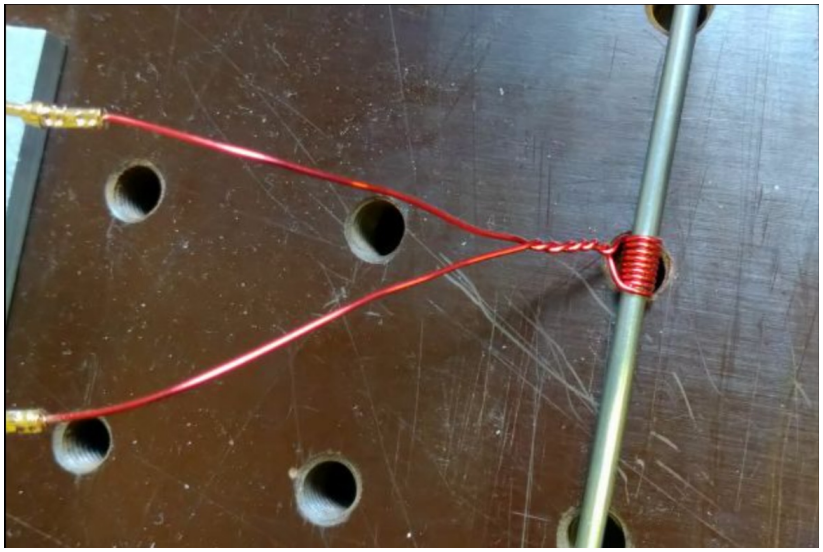


Figure 5.9: Photograph of a probe coil wrapped around a conducting wire.

Table 5.1: Properties of first coil.

Parameter	Value
b	(1.666 ± 0.001) mm
r_1	(1.210 ± 0.010) mm
r_2	(1.710 ± 0.010) mm
l	(5.450 ± 0.270) mm
No. Turns	9

Table 5.2: Properties of second coil.

Parameter	Value
b	(1.167 ± 0.001) mm
r_1	(1.190 ± 0.010) mm
r_2	(1.500 ± 0.010) mm
l	(2.810 ± 0.180) mm
No. Turns	7

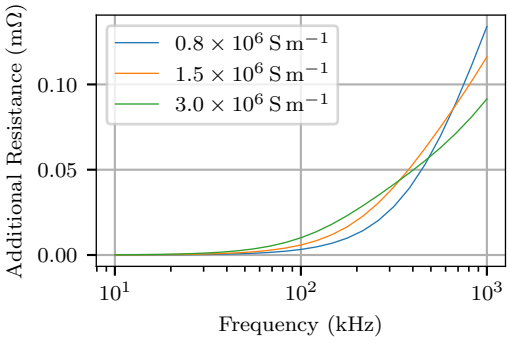


Figure 5.10: Real part of coil impedance versus frequency as predicted by Equation (F.10), for three different sample conductivities and the coil parameters in Table 5.2.

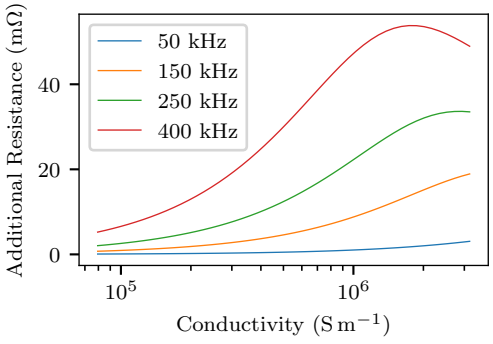


Figure 5.11: Real part of coil impedance versus conductivity as predicted by Equation (F.10), for four different excitation frequencies and the coil parameters in Table 5.2.

additional resistive losses from Eddy currents in the sample wire appear in series with it. Conductivity can be measured by finding the value for which Equation (F.10) predicts the observed difference in probe coil impedance. Whilst the equation is for a complex impedance, its real part provides a unique solution provided the conductivity can be assumed to be within a range. Since this simplifies the numerical integration and a suitable range can be specified, only the real part has been used.

To measure the sample conductivity and its uncertainty, a random normal distribution was generated for the values listed in Tables 5.1 and 5.2 and the measured resistance. To compute the conductivity, samples were drawn from these distributions and used as inputs to the calculation in Equation (F.10), and the Ridder root-finding algorithm used to find the conductivity [191]. To compute the uncertainty, the procedure was repeated twenty times per sample frequency and a standard deviation computed.

Figure 5.12 shows the conductivity measured as a function of frequency for both probe coils. Since no frequency dependence is apparent in these results, a weighted mean was computed for coils 1 and 2 giving $(1.31\pm0.02)\times10^6\,\mathrm{S\,m^{-1}}$ and $(1.34\pm0.01)\times10^6\,\mathrm{S\,m^{-1}}$ respectively. The weighted mean of these two conductivities is $(1.33\pm0.01)\times10^6\,\mathrm{S\,m^{-1}}$, which is taken as the RF screen wire's conductivity.

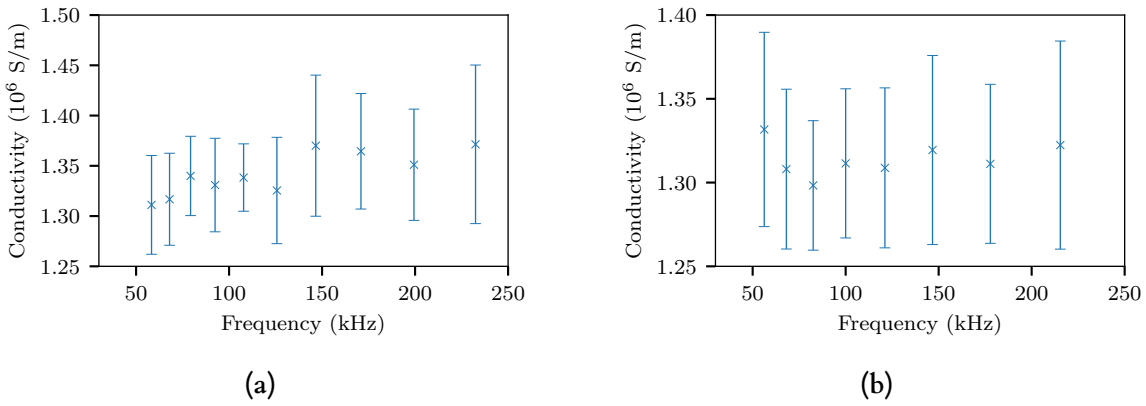


Figure 5.12: Conductivity output from Ridder root finding algorithm for first probe coil (a) and second probe coil (b). Uncertainties are the standard deviation of 20 calculations.

5.3.1.2 Alumina Vacuum Vessels

The ceramic vacuum vessels at ISIS are composed of 97.6 % purity alumina [77]. Their dielectric properties are not well known, however no suitable samples are available to perform a characterisation, so typical dielectric properties have been taken from literature. Figure 5.13 shows a reconstructed plot of dielectric loss tangent versus frequency for a *Morgan Matroc MM975* 97.5 % purity Alumina [192]. Since the frequency range of interest for ISIS is between around 100 kHz and some tens of MHz, the loss tangent will be taken to be the largest value in this range; a constant of 3×10^{-3}. The permittivity of *MM975* is reported as 9.22 at 15 GHz [192], so a typical value of 10 will be taken over the full frequency range.

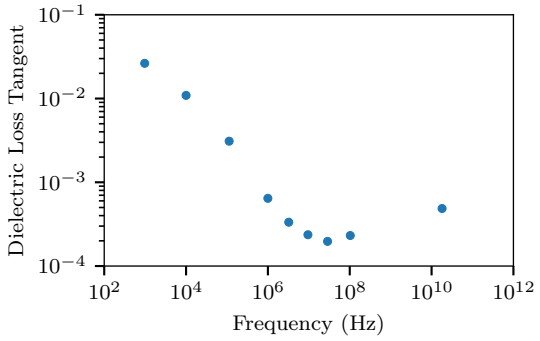


Figure 5.13: Reconstructed plot of dielectric loss tangent versus frequency, for *MM975* alumina ceramic [192].

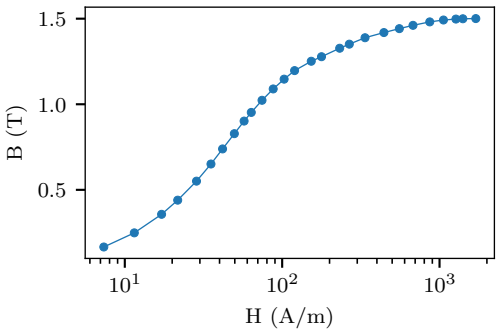


Figure 5.14: Approximate anhysteretic BH curve for the ISIS steel laminations [193].

5.3.1.3 Magnet Laminations

Main magnet yokes are all constructed from laminations of British Steel *TRANSIL 315-35*, which is a silicon transformer steel that is no longer manufactured. The laminations are glued together and straps are welded down the sides [73]. Each lamination is 0.35 mm thick, and the magnets have packing factors exceeding 92%. Whilst the anhysteretic BH curve of this steel is available, see Figure 5.14, and the DC permeability

at $\sim 0.8\,\mathrm{T}$ is known to be around 7000, these results will not be valid in the frequency range of $\geq 50\,\mathrm{kHz}$.

With no suitable sample available for characterisation, typical values of high-frequency permeability have been taken from literature [194]. The steel tested in this report, *DI MAX M-22*, are expected to be somewhat similar to those of *TRANSIL 315*. In the frequency range between $10\,\mathrm{MHz}$ and $1\,\mathrm{GHz}$, the real part of the magnetic permeability varies between around 35 and 1, whilst the imaginary part varies between around -10 and 0. Given this very large percentage variation, where necessary a range of values will be investigated and otherwise $\mu = 35 + 0j$ will be used.

5.3.2 Simplifications to RF Screen and Magnet Model

Impedance calculations will be performed using the low-frequency finite-element technique described in Chapter 3. Generating an accurate mesh of a realistic RF screen and magnet assembly would be computationally challenging; for example, the dipole RF screens are more than $4\,\mathrm{m}$ long, whilst the laminations are $0.35\,\mathrm{mm}$ thick, $0.84\,\mathrm{m}$ tall and $1.075\,\mathrm{m}$ wide. To obtain a prediction of the structure's impedance, it is necessary to simplify the geometry by removing features which do not contribute significantly in the frequency range of interest. The primary impedance sources will be identified with RWAL, CST simulations and dedicated analytical models.

Whilst each magnet family has its own RF screen geometry, the general structure consists of five layers, as indicated by Figure 5.15:

1. Beam aperture
2. RF Screen wires
3. Small vacuum gap
4. Alumina ceramic chamber
5. Small air gap
6. Laminated magnet yoke

As found in Chapter 3, the impedance of a multi-layered conducting vacuum vessel can be understood in terms of the impedance of each individual layer in certain frequency ranges. Since the resistivity of Alumina is close to $1 \times 10^{14}\,\Omega\,\mathrm{cm}$, the ceramic layer is not expected to provide effective electromagnetic shielding of outer layers, and so does not conform to this intuitive picture for conductors. The new code RWAL, introduced in Chapter 3, was first used to investigate the Alumina vessel's contribution to $Z_1^{\perp}$.

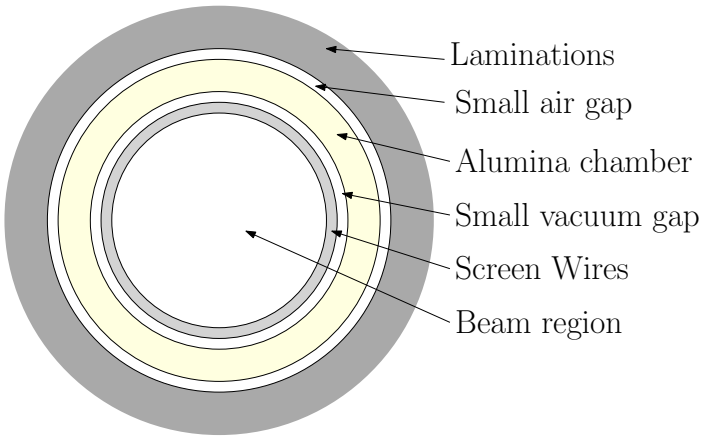


Figure 5.15: Layers of an ISIS RF screen, vacuum vessel and magnet laminations. Circular cross-section is not of a physical magnet, but will resemble the model computed by RWAL.

5.3.2.1 Alumina Vacuum Vessels

The dimensions shown in Figure 5.16 have been used as inputs to RWAL. Initially no inner stainless-steel (SS) layer was included, leaving the alumina layer directly exposed to the beam to assess its impact on $Z_1^{\perp}$. The outermost layer was assumed to be a solid steel conductor with properties set to those of the yoke laminations; although the exact properties of this outermost layer are not considered very significant in this section. All air gaps have been neglected from the layer stack because they are not considered to be significant for this analysis. Impedances will be calculated for $\beta = 0.999$ and $\beta = 0.45$, to better understand the impact of β at ISIS.

RWAL calculations of $Z_1^{\perp}$ are shown in Figure 5.17, both with and without the alumina layer. For $\beta = 0.999$, $Z_1^{\perp}$ shows the same four peaks in its real part around 1 GHz,

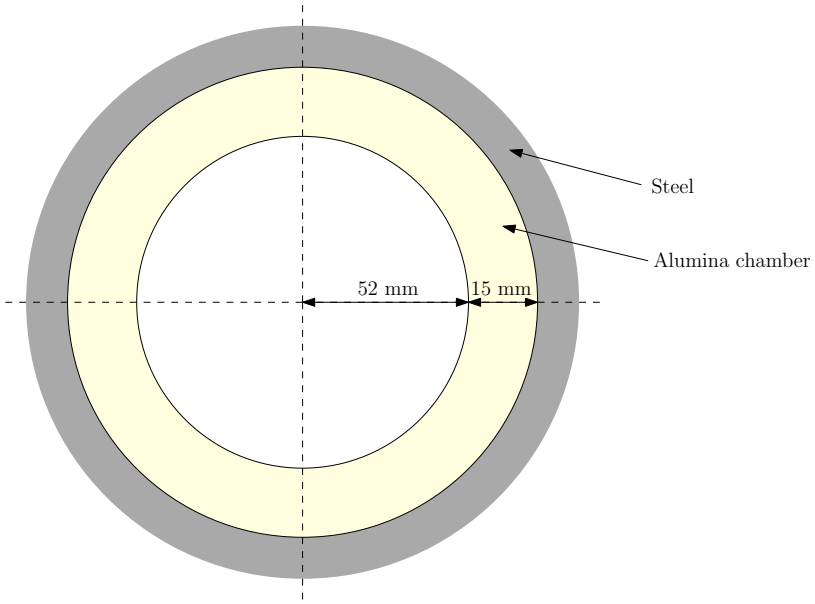


Figure 5.16: Geometry of the RWAL model used to understand the impact of the ceramic properties on $Z_1^\perp$. Relevant dimensions are indicated.

which are also seen in Figure A.1, which was computed for $\beta = 1$. These peaks are not present in the $\beta = 0.45$ case, where a waveguide cut-off effect appears to significantly reduce the impedance above around $500\,\mathrm{MHz}$. The imaginary part is larger than the steel-only case for both high and low beta. For $\beta = 0.45$ the case with Alumina is around twice that of the steel-only case, and nearly seven times larger for $\beta = 0.999$ at $100\,\mathrm{kHz}$. This increased imaginary impedance was one of the primary motivations for installing conducting wires inside the ceramic chamber during its design [184].

Figure 5.18 compares $Z_1^\perp$ for the case that a conducting layer is inserted between the beam and the ceramic layer. This is assumed to have a similar impact on $Z_1^\perp$ as the conducting RF screen wires, and so has been made $2\,\mathrm{mm}$ thick. Over the tested frequency range, the electromagnetic properties of the ceramic have no visible impact on $Z_1^\perp$for both $\beta = 0.45$ and $\beta = 0.999$. This indicates that the alumina layer will not have a significant impact on $Z_1^\perp$ of the RF screen structure. Models of the RF screens will therefore be simplified by replacing the alumina layers with free space.

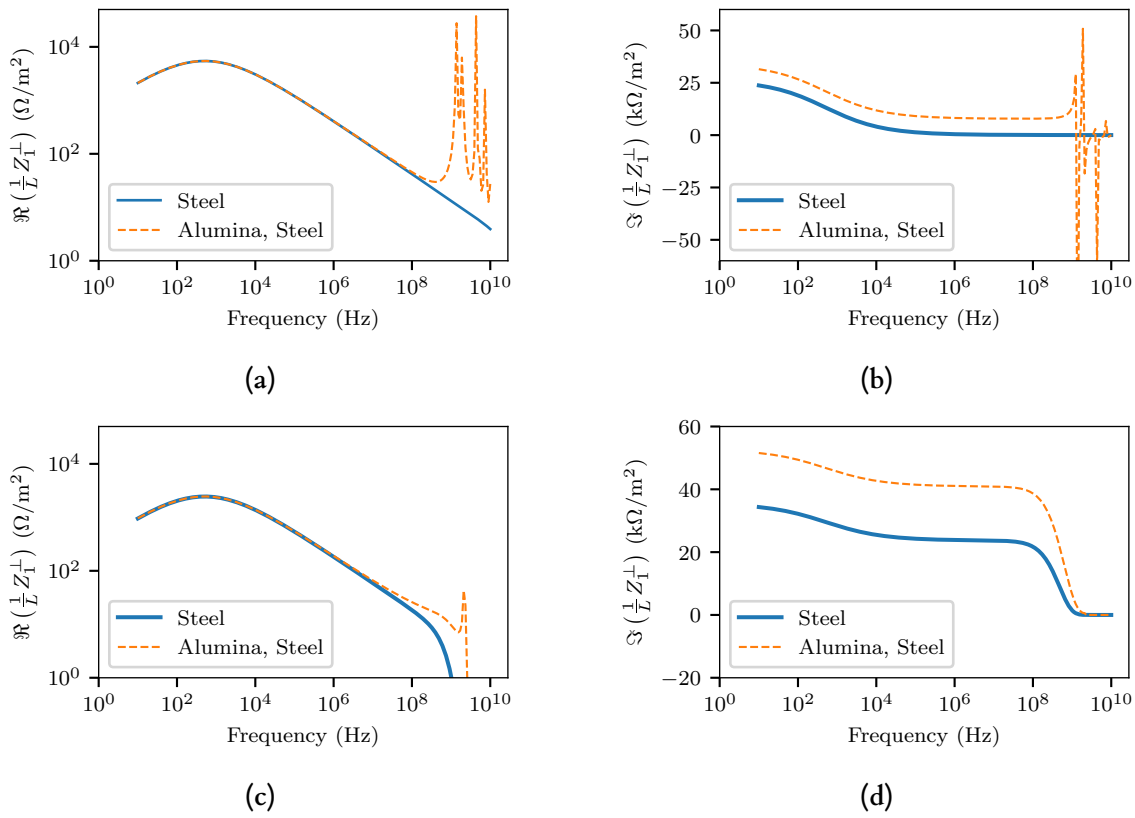


Figure 5.17: $Z_1^\perp$ per unit length computed by RWAL for a 1.5 cm thick Alumina layer surrounded by steel extending to infinity, with (a, b) $\beta \approx 1$ and (c, d) $\beta = 0.45$.

5.3.2.2 Laminated Magnet Yokes

In calculating $Z_1^\perp$ with and without the alumina vessels, the outermost layer was generally taken to be steel, although the exact properties of the steel were not considered significant. Since the Alumina layer will now be neglected, the overall structure consists of a conducting layer to represent the innermost RF screen, a vacuum gap and then the laminations extending to infinity. The lamination properties could be significant at low frequencies, where a large skin depth would allow electromagnetic fields to penetrate through the RF screen wires. The impact of these laminated structures on $Z_1^\perp$ will now be investigated.

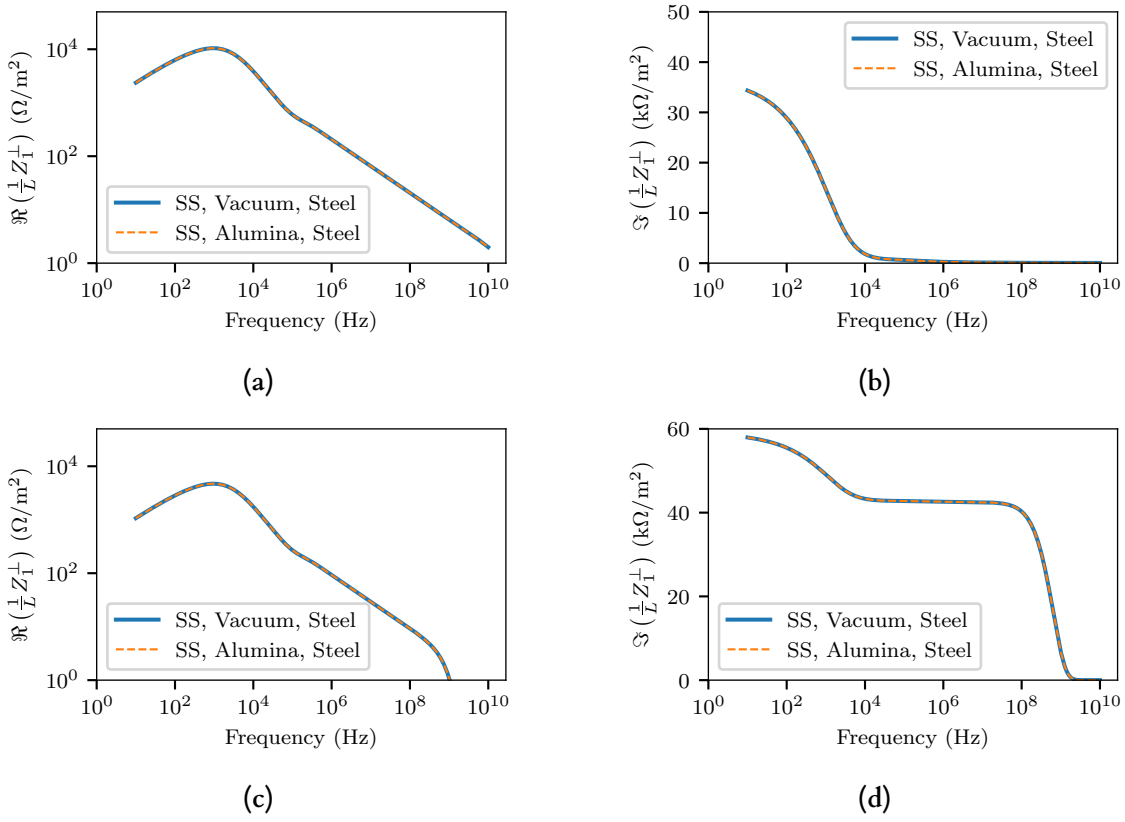


Figure 5.18: $Z_1^\perp$ per unit length for the Alumina and steel layers of Figure 5.17, but now with a 2 mm inner layer of stainless-steel, with (a, b) $\beta \approx 1$ and (c, d) $\beta = 0.45$.

Since RWAL assumes constant material properties in the longitudinal direction, it is not possible to include the lamination geometry. Instead, the impedance contribution of the laminations will be understood using a dedicated theoretical model which does not include a conducting RF screen. Nevertheless, insights gained from this model will be used to identify simplifications to the overall RF screen model.

The transverse impedance of laminated structures has been derived in the ultra-relativistic approximation ($k = \frac{\omega}{c}$), for both flat-pole and annular laminations [107, 106]. Annular laminations are considered, because it was found that the transverse impedance of a flat-pole is reasonably well approximated by annular laminations with a suitable Yokoya factor. A cross-section of the model's geometry is shown in Figure 5.19. In this

case, $Z_1^{\perp}$ is expressed in terms of average surface impedances

$$\bar{\mathcal{R}}_{z1} = \frac{h\mathcal{R}_{z1}^{\text{lam}} + \tau\mathcal{R}_{z1}^{\text{crack}}}{h+\tau}, \tag{5.1}$$

$$\bar{\mathcal{R}}_{\theta 1} \approx \frac{1+j}{\delta^{\text{lam}}\sigma^{\text{lam}}}, \tag{5.2}$$

where $\mathcal{R}_{z1}^{\text{lam}}$ and $\mathcal{R}_{z1}^{\text{crack}}$ are the $\hat{z}$-directed surface impedances of the lamination and insulating crack respectively. These are given by

$$\mathcal{R}_{z1}^{\text{lam}} = \frac{1+j}{\delta^{\text{lam}}\sigma^{\text{lam}}}, \tag{5.3}$$

$$\mathcal{R}_{z1}^{\text{crack}} = -jZ_0\frac{qc\varepsilon_0}{\omega\varepsilon^{\text{crack}}}\frac{J_1(qb)\,Y_1(qd) - Y_1(qb)\,J_1(qd)}{J\prime_1(qb)\,Y_1(qd) - Y\prime_1(qb)\,J_1(qd)}, \tag{5.4}$$

$$q^2 = \omega^2\varepsilon^{\text{crack}}\mu_0\left(1 + (1-j)\frac{\mu^{\text{lam}}}{\mu_0}\frac{\delta^{\text{lam}}}{h}\right) \tag{5.5}$$

and the complex conjugate of the transverse impedance is

$$\left(Z_1^{\perp}(\omega)\right)^* = \frac{\frac{c\bar{\mathcal{R}}_{z1}}{\omega\pi b^3}}{1 + j\frac{\bar{\mathcal{R}}_{z1}}{Z_0}\left(\frac{kb}{2} - \frac{1}{bk}\right) + \frac{\bar{\mathcal{R}}_{z1}\bar{\mathcal{R}}_{\theta 1}}{Z_0^2}}, \tag{5.6}$$

where $Z_0 = \mu_0 c$ is the impedance of free space.

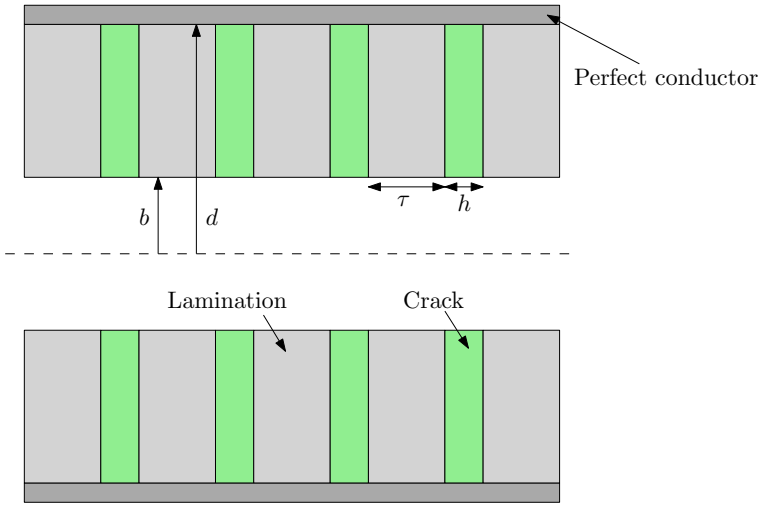


Figure 5.19: Cross-sectional geometry for the annular lamination model. Conducting laminations, dielectric cracks and an outer perfect conductor are indicated.

Whilst this has been rigorously derived, it is an approximation to represent the magnet laminations with a single surface impedance. Extensive numerical or experimental benchmarking is required if it is to be used in a practical scenario. Experimental benchmarking is often challenging due to uncertain material properties, whilst meshing a numerical model can be challenging because typically τ and h are much smaller than the transverse dimensions and overall length. Numerical benchmarks will therefore be performed for dimensions that are readily solvable. Since the only restriction on τ and h in Equations (5.1) and (5.2) is that their sum is small compared to the propagating field's wavelength, successful benchmarks in this solvable regime implies the approach is also valid for practical lamination dimensions.

Numerical benchmarking has been performed by computing the real part of $Z_1^\perp$ with the low-frequency CST technique described in Chapter 3, and comparing with the predictions of Equation (5.6). Key parameters, including: b, d, τ, h, μ^{lam}, have been varied. An example of the model geometry is shown in Figure 5.20.

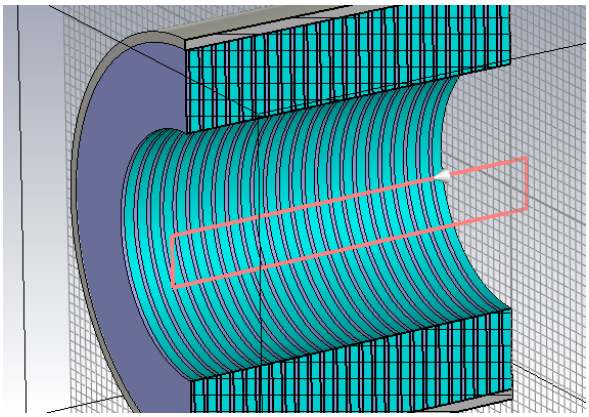


Figure 5.20: An example laminated magnet CST model. Blue laminations are highly permeable and have a conductivity of $1 \times 10^6\,\mathrm{S\,m^{-1}}$; purple laminations or cracks, are free space. The grey material surrounding the laminations is a perfect conductor.

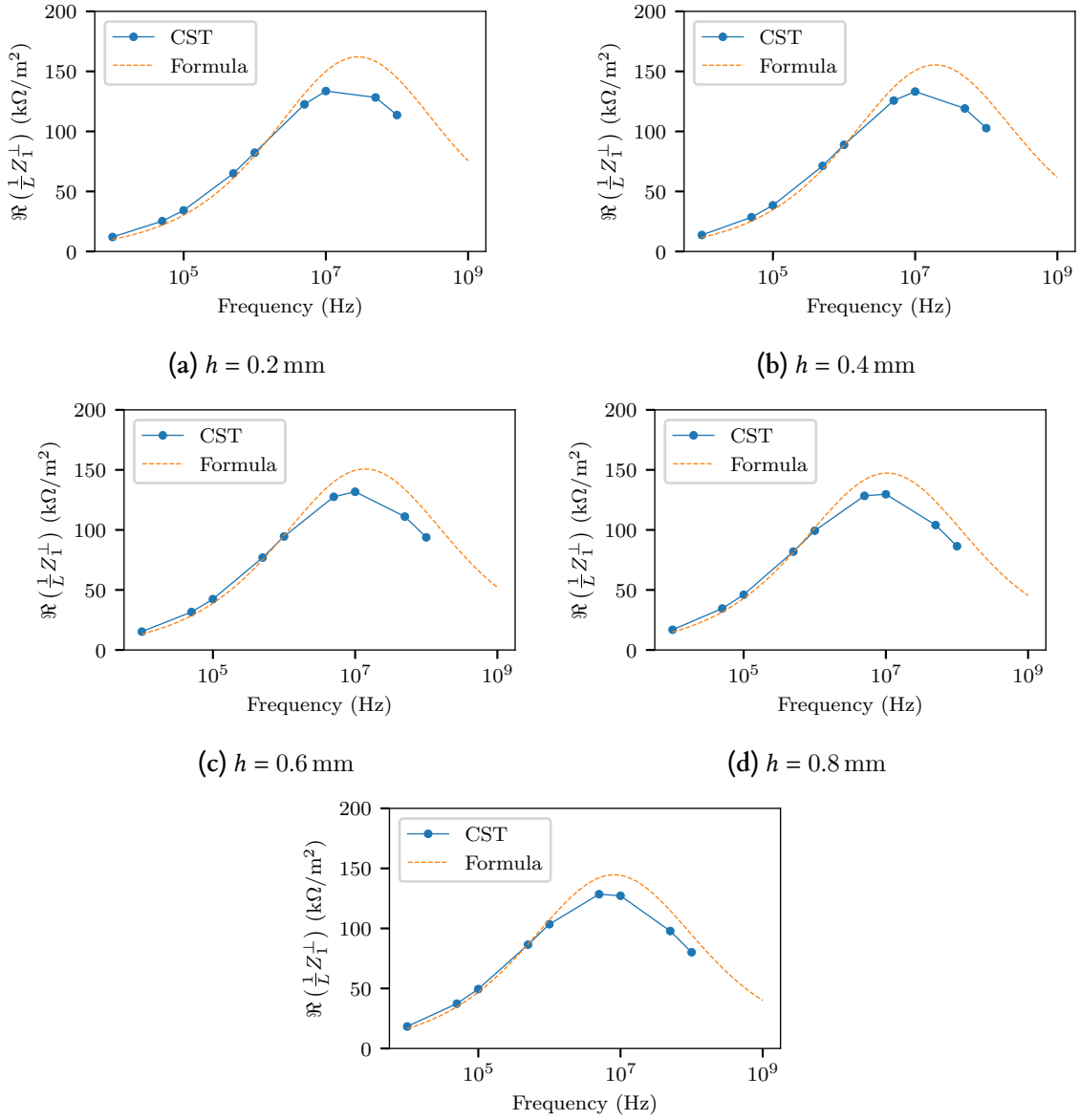
Figure 5.21 shows the variation of $\mathrm{Re}\,(Z_1^\perp)$ for a number of crack lengths h. Both numerical and analytical results predict that the inductive bypass frequency should reduce with increasing crack thickness. Changes in the maximum $Z_1^\perp$ are predicted to be relatively small within the tested range, which is demonstrated in the numerical results.

Figure 5.22 shows the variation of $\mathrm{Re}\,(Z_1^\perp)$ for a number of inner radii values b. Both numerical and analytical results show that the maximum value of $\mathrm{Re}\,(Z_1^\perp)$ should reduce with increasing b, and that the inductive bypass frequency should reduce. Both behaviours are observed in the numerical results.

Figure 5.23 shows the variation of $\mathrm{Re}\,(Z_1^\perp)$ for a number of outer radii values d. Both numerical and analytical results show that the inductive bypass frequency should increase by an order of magnitude with d in the range of 14 to $28\,\mathrm{mm}$.

Figure 5.24 shows the variation of $\mathrm{Re}\,(Z_1^\perp)$ for a number of lamination permeabilities μ^{lam}. Both numerical and analytical results show that the inductive bypass frequency should increase with increasing μ^{lam}, whilst the maximum value of $\mathrm{Re}\,(Z_1^\perp)$ is almost constant.

It can be seen from these figures that Equation (5.6) has predicted $\mathrm{Re}\,(Z_1^\perp)$ to within a few 10's of percent, and that the inductive bypass frequency where it peaks has been predicted to better than an order of magnitude. High-frequency discrepancies in the magnitude of $\mathrm{Re}\,(Z_1^\perp)$ are likely attributable to mesh quality, but since the goal here is only to verify the formula is approximately correct, this has not been investigated systematically. It is therefore concluded that Equation (5.6) is sufficiently accurate to estimate the impedance of laminated magnets at ISIS, which is further justified by the fact that these laminations are anyway shielded by the RF screens.

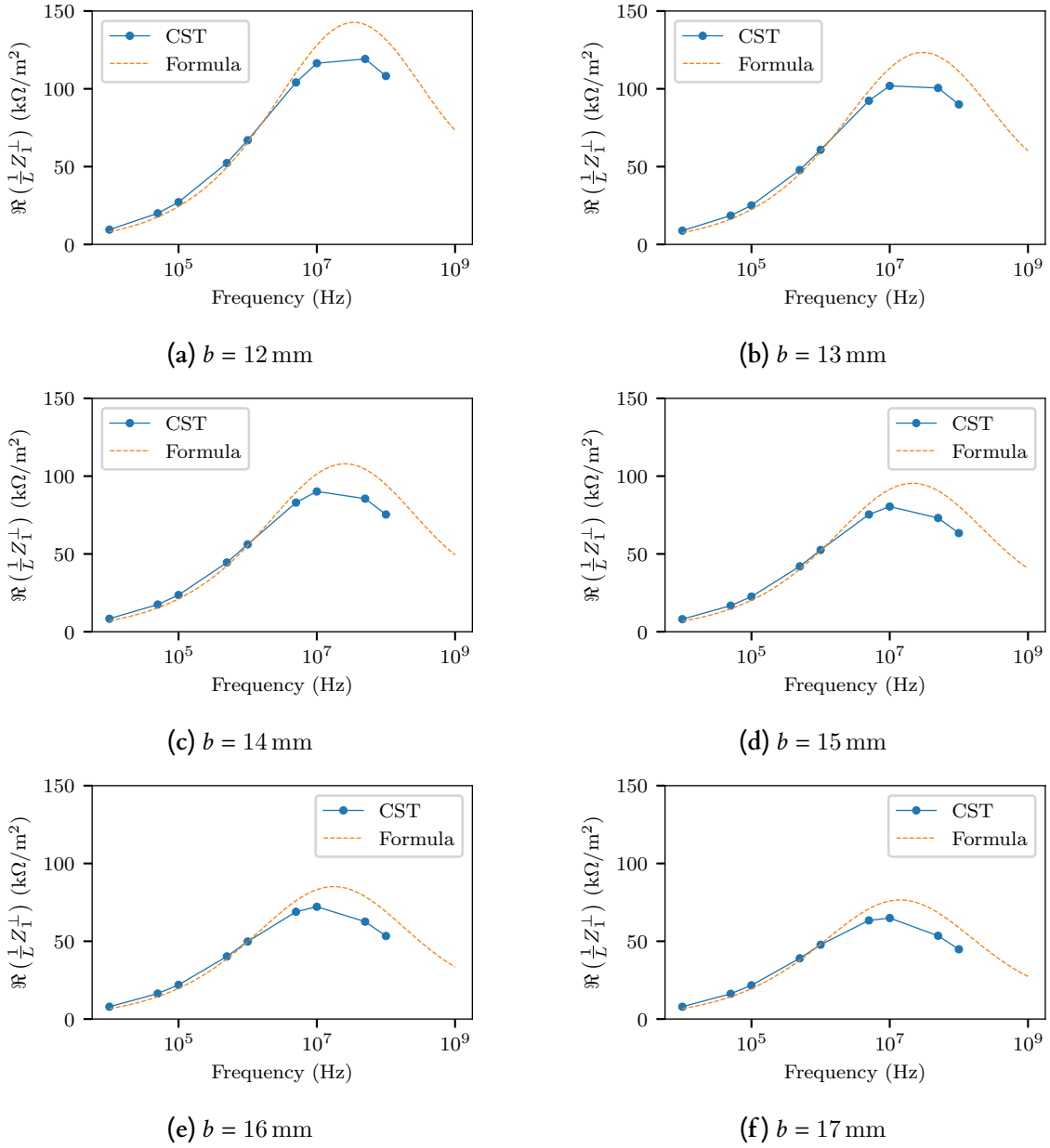


(a) $h = 0.2\,\text{mm}$ (b) $h = 0.4\,\text{mm}$

(c) $h = 0.6\,\text{mm}$ (d) $h = 0.8\,\text{mm}$

(e) $h = 1.0\,\text{mm}$

Figure 5.21: Real part of $Z_1^\perp$ per unit length, for the laminated model shown in Figure 5.20 and different values of crack thickness, h.

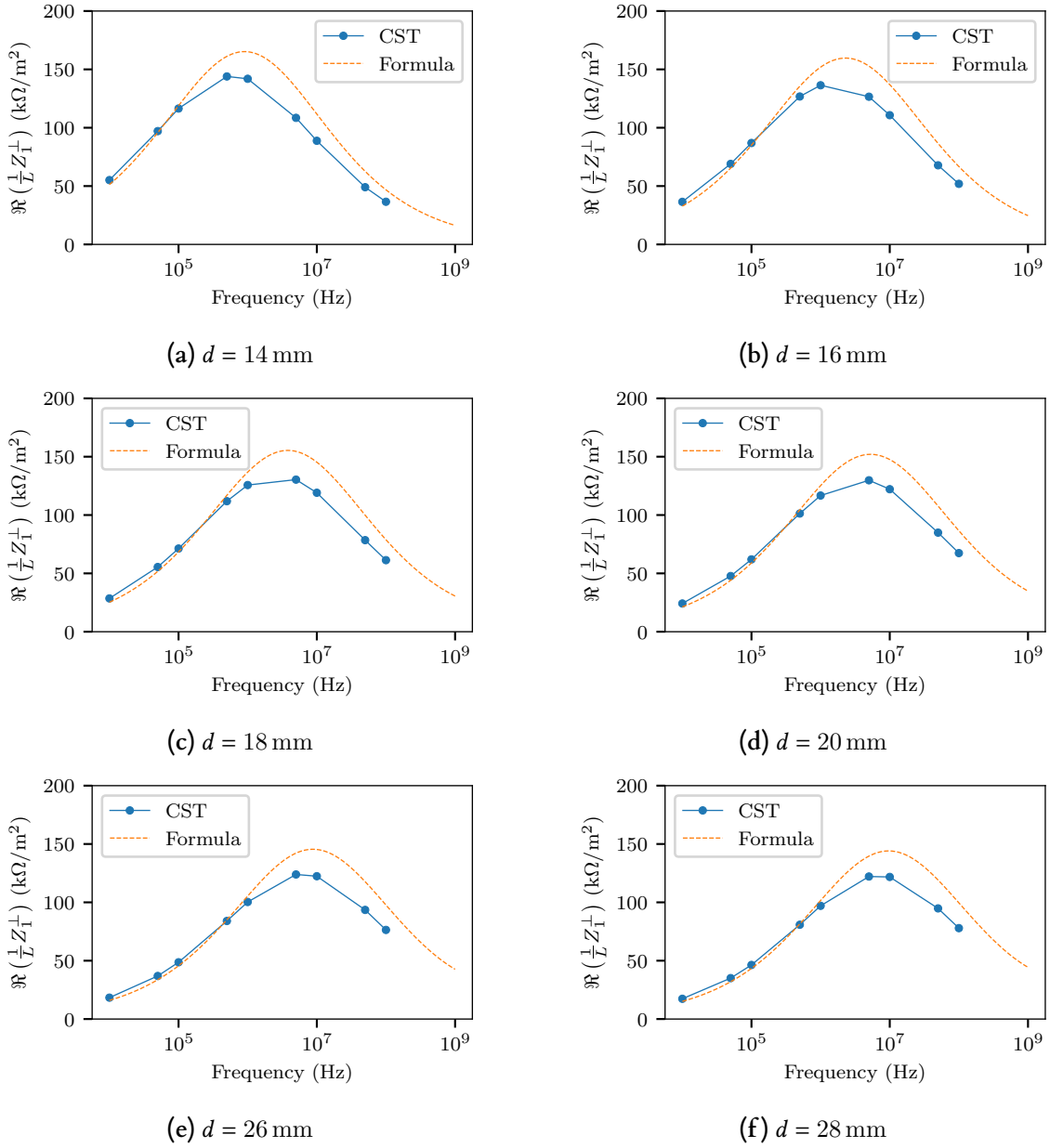


(a) $b = 12\,\text{mm}$ (b) $b = 13\,\text{mm}$

(c) $b = 14\,\text{mm}$ (d) $b = 15\,\text{mm}$

(e) $b = 16\,\text{mm}$ (f) $b = 17\,\text{mm}$

Figure 5.22: Real part of $Z_1^\perp$ per unit length, for the laminated model shown in Figure 5.20 and different values of inner radius.

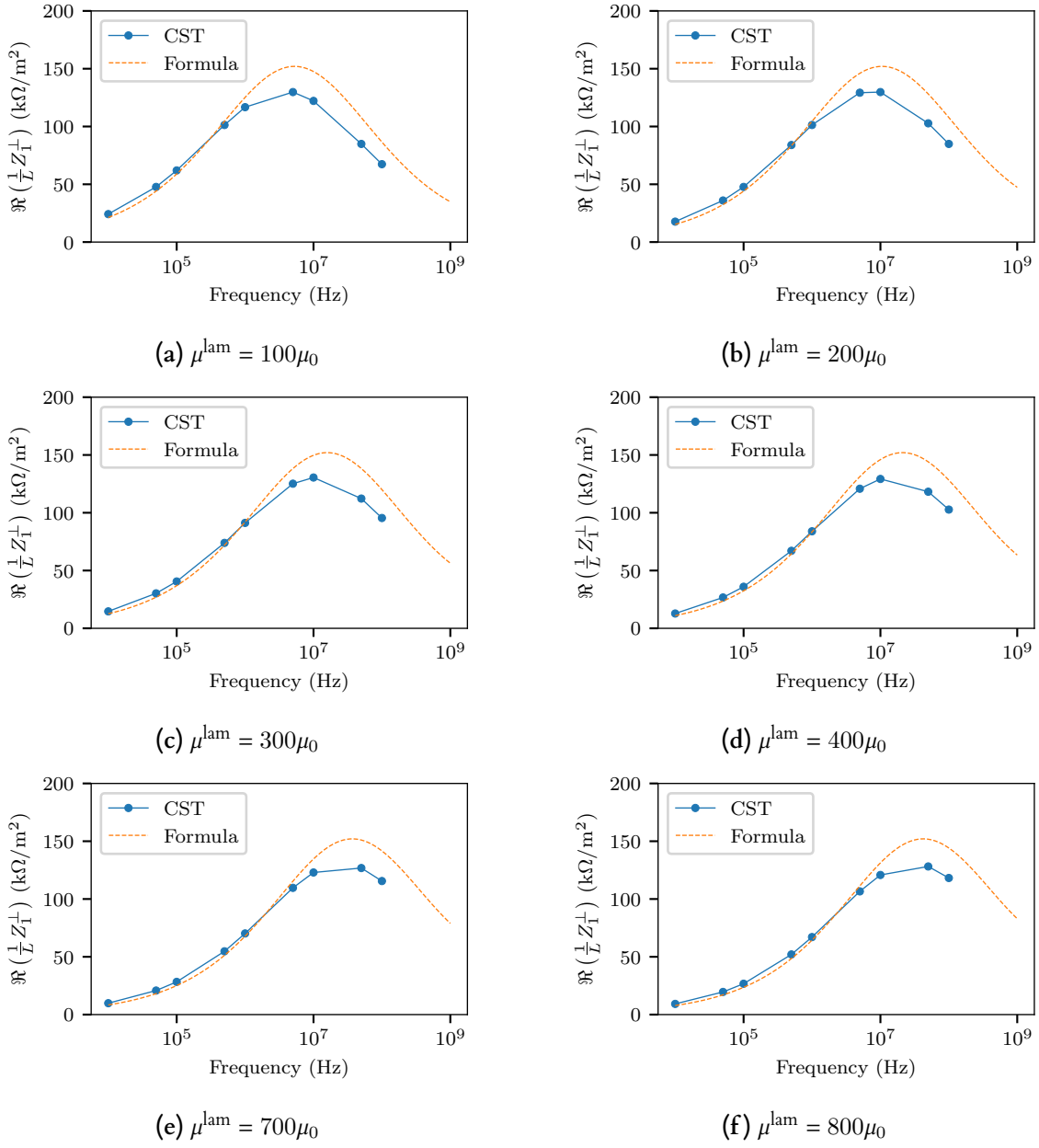


(a) $d = 14\,\text{mm}$ (b) $d = 16\,\text{mm}$

(c) $d = 18\,\text{mm}$ (d) $d = 20\,\text{mm}$

(e) $d = 26\,\text{mm}$ (f) $d = 28\,\text{mm}$

Figure 5.23: Real part of $Z_1^\perp$ per unit length, for the laminated model shown in Figure 5.20 and different values of outer radius.



(a) $\mu^{\text{lam}} = 100\mu_0$ (b) $\mu^{\text{lam}} = 200\mu_0$

(c) $\mu^{\text{lam}} = 300\mu_0$ (d) $\mu^{\text{lam}} = 400\mu_0$

(e) $\mu^{\text{lam}} = 700\mu_0$ (f) $\mu^{\text{lam}} = 800\mu_0$

Figure 5.24: Real part of $Z_1^\perp$ per unit length, for the laminated model shown in Figure 5.20 and different values of lamination permeability.

Having verified its accuracy, Equation (5.6) will now be be used to predict the impedance of an ISIS dipole's laminated, unshielded yoke. Figure 5.25 shows $\mathrm{Re}\left(Z_1^\perp\right)$ computed with the properties from Section 5.3.1.3 and a Yokoya factor of $\pi^2/12$ to approximate the case of a flat yoke. In computing Figure 5.25, 10000 calculations were performed with inputs derived from the normally distributed input parameters listed in Table 5.3. The results are consistent with an inductive bypass turning point close to $100\,\mathrm{MHz}$, and with observations on other laminated magnets [107, 106].

The RF screens will shield the magnet laminations above $\sim 40\,\mathrm{kHz}$, where the skin depth is comparable to the wire diameter. The lowest frequency vertical sideband at ISIS is at $\sim 100\,\mathrm{kHz}$, which is comparable to this frequency, so some field may penetrate the RF screen. In the worst case of a totally unshielded lamination, Figure 5.25 shows that $Z_1^\perp$ is less than that of a typical conducting pipe around at this frequency; see for example Figure 5.18. Since the laminations will be at least partially shielded, it is concluded that the low frequency impedance will be dominated by the RF screen itself.

Gaps between the wires mean that perfect shielding cannot be achieved even at high frequencies where the skin depth is small, however it has been found that shielding will remain effective provided the spacing between wires is less than the distance between the wires and the laminations [135]. On an ISIS dipole, the vertical RF screen aperture is $\sim 100\,\mathrm{mm}$, whilst the yoke aperture is $\sim 160\,\mathrm{mm}$, leaving a $\sim 30\,\mathrm{mm}$ gap, which is significantly larger than the typical wire spacing of $\sim 5\,\mathrm{mm}$. It is therefore concluded that even above $\sim 10\,\mathrm{MHz}$ where the yoke impedance is larger, the RF screen will shield the laminations and the screen's conductors will dominate the impedance.

It is concluded that at both high and low frequencies the conductive RF screen dominates the impedance and not the laminated yokes. The yokes will therefore be neglected from the overall RF screen model. By neglecting the yokes and the alumina chambers, the RF screen model becomes a set of conducting wires in free space. This important result simplifies the model to such an extent that it can can be solved using finite element tools, such as the low-frequency EM solver technique introduced in Chapter 3.

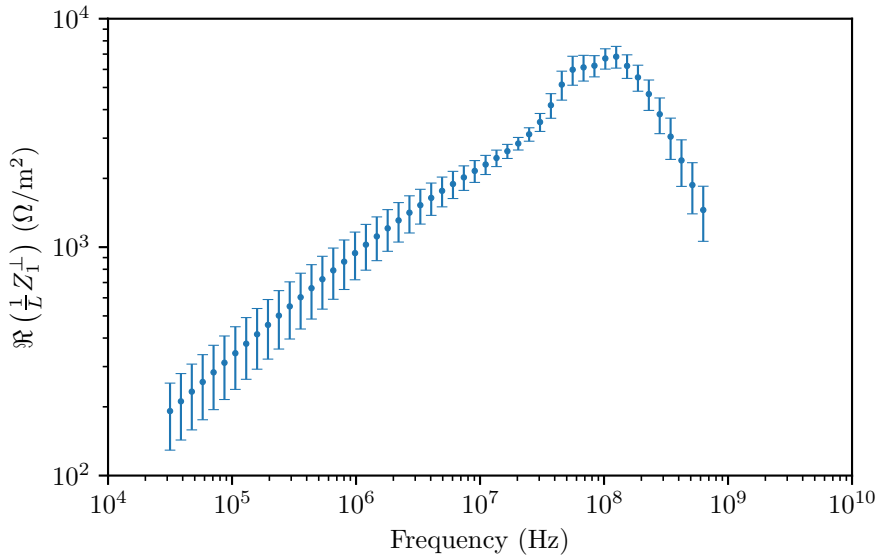


Figure 5.25: Real part of the transverse impedance per unit length computed with Equation (5.6) using the normally distributed parameters listed in Table 5.3 and a Yokoya factor of $\frac{\pi^2}{12}$. This result is representative of the ISIS main dipole magnet impedance. Error bars are the standard deviation of 10000 calculations.

Parameter	Mean	Uncertainty
b	8 cm	n/a
d	42 cm	n/a
σ^{lam}	$2 \times 10^6\,\text{S m}^{-1}$	$5 \times 10^5\,\text{S m}^{-1}$
μ^{lam}	$35\mu_0$	$10\mu_0$
τ	350 µm	30 µm
h	30 µm	5 µm
$\varepsilon^{\text{crack}}$	$3\varepsilon_0$	$1\varepsilon_0$

Table 5.3: Parameters used to calculate the impedance of the ISIS magnet laminations.

5.3.3 CST Simulations of RF Screens

5.3.3.1 Description of Simulation Models

Having determined that the Alumina ceramic and laminated magnet yokes can reasonably be neglected from the RF screen models, $Z_1^\perp$ of five different RF screens will now be computed with the low-frequency CST simulation introduced in Chapter 3. The simulated RF screens will include additional simplifications to the ones already intro-

duced. These were applied to remove complexity from the simulation models, whilst retaining the key features for an impedance calculation. These additional simplifications will now be described.

The real RF screen wires are connected to the coupling capacitors via RF finger-strips[1], which are challenging to simulate since their contact properties are not generally known. Instead, a 5 mm gap will be made in each wire and capacitors inserted to bridge this gap[64]; see Figure 5.26.

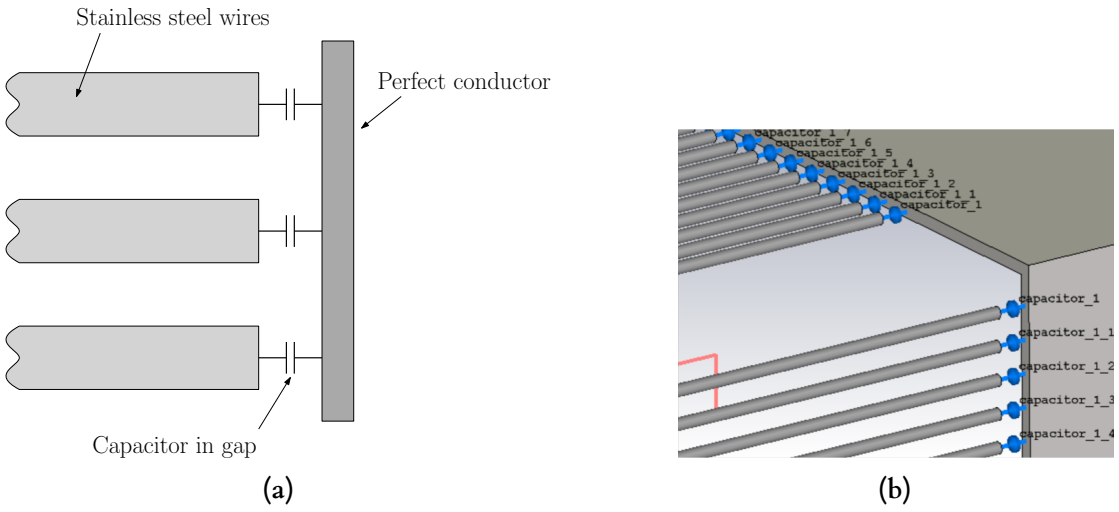


Figure 5.26: Schematic (a) and screenshot (b) of simplified geometry for capacitor connections in CST simulations.

A second simplification is that the transverse cross-sectional dimensions are held constant over the screen's length, whilst the apertures of real dipole and doublet RF screens vary to follow the design envelope [195]. The simulated screen's horizontal and vertical apertures will be taken from the point on the screen geometry with the smallest vertical opening; widths and height dimensions are defined in Figure 5.27. Since the apertures vary slowly compared to the wavelengths of interest, this is assumed to provide a "worst-case scenario" in its prediction of $Z_1^{\perp}$. A consequence of this simplification is that the curvature of the dipole's RF screen is neglected.

[1] RF finger-strips are a type of conducting spring for making contact electrical connections.

Table 5.4: Dimensions of the simulated RF screens, with parameters as indicated in Figure 5.27.

Screen Name	Module	Width (mm)	Height (mm)	No. Wires (h)	No. Wires (v)	Wire Sep. (mm)	Length (m)
Dipole	1	181.0	104.0	46	n/a	4.76	5.02
Doublet	11/ 61	235.2	117.2	66	42	4.76	2.86
Singlet	30	102.0	151.2	38	58	4.73	0.59
Oct/ Other	13	200.2	115.1	82	46	4.76	0.53
Oct/ Other	9/ 10	164.8	170.2	66	70	4.76	0.53

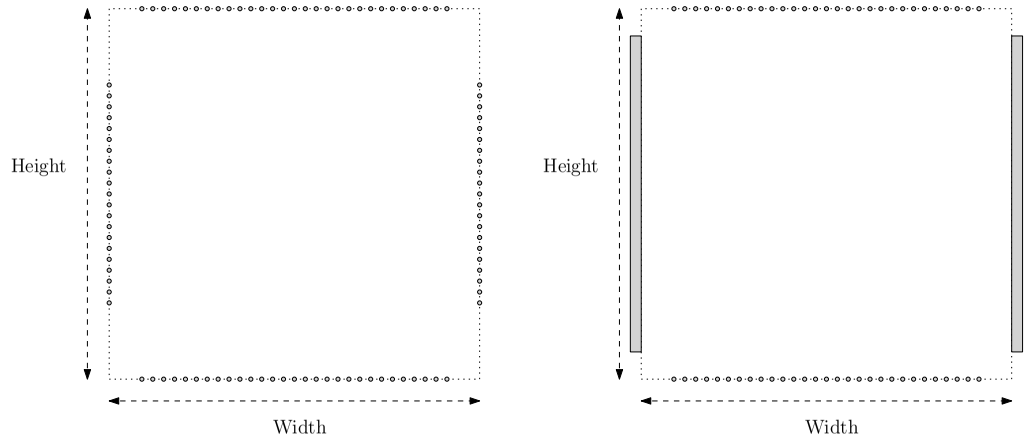


Figure 5.27: Schematic of simulated (a) and dipole (b) RF screens, with width and height dimensions labelled.

Dimensions used for all the simulations of simplified RF screens are listed in Table 5.4. Whilst the dipole length is often quoted as $4.4\,\mathrm{m}$, the length listed is larger because the nominal wire length is $5.05\,\mathrm{m}$. The listed value was chosen because RF finger strips typically make contact a few cm before the end of a wire.

In all but the dipole RF screens, all wires are connected with $0.1\,\mu\mathrm{F}$ capacitors. The side-plates of the dipoles are each connected with $25 \times 0.01\,\mu\mathrm{F}$ capacitors in parallel, whilst the wires at the top and bottom of the aperture are each connected with $0.1\,\mu\mathrm{F}$ capacitors; see Figure 5.27.

5.3.3.2 Results

The real part of the impedance for the 5 RF shield modules with capacitors included are shown in Figure 5.28, and all plots are overlaid with the impedance for the case with capacitors replaced by resistors. Each lumped resistance is set equal to the resistance of the missing $5\,\mathrm{mm}$ of wire, which was $1\,\mathrm{m}\Omega$; this same resistance was also used for the dipole side-plates.

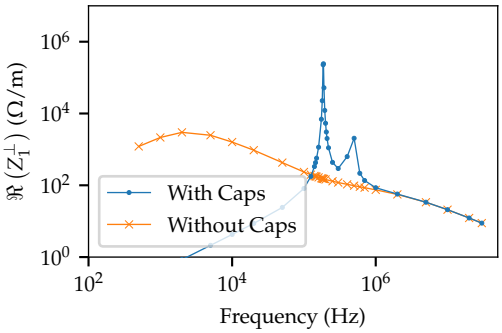
Results with capacitors show resonant peaks in the frequency range between ~ 80 and $200\,\mathrm{kHz}$. At their peaks, the real parts of these resonance magnitudes are three orders-of-magnitude larger than the resistive-wall impedance at $1\,\mathrm{MHz}$. Given their large amplitudes, a transverse resonator impedance can reasonably be fitted to the largest peaks without subtracting the background resistive wall impedance. Performing least squares fits to the maxima and two surrounding points give the resonator parameters listed in Table 5.5. In all cases, a second peak can be seen at higher frequencies, but it will be neglected because its amplitude is invariably an order-of-magnitude lower than the largest peak.

At $2\,\mathrm{MHz}$, the results with and without capacitors differ by less than $2.3\,\%$ across all RF screens, which is considered to be good agreement. Above this frequency, $Z_1^\perp$ resembles a thick resistive-wall impedance with a roughly $(\omega)^{-1/2}$ dependence. This implies that neglecting the capacitors is a good approximation at this frequency and

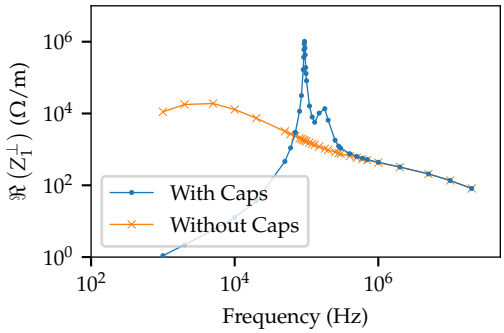
above. In that higher frequency range, quality of the finite-element mesh is a possible source of error, because the wires were modelled as a CST "normal" material which requires an accurate volume mesh. Equation (3.30) suggests that the skin depth at $10\,\mathrm{MHz}$ is $0.14\,\mathrm{mm}$, or $6\,\%$ of the wire diameter. To verify that meshing issues have not caused significant inaccuracies at frequencies where the skin depth is much smaller than the wire diameter, simulations with CST's "lossy metal" approximation have been carried out. In this case, the wire volumes are treated as perfect conductors during simulation and a surface impedance approximation used to estimate resistive losses. A volume mesh is then not required in the region where current flows, and a surface mesh is generated instead. This approximation is valid where the skin depth is much smaller than the thickness of a material, and can improve accuracy for these frequencies. A comparison of $\mathrm{Re}\,(Z_1^\perp)$ for the two different material types without capacitors is shown in Figure 5.29. At $2\,\mathrm{MHz}$, differences between the two material types are less than $100\,\Omega\,\mathrm{m}^{-1}$, which is not considered significant compared to peaks of up to $1\,\mathrm{M}\Omega\,\mathrm{m}^{-1}$. The accuracy of the "normal" material simulations is thus considered sufficient over the whole simulated frequency range.

Table 5.5: Simulated RF screen fitted resonator $Z_1^\perp$ parameters. * - It has been assumed that all ten doublet RF screens are identical; mechanical differences of the doublet in the extraction straight are considered negligible.

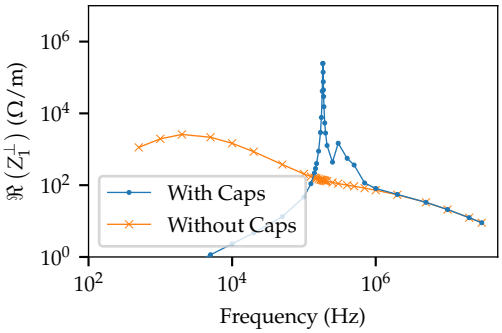
RF Screen	$\frac{\omega_r}{2\pi}$ (kHz)	$R_\perp$ ($\mathrm{M}\Omega\,\mathrm{m}^{-1}$)	Q_r	Quantity
Dipole (Module 1)	86	1.37	17	10
Doublet (Module 11)	94	1.03	27	10*
Singlet (Model 30)	186	0.31	53	10
Octupole (Module 13)	184	0.27	60	6
Octupole (Module 9/10)	162	0.20	68	6



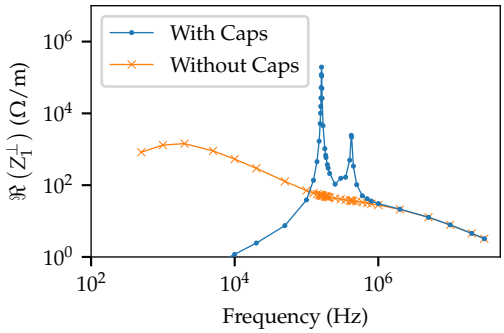
(a) Singlet



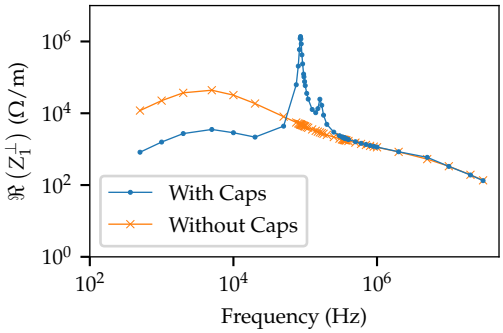
(b) Doublet



(c) Module-13

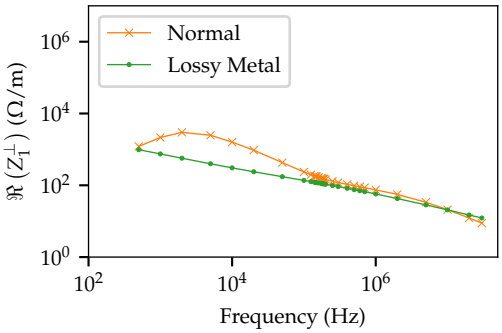


(d) Module-9/10

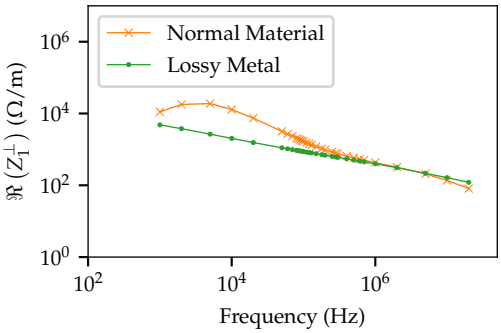


(e) Dipole

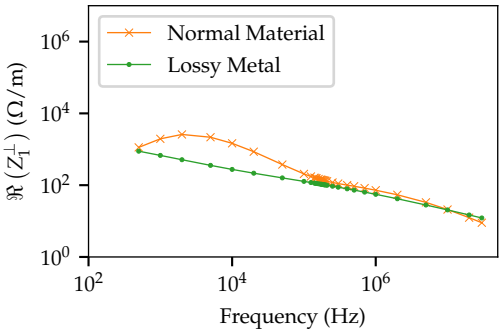
Figure 5.28: Real part of $Z_1^\perp$ computed by low-frequency CST simulations of the singlet (a), doublet (b), module-13 (c), module-9/10 (d) and dipole (e) RF screens, with and without capacitors.



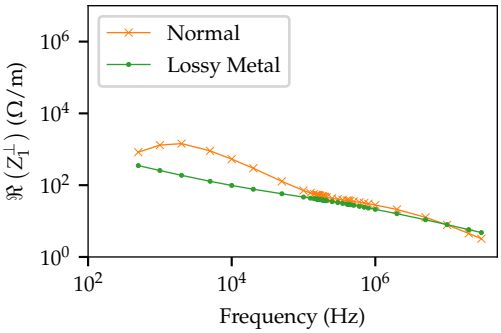
(a) Singlet



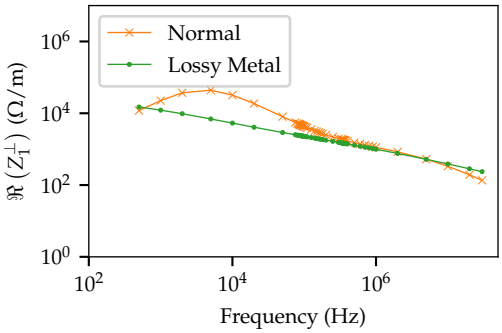
(b) Doublet



(c) Module-13



(d) Module-9/10



(e) Dipole

Figure 5.29: Real part of $Z_1^\perp$ computed by low-frequency CST simulations of the singlet (a), doublet (b), module-13 (c), module-9/10 (d) and dipole (e) RF screens, without capacitors but for "normal" and "lossy metals."

5.3.4 Probe Coil Measurements of RF Screen Impedance

Resonator impedances predicted by the low-frequency CST simulations have very large amplitudes and occur at the frequencies of interest for instabilities on ISIS. To verify these predictions, a series of probe-coil experiments have been carried out on spare RF screen assemblies inside their respective magnets. Access to these assemblies is generally limited because they are operational spares for the ISIS facility, but full access was granted for a singlet RF screen and partial access for a dipole RF screen.

These experiments have been described in Chapter 3. They involve inserting a rectangular probe coil into the RF screen, and driving a current to simulate a beam's dipole moment. $Z_1^\perp$ is obtained from the coils impedance, which can be measured using standard circuit techniques. In these measurements, an LCR meter was the primary apparatus used to measure the probe coil impedance, with the set-up shown in Figure 5.30a. Device-under-test (DUT) measurements were performed with the probe coil inserted into the RF screen, and reference (REF) measurements were performed with the probe coil in free space. The difference between these two impedance measurements can be used with Equation (3.54), to compute $\mathrm{Re}\left(Z_1^\perp(\omega)\right)$; an alternative type of reference measurement is required for $\mathrm{Im}\left(Z_1^\perp(\omega)\right)$. Since only partial access to the dipole was granted, it was not possible to insert a probe coil through the full length of the dipole, so only a partial characterisation was possible.

To verify the LCR results, and identify some types of systematic errors, a Vector Network Analyser (VNA) was also used to measure the probe-coil's impedance. As with the LCR measurements, the probe coil was treated as a lumped impedance, and signal transmission was measured between two VNA ports; see Figure 5.30b. In this configuration, each end of the probe coil was connected to the central conductor of a port, whilst the outer conductors were shorted together. The electrical connections in this configuration are the same as for the LCR experiment, so both devices can be

used without disturbing the experimental set-up. The impedance in this case can be measured from the transmission parameters, s_{21}, with

$$Z_{\mathrm{pr}}(\omega) = 2Z_0 \frac{1 - s_{21}(\omega)}{s_{21}(\omega)}. \tag{5.7}$$

After measuring $Z(\omega)$ for the DUT and REF configurations computation of the transverse impedance $Z_1^{\perp}(\omega)$ is the same as for the LCR meter.

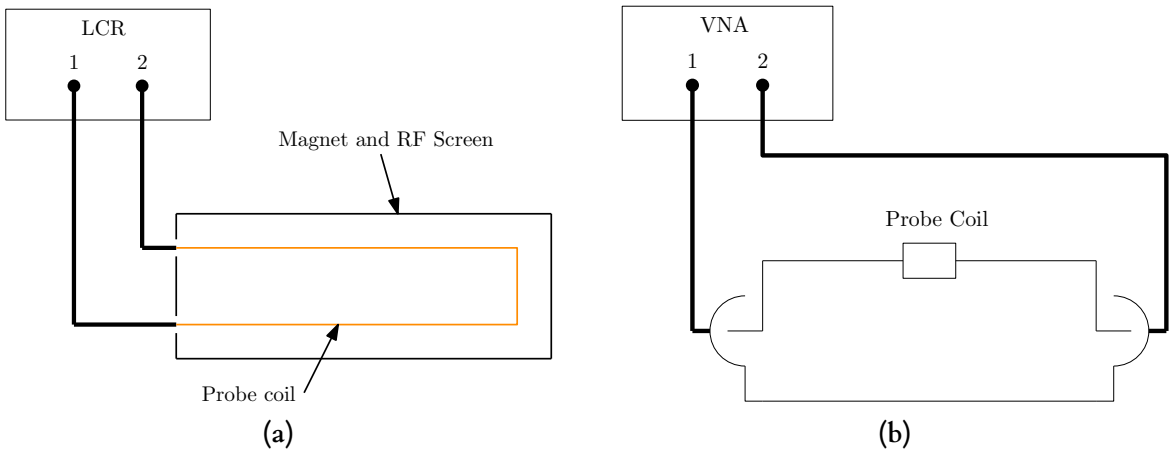


Figure 5.30: Schematic of the LCR (a) and VNA (b) experimental set-ups for the RF screen measurements.

5.3.4.1 Singlet Quadrupole Measurement

The transverse impedance of an unpowered, singlet RF screen and yoke was measured using the probe coil technique. Photographs of the magnet with dedicated impedance-measurement flanges are shown in Figure 5.31 for the DUT and REF configurations. Probe coils with $N_t = 2$ and 3 turns of wire were used to identify systematic errors with the probe, such as those caused by resonances on the coil itself.

To prevent systematic errors associated with objects moving near to the measurement set-up, the probes were fully enclosed in the RF screen and flanges. Probe coils were wound on Tufnol supports to improve repeatability and prevent wire sagging; these were non-conducting and non-magnetic. Alignment of the flanges was achieved using precise dowel locations, which were necessary to ensure proper contact of the RF

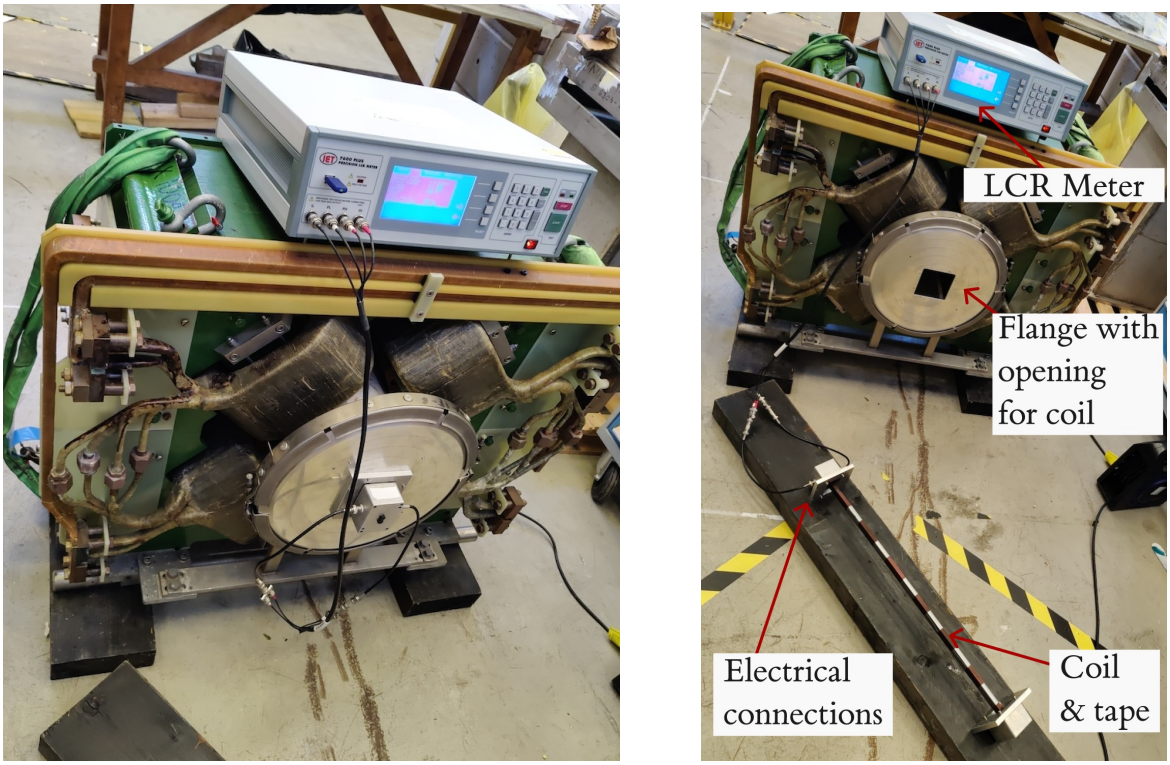


Figure 5.31: Experimental set-up of the singlet RF screen measurements, in the DUT (a) and REF (b) configurations.

screen wires with the finger strips. A 90 mm by 90 mm cutout at the centre of both flanges allowed space for the probe coils to pass through. Connection to the flange was made by a small adaptor plate, to allow different experimental set-ups to be tested without modifying the flanges. To prevent electrical feedthroughs from impinging into the RF screen aperture and partially shield the ends of the coils, diecast boxes with dedicated mounting holes provided the fixing point for the probe support. Since all fittings were tight, sag of the probe support was considered negligible. The probe coil axis was centered by mechanical tolerances to within ±0.65 mm of the vertical aperture (~ ±0.4 %), but the affect of any residual offsets was randomised by performing REF and DUT measurements alternatively, so that the probe was reconnected for each repeat DUT measurement.

Table 5.6: Resonator least-squares fit parameters from measurements for a singlet RF screen.

Probe	$\frac{\omega_r}{2\pi}$ (kHz)	$R_\perp$ ($\mathrm{k\Omega\,m^{-1}}$)	Q_r
Two-turn	(188.6 ± 0.3)	(31.1 ± 0.5)	(4.0 ± 0.1)
Three-turn	(188.9 ± 0.3)	(32.4 ± 0.5)	(4.1 ± 0.1)

The results for both coils are shown in Figure 5.32, which also shows the predicted resonant frequency from Table 5.5. In the frequency range of 141 and 550 kHz, results from the two probes are consistent. A least-square fit to a resonator impedance was performed for both probes, with results listed in Table 5.6. The measured resonant frequencies and quality factors are consistent within one standard uncertainty, whilst $R_\perp$ are consistent within two. In both cases, the uncertainty in $R_\perp$ is less than 2 %, which could be explained by temperature variations in the storage building on the days that the experiments were performed.

A weighted mean of these results gives $\omega_r/(2\pi) = (188.8 \pm 0.2)\,\mathrm{kHz}$, $R_\perp = (31.8 \pm 0.4)\,\mathrm{k\Omega\,m^{-1}}$ and $Q_r = (4.1 \pm 0.1)$. These parameters are to be compared with the CST predictions listed in Table 5.5. The measured resonant frequency differs from the prediction by less than 2 %. The simulated value of $R_\perp$ is a factor of ~ 10 larger than the measured, which is a significant discrepancy; although the measured value is still two orders-of-magnitude larger than the singlet's resistive-wall impedance at 1 MHz. The simulated quality factor is a factor of ~ 13.7 larger than the measured, which is again a significant discrepancy.

As discussed in Chapter 3, probe coil measurements do not accurately measure the imaginary part of the transverse impedance. Nevertheless, the imaginary part of a resonator impedance has a characteristic distribution, which would be expected to be observed in the experimental data even if its absolute value were offset. The measured $\mathrm{Im}\left(Z_1^\perp(\omega)\right)$ is shown in Figure 5.33 for the two different probes; to aid in comparing these results, offsets have been manually adjusted. The distribution of these results is reminiscent of the imaginary part of a resonator impedance.

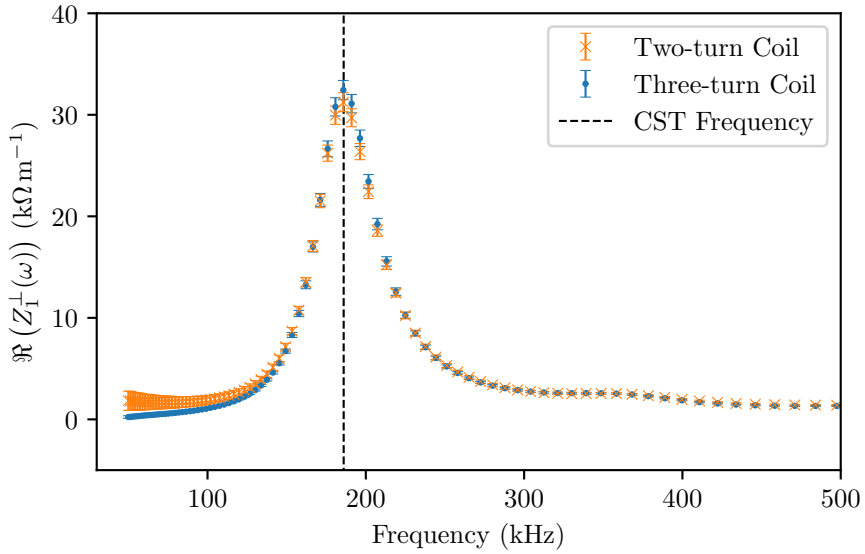


Figure 5.32: Real part of a singlet RF screen's $Z_1^\perp$, measured using an LCR meter and probe coils with two and three turns. The resonant frequency predicted by CST is indicated.

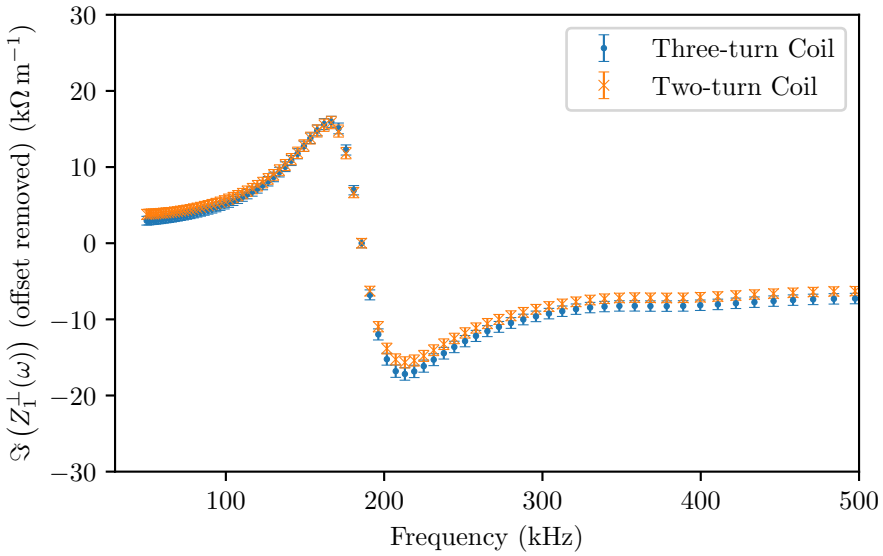


Figure 5.33: Measured imaginary part of a singlet RF screen's $Z_1^\perp$, measured using an LCR meter and probe coils with two and three turns. Offsets have been manually adjusted so that the distributions may be more easily compared.

To verify the LCR-meter results, impedance measurements were also made using a vector network analyser in the configuration shown in Figure 5.30b. The same probe coils and experimental configurations were used, and the results are shown in Figure 5.34. A peak appears in $\mathrm{Re}(Z_1^{\perp})$ for all probe coils and measurement devices, whilst $\mathrm{Im}(Z_1^{\perp})$ shows the same characteristic distribution in all results. The results are consistent within one or two standard uncertainties for most of the observed bandwidth. An exception is clear at low frequencies, where the difference in probe resistance was typically on the order of $0.001\,\Omega$ at $100\,\mathrm{kHz}$ and below. At that point, variations can be explained by changes in electrical contacts between repeat measurements or variations in the atmospheric conditions. Apart from this region, the results are considered to be sufficiently consistent to conclude that a resonator impedance is present.

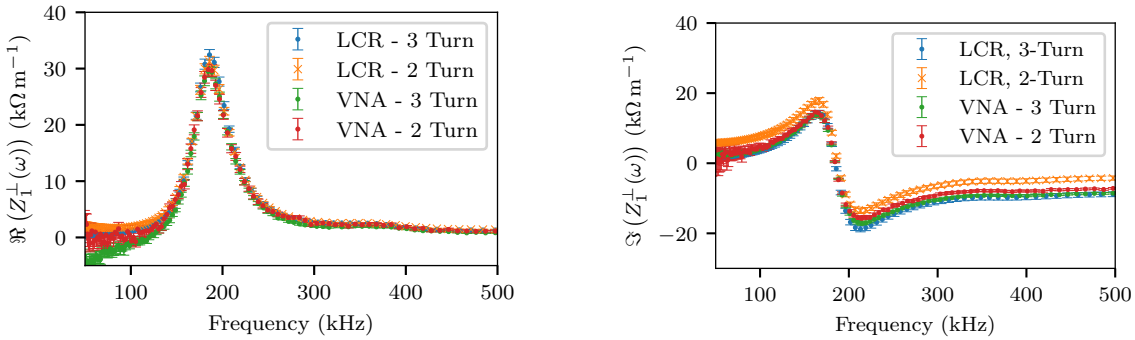


Figure 5.34: Comparison of real (a) and imaginary (b), values of $Z_1^{\perp}$ as measured with the LCR meter and VNA for the singlet RF screen. The imaginary part is not accurate for probe coil measurements.

Uncertainties in $\mathrm{Re}\,(Z_1^{\perp}(\omega))$ from Equation (3.54) have been estimated by considering the real and imaginary parts of the impedance separately. $\mathrm{Re}\,(Z_1^{\perp}(\omega))$ can be written explicitly as

$$\mathrm{Re}\,(Z_1^{\perp}(\omega)) = \frac{c}{\omega}\frac{1}{\Delta^2 N_t^2}\,\mathrm{Re}\left(Z_{\mathrm{pr}}^{\mathrm{DUT}} - Z_{\mathrm{pr}}^{\mathrm{REF}}\right). \tag{5.8}$$

The uncertainty in this quantity is

$$\sigma_{z\perp}^2 = \left(\frac{\partial \mathrm{Re}(Z_1^\perp)}{\partial \mathrm{Re}(Z_{\mathrm{pr}}^{\mathrm{DUT}})}\,\mathrm{Re}(\sigma_{Z_{\mathrm{pr}}^{\mathrm{DUT}}})\right)^2 + \left(\frac{\partial \mathrm{Re}(Z_1^\perp)}{\partial \mathrm{Re}(Z_{\mathrm{pr}}^{\mathrm{REF}})}\,\mathrm{Re}(\sigma_{Z_{\mathrm{pr}}^{\mathrm{REF}}})\right)^2 + \left(\frac{\partial \mathrm{Re}(Z_1^\perp)}{\partial \Delta}\sigma_\Delta\right)^2 \quad (5.9)$$

where $\mathrm{Re}(\sigma_{Z_{\mathrm{pr}}^{\mathrm{REF}}})$ must be computed from the measured magnitudes and phases. From the means and standard errors on these quantities, the uncertainty on the real parts are

$$\mathrm{Re}\left(\sigma_{Z_{\mathrm{pr}}}\right)^2 = \left(\frac{\partial}{\partial |Z_{\mathrm{pr}}|}\left(|Z_{\mathrm{pr}}|\cos\left(\theta_{\mathrm{pr}}\right)\right)\sigma_{|Z_{\mathrm{pr}}|}\right)^2 + \left(\frac{\partial}{\partial \theta_{\mathrm{pr}}}\left(|Z_{\mathrm{pr}}|\cos\left(\theta_{\mathrm{pr}}\right)\right)\sigma_{\theta_{\mathrm{pr}}}\right)^2. \quad (5.10)$$

Variations in Z_{pr} were primarily observed when moving between the REF and DUT configurations, and are thought to be associated with changes in the electrical connection properties. This change in configuration was made for each repeat measurement to prevent systematic errors associated with alignment, so variations in the electrical connections were also expected to be random. Limited time meant that a systematic offset in the imaginary part of the impedance can be seen in Figure 5.34, but since all resonator parameters were obtained from the real part, confirming the functional shape of the imaginary part was considered sufficient for the present purpose. All LCR meter measurements were performed with eight REF and eight DUT repeats, whilst VNA measurements were made with five. These numbers were primarily chosen due to time constraints.

The physical width of the coil, Δ, was defined in Equation (3.51), and in this experiment was taken as the distance between the central axis of the wire on either side of the probe. This was justified because the stripped wire diameter of $0.5\,\mathrm{mm}$ was only $\sim 2.5\,\%$ of Δ. The uncertainty in Δ was minimised at the design stage by using the tufnol support. Grooves were cut into the support which allowed the probe wires to extrude slightly from its surface. Δ was initially obtained by measuring the outside width of the probe wires with a set of calibrated vernier calipers, and subtracting from this the diameter of the insulated wire, which was itself measured with a digital micrometer.

The probe was wound by hand, with friction at the ends maintaining tension; the tape seen in Figure 5.31b provided additional support. This imperfect winding was the primary source of uncertainty in Δ and introduced a systematic uncertainty, as it allowed the wire to extrude beyond the support. To estimate these uncertainties, a set of vernier calipers were held tight on one side, and gradually closed until there was visible contact between the caliper edge and the wire. This was repeated at five positions along the length of a probe and a mean width computed. To correct for the systematic error, the difference between this and the previous outside width measurements were added to the value of Δ for both probes, and also taken as their uncertainty. For two and three turn probes, Δ was $(20.5 \pm 0.3)\,\mathrm{mm}$ and $(20.6 \pm 0.3)\,\mathrm{mm}$ respectively.

5.3.4.2 Dipole Measurement

The CST model of the dipole RF screen was the most simplified because it neglected the screen's curvature and aperture changes along its length. For this reason, some experimental verification of the simulated results was necessary. A spare dipole magnet is stored for operational purposes in the synchrotron hall, but since access to the magnet is required for operations, it was not possible to install a full length probe coil as was done with the singlet measurements. Instead, access was granted for a less invasive measurement where a short probe coil was inserted into one side of the dipole. This novel experimental method would not provide a full characterisation of $\mathrm{Re}\,(Z_1^{\perp})$, but a narrowband increase in the probe coil's resistance was expected at the shield's resonant frequency, and the coil could be removed quickly in the event that the magnet was required for operations.

The probe coil for this experiment was $17.5\,\mathrm{cm}$ long, $4.8\,\mathrm{cm}$ wide and had 12 turns. The number of turns was increased compared to the singlet measurement to improve the inductive coupling between the RF screen and the relatively small probe. Figure 5.35 shows the experimental set-up for DUT and REF configurations.



(a) (b)

Figure 5.35: Experimental set-up of the dipole RF screen measurements, in the DUT (a) and REF (b) configurations.

Figure 5.36 shows the difference between the probe coil resistance in the DUT and REF configurations. A peak was observed in the DUT configuration, within 5% of the resonant frequency predicted by CST and with both an LCR meter and a VNA. Since the measured peak amplitude is the same order-of-magnitude as the background, fits to a resonator impedance would require this background to be subtracted. A least-squares fit to $f(x) = \sqrt{x} + a$ was made for all frequencies above 130 kHz, which gave a reduced chi-squared of 17 for the LCR results and 0.96 for the VNA results. The apparently large value of reduced chi-squared for the LCR results is attributable to the smaller peak at close to 170 kHz. These fits were then extrapolated to lower frequencies and subtracted from the coil resistance; the extrapolated fit for the VNA is overlaid in the figure. Figure 5.37 shows the difference in probe coil resistance with the offset subtracted, and uncertainties in the fit have been applied to each point.

In order to estimate transverse resonator parameters, Equation (3.54) was applied to the probe coil resistance with background subtraction. Since the probe coil was short, $R_\perp$ was not expected to be accurately measured, however $\omega_r/(2\pi)$ and Q_r were expected

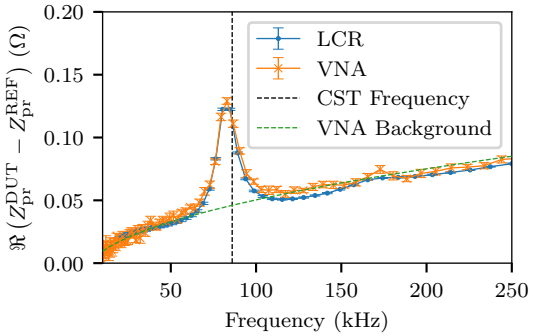


Figure 5.36: LCR meter and VNA measurements of the real part of the probe coil resistance for the dipole RF screen with the reference resistance subtracted.

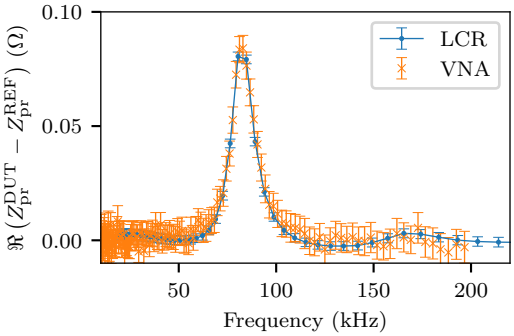


Figure 5.37: Real part of the difference in probe coil resistance for the dipole RF screen with background subtraction.

Table 5.7: Least-squares fit parameters from measurements for a dipole RF screen.

Equipment	$\frac{\omega_r}{2\pi}$ (kHz)	Q_r
LCR	(82.2 ± 1.3)	(6.7 ± 2.8)
VNA	(82.3 ± 0.4)	(6.1 ± 0.8)

to be accurate. A least-squared fit to a resonator impedance was performed for both LCR and VNA results. The resulting resonant frequency and Q_r are listed in Table 5.7, which are both consistent within a single uncertainty. A weighted mean of these quantities were computed giving $\omega_r/(2\pi) = (82.3 \pm 0.3)\,\text{kHz}$ and $Q_r = (6.1 \pm 0.7)$. This resonant frequency is within 5 % of the CST prediction in Table 5.5, which is considered an excellent level of agreement considering the simplified geometry. The quality factor is significantly lower than predicted, which was also the case for the singlet, and will need to be taken into account in the impedance model.

5.3.5 RF Screen Impedance Model for the ISIS Synchrotron

Simulations of the five most common RF screens have been carried out. Table 5.5 contains a summary of fits to the simulated RF screens, and Figure 5.38 shows $\mathrm{Re}(Z_1^{\perp})$ for all the simulated RF screens multiplied by their quantity, giving the simulated RF screen impedance of the ISIS synchrotron. Probe coil impedance measurements have confirmed large resonator impedances close to the predicted frequencies, but differences between measured and simulated $R_{\perp}$ and Q_r mean that these values cannot be taken directly from the simulated values in Table 5.5. Since experimental data from other RF screens is not expected to become available, any unmeasured quantities must be extrapolated from the available data to produce an impedance model. This section will describe how this extrapolation will be carried out for the RF screens in the ISIS Synchrotron, with a single model being adopted for each family of RF screen. The resulting resonator parameters are listed in Table 5.8.

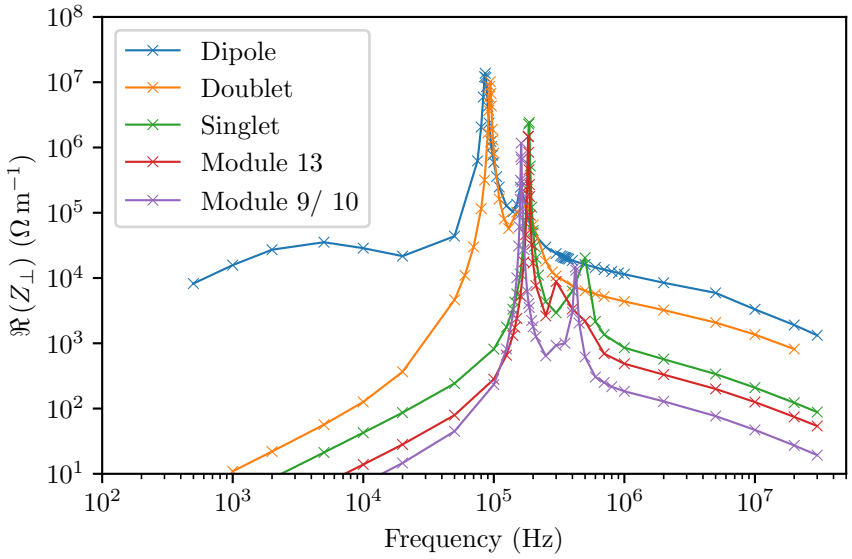


Figure 5.38: Overlay of $\mathrm{Re}(Z_1^{\perp})$ of each RF screen family in the ring, as computed by CST.

5.3.5.1 Resonant Frequencies

Two distinct probe coil experiments were carried out on a singlet and a dipole RF screen. Both demonstrated resonances within 5% of the frequencies listed in Table 5.5, which is considered a good level of agreement. The resonant frequencies will therefore be taken as the measured values on the singlet and the dipole RF screens, and the simulated values will be used for the rest. The singlet and dipole measurements were both made on a single device, but since the capacitors in the synchrotron have been in-use for up to forty years, their X7R dielectric will have aged causing a lowering of their capacitance. This will be accounted for by considering the expected drift in resonant frequency as an uncertainty.

With typical ageing characteristics of 1 % per-decade-hour [2], their capacitance could have reduced by as much as 6 %. Assuming the resonant frequency follows $\frac{1}{\sqrt{C}}$, its value could have changed by as much as 3 %. If initial capacitances were within $\sim$ 10 % of their nominal values then the resonant frequencies could vary by up to 5 %. Combining these gives 6 %, which will be taken as the uncertainty on the resonant frequency of all RF screen families, which are listed in Table 5.8.

5.3.5.2 Resonator Amplitudes and Quality Factors

The singlet measurement revealed reductions in both $R_\perp$ and Q_r compared to the CST simulations. Whilst the physical source of this discrepancy has not been conclusively identified, the simultaneous reduction of both quantities indicates that a resistive element is missing from the models.

This resistive element can be approximated in the CST models by adding a resistor in series with each capacitor. To validate this method, the singlet RF screen was simulated with a range of series resistors and $Z_1^\perp$ computed for each value; see

[2] The rate of capacitor ageing is commonly specified as a percent per-decade-hour because the drop in capacitance follows a logarithmic curve. τ_h hours after a capacitor's last heat-cycle, its capacitance will have dropped to a percentage of $100 - x\log_{10}(\tau_h)$ of its original value, where x is the ageing rate in percent-per-decade-hour.

Figure 5.39. The peak of $\mathrm{Re}(Z_1^\perp)$ and several surrounding points were then fitted to a transverse resonator impedance. No background was subtracted prior to these fits because the peak impedance was consistently an order-of-magnitude above background values. Figure 5.40 shows the fit values of $R_\perp$ and Q_r with an overlaid linear fit computed by Orthogonal Distance Regression; the reduced χ^2 of this fit was 0.41.

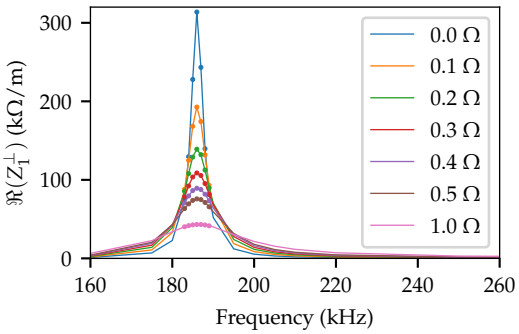


Figure 5.39: Simulated impedances for the singlet RF screen, with a range of series resistors. Points fit to the resonator impedance are overlaid.

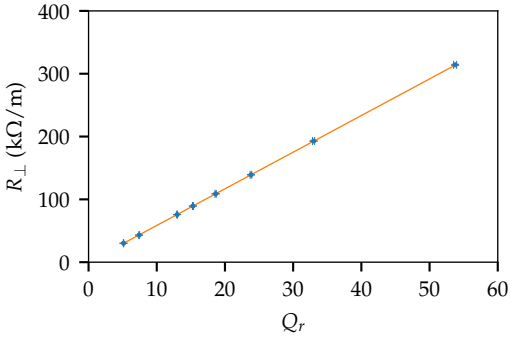


Figure 5.40: Fit values of $R_\perp$ and Q_r for the singlet RF screen with different resistances added in series with the capacitors. Fits are shown in Figure 5.39.

The linear fit in Figure 5.40 allows $R_\perp$ to be estimated from a measured value of Q_r. To verify the accuracy of this technique, $R_\perp$ was computed from the fit with the measured Q_r listed in Table 5.8, giving $R_\perp = (24 \pm 1)\,\mathrm{k\Omega\,m^{-1}}$. The measured value listed in Table 5.8 is 32 % larger than this prediction, which is a significant improvement on the simulated predictions without resistors listed in Table 5.5. The same technique of using simulated resistors can be applied to the dipole measurements, where it was not possible to measure $R_\perp$ directly. Figure 5.41 shows $\mathrm{Re}(Z_1^\perp)$ from a series of CST simulations of the dipole RF screen with different series resistors, and Figure 5.42 shows $R_\perp$ and Q_r from fits to resonator impedances. A linear fit to these quantities has a reduced χ^2 of 1×10^{-3}. $R_\perp$ can be estimated from this fit, giving $(500 \pm 180)\,\mathrm{k\Omega\,m^{-1}}$. As well as the standard errors from Q_r and the fit parameters, a 32 % uncertainty has been included to account for the systematic error observed when this technique was applied to the singlet.

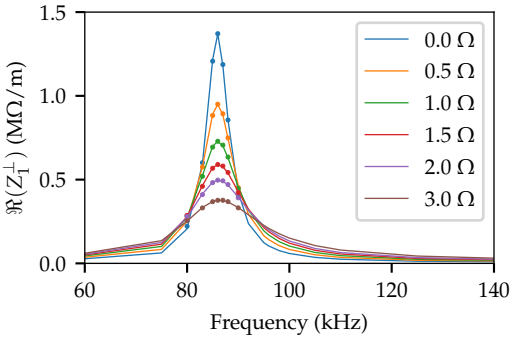


Figure 5.41: Simulated impedances for the dipole RF screen, with a range of series resistors. Points fit to the resonator impedance are overlaid.

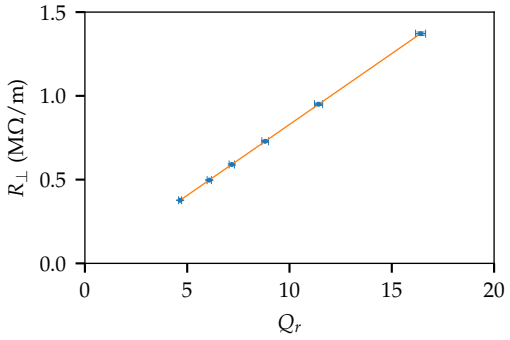


Figure 5.42: Fit values of $R_\perp$ and Q_r for the dipole RF screen with different resistances added in series with the capacitors. Fits are shown in Figure 5.41.

Since Q_r was measured for both the singlet and the dipole RF screens, it is possible to find the effective series resistance that reproduces these two measured results. From the fit between simulated values of Q_r and series resistance, r_{eff}, shown in Figure 5.43 it is possible to estimate an effective series resistance of $(1.9 \pm 0.1)\,\Omega$ for the singlet and $(2.0 \pm 0.4)\,\Omega$ for the dipole. These two measurements are consistent, and give a weighted mean of $r_{\text{eff}} = (1.9 \pm 0.1)\,\Omega$.

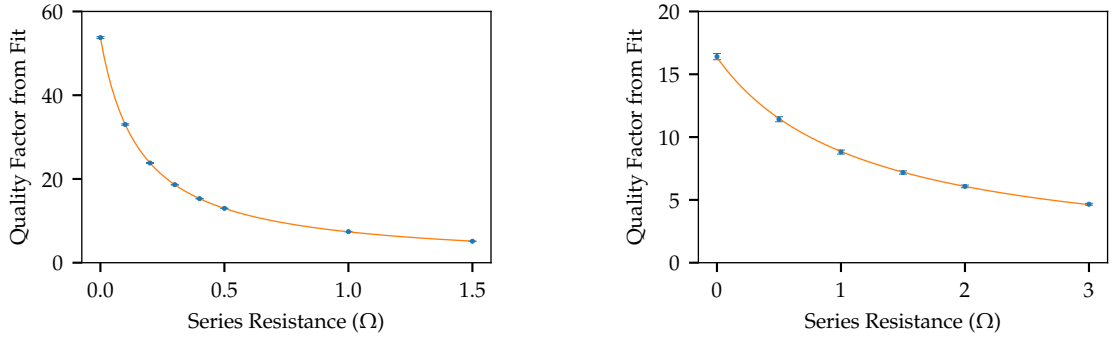


Figure 5.43: Quality factor from fits to a resonator impedance for (a) singlet and (b) dipole RF screens, with a range of series resistors. Fits have reduced χ^2 of (a) 0.42 and (b) 0.12.

Since further experimental data is not expected to become available, unmeasured properties must be estimated from CST simulations. The apparent consistency of r_{eff}

on the singlet and dipole RF screens justifies the approach of estimating $R_\perp$ and Q_r by including the same effective series resistance in their CST models, and producing plots similar to that of Figures 5.43a and 5.40. Fits to these plots were used to estimate Q_r for the effective series resistance, and $R_\perp$ was then estimated for this Q_r. The uncertainty in Q_r was obtained from the uncertainty in r_{eff} and the fit. The uncertainty in $R_\perp$ includes a fitting uncertainty, and 32 % has been added to account for the discrepancy between the measurement and simulation on the singlet. The resulting resonator parameters will be used for the ISIS impedance model, and are summarised in Table 5.8. Refinements such as including the impact of Lorentz-β will be considered in Section 5.7, but this table marks a substantial advance in understanding of transverse instabilities on ISIS.

Table 5.8: Resonator parameters used for ISIS impedance model. * - Assumed

RF Screen	$\frac{\omega_r}{2\pi}$ (kHz)	$R_\perp$ ($\mathrm{k\Omega\,m^{-1}}$)	Q_r	Quantity
Dipole (Module 1)	(82 ± 5)	(500 ± 170)	(6.1 ± 0.7)	10
Doublet (Module 11)	(94 ± 6)	(255 ± 82)	(6.7 ± 0.2)	10*
Singlet (Model 30)	(189 ± 12)	(31.8 ± 0.4)	(4.1 ± 0.1)	10
Octupole (Module 13)	(184 ± 12)	(18 ± 6)	(4.30 ± 0.02)	6
Octupole (Module 9/10)	(162 ± 10)	(14 ± 5)	(4.66 ± 0.02)	6

5.3.5.3 Resistive Wall Impedance

The resistive-wall and indirect space-charge impedances of the RF screens must be included in the model in addition to the resonator impedance. The resistive-wall part will be described here, whilst the indirect space-charge contributions of several structures will be described in Section 5.6.

Since all the RF screens show a thick-resistive-wall type impedance at higher frequencies, a single resistive-wall element will be included to account for all the screens. Figure 5.44 shows the sum of all simulated RF screens with no series resistance, interpolated onto a single frequency axis. Above 1 MHz this sum follows a $\frac{1}{\sqrt{\omega}}$ relationship, so a single resistive-wall impedance will be applied for all RF screens collectively. A

stainless-steel vacuum vessel, with conductivity of $1.33 \times 10^6\,\mathrm{S\,m^{-1}}$and an inner radius of $50\,\mathrm{mm}$ was assumed and a least-squares fit performed that gave a Yokoya factor of 0.93. This resistive-wall impedance, which will be taken to apply for all the RF screens, is overlaid in Figure 5.44

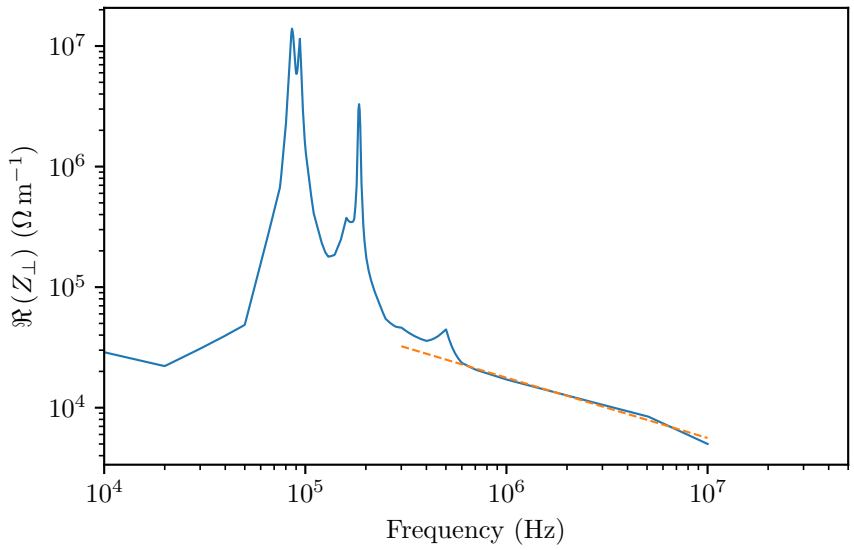


Figure 5.44: Sum of $Z_1^\perp(\omega)$ for simulated RF screens, interpolated onto a single frequency axis. A thick-resistive wall impedance has also been overlaid above 300 kHz.

5.4 RF Cavities

An $h = 2$ ISIS RF cavity is shown schematically in Figure 5.45. Like the second harmonic ($h = 4$) cavities, they are ferrite-loaded, shorted coaxial resonators and their combined length is approximately 15% of the machine's circumference. As the second most-common repeating structure after the RF-screens, it is necessary to include their contribution to the resistive-wall impedance. Whilst they can sustain higher-order modes, simulations on cavities of a similar construction and resonant frequency to those at ISIS, have shown that they primarily occur above 10 MHz and are thus outside the frequency range of interest [196]. Only the resistive-wall contribution of the RF cavities will be considered.

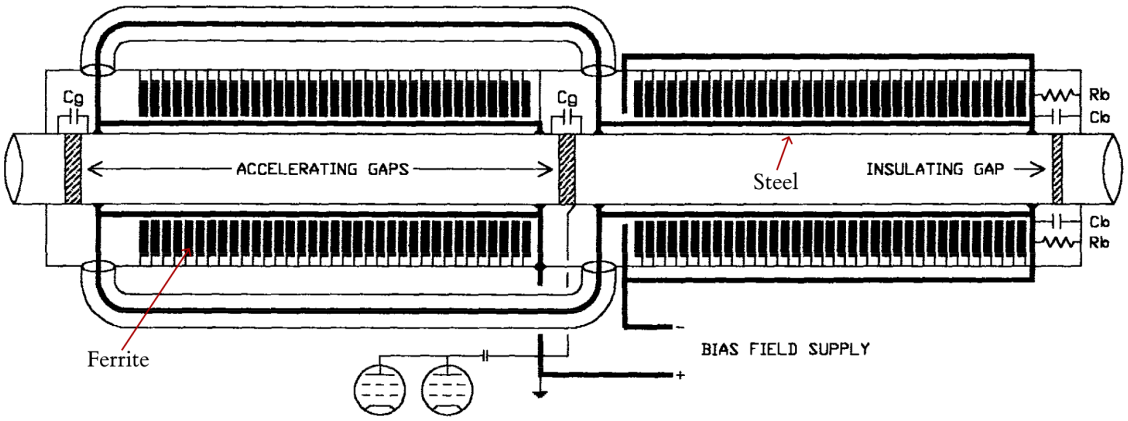


Figure 5.45: Schematic of an ISIS fundamental RF cavity [81] with labelled ferrite and steel.

The vacuum vessel is made from a 2 mm thick, BS. 4360 GRADE 43A mild steel cylindrical pipe, with an inner diameter of 224 mm. Mild steel was chosen to shield the beam from stray magnetic-fields produced by the cavity bias-current. Whilst properties of the mild steel are not well known, it is assumed that they do not depart significantly from published values of a more general mild steel [190, pp. 12–119]. Its conductivity will be taken to be that of plain carbon steel, at $5.5\times10^{6}\,\mathrm{S\,m^{-1}}$ [190, pp. 12–204]. Whilst the initial permeability of mild steel is around 800 at low frequencies, it is expected to be significantly reduced above 100 kHz, as was the case for the laminated magnet yokes described in Section 5.3.1.3. A range of values were investigated to understand the significance of the initial permeability.

The steel vacuum vessel is plated with nickel to prevent rusting. The thickness of this plating is between 10 and 20 µm, so a range of parameters were investigated. Since the Nickel was electroplated, it is expected to have a low phosphorous content and have properties similar to that of pure nickel [197]. The conductivity of this layer will be taken to be that of commercial grade nickel at $1\times10^{7}\,\mathrm{S\,m^{-1}}$ [190, pp. 12–204]. Although nickel is a non-linear magnetic material, its magnetic permeability has been derived as a function of frequency by compiling several different published results [198]; the assumed permeability is shown in Figure 5.46 as well as the polynomial fit used in calculations.

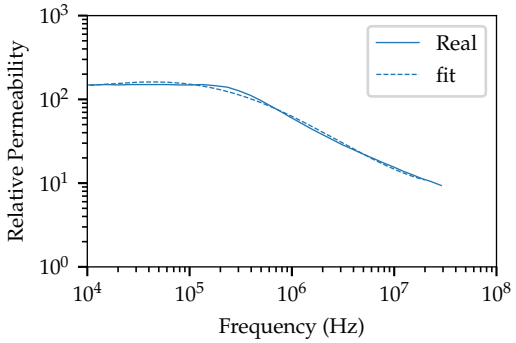


Figure 5.46: Assumed relative permeability of nickel [198] and a polynomial fit.

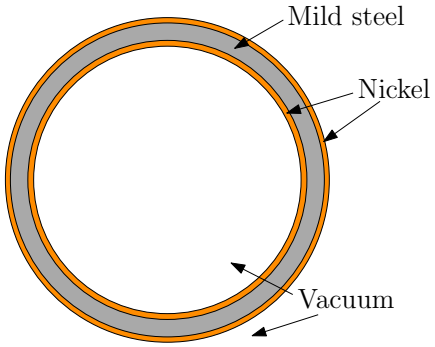
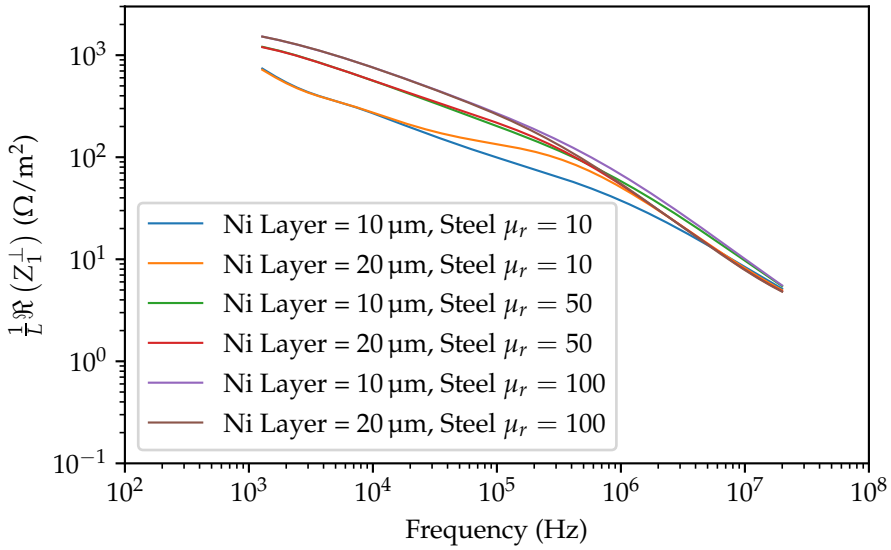


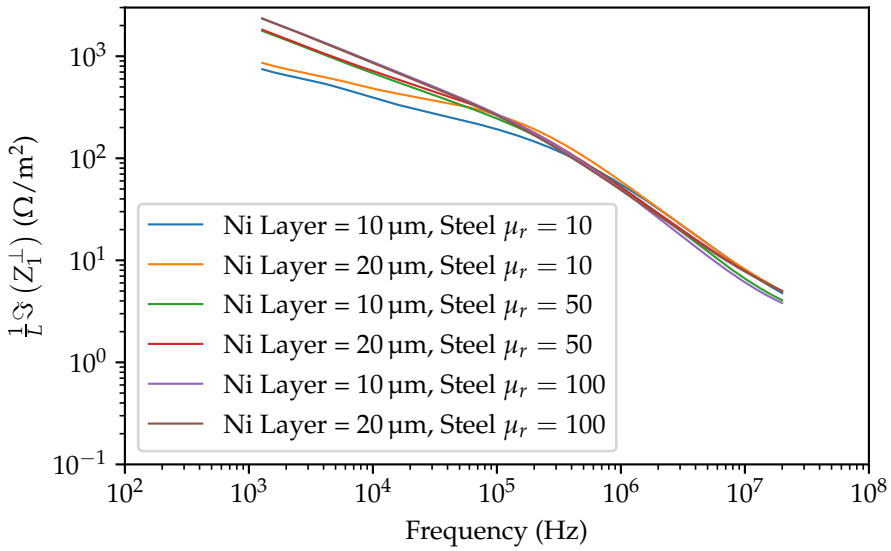
Figure 5.47: Material layers of the RF cavity calculation for RWAL.

A resistive-wall contribution from RF cavities has been estimated with RWAL. A cross-sectional schematic is shown in Figure 5.47. Comparing this with Figure 5.45, it is clear that the bias-current conductors and ferrite have not been included in this model. This is because the skin-depth in mild-steel at 100 kHz is $\approx 0.7\,\mathrm{mm}$ assuming $\mu_r = 1$, whilst the thickness of this layer is 2 mm. As such, structures outside the mild-steel layer can reasonably be neglected in the frequency range of interest. The outermost layer is taken to be the air-gap separating the nickel-plated vacuum vessel from the bias-current conductors.

The real and imaginary parts of $Z_1^\perp$ computed by RWAL with $\beta \approx 1$ are shown in Figure 5.48. As the frequency increases and the skin-depth in the innermost nickel layer reduces, the four results appear to converge. Around 100 kHz the predictions differ significantly, although they remain the same order-of-magnitude. Without a detailed characterisation of the mild-steel vacuum vessels, a worst-case scenario will be assumed. This will take the result with the largest real impedance at the baseband frequency. This is the case with a 10 µm thick nickel layer and a steel layer with $\mu_r = 100$.



(a)



(b)

Figure 5.48: Real (a) and imaginary (b) part of the resistive-wall impedance for an RF cavity per unit length for a range of possible nickel and steel parameters.

5.5 Extraction Kickers

5.5.1 Description of Extraction Kicker System

Extraction from the ISIS synchrotron is realised by three window-frame, ferrite-loaded pulsed kicker magnets and an extraction septum. The three magnets differ in both their length and transverse dimensions, and have identifiers EK1, EK2 and EK3; these are contained within a single vacuum vessel, as indicated Figure 5.49. This figure shows the kickers in their original configuration, but the feeding cables are now connected at the sides; these are the red cables in Figure 5.50. Figure 5.51 indicates kickers dimensions, which are listed in Table 5.9.

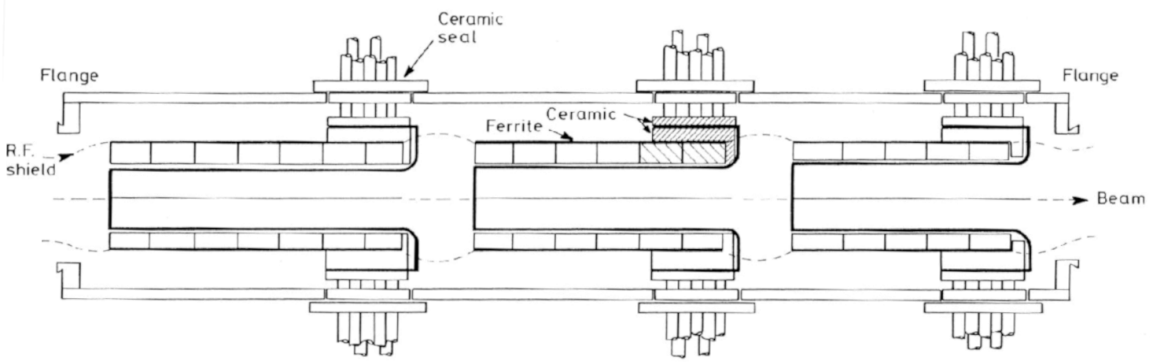


Figure 5.49: Schematic layout of the ISIS vertical extraction kickers viewed from the side, inside a single vacuum vessel [199]. Kicker identifiers from left to right are EK1, EK2 and EK3.

Table 5.9: Extraction kicker dimensions, for variables shown in Figure 5.51.

Kicker	w_k (mm)	h_k (mm)	L_k (mm)
EK1	181	142	714.5
EK2	173	160	614.5
EK3	168	175	539.5

The low-frequency vertical driving impedance of a vertical kicker magnet can be dominated by effects associated with the external kicker circuit, and not just the ferrite and copper assembly [102]. This crucially includes the long coaxial cables shown in

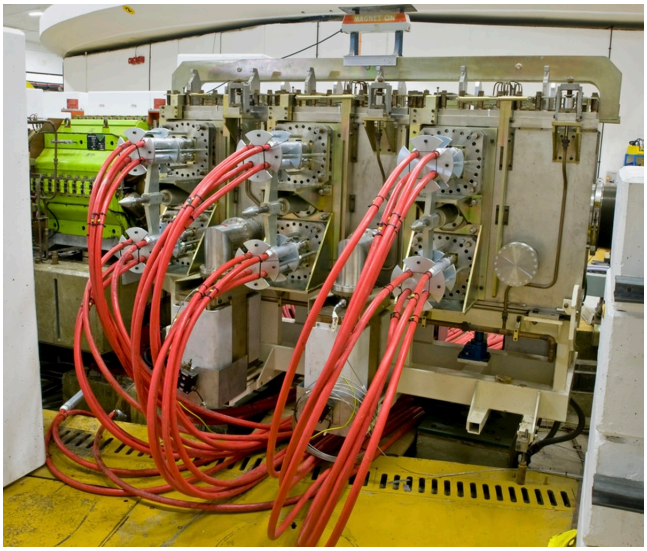


Figure 5.50: Photograph of the ISIS extraction kicker vacuum vessel, with cables connected from the sides [186].

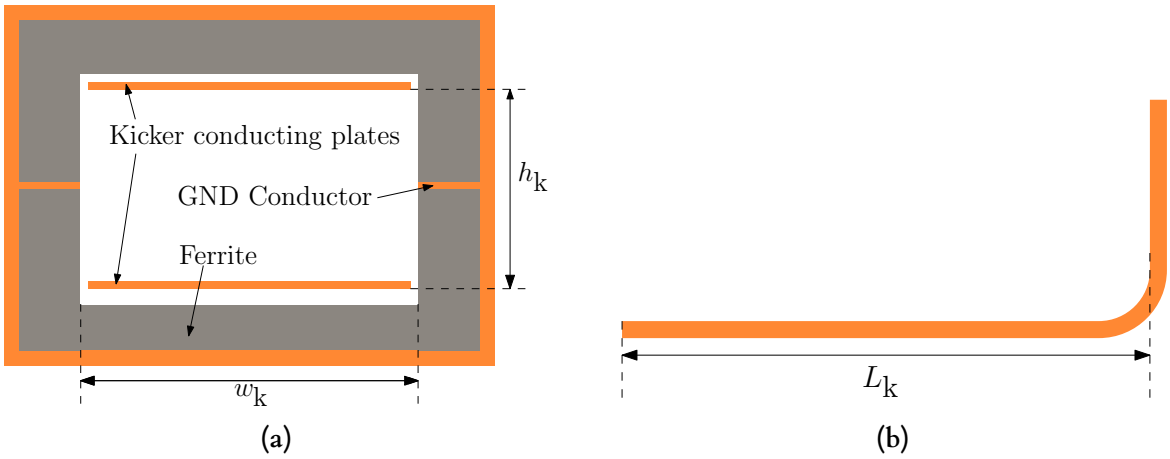


Figure 5.51: Transverse cross-section of an extraction kicker (a). Side-view of a single conducting plate for an extraction kicker. This conductor is typically between 1.2 and 1.6 mm thick (b).

Figure 5.52, and everything to the right of the thyratron at the centre of the figure, which isolates the kickers from the pulse-forming-network until the beam is extracted. For ISIS, the circuit therefore includes 8 parallel, 50 Ω coaxial cables per-kicker-plate, with a $\frac{1}{8} \times 50\,\Omega = 6.25\,\Omega$ terminating resistor at one end and a short on the other. Similar kicker configurations are used at other RCS-based facilities, although usually without the terminating resistors [60, 148].

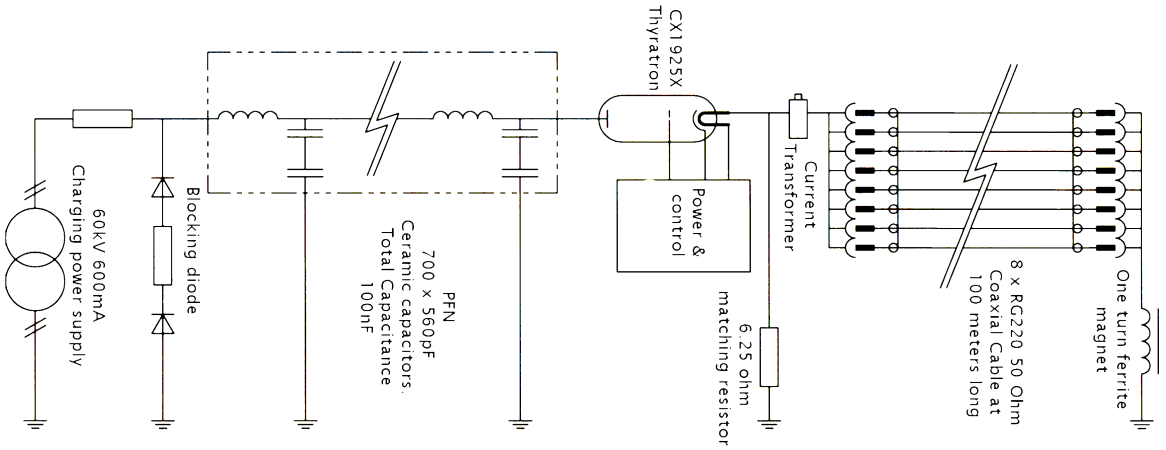


Figure 5.52: Schematic of the extraction kicker circuit, including the pulse-forming network to the left, thyratron and terminating resistor near the centre and cables and kicker to the right [200].

As mentioned in Appendix A, resistors were included in the kicker circuit to terminate beam-induced voltages on the kicker supply cables. They should damp the resonances responsible for large transverse impedances on kickers [102, 201], and also dissipate half of the power in the kicker's pulse forming network without it ever reaching the kicker magnet. The resistors must therefore be suitable for high-power operation, and so are constructed from a $\sim 1\,\mathrm{m}$ long assembly of ceramic resistors, embedded in oil and stored in a grounded tank; see Figure 5.53.

5.5.2 Probe Coil Measurements of Extraction Kicker Impedance

Since the extract kicker can support low-frequency resonances in principle, and similar effects are thought to drive instabilities at other facilities [102, 202, 201], they were considered to be of particular interest for this study. To optimise usage of the available time, it was decided that detailed simulations of the kicker would only be performed if measurements revealed impedances considered capable of driving the $2\,\mathrm{ms}$ head-tail instability. Probe loop measurements were performed on a spare EK1 kicker-magnet, with the associated cables and terminating resistors. Measurements were performed with the single-turn probe loop shown in Figure 5.54 as well as a three-turn probe loop

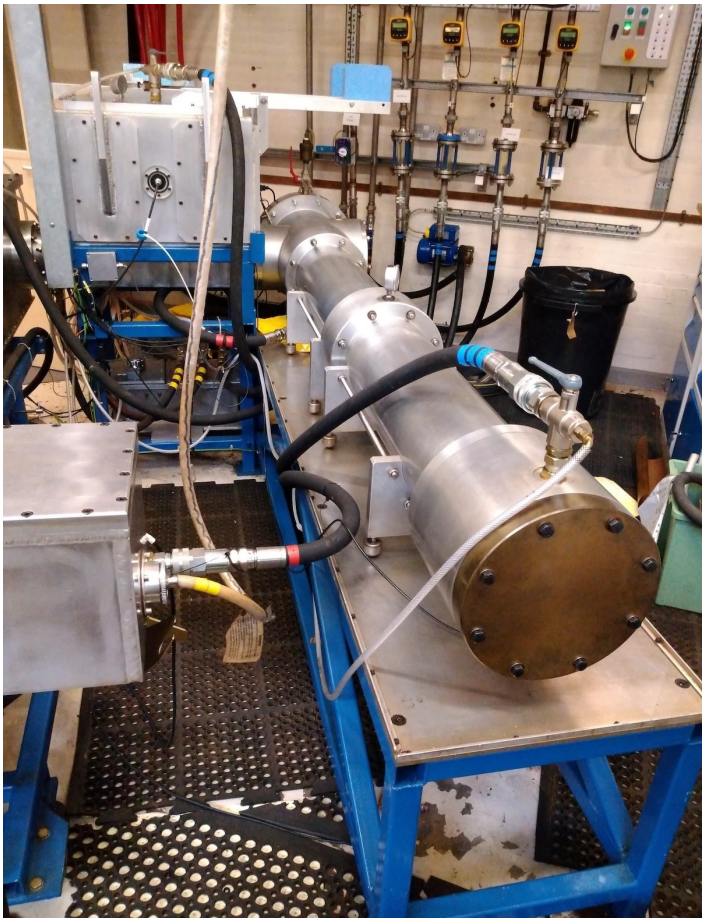


Figure 5.53: Photograph of a grounded tank which houses a terminating resistor for the ISIS extraction kicker system.

of a similar construction. Both an IET 7600+ Precision LCR meter and a Keysight E5071C VNA were used to measure the probe loop resistance, with the experimental set-ups in Figure 5.55.

A full characterisation of $\mathrm{Re}\left(Z_1^{\perp}(\omega)\right)$ requires a DUT measurement with the probe loop inserted in the kicker and a reference measurement taken in free space. The mechanical changes required to make these measurements with the same probe loop can be a significant source of systematic error [203]. To avoid making these mechanical changes, reference measurements were performed with the probe loop inserted, and the kicker bus-bars disconnected from the external circuit and shorted to the vacuum vessel by short conducting leads. The kicker's resistive-wall impedance contribution

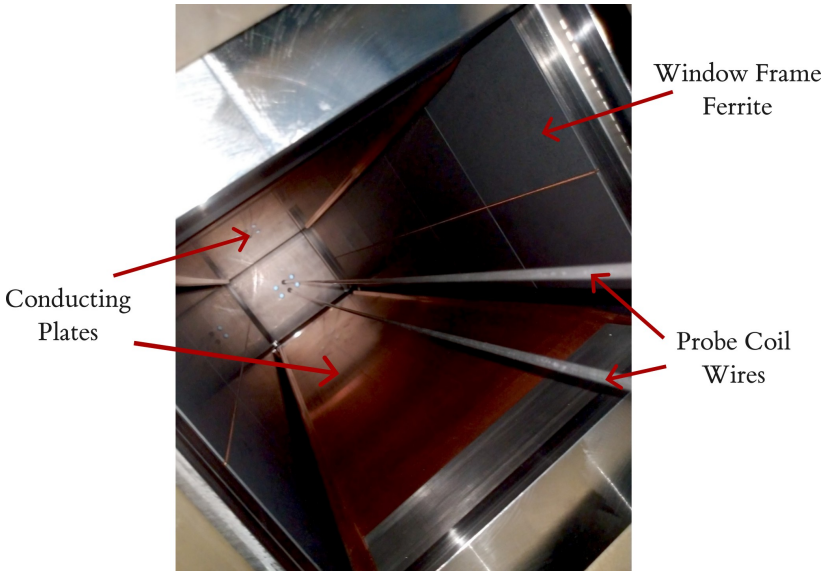


Figure 5.54: Photograph of the spare EK1 kicker magnet, with probe loop wires extending between apertures.

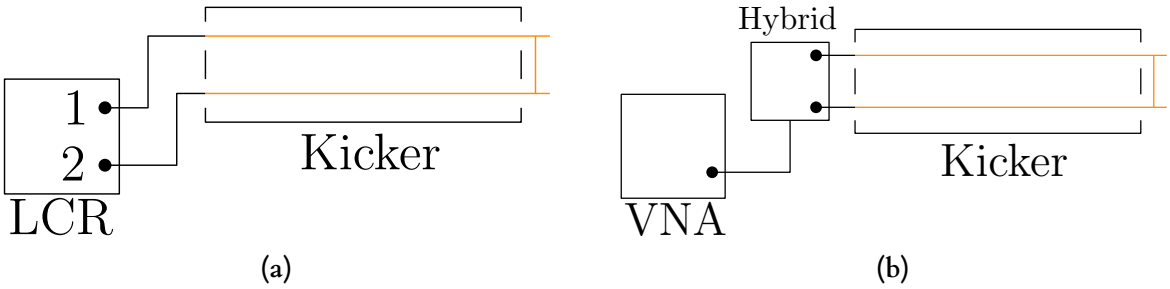


Figure 5.55: Schematic of the LCR (a) and VNA (b) experimental set-ups for the kicker measurements.

was present in both the DUT and REF measurements, so that their difference leaves only impedances associated with the external kicker circuit. These are the primary impedances of interest, because they include the low frequency resonances associated with the kicker cables. Since the overall kicker length represents only around 2 % of the ISIS circumference, their resistive wall impedance will be approximated without a detailed characterisation.

5.5.2.1 Measurement without Terminating Resistors

$Z_1^\perp$ was first measured without terminating resistors, both to verify the measurement set-up and to ascertain the impact of including the resistors. Figure 5.56 shows $Z_1^\perp(\omega)$ with the cables disconnected from the thyratrons and terminating resistors. The results are weighted means of three distinct measurements, each of which consisted of 10 repeat DUT and REF measurements. The first four resonant frequencies were identified from maxima in the FFT magnitude as (439 ± 2) kHz, (1.36 ± 0.01) MHz, (2.32 ± 0.02) MHz and (3.32 ± 0.02) MHz.

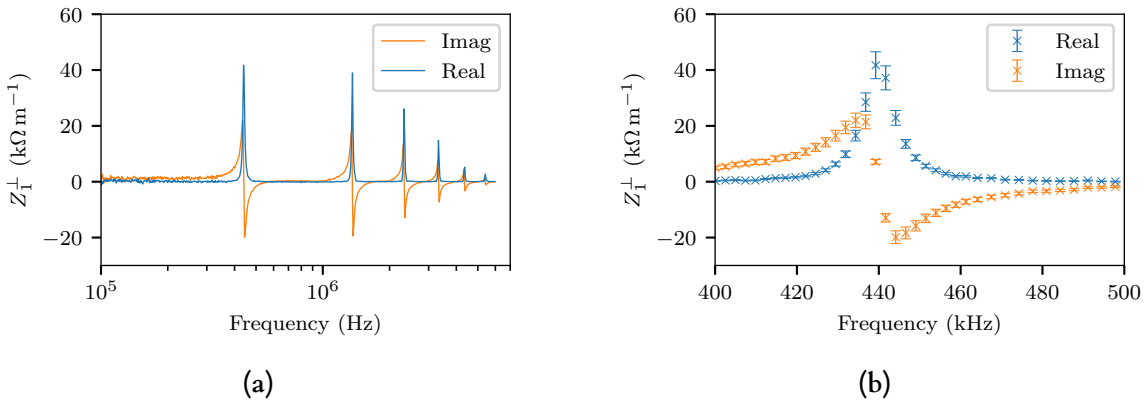


Figure 5.56: $Z_1^\perp(\omega)$ measured by a one-turn loop in the spare EK1 kicker, with grounded busbars as a reference and the cables disconnected from the terminating resistors. Several resonances are observed in the bandwidth of (a) and errorbars are not shown for clarity. Only the first resonance is shown in (b), where errorbars are the standard error on the mean of three distinct measurements.

Without simulated results to compare to, the measurement set-up was verified by comparing the observed resonant frequencies with theoretical predictions for the case with an open-circuit termination. Since phase advance is expected to be much larger in the cables than in the kicker itself, the first resonance was expected at

$$f_{\mathrm{k},1} = \frac{v}{4L_{\mathrm{cable}}}, \tag{5.11}$$

where v is the phase velocity in the cable and L_{cable} is the length of the kicker cables [148].

The cables for the spare kicker are the same length as those used in the operational system. They are 50 Ω, RG220 coaxial cables with a nominal velocity factor of 0.66. They are constructed from a 6.6 mm diameter, copper inner conductor, a 23.1 mm diameter LDPE+graphite insulator and a braided copper outer conductor. The length of two cables was measured with an AEA E20/20 time-domain reflectometer (TDR). An RG58 test lead was used to connect the RG220 cable and crocodile clips were used with an adaptor to avoid scratching the surface of the high-voltage connectors; see Figure 5.57. TDR results for the test-lead on its own and with the RG220 cables connected are shown in Figure 5.58. By taking the end of the cable as the point where the measured impedance is 10 % above the nominal cable impedance, and assuming a 5 % uncertainty of the velocity factor gives the length of the RG220 cable was estimated at (91 ± 5) m. The expected resonant frequency for this length, (542 ± 40) kHz, is 24 % larger than observed, and not consistent with the measured frequencies.

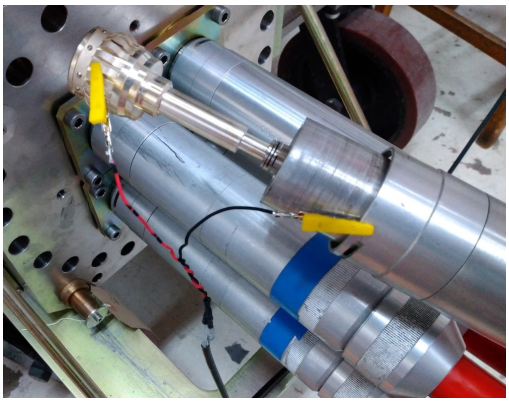


Figure 5.57: Photograph of the connections for TDR measurements. An adaptor and crocodile clips were used to avoid scratching the HV connector.

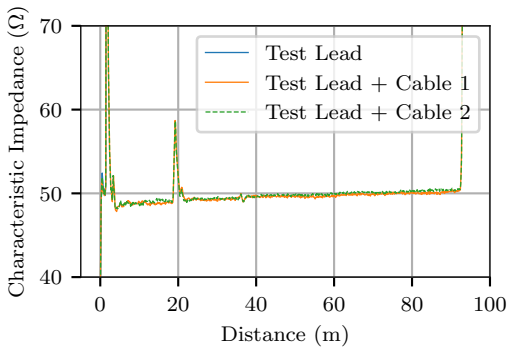


Figure 5.58: TDR results for two kicker cables and one only the test lead.

Equation (5.11) neglects mismatches in the characteristic impedance of the kicker and the cables, as well as phase advance on the kicker bus bars. In order to include these, transmission line parameters for the kicker were obtained from a CST microwave simulation; see Figure 5.59. This applied a differential excitation on a simplified kicker

geometry, which predicted a quasi-TEM mode with a characteristic impedance of 83 Ω and a phase velocity of $0.28c$. The kicker circuit up to the thyratron was simulated with the Quite Universal Circuit Simulator (QUCS) [204], as shown in Figure 5.60. This included a section of coax to represent the kicker, which had a characteristic impedance of 41.6 Ω and a phase velocity of $0.28c$. Resonant frequencies can be seen in Figure 5.61, at 482 kHz, 1.46 MHz, 2.46 MHz and 3.47 MHz, which are all within 10 % of the measured resonant frequencies. The remaining discrepancy could reasonably be attributed to imperfect knowledge of the kicker material properties or neglecting phase advance between the kicker connectors and the bus bars. Since resonances are observed at the expected frequencies and peaks in $\mathrm{Re}(Z_1^{\perp})$ are of the same order-of-magnitude as measurements of similar kickers [60, 148], the measurement set-up was considered verified. The impedance of the operational kicker configuration with terminating resistors will now be investigated.

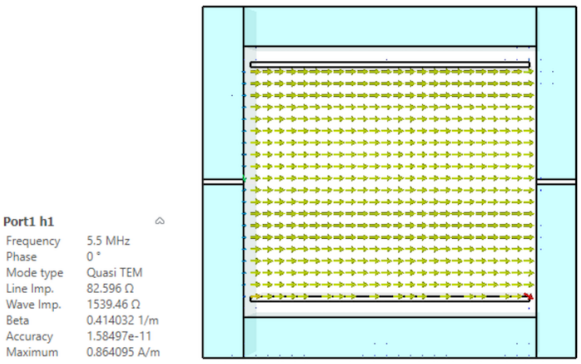


Figure 5.59: Quasi-TEM mode on an idealised CST simulation of the extraction kicker. Mode properties are listed, and arrows indicate the H field.

5.5.2.2 Measurement with Terminating Resistors

The impedance of the extraction kickers without terminating resistors has verified the measurement set-up, but in practice the matched resistors will damp the resonances shown in Figure 5.56a. To find the impedance contribution of the kickers in ISIS, the cables feeding the kicker were connected to the terminating resistors such as the one in

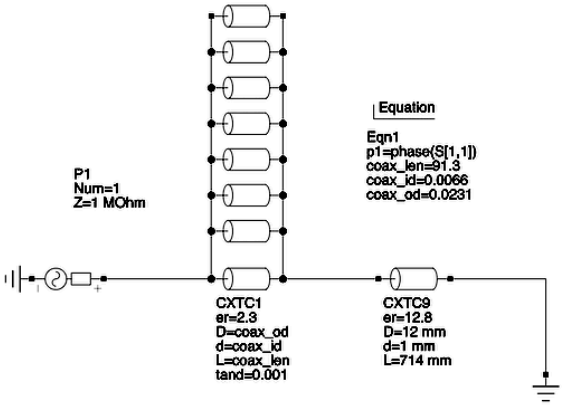


Figure 5.60: Schematic kicker circuit simulation. Eight 50 Ω cables in parallel are the feeder cables, and the one coax represents one side of the kicker magnet.

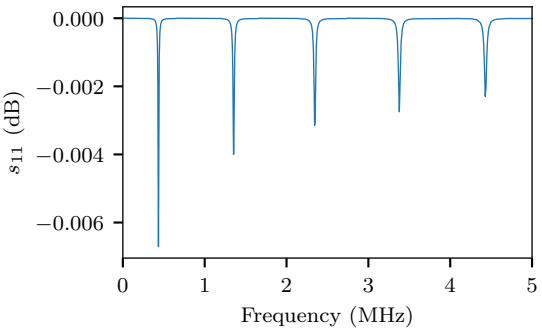


Figure 5.61: Scattering parameter from the QUCS circuit in Figure 5.60. Resonances are indicated by a narrowband minima in S_{11}.

Figure 5.53. The resulting $Z_1^\perp$ is shown in Figure 5.62, which should be compared with Figure 5.56 to see the impact of the resistors. There is order-of-magnitude reduction in the peaks of $\mathrm{Re}\,(Z_1^\perp)$, and the resonant frequencies have increased, with the lowest frequency resonance now at $\sim$ 800 kHz.

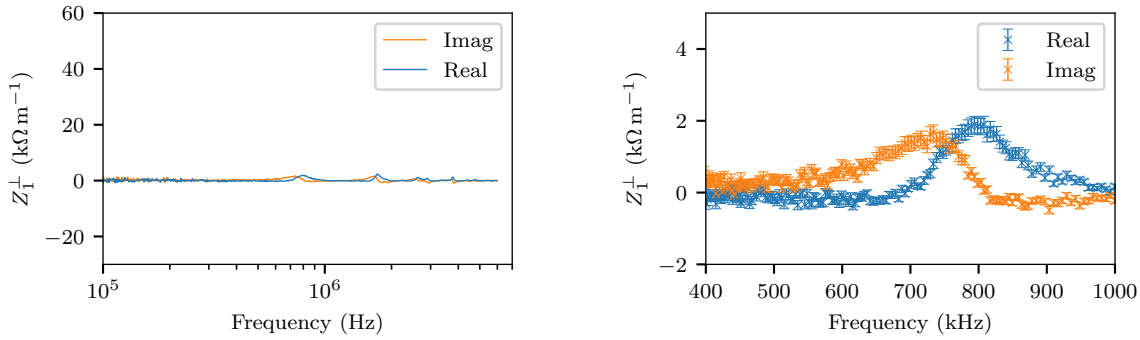
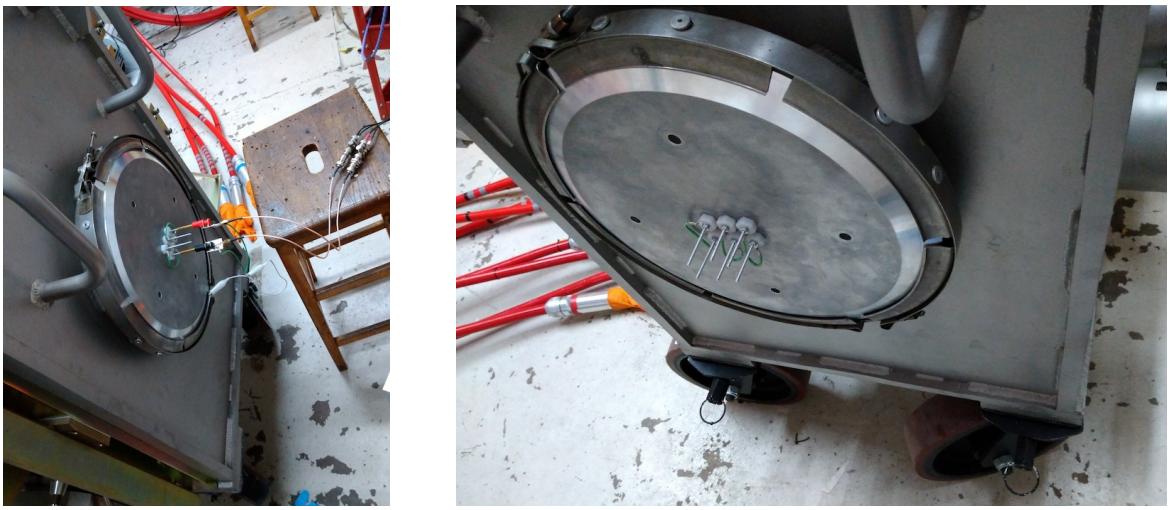


Figure 5.62: $Z_1^\perp(\omega)$ measured by a one-turn loop in the spare EK1 kicker, with grounded busbars as a reference and the cables connected to the terminating resistors. Several resonances are observed in the bandwidth of (a) and error bars are not shown for clarity. The vertical scale is the same as in Figure 5.56a. Only the first resonance is shown in (b), where errorbars are the standard error on the mean of three distinct measurements.

To verify that systematic errors due to resonances on the probe coil were negligible, impedance measurements were also made with a three-turn probe coil. It was constructed by adding four additional aluminium rods and connecting them at the ends using short connecting wires and nuts; see Figure 5.63. Figure 5.64 shows the first two resonant impedances for both probe coils with the termination resistors connected. Three-turn measurements are the weighted means of two distinct measurements, each consisting of ten REF and ten DUT measurements. In both cases, the real part of these impedances are consistent at their maxima, and also are largely consistent throughout the plotted range. The imaginary part shows a discrepancy above around 800 kHz, which was found to be due to an offset present in one of the measurements. This was likely due to a lack of repeatability in the electrical connections or atmospheric conditions and does not affect the conclusion that a resonator impedance exists at around 800 kHz. To avoid the impact of such offsets, resonator properties were obtained from the real part.



(a) (b)

Figure 5.63: Photographs showing both ends of the three-turn probe coil. The aluminium rods which make up the probe are held in position by insulating vented screws, and connections between them made by short conducting leads.

Repeat measurements were also made with an LCR meter to identify any significant systematic errors with the VNA set-up. Figure 5.65 shows a comparison of results

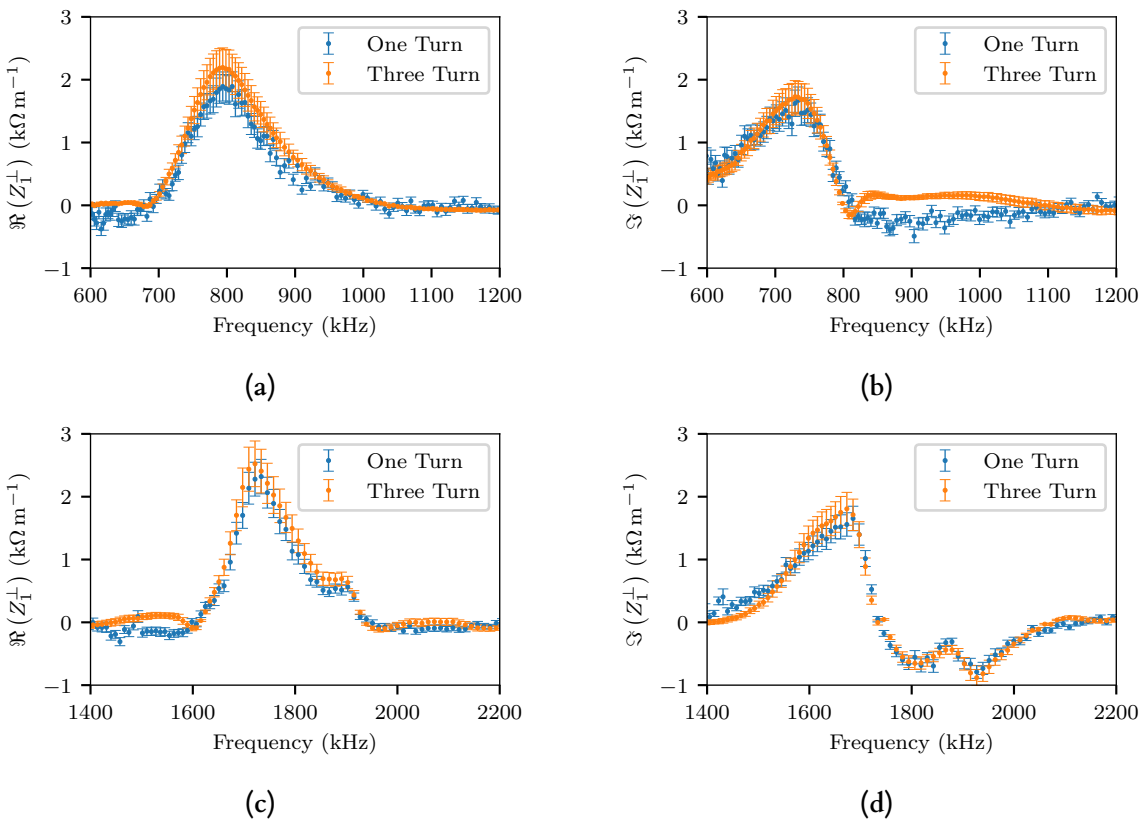


Figure 5.64: $Z_1^\perp$ as measured by a VNA with one and three-turn probe coils. The first and second resonance's real (a), (c) and imaginary (b), (d) parts are shown.

obtained with both devices and both probe coils. The real parts are mostly consistent in the plotted range, and are consistent close to the peak. Although the distribution of the imaginary parts are all similar, the three results show systematic offsets. These are also thought to be associated with a lack of repeatability in how the bus bars were shorted to the body or changes in atmospheric conditions. Nevertheless, from the consistency in the real part of $Z_1^\perp$, the VNA results are considered validated, and conclusions can now be drawn.

Resonator parameters were estimated from the data shown in Figure 5.62 by fitting $\sim 50\,\mathrm{kHz}$ either side of the peaks in $\mathrm{Re}(Z_1^\perp)$ to a resonator impedance. The first resonant frequency has been increased to $(799 \pm 2)\,\mathrm{kHz}$ from $\sim 400\,\mathrm{kHz}$ without resistors, which is presumably due to the parasitic capacitance and inductance of the terminating

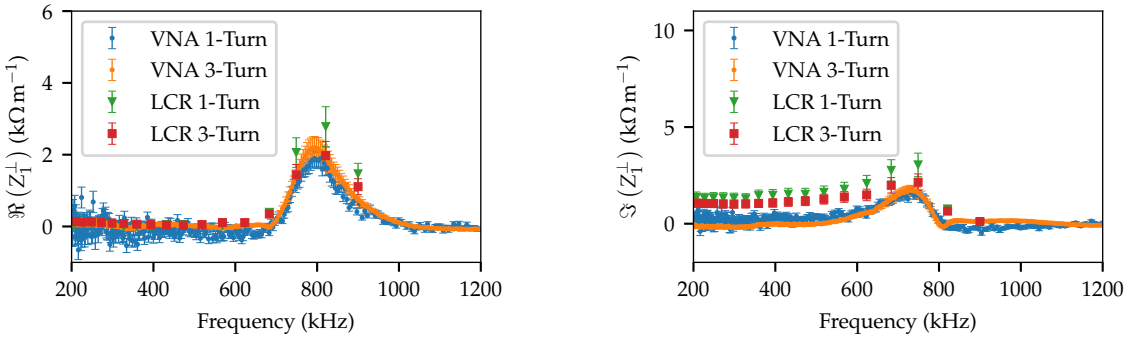


Figure 5.65: Comparison of VNA and LCR measurements of real (a) and imaginary (b) parts of $Z_1^\perp$ for the first resonance with the terminating resistors connected.

resistors. The first resonance is therefore above the lowest ($\sim 100\,\mathrm{kHz}$) betatron sideband frequency for the full $10\,\mathrm{ms}$ acceleration cycle. It also has $R_\perp = (1.8 \pm 0.1)\,\mathrm{k\Omega\,m^{-1}}$, which can be seen by eye to be more than an order-of-magnitude improvement compared to the case without terminating resistors and lower than the resistive-wall impedance of the RF screens in Figure 5.44 at this frequency; this resonance also has $Q_r = (6.7 \pm 0.7)$. The second peak has a resonant frequency of $(1731 \pm 4)\,\mathrm{kHz}$, $R_\perp = (2.3 \pm 0.2)\,\mathrm{k\Omega\,m^{-1}}$ and $Q = (15 \pm 3)$. Higher frequency resonances have lower amplitudes and will not be considered further as they are not expected to significantly affect beam stability.

5.6 Indirect Space Charge

Studies of coherent beam instabilities on ISIS have not directly included an indirect space-charge impedance, although direct space-charge contributions have been investigated with tracking simulations [80]. This was justified because simplified theories conclude that instability growth rates depend only on the real part of the transverse impedance [89], and including indirect space-charge can lead to computational difficulties. Instead, these studies have used the measured coherent tune in-place of the single-particle betatron tune. In other studies [205], the indirect space-charge is included explicitly.

In this study an indirect space-charge impedance will be specified, and included in the impedance model unless stated explicitly. The specification of this impedance will use Equation (3.29), and follow the definition of the resistive-wall impedance: the RF screens will contribute $91.06\,\mathrm{m}$ of $50\,\mathrm{mm}$ radius pipe with a Yokoya factor of 0.93, the RF cavities will contribute $25.12\,\mathrm{m}$ of $100\,\mathrm{mm}$ radius circular pipe, and the remaining $\sim 47.12\,\mathrm{m}$ considered to be a $50\,\mathrm{mm}$ radius pipe with a Yokoya factor of 1.

5.7 ISIS Vertical Driving Impedance Model

5.7.1 Lorentz Beta Dependence

CST simulations of the RF screens and the probe loop impedance measurements, return $\mathrm{Re}\left(Z_1^{\perp}\right)$ for $\beta = 1$. Since ISIS accelerates from $\beta = 0.37$ to 0.84, the dependence of the RF screen resonator impedances which dominate the low-frequency model cannot be neglected. Since the dependence cannot be investigated using the tools introduced so far, a relationship will be assumed based on the behaviour of similar transverse impedances.

Some common transverse impedances, such the classical resistive-wall impedance are linearly proportional to β [135]. This has led to conventions where the transverse impedance is divided by β, so that impedances can be presented without a β dependence [102]. Resonator-type impedances, such as those on kicker magnets, have been found to have a roughly linear dependence on β [206]. It will therefore be assumed that all resonator impedances presented so far are linearly proportional to β.

5.7.2 Summary of Overall Smooth Focusing Impedance Model

The dominant low frequency transverse driving impedances are contributed by the RF screens inside the AC magnets. Due to the significance of this contribution and the complicated steps required to obtain an accurate model from CST, this part of the overall impedance model has been described separately in Section 5.3.5. In summary, each of the most common RF-screens will be modelled as resonator impedances with

parameters listed in Table 5.8, and a single resistive-wall impedance will be defined for the combination of all RF screens, using their combined length of $91.06\,\mathrm{m}$.

The RF cavities are considered only to contribute a resistive-wall type impedance. They will be included by increasing the length of the existing resistive-wall impedance to $116.18\,\mathrm{m}$ and updating the Yokoya factor to 0.81. This updated factor was obtained by fitting a thick resistive wall impedance to the sum of the RF-screen's resistive-wall impedance and the RF cavity impedance between $100\,\mathrm{kHz}$ and $10\,\mathrm{MHz}$. Residuals for the real part on the order of $100\,\Omega\,\mathrm{m}^{-1}$, or less than $10\,\%$ over the whole frequency range. The remaining $47.12\,\mathrm{m}$ will be modelled as circular cross-section, stainless steel pipe with an inside radius of $5\,\mathrm{cm}$.

Measurements on the EK1 extraction kicker demonstrated that the termination resistors effectively damp resonances on the kicker cables. Smaller resonances were still observed, although at higher frequencies. The impedance of this kicker will therefore be represented by two resonator impedances; higher frequency impedances are not considered in this analysis. Spare EK2 and EK3 kickers are not available for measurements, but given the similarity in their dimensions and construction, these will both be considered identical to EK1. The resulting resonator properties are listed in Table 5.10. The resonant frequencies will vary by as much as $\sim 3\,\%$ from differences in bus-bar length, whilst minor variations in the cross-sectional geometry will affect transmission line parameters. An uncertainty in the resonant frequency of $10\,\%$ is therefore assumed, and considered conservative. To include all three kickers in a single resonator model, $R_\perp$ from the EK1 measurement and its uncertainty will be scaled by three. Q_r and its uncertainty will be taken directly from the EK1 measurements.

Table 5.10: Model extraction kicker resonator impedance parameters.

$\frac{\omega_r}{2\pi}$ (kHz)	$R_\perp$ ($\mathrm{k\Omega\,m^{-1}}$)	Q_r
(0.8 ± 0.1)	(5.4 ± 0.3)	(6.7 ± 0.7)
(1.7 ± 0.2)	(6.9 ± 0.6)	(15.0 ± 3.0)

In the smooth focusing impedance model, all of the impedances discussed will simply be added together. The resulting vertical driving impedance model is shown in Figures 5.66 and 5.67. Given the simple assumed dependence on β, this has been plotted for $\beta = 1$, but the imaginary part has also been plotted for a lower value to demonstrate the impact of indirect space charge.

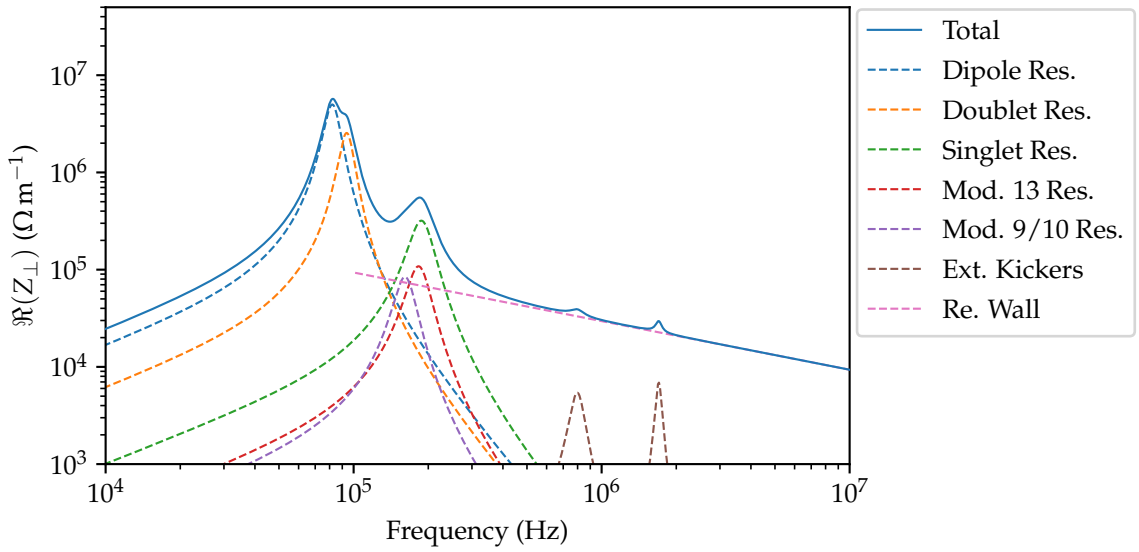


Figure 5.66: Real part of the smooth focusing vertical driving impedance model for $\beta = 1$.

5.7.3 Twiss-β_y Weighted Impedance Model

For machines where smooth focusing is not a good approximation, it is generally accepted that variations in β_y can be partially included in coherent instability calculations by suitably weighting elements of the impedance model [207, 132]. The weighting, which accounts for local variations in β_y at the impedance location, is given by the substitution

$$Z_1^\perp(\omega) \rightarrow \frac{\beta_y(s_0)}{\beta_y^{\mathrm{smooth}}} Z_1^\perp(\omega), \tag{5.12}$$

where s_0 is the location of the impedance source within the ring. Where the physical length of an impedance source is small compared to changes in β_y, s_0 can be uniquely

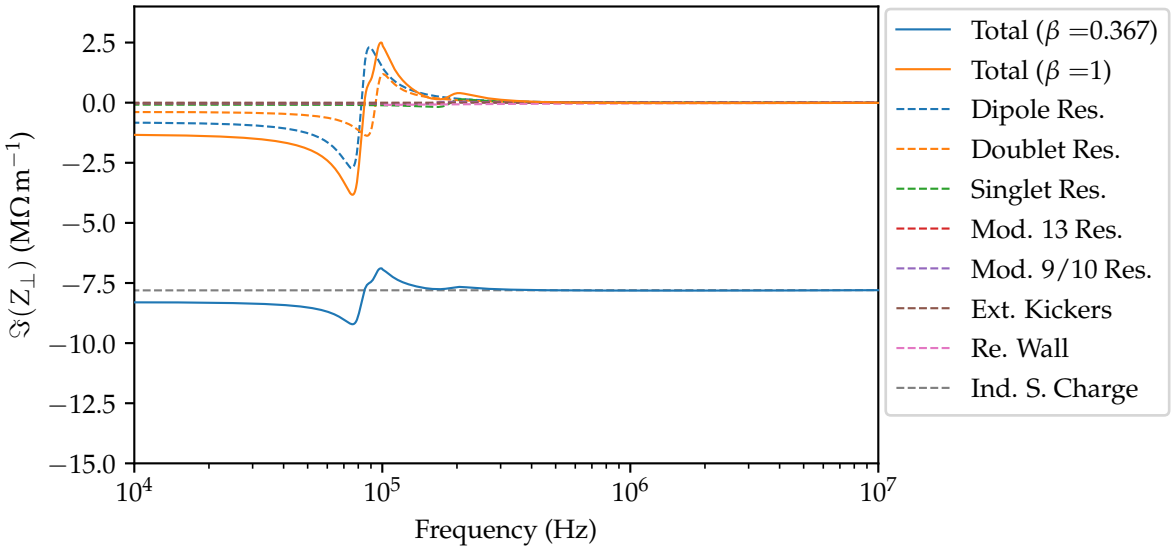


Figure 5.67: Imaginary part of the smooth focusing vertical driving impedance model for $\beta = 1$. Indirect space-charge impedance is zero in that limit, so a total is also shown for a lower β.

defined. This is not the case for ISIS, where β_y varies by as much as a factor of 3 over the length of the RF-screens. Instead, an average value of β_y will be substituted as

$$Z_1^\perp(\omega) \rightarrow \frac{\bar{\beta}_y(s_0)}{\beta_y^{\text{smooth}}} Z_1^\perp(\omega), \tag{5.13}$$

where the average is computed over the length of each impedance source.

$\beta_y(s)$ has been computed from a MADX lattice of the ISIS synchrotron. Its value for a single superperiod is shown in Figure 5.68, and regions used to compute $\bar{\beta}_y(s)$ are highlighted. Weights are listed in Table 5.11. Resistive-wall and indirect space-charge impedance terms are inherently distributed, and won't be weighted. The resulting impedance model is shown in Figures 5.69 and 5.70.

Uncertainties in these scale factors were investigated by assuming an uncertainty in the start and end positions of the RF-screen, each equal to 10 % of the nominal equipment length. In all cases, the resulting uncertainty in the scale factors was computed to be less than 1 %. The uncertainty in the weighting factors is therefore considered negligible.

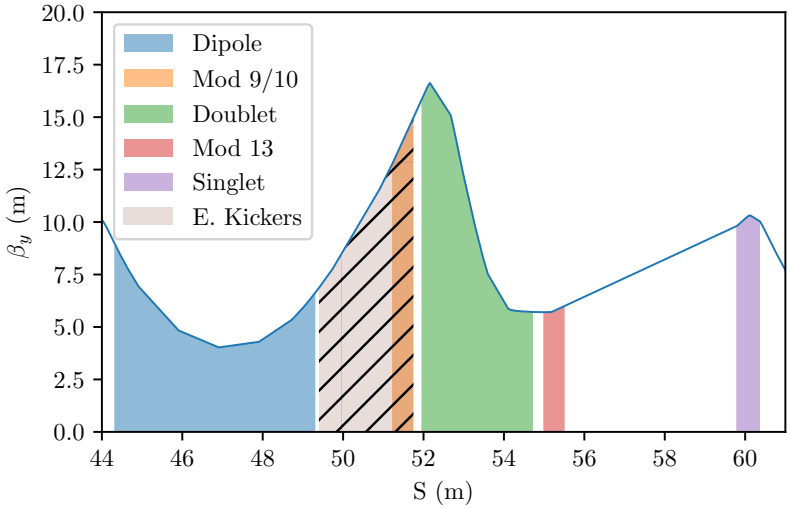


Figure 5.68: β_y for a single superperiod of the ISIS synchrotron, computed by MADX. Regions used to compute and average β_y for different sources of impedance have been highlighted.

Table 5.11: Weights for $Z_1^\perp$ due to variations in β_y, as defined by Equation (5.13).

Impedance Source	$\bar{\beta}_y(s)$ (m)	$Z_1^\perp$ **Weight**
Dipole RF Screen Resonator	5.3	0.8
Doublet RF Screen resonator	10.4	1.5
Singlet RF Screen Resonator	10.1	1.5
Mod 13 RF Screen Resonator	5.8	0.9
Mod 9/10 RF Screen Resonator	13.9	2.0
Extract Kicker Resonators	10.6	1.6

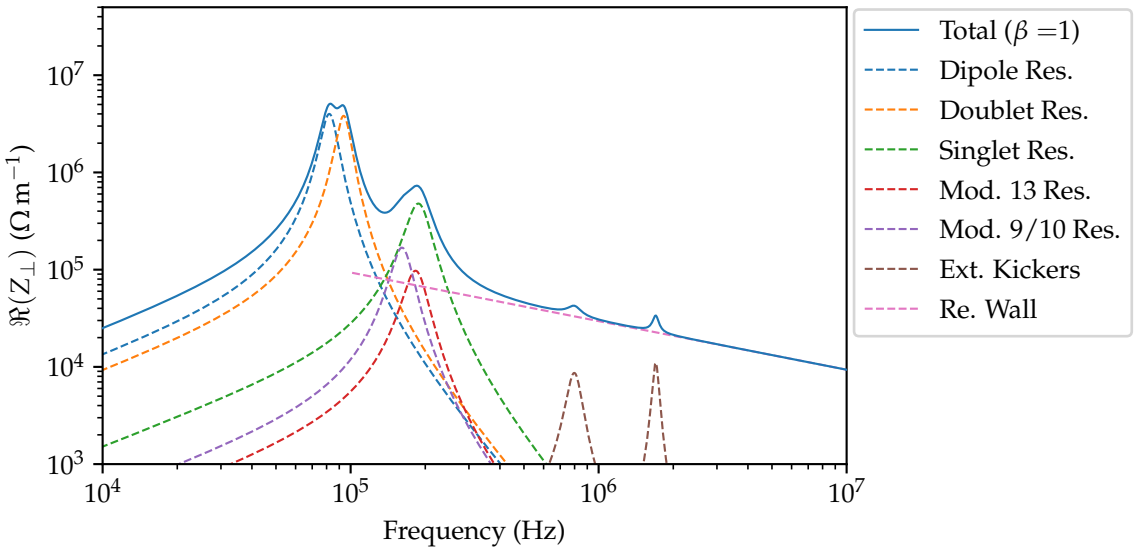


Figure 5.69: Real part of the $\beta = 1$ vertical driving impedance model weighted as per Equation (5.13).

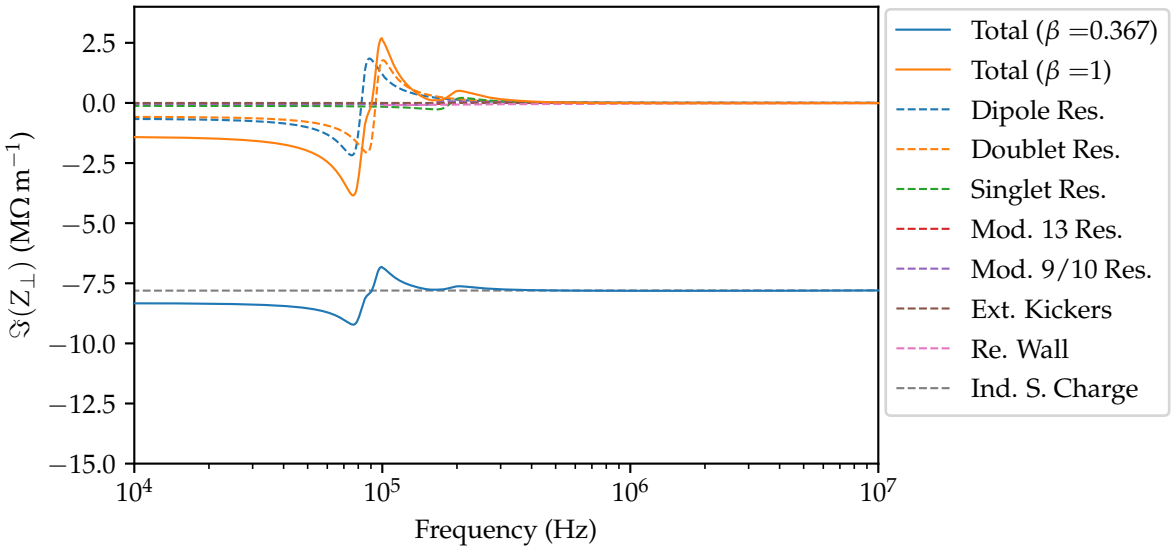


Figure 5.70: Imaginary part of the $\beta = 1$ vertical driving impedance model weighted as per Equation (5.13). Since the indirect space-charge impedance is zero in that limit, a total is also shown for a lower β.

5.8 Summary and Conclusion

The impedance model introduced in this chapter is considered to have satisfied the first objective of Section 1.3, to determine the driving impedance contributions of key machine elements. Resonances identified on the RF-screens at ISIS produce transverse impedances that are up to two orders-of-magnitude larger than impedances reported on equipment such as an unterminated kicker magnet [60]. To understand the scale of these impedances for ISIS, consider that the low-frequency impedance of more modern machines is dominated by the resistive-wall contribution [205]. At ISIS, the dipole RF screens alone are nearly two orders-of-magnitude larger than the resistive-wall contribution of the whole synchrotron. Such large impedances may not be a concern if their frequency is far from unstable betatron sidebands, but on ISIS an unstable sideband passes through the relevant frequencies during the first few ms of the acceleration cycle. Since ISIS operates at its natural chromaticity, head-tail mode spectra are not expected to be small in this frequency range. As such, the resonator impedances identified on the RF-screens are a likely driver of the $2\,\mathrm{ms}$ instability introduced in Chapter 2. This is a key result of this thesis.

Not all devices in the ISIS synchrotron have been characterised. This is primarily because devices which could support low-frequency resonances were prioritised. Future studies should look to add these missing elements into the impedance model. Most notably, there are as many as six RF-screens which appear only once in Figure 5.8 that have not been characterised. If their behaviour is similar to that of the shorter modules 9, 10 or 13, then they could contribute peaks on the order of $100\,\mathrm{k\Omega\,m^{-1}}$ in total, which is larger than contributions from the extract kickers. Being a horizontal kicker, the injection dipole is thought to make only a small contribution to the vertical driving impedance at low frequencies. However the thick ferrite within this magnet could make a considerable contribution above $10\,\mathrm{MHz}$. Such higher frequency contributions could come to dominate the impedance model if the RF-screen resonances were remedied.

Capacitively coupled RF-screens are not only present on ISIS, but are a common feature of high-intensity RCS accelerators [208, 55]. Although intensity limitations have in some cases been overcome by sophisticated beam based mitigation schemes, coherent instabilities can be observed on many of these machines [57]. Given the discovery of resonances on these structures at ISIS, it seems reasonable that similar structures should be investigated for all existing and future RCS-based facilities. This work has shown that these structures can be a major source of low frequency impedance and the resulting instabilities can seriously compromise operational performance.

Soon the fury of the waves and the sight of the sharp rocks announced the approach of death, and death then terrified me, and I used all my skill and intelligence as a man and a sailor to struggle against the wrath of God. But I did so because I was happy, because I had not courted death, because to be cast upon a bed of rocks and seaweed seemed terrible, because I was unwilling that I, a creature made for the service of God, should serve for food to the gulls and ravens.

— A. Dumas, "The Count of Monte Cristo"

6 Coherent Vertical Instabilities on the ISIS Synchrotron

6.1 Introduction

With the impedance model developed in Chapter 5, the theory outlined in Chapter 4 can now be used to predict how instabilities will develop on ISIS. The primary goal of this thesis is to understand the 2 ms vertical instability described in Chapter 2, however for reasons that will be described in the next section, it isn't clear whether the theory outlined in Chapter 4 can be directly applied to ISIS in its operational RCS mode. For that reason, this first experiment described in this chapter will be for a Bunched Storage Ring Mode (BSRM) beam without the $h = 4$ RF cavities and with the intensity reduced by a factor of ~ 10 compared to an operational beam. A comparison of experimental results with predictions will partially satisfy the second thesis objective, which is to determine whether the theory of Chapter 4 without space charge can make partially accurate predictions for ISIS.

The second experiment described in this chapter will allow the second thesis objective to be fully satisfied by comparing predictions and observations of instabilities

in RCS mode. To improve the applicability of the theory, a low gap voltage will be demanded for the $h = 4$ RF cavities. The intensity in this case will be sufficiently high that similar levels of direct space-charge at other machines have reduced the effect of Landau damping [209], so that completely accurate predictions would require direct space-charge to be considered. Since it will not be considered in this thesis, emphasis will be placed on comparing the growth rate's order-of-magnitude, and other general features of the $2\,\mathrm{ms}$ instability. If the newly developed impedance model makes predictions that are correct to within an order-of-magnitude in this experiment, then it is reasonable to conclude that the identified impedances are also responsible for the instability in operational RCS mode.

In earlier studies of beam stability on ISIS, analytical predictions have been made with assumptions beyond those introduced in Chapter 4, such as neglecting the coupling of azimuthal modes [98]. As described in Chapter 2, these earlier calculations predicted instabilities that grew an order of magnitude or more slower than the observed instability. A key aim of this chapter is to apply the more general form of the theory, with the new impedance model developed in Chapter 5.

6.2 Linearised Vlasov Theory for ISIS

6.2.1 Validity of Assumptions

Even in BSRM, particle trajectories in the longitudinal phase space can deviate significantly from the circular trajectories assumed by the theory. This is primarily because of its dual harmonic RF system in its operational RCS mode [210], but it is even true for large amplitude particles in BSRM. Although efforts to incorporate second harmonic cavities into the theory have been made [170, 211], they have not yet been widely adopted and so will not be applied in this thesis. It is argued that the similarity of the instabilities observed on ISIS with and without second harmonic cavities, justifies an analysis based on a single-harmonic theory.

Another important simplification is the neglect of direct space-charge, which is known to impact on the behaviour of coherent instabilities [80, 177, 88]. In its operational RCS mode, ISIS has a space-charge tune spread exceeding $\Delta Q_{\mathrm{SC}} \sim 0.5$ at injection [212] and space-charge parameters, defined as $\Delta Q_{\mathrm{SC}}/\nu_s$ of $\sim 30 - 50$ at 2 ms. Some studies have demonstrated that space charge at this level can impact the behaviour of coherent instabilities [139, 177, 209], but some key features such as unstable tunes and typical growth rates can sometimes still be reasonably well predicted without considering space charge [80, 201, 213]. At the time of writing, work to incorporate direct space-charge into the theoretical framework of coherent instabilities is ongoing, and so the analytical solutions presented will neglect direct space-charge. If the theory is found to be accurate at low intensities, but discrepancies are observed for higher intensities, then this could be evidence of the role that space-charge is playing.

6.2.2 Application of the Theory for ISIS

Chapter 4 outlined several methods for finding approximate solutions to the interaction matrix. Which method is most appropriate depends on the impedance model of a machine. As a high-intensity machine with comparatively large vertical driving impedances, azimuthal-mode coupling cannot reasonably be neglected. A more general solution is required for ISIS, than the simplified theories which assume decoupled azimuthal modes. The properties of coherent modes will therefore be found from eigenvalues and vectors of a truncated interaction matrix with off-diagonal elements included.

The impedance on the RHS of Equation (4.45) would ideally be evaluated at the coherent mode frequency, but this is not usually a known quantity. The perturbation method overcomes this by substituting the zero-intensity mode frequencies $\Omega^{(l)} \approx \omega_\beta + l\omega_s$. Since ISIS operates with $\beta \ll 1$, the indirect space-charge impedance can cause coherent mode frequency shifts on the order of 10 kHz from the zero-intensity case. For a sufficiently smooth impedance, such frequency shifts could reasonably be neglected, however the very narrow resonances in the ISIS impedance model mean that

neglecting this shift by substituting zero-intensity mode frequencies could significantly affect the sampled impedance. To partially mitigate this inaccuracy, ω_β on the RHS of Equation (4.48) will be interpreted as the angular frequency of the most unstable coherent mode. This can be measured from the spectrum of a BPM difference signal using the same techniques as a tune measurement, where an integer number of transverse oscillations per-revolution must be assumed. Typically this can be taken as the integer part of the zero-intensity tune because coherent mode frequency shifts are not large enough to change the integer part; even a 100 kHz shift would not change the integer part at ISIS.

Furthermore, it is often justified to make the substitution $\omega_\beta + l\omega_s \rightarrow \omega_\beta$ on the basis that $\omega_\beta \gg \omega_s$, and so $Z_1^\perp(\omega_\beta + l\omega_s) \approx Z_1^\perp(\omega_\beta)$. This is not necessarily a good approximation for ISIS, because the synchrotron frequency, which can reach almost 4 kHz, is comparable to the resonator widths, $\frac{\omega_r}{2\pi Q_r}$, which are on the order of 10 kHz. Variations in azimuthal-mode frequencies will therefore be included by retaining the $l\omega_s$ terms when the impedance is sampled. This substitution is not perfectly accurate, because mode frequencies are not guaranteed to be equally shifted, and it is not clear which mode the measured frequency corresponds to. Despite these shortcomings, this variation on the usual perturbation method is expected to be more accurate because it includes mode-frequency shifts and doesn't assume all modes have the same frequency.

The theory of Chapter 4 assumes that parameters such as the betatron tune, synchrotron tune and revolution frequency are constant, but on ISIS these quantities can vary with time. To apply the theory to ISIS, it will be necessary to adopt a quasi-stationary model, where PyTMCI calculations are performed with input parameters that are measured at a given time. This approach will be adopted throughout this chapter.

6.3 Instabilities in BSRM as a Function of Vertical Tune

Even with these assumptions, it would be challenging to apply the theory outlined in Chapter 4 to the operational RCS mode of ISIS due to the rapid sweeping of beam parameters and its dual harmonic RF system. The BSRM described in Section 2.2.2, has conditions that are closer to those assumed by the theory. In brief, in BSRM, a beam is accumulated in the synchrotron at $70\,\mathrm{MeV}$ and formed into two bunches by the fundamental RF cavities. The second harmonic RF cavities are set off-tune and have a demand gap voltage of $0\,\mathrm{V}$, whilst the main magnets are powered with DC. A vertical sweeper magnet provides control over vertical beam size in the synchrotron, whilst there is no horizontal painting because of the lack of an AC main magnetic field. The resulting bunched beam is stored until it is eventually completely lost due to equipment resetting, and repeated interactions with the stripping foil. Horizontal and vertical tunes can be controlled using programmable trim-quadrupoles. This steady-state beam is ideal for applying the theory of coherent beam instabilities.

In this section, data from a previous BSRM experiment [80] will be re-examined. In the previous study, experimental results were compared with outputs from tracking simulations and predictions from analytical methods which assumed azimuthal decoupling and used an impedance model derived from beam-based impedance measurements. Here the experimental data will be analysed using different methods and then compared with the results of the theory outlined in Chapter 4 with the impedance model derived and presented in Chapter 5 from equipment properties.

6.3.1 Experimental Set-up

Figure 6.1 shows the total RF-cavity gap potential versus the RCS cycle time [1]. This is maintained below 10 % of its flat-top value before −0.3 ms, but then reaches it's final value by 1 ms. The RF frequency is held at 1.35 MHz, which is harmonic $h = 2$ of the injection revolution frequency.

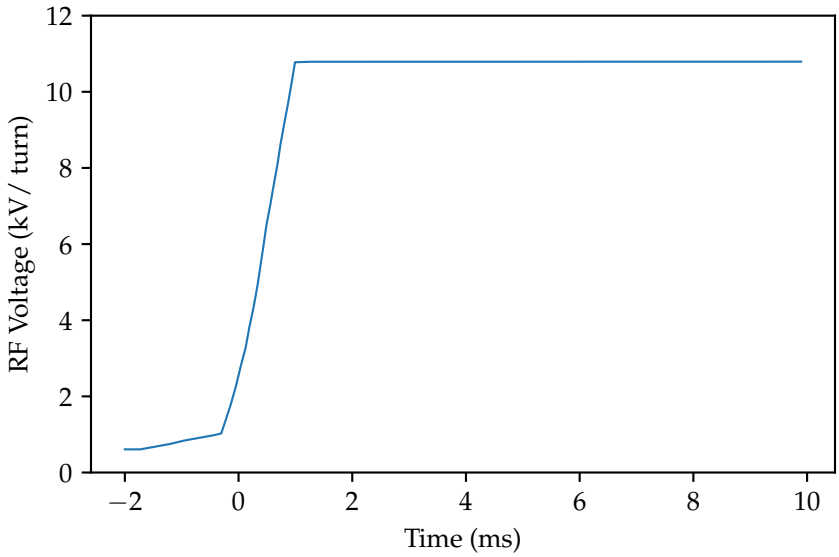


Figure 6.1: Total RF voltage versus time during the BSRM experiment, with injection typically completed by −0.2 ms.

The ISIS control system defines a lattice "set tune", which is distinct and different from the machine's coherent tune at a given intensity. In this experiment, the horizontal set tune was held constant at 4.330, whilst sweeps of the vertical set tune were performed. The baseband coherent oscillation frequency was measured from the experimental data and used to calculate a coherent tune. In each measurement, vertical tune was held constant over the full acquisition time, including the injection period.

In its operational RCS mode, ISIS operates with a large space charge parameter, which is known to affect the behaviour of coherent instabilities [209] and would make

[1] The term "RCS cycle time" is still used in BSRM because much of the injection process is similar to in RCS mode.

it difficult to apply the theory of Chapter 4. In this experiment, the vertical sweeper current was reduced to reduce the vertical beam size, and allow more free aperture for a coherent instability to develop [80]. A reduction in vertical beam size would increase the peak space charge tune spread [89] and therefore the space charge parameter, which could limit the applicability of the theory. To offset this increase, the injected intensity was reduced to 1.68×10^{12} protons-per-bunch (PPB), which reduced the space charge parameter to $\sim\ 3 - 5$.

6.3.2 Experimental Results

Figure 6.2 shows BPM difference and intensity monitor signals for each vertical tune setting. Instability growth rates will be measured from the envelope of the BPM difference signal. Since these are intensity dependent, and therefore change with time during periods of beam-loss, growth rates will be analysed in time windows with approximately constant intensity monitor signals. These windows are indicated by the highlighted regions in the figure. To simplify comparisons between theory and experiment, these windows will usually coincide with the flat-top RF voltage; in three cases rapid beam-losses necessitated a window before $1\,\mathrm{ms}$.

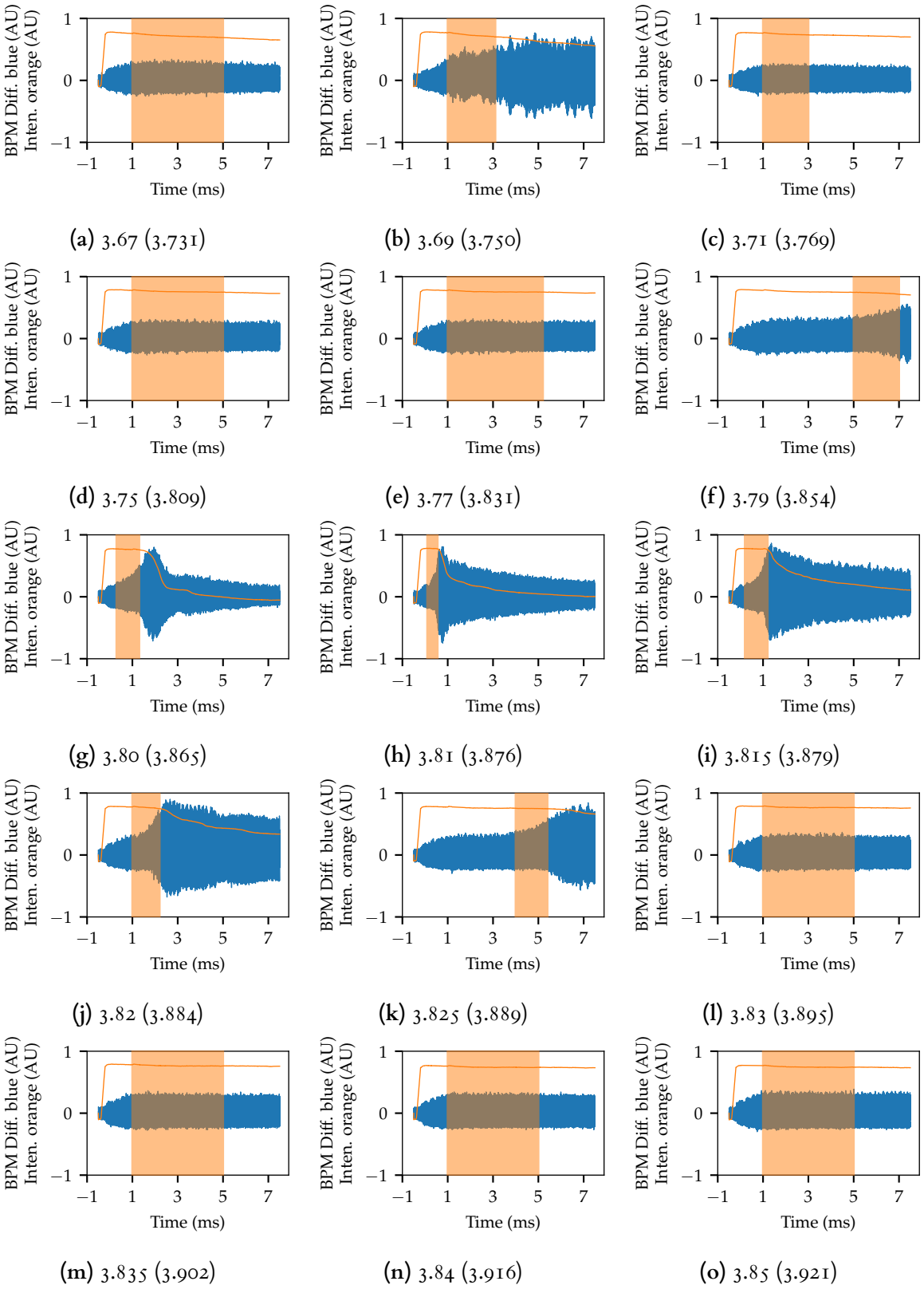
Figure 6.3 shows twenty turns of a BPM difference signal towards the end of the time-window, for several set tunes. A coherent oscillation within the bunch can be seen with a set tune of 3.69 and in the range of 3.79-3.825, whilst the other results show a closed-orbit offset without an oscillation. The two nodes observed with the set tunes of 3.79 and 3.80 could be indicative of an azimuthal $l = \pm 2$ instability. The distribution of the dipole moment at other set tunes, such as 3.81, cannot be identified as a single azimuthal head-tail mode, but could be explained by mode coupling, or there being more than one unstable, decoupled head-tail mode.

Figure 6.4 shows the FFT of the analysed time windows for several set tunes; in most spectra, a baseband sideband can be seen by eye. The amplitude of this baseband peak is linearly correlated with the amplitude of the coherent oscillation, but the FFT amplitudes

will not be used to measure instability growth rates directly. These plots were instead used to establish suitable filters to isolate the baseband sidebands, which are indicated by the shaded regions. For tune settings between 3.67 and 3.79, two peaks can be seen, but the frequency of one was found to be independent of vertical tune, and is thought to be driven by the $4Q_V = 15$ transverse resonance. Since in most cases these two peaks can be distinguished, only the peak associated with a coherent instability will be analysed. This was identified by its dependence on set tune, although the proximity of the two peaks made automatic identification challenging for at least set tunes between 3.67 and 3.71. To assist with the identification, the resonance peak was positioned outside the passband of a 5^{th}-order Butterworth bandpass filter, and the peak associated with the instability positioned at the edge of the pass-band. This was not possible for a set tune of 3.69 because the two peaks overlapped, but this combined peak was processed with the same procedure as the other set tunes and results drawn from it will be shown.

Each time-window in Figure 6.2 was divided into segments of between 0.1 and $1\,\text{ms}$. The number of segments was increased by allowing adjacent windows to overlap by $50\,\%$. The BPM difference signal in each segment was bandpass filtered to ensure the baseband sideband was dominant, and the Numerical Analysis of Fundamental Frequencies (NAFF) algorithm used to obtain amplitudes and frequencies [214].

Figure 6.5 shows the harmonic amplitude obtained with NAFF for each time segment. At the set tune of 3.69 and between 3.79 and 3.825, the oscillation amplitude grew with time. At the other set tunes there is no visible growth on the plotted scale. Least-squares fits of this data were performed to the function $f(t) = \alpha_1 e^{\alpha_2 t}$, where α_1 and α_2 were the fitting parameters. Growth rates from the fit parameter α_2, and the mean frequency for each time segment are plotted in Figure 6.6. Vertical error bars were taken from the least-squares fits, and the horizontal error bars are the standard error in the mean of the frequencies obtained in each segment. Results for two identical sweeps of set tune are overlaid and are largely consistent. The peak around $85\,\text{kHz}$ is indicative of a narrowband impedance at this frequency, as has been reported previously [84].



(a) 3.67 (3.731) (b) 3.69 (3.750) (c) 3.71 (3.769)

(d) 3.75 (3.809) (e) 3.77 (3.831) (f) 3.79 (3.854)

(g) 3.80 (3.865) (h) 3.81 (3.876) (i) 3.815 (3.879)

(j) 3.82 (3.884) (k) 3.825 (3.889) (l) 3.83 (3.895)

(m) 3.835 (3.902) (n) 3.84 (3.916) (o) 3.85 (3.921)

Figure 6.2: Intensity monitor signals in orange and vertical BPM difference signals in blue, both with an arbitrary scale. Time windows where data was analysed are indicated by the orange shaded regions on each plot. Captions show the set tune and measured tune in brackets.

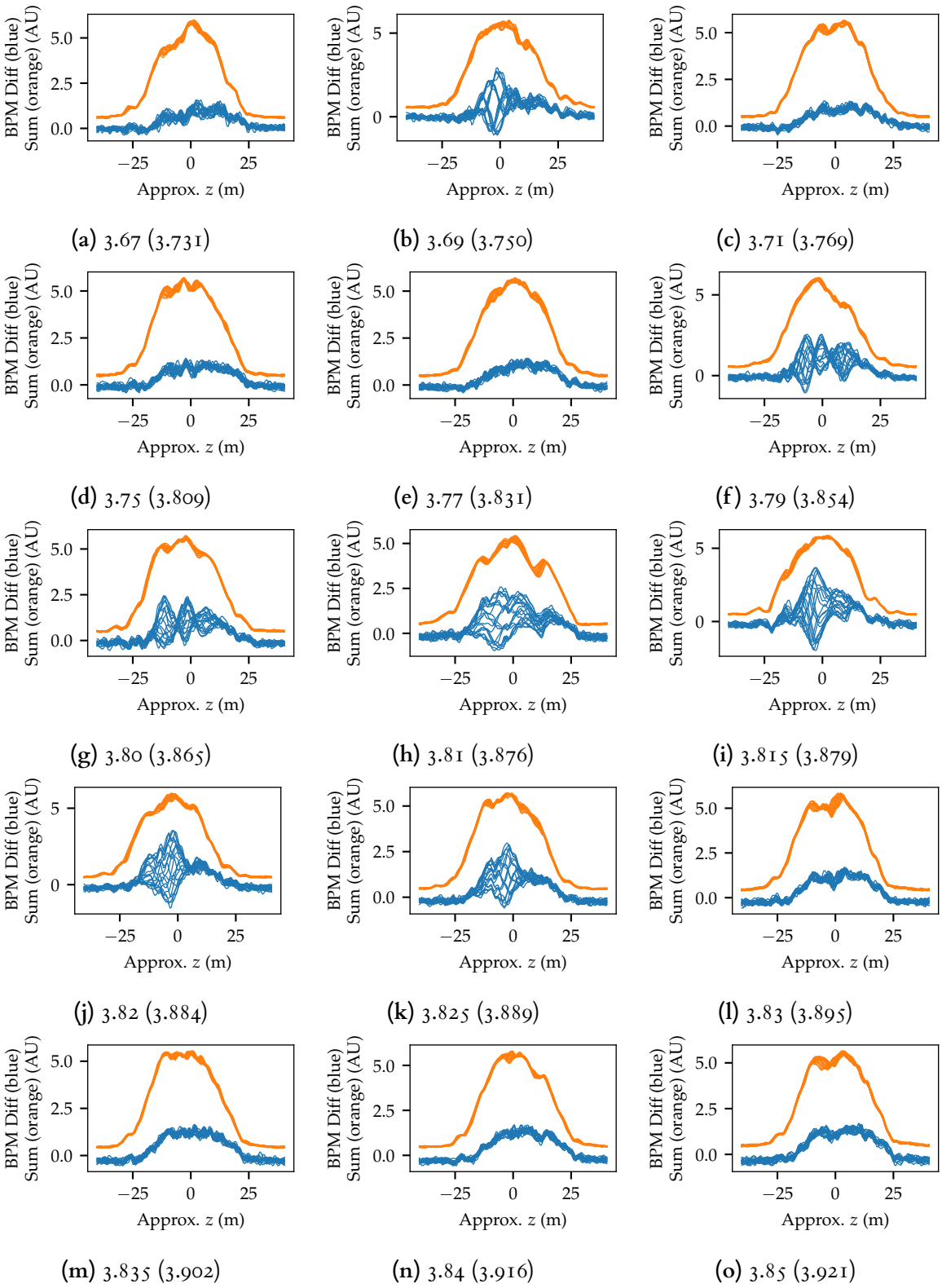


Figure 6.3: Vertical BPM sum (orange) and difference (blue) signals of a single bunch, acquired over 20 turns and overlaid. The sum signals indicate the line charge density, whilst the difference signals show the distribution of the bunch's dipole moment. Captions show the set tune and measured tune in brackets. Horizontal axes have zero offsets, but the bunch head is on right.

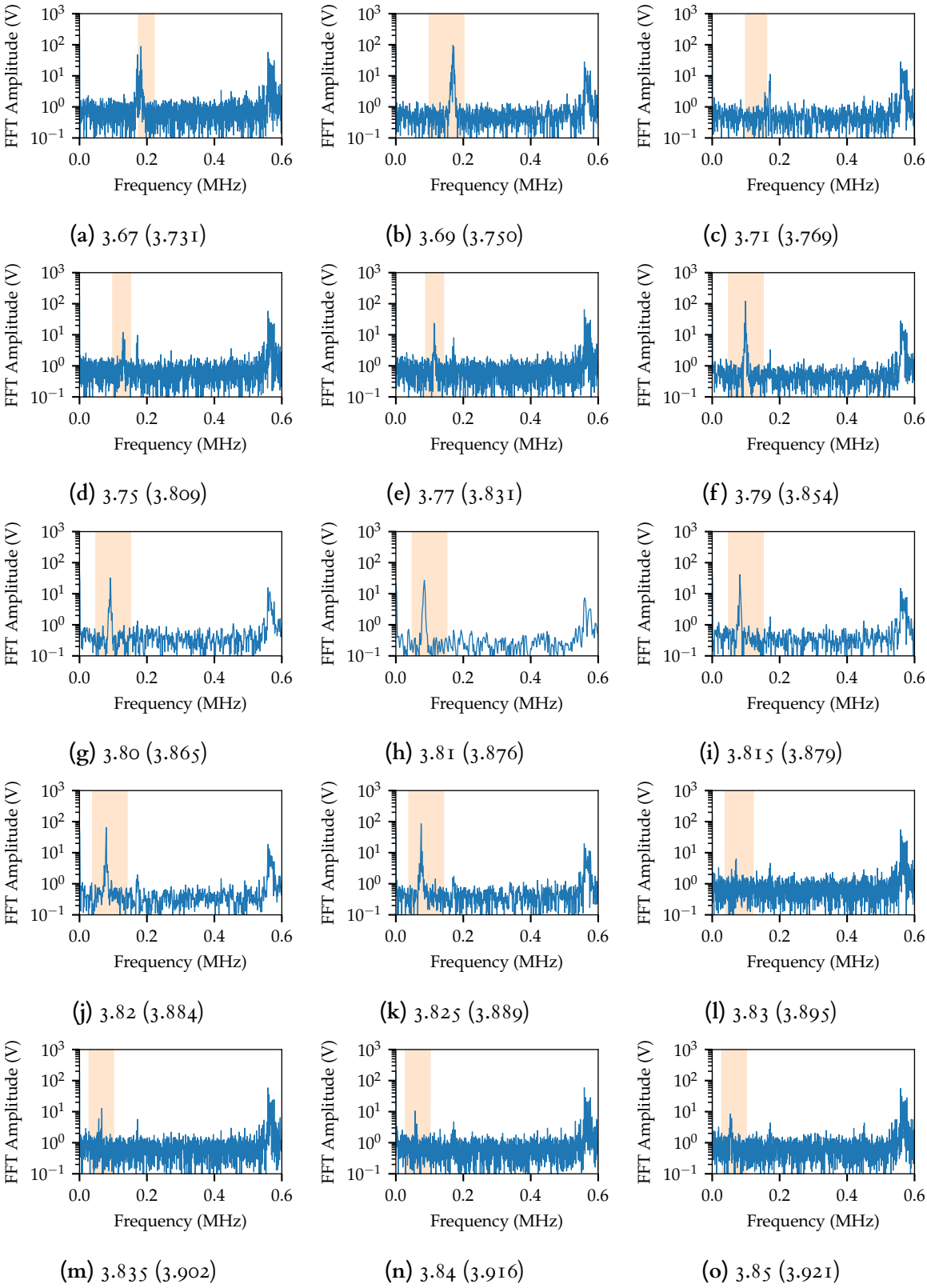
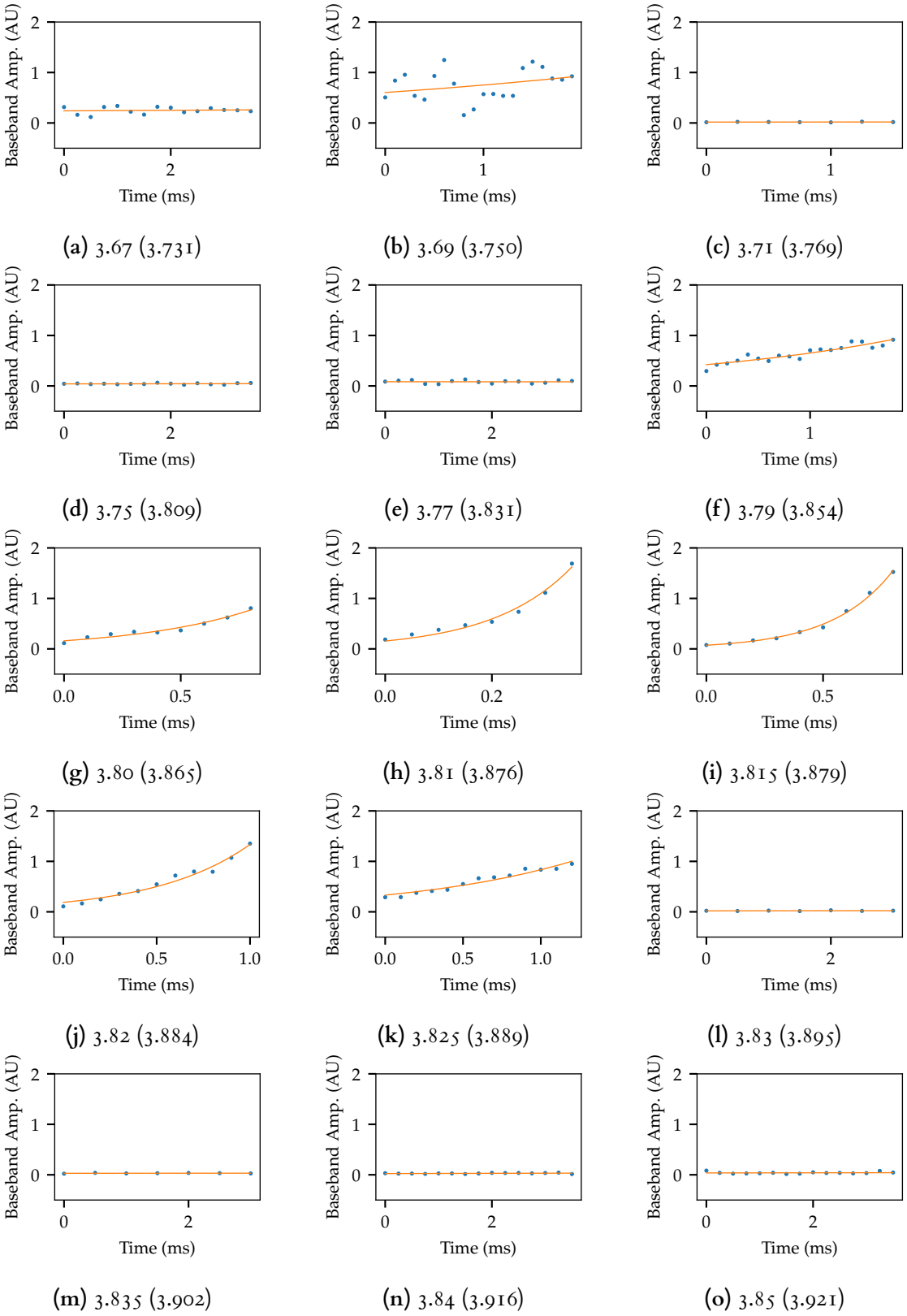


Figure 6.4: FFTs of the vertical BPM difference signals inside the time windows indicated in Figure 6.2. Highlighted regions indicate passband of the filters applied to isolate the baseband peak. Captions show the set tune and measured tune in brackets.



(a) 3.67 (3.731) **(b)** 3.69 (3.750) **(c)** 3.71 (3.769)

(d) 3.75 (3.809) **(e)** 3.77 (3.831) **(f)** 3.79 (3.854)

(g) 3.80 (3.865) **(h)** 3.81 (3.876) **(i)** 3.815 (3.879)

(j) 3.82 (3.884) **(k)** 3.825 (3.889) **(l)** 3.83 (3.895)

(m) 3.835 (3.902) **(n)** 3.84 (3.916) **(o)** 3.85 (3.921)

Figure 6.5: Harmonic amplitudes of the baseband peaks obtained with NAFF at time intervals within the windows indicated in Figure 6.2. Exponential fits to the points are overlaid. Captions show the set tune and measured tune in brackets.

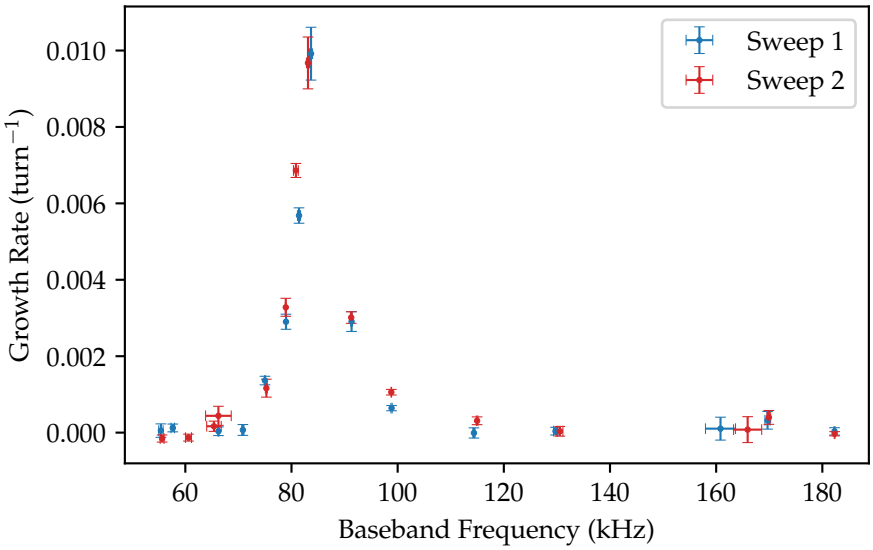


Figure 6.6: Growth rates from the exponential fits in Figure 6.5 versus frequency of the observed oscillation for a number of different set tunes. Results from two sweeps of set tune are overlaid.

6.3.3 PyTMCI Input Parameters

Experimentally obtained growth rates will now be compared with predictions of PyTMCI using the impedance model outlined in Chapter 5. In addition to the impedance model and tune settings, PyTMCI requires the number of bunches and the number of protons per bunch, as well as a synchrotron tune and an initial longitudinal distribution, $g_0(r)$, for a beam that is unperturbed by wake fields. It also requires the maximum number of azimuthal and radial modes to solve for, which will truncate the size of the interaction matrix. For this experiment, the number of bunches was 2, with each having an intensity of $N = 1.68 \times 10^{12}$ for all calculations. Variations in intensity between different tune settings, which can be seen in Figure 6.2, will not be considered because the systematic variations are small compared to the uncertainties introduced by the impedance model. Other input parameters will now be discussed in-turn.

6.3.3.1 Longitudinal Distribution

The unperturbed longitudinal distribution was derived from BPM sum signals. As can be seen from the sum signals in Figure 6.3, the longitudinal distribution differed between tune settings. To simplify the calculation procedure, the initial distribution input into PyTMCI will be the same for all tune settings and derived from the first three turns into the analysis time window of the most unstable tune setting (3.81).

A mean of three turns of data is computed to reduce noise, and the distribution mirrored about an assumed centre to satisfy the assumption of azimuthal symmetry. A moving average further smoothed the distribution before filtered back-projection tomography was used to compute a distribution as a function of radial distance. The distribution is shown in Figure 6.7, and is also overlaid by the Laguerre series expansion used by PyTMCI in Figure 6.8 . This series included ten terms, which is the maximum number currently accepted by PyTMCI.

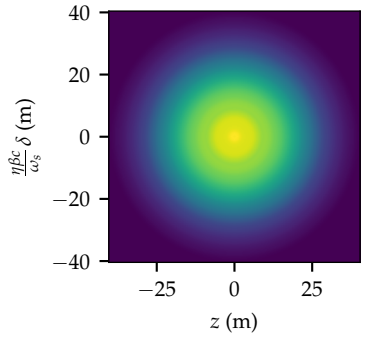


Figure 6.7: Longitudinal distribution computed by filtered back-projection tomography using processed BPM sum signals.

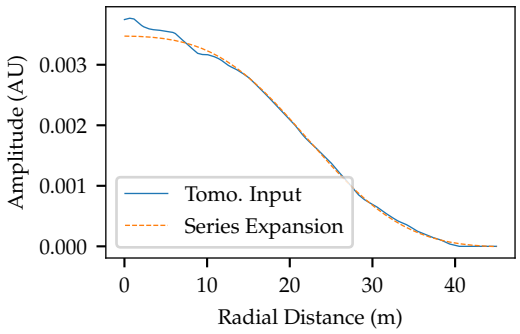


Figure 6.8: Unperturbed longitudinal distribution as a function of radial distance in longitudinal phase space. Input is from the tomographically reconstructed distribution, and the series expansion used to approximate the distribution in PyTMCI is overlaid.

6.3.3.2 Synchrotron Tune

The synchrotron tune is given by

$$\nu_s = \sqrt{\frac{V_{\mathrm{rf}} N_{\mathrm{gap}} \eta h}{2\pi\beta^2 E_{\mathrm{t}}} \cos(\phi_s)}, \tag{6.1}$$

where V_{rf} is the peak gap voltage (per-gap), N_{gap} is the number of gaps per-revolution and E_{t} is the total particle energy [215]. Before $1\,\mathrm{ms}$, Figure 6.1 shows that V_{rf} was ramped, so ν_s was not constant at this time.

The theory on which PyTMCI is based assumes a constant synchrotron tune, so to apply the code to this scenario requires that a tune be assumed. In making this assumption, it is implicitly assumed that the behaviour of coherent instabilities will not depart significantly from that of the quasi-stationary model. One scenario where it could be argued this was the case would be where instability growth rates were fast compared to the synchrotron period. The peak growth rate in Figure 6.6 of $\sim 0.01\mathrm{turn}^{-1}$ corresponds to a growth time of $\sim 0.15\,\mathrm{ms}$, whilst the synchrotron period calculated by Equation (6.1) with the RF voltage at $0.1\,\mathrm{ms}$, is closer to $0.6\,\mathrm{ms}$. It is therefore assumed that the analytical model can reasonably be applied to this experimental scenario.

A further complication of the ramping synchrotron tune is in application of the perturbation technique described in Chapter 4. With that approximation, the impedance is sampled at frequencies $pM\omega_0 + \omega_\beta + l\omega_s$. Inaccurate values of ω_s may not affect results considerably for a broadband impedance model, but the ISIS impedance model contains peaks with widths comparable to $\approx 14\,\mathrm{kHz}$, whilst Equation (6.1) predicts synchrotron-tune variations of around $1.5\,\mathrm{kHz}$ between 0 and $1\,\mathrm{ms}$. Integer multiples of such variations could introduce large systematic errors in predicting which modes will be unstable and their growth rates. To ensure that some variation in synchrotron tune is included, a value was computed from the RF voltage at the beginning of the windows indicated in Figure 6.2, and linear interpolation used for intermediate tune values.

6.3.3.3 Number of Radial and Azimuthal Modes

The set number of radial and azimuthal modes truncates the interaction matrix, and therefore must be sufficiently large to obtain accurate results. For this calculation, instability growth rates were calculated for a sweep of betatron tunes, and increasing numbers of radial and azimuthal modes; see Figure 6.9. To ensure sufficient accuracy of the PyTMCI solution, the number of radial and azimuthal modes was increased to 10 radial modes and 20 azimuthal modes (the maximum currently available in PyTMCI), which produced changes in peak growth rate of less than 10 % between subsequent runs. These numbers will be used in subsequent calculations.

The maximum number of frequencies at which to sample the impedance model was also increased until the peak growth rate converged. Growth rate versus baseband frequency is shown in Figure 6.10 for several numbers of sample frequencies. The number of sample frequencies did not significantly affect computation time, so 1001 was used for all computations, which produced less than 1 % difference in peak growth rate between results with 1001 and 21 frequencies.

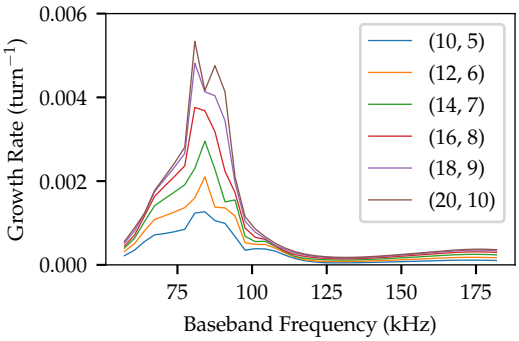


Figure 6.9: Growth rate of the most unstable mode versus baseband frequency of the instability. The number of azimuthal and radial modes used in each calculation is shown.

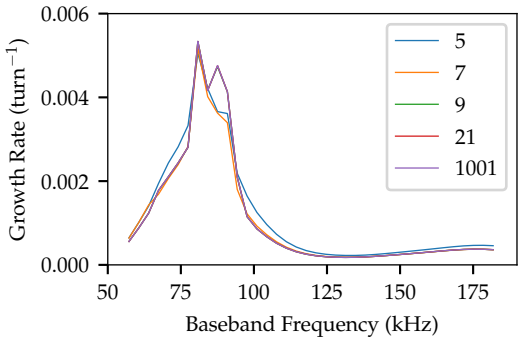


Figure 6.10: Growth rate of the most unstable mode versus baseband frequency of the instability. The number of harmonics used in each calculation is shown.

6.3.4 Comparison of PyTMCI and Experimental Results

6.3.4.1 Instability Growth Rates

PyTMCI was run with several inputs for ω_β, which are here interpreted as the angular frequency of the most unstable coherent mode. To account for the uncertainties on the RF screen resonators listed in Table 5.8, 100 PyTMCI calculations were run for each ω_β, with a sample from a randomly generated normal distribution of each each parameter substituted into Equation (3.35). Uncertainties on other impedance sources were considered negligible compared to the RF screen resonators, so no other sources of uncertainty were considered. The fastest growth rate was computed for each calculation, and a mean and standard deviation found. These are overlaid with the experimental results in Figure 6.11.

Predictions are not consistent with observations for all frequencies, but the functional dependence is well described and the growth rate is consistent to within an order-of-magnitude in the frequency range of $75 - 170\,\mathrm{kHz}$. The peak predicted growth rate is $0.005 \pm 0.002\ \mathrm{turn}^{-1}$, corresponding to a characteristic growth time of $0.3\,\mathrm{ms}$. This is $\sim 50\,\%$ of the experimentally observed value, or a ≈ 2.5-sigma difference. The frequency at which this peak occurs is within $3.4\,\mathrm{kHz}$ $(4.1\,\%)$ of the experimental value. This level of agreement between theory and experiment, both for growth rate and baseband frequency is considered excellent, considering the simplified analytical model.

Predicted growth rates in the 50 to $70\,\mathrm{kHz}$ region are consistently larger than observation. Since this frequency range is not significant for ISIS operations, no attempt will be made to identify the source of the inconsistency in this region, although it could indicate an error in the impedance model for this region.

Whilst previous studies have also shown agreement of predicted growth rates [80], these were based on an impedance model derived from beam-based impedance measurements. The results presented here are the first time this level of agreement has been achieved with an impedance model derived from the properties of equipment, as

described in Chapter 5. That model suggests the 85 kHz peak in growth-rate is primarily caused by RF screens in the dipole and doublet magnets. It also predicts that RF screens in the the singlet and high-order magnets will cause a smaller peak in growth rate around ~ 180 kHz, and some preliminary evidence of this can be seen in this data. Figure 6.11 shows that PyTMCI predicts a small increase in growth rate on the right hand side of the plot, which is consistent with at least one point at 170 kHz. That point corresponds to the set tune of 3.69, where Figure 6.3b shows that coherent motion was observed. Despite this agreement, the growth rate at 180 kHz is not consistent with predictions, which might indicate a dip in the impedance that isn't seen in Figure 5.69.

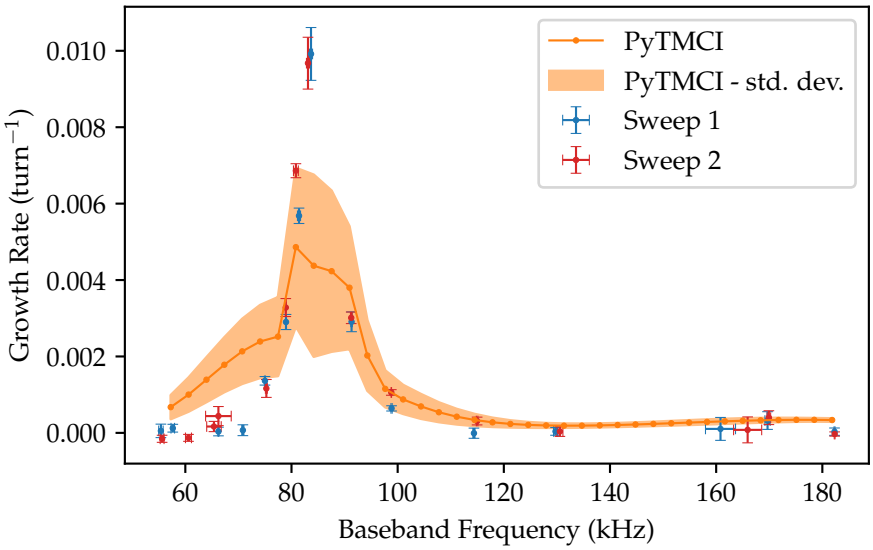


Figure 6.11: Overlay of the experimentally obtained growth rates from Figure 6.6 with growth rates computed by PyTMCI. The shaded region represents the uncertainty, taken as the standard deviation of the 100 computed growth rates.

6.3.4.2 Instability Distribution

Earlier studies of instabilities on ISIS have placed much emphasis on the observed distribution of the beam's dipole along the bunch. This is because in those studies, the number of nodes in the BPM difference was interpreted as giving the dominant azimuthal head-tail mode [86, 216, 212, 84, 80]. No explicit prediction of dipole distribution was

necessary, because it was sufficient to state the azimuthal mode number from which a dipole distribution automatically followed. This interpretation assumed that no mode coupling occurred, which is a common assumption for low-intensity beams or when the impedance is small. Neither of these conditions were satisfied during this experiment, and nor are they satisfied during RCS operations. Features of the distributions observed on ISIS are not consistent with this interpretation, for example that only part of the bunch oscillates [88] and that the distribution is asymmetric [212], which is known as a consequence of mode coupling [117]. In this analysis, mode decoupling will not be assumed, so the distribution of the dipole moment along the bunch will be computed by PyTMCI and shown explicitly.

Even when no mode-coupling occurs, it is possible for several head-tail modes to become unstable simultaneously. A BPM difference signal shows a superposition of all these modes, however the most unstable mode will dominate after its amplitude far exceeds that of the other modes. The time required for this depends on the difference in growth rates between modes. Before this time, accurately predicting the distribution is expected to be challenging as interference between the modes will depend on their relative amplitudes. Dipole moment distributions were therefore computed as the sum of the five most unstable modes. Initial amplitudes were defined by the unit-length normalisation of the computed eigenvectors, but distributions were computed after a number of turns corresponding to the end of the analysed time window. In this way, modes with a faster growth rate tended to dominate the signal, as would happen experimentally.

Figure 6.12 shows computed distributions of the beam's dipole moment along the bunch. These are to be compared with the experimental results in Figure 6.3. Some features are reproduced, for example with a set tune of 3.79, the distribution contains three large-amplitude regions and at a set tune of 3.815, the tail of the bunch is predicted to have a large-amplitude oscillation. Despite these similarities, in general, the predicted distributions bear limited resemblance to observation, containing different numbers of nodes and relative amplitudes between the head and tail. An important feature of the

experimental results that agree with predictions, is that tune changes on the order of 0.005 are predicted to produce very different distributions of the dipole moment. It was also observed that the distributions evolve with time, indicating that a single mode has not yet dominated the distribution.

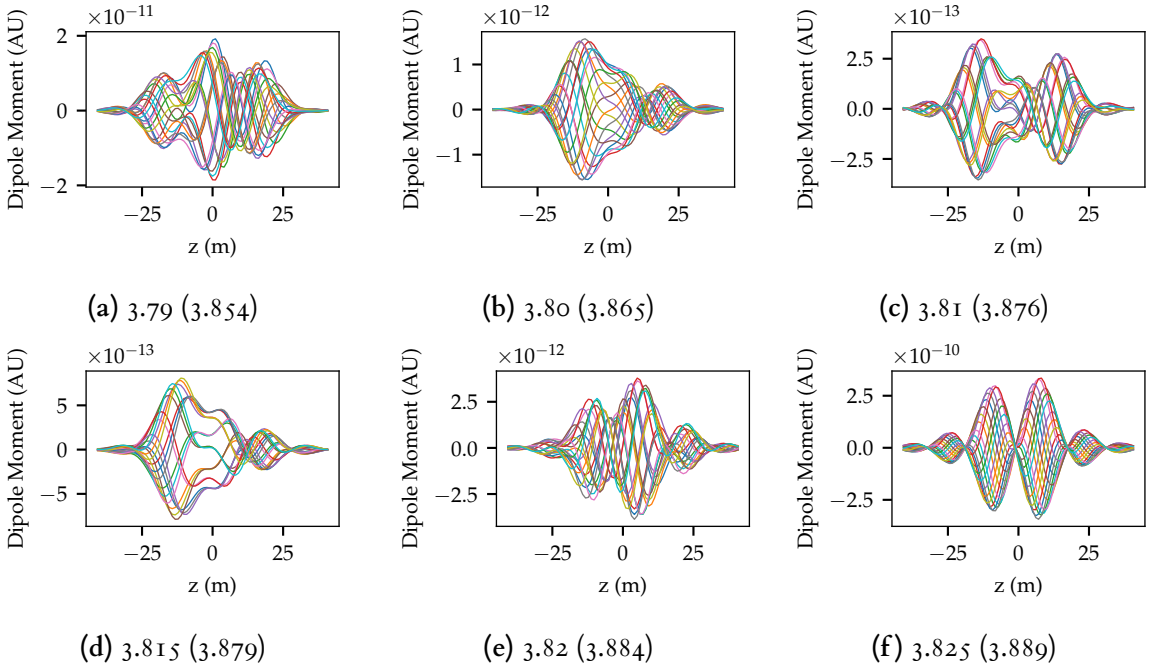
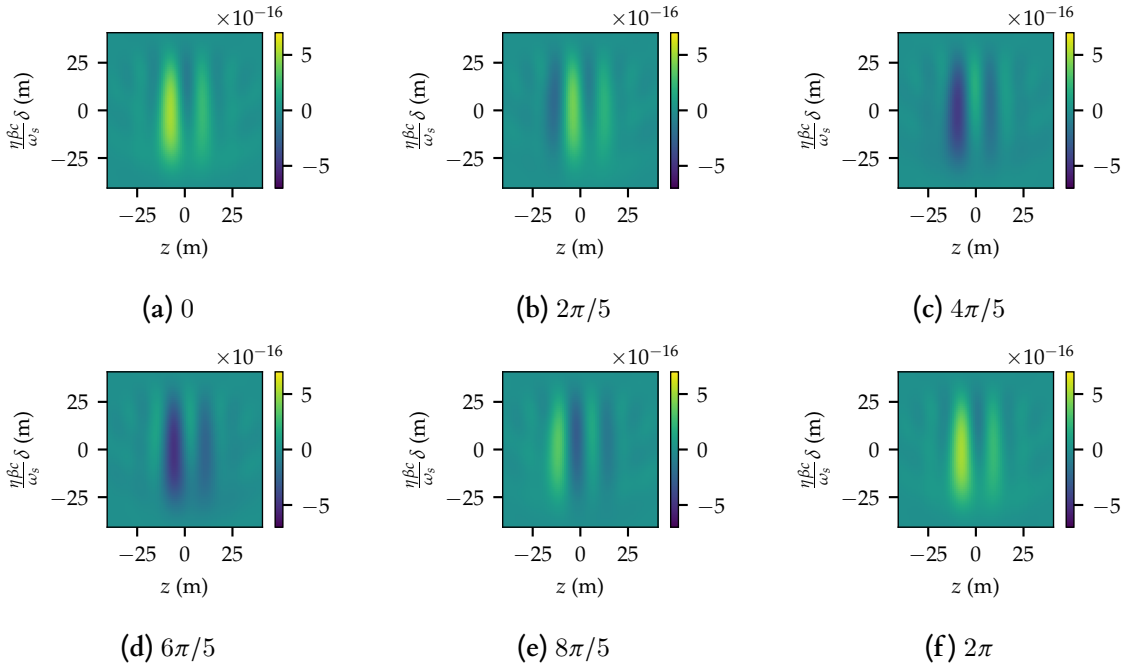


Figure 6.12: Dipole moment along the bunch computed by PyTMCI, using the measured tune indicated inside brackets in the caption. Set tune is shown in the caption to assist with comparisons with experimental data.

As well as projections, $g_1(r, \phi)$ as it was defined in Equation (4.21), can be computed from eigenvectors associated with an unstable eigenvalue. The most unstable eigenmode is plotted in Figure 6.13. These show a coherent offset propagating from the tail to the head of the bunch, and not a rotation as would be expected for an azimuthally decoupled head-tail mode.



(a) 0 (b) $2\pi/5$ (c) $4\pi/5$

(d) $6\pi/5$ (e) $8\pi/5$ (f) 2π

Figure 6.13: Longitudinal phase-space distribution of the beam's dipole moment, $g_1(r, \phi)$, for the most unstable baseband frequency observed (set tune of 3.81). From left-to-right top-to-bottom, plots show an advancing phase as indicated by captions. Colours indicate a quantity proportional to the vertical dipole moment in arbitrary units.

6.3.5 Discussion of BSRM Results

In this experiment, measurements of instability growth rates and the dipole moment distribution along a BSRM bunch have been compared with analytical predictions from PyTMCI. The theory, which was introduced in Chapter 4, assumes bunches with constant beam parameters which was not always the case in this experiment due to the ramping RF cavity gap volts seen in Figure 6.1. Furthermore, evaluating the interaction matrix in Equation 4.45 requires knowledge of a large number of mode frequencies that are likely to be large compared to the synchrotron frequency, but these shifted frequencies are not known. To overcome this, Section 6.2.2 explained the assumption made here that ω_β on the RHS of Equation (4.48) could be obtained from the sideband frequency of the BPM difference signal, and that all other modes are shifted by integer multiples of ω_s from this.

Because these are understood to be imperfect assumptions, exact agreement with theory is not expected, and indeed some growth-rate predictions were inconsistent with experiment. Nevertheless, the observed peak growth rate in Figure 6.11 has been predicted to within an order of magnitude and key features of its frequency dependence, namely a narrowband peak around 80 kHz, have also been predicted very effectively. Inconsistencies in the 60–70 kHz frequency range could indicate that the impedance is overestimated here, but this is below the operational frequency range and won't investigated further. Whilst agreement between analytical predictions of growth rate in BSRM have been reported previously [80], this is the first time such predictions have been made with an impedance model derived from equipment properties.

The difficulty in evaluating the interaction matrix also offers a possible explanation for the imperfect predictions of the beam's dipole moment distribution, which can be seen by comparing Figures 6.3 and 6.12. Despite this, both experimental and predicted results agree that this distribution has a strong dependence on ω_β. PyTMCI predicted that multiple modes would have growth times on the order of 100 µs, and in that case the observed distribution would be an interference between modes. If the fastest growing mode has time to dominate the distribution then it is sufficient to consider only one mode, but if not then the relative phases and amplitudes of several modes must be known and predicting the distribution would be very challenging.

For a single mode to dominate, its exponential growth factor should be an order-of-magnitude larger than the next most unstable mode. To understand the conditions for this, consider

$$\frac{e^{t/\tau_1}}{e^{t/\tau_2}} = e^{t/\tau_1 - t/\tau_2}$$

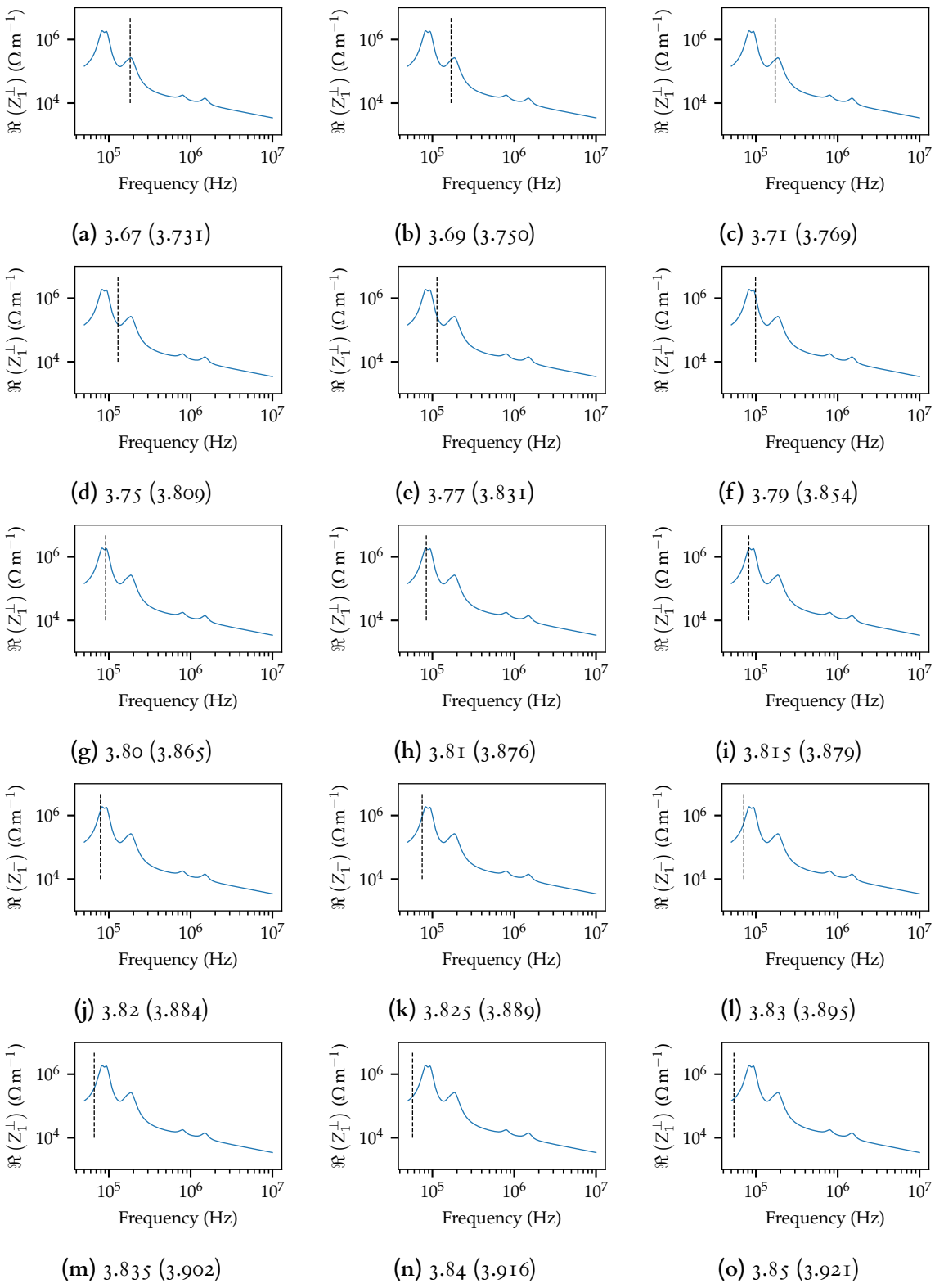
where τ_1 is the characteristic growth time of the most unstable mode and $\tau_2 = \tau_1 + \Delta$ is that of the next most unstable mode. After some algebra and assuming $\tau_1 \approx \tau_2$, we find that this is approximately equal to $\approx e^{\frac{\Delta}{\tau_1^2}t}$. Growth rates predicted by PyTMCI suggest that $\frac{\Delta}{\tau_1}$ is on the order of ~ 0.1, so that the most unstable mode will dominate

after $t \approx 23\tau_1$. Experimentally, the peak growth rate in Figure 6.6 is ~ 0.01 turn^{-1} ($\tau_1 \sim 150\,\mu$s), suggesting that $\sim 3.4\,$ms would be required for a single dominant mode. Beam-losses were observed from $\sim 0.55\,$ms, so the most unstable mode is not likely to have been dominant. That being the case, it is impossible to determine the azimuthal mode number from Figure 6.3.

Since the dominant evolution of $g_1(r, \phi)$ shown in Figure 6.13 is not a rotation, it is expected that the observed instability was not a decoupled head-tail mode. Asymmetry in the measured distributions is evidence that mode coupling plays a role [117], but whether this is in the form of a TMCI, a convective instability [176], or some other mechanism is beyond the scope of this thesis. Whilst previous studies have raised the possibility of mode coupling being significant on ISIS, these are the first analytical predictions of its significance.

Because the impedance model developed in Chapter 5 was derived from equipment properties, instabilities caused by features of the model can now be associated with particular pieces of equipment. Figure 6.14 shows the measured baseband frequency for each set tune overlaid with that impedance model. It can be seen that the 85 kHz peak in growth rate occurs for a set tune where the baseband frequency coincides with the 85 kHz peak associated with the dipole and doublet RF screens. It is therefore asserted that this peak in growth-rate is caused by the resonator impedances in those screens.

With the impedance model developed in Chapter 5, the PyTMCI code from Chapter 4 has made partially accurate predictions for ISIS in BSRM. This partially satisfies the second objective of Section 1.3, to understand whether the theory of coherent instabilities can make partially accurate predictions for ISIS. By identifying a probable cause of the BSRM instability, it has laid the foundation for achieving the third objective, to find ways of improving beam stability. Despite these successes, the 85 kHz impedance peak is not thought to be responsible for the 2 ms instability because its frequency is too low. Since this thesis is primarily interested in the instability affecting operational beams, an experiment in RCS mode is required to fully satisfy the second objective.



(a) 3.67 (3.731) **(b)** 3.69 (3.750) **(c)** 3.71 (3.769)

(d) 3.75 (3.809) **(e)** 3.77 (3.831) **(f)** 3.79 (3.854)

(g) 3.80 (3.865) **(h)** 3.81 (3.876) **(i)** 3.815 (3.879)

(j) 3.82 (3.884) **(k)** 3.825 (3.889) **(l)** 3.83 (3.895)

(m) 3.835 (3.902) **(n)** 3.84 (3.916) **(o)** 3.85 (3.921)

Figure 6.14: Measured baseband frequencies for different set tunes, indicated by a vertical line and overlaid with the impedance model of Chapter 5. Caption shows the set tune and measured tune in brackets.

6.4 Instabilities in RCS Mode with Fundamental RF

Section 6.3 demonstrated that when combined with the impedance model of Chapter 5, PyTMCI can predict key features of instabilities on ISIS in BSRM. It was not able, however, to probe the 2 ms instability introduced in Section 2.3.1, which limits operational performance. In this section, PyTMCI will be applied to beam parameters close to those during the instability. Its predictions will be compared with the results of a dedicated experiment performed in RCS mode. PyTMCI's predictions were not completely accurate in BSRM, and its accuracy is not expected to improve for an RCS experiment. Nevertheless, key features of the BSRM instability were predicted, so it is of significant interest to see whether PyTMCI can predict any features of the 2 ms instability. If so, this could indicate that the source of the instability has been included in the impedance model developed in Chapter 5, and satisfy the second thesis objective.

PyTMCI is based on a theory whose assumptions are incompatible with a dual-harmonic RF system, so for the duration of this experiment the second-harmonic RF cavities were disabled for the relevant part of the RCS cycle. Such an experiment would be of little practical interest were it not for the fact that vertical coherent instabilities have been observed from around 2 ms into the RCS cycle both with and without the second harmonic cavities. The similarity between these instabilities, which was discussed in Chapter 2, justifies the assumption that they share a common cause.

6.4.1 Experimental Set-Up

Figure 6.15 shows the demanded gap voltage on the fundamental RF cavities throughout the RCS cycle. Each of the six fundamental RF cavities contains two gaps, so that the effective overall voltage is twelve times the value shown. For this experiment, the second-harmonic cavities had a demand gap voltage of 0 kV between 0 and 4 ms, as shown in Figure 6.16. Only data from this window will be analysed, which includes the time that an instability typically develops.

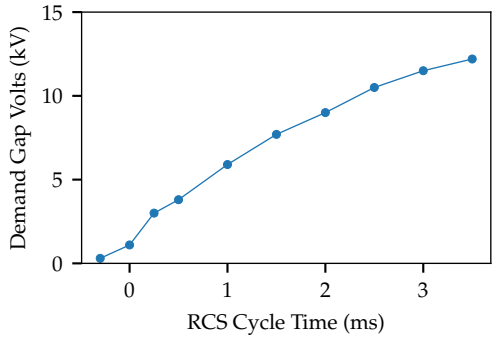


Figure 6.15: Peak voltage-per-gap on the fundamental harmonic ($h = 2$) cavities.

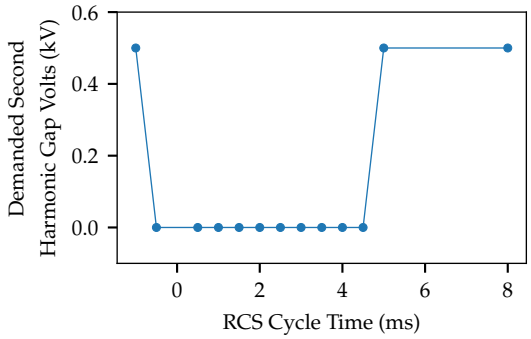


Figure 6.16: Peak voltage-per-gap on the second harmonic ($h = 4$) cavities.

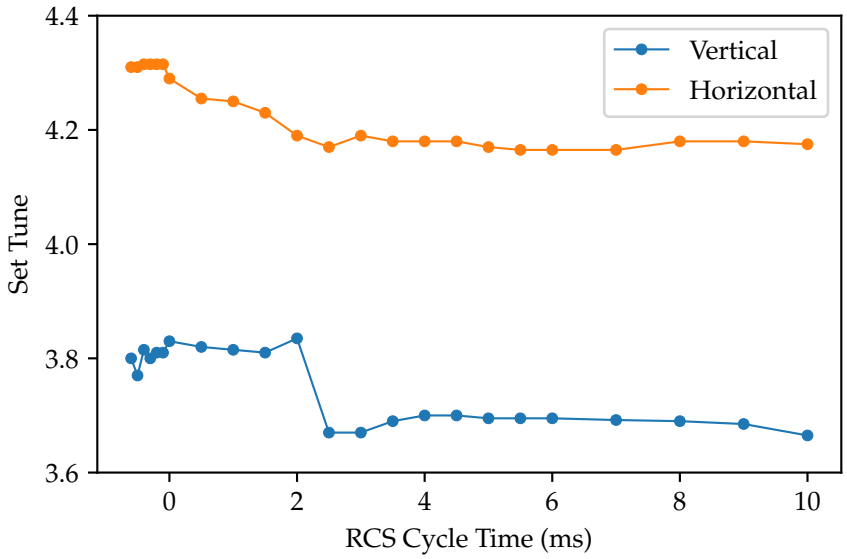


Figure 6.17: Horizontal and vertical set tunes through the RCS cycle.

Figure 6.17 shows the demanded set tune throughout the RCS cycle. These deviate from the nominal values of $(Q_H, Q_V) = (4.33, 3.83)$ because they have been optimised to minimise beam-loss throughout the RCS cycle. Horizontally, there is a gradual reduction over the first 2.5 ms of the cycle, after which it varies by less than 0.025. Vertically the set tune remains within 0.035 of 3.80 before 2 ms, after which it ramps from 3.835 to 3.670 over 0.5 ms. This rapid change of the vertical tune has been used to mitigate the 2 ms instability since the early stages of ISIS commissioning [62].

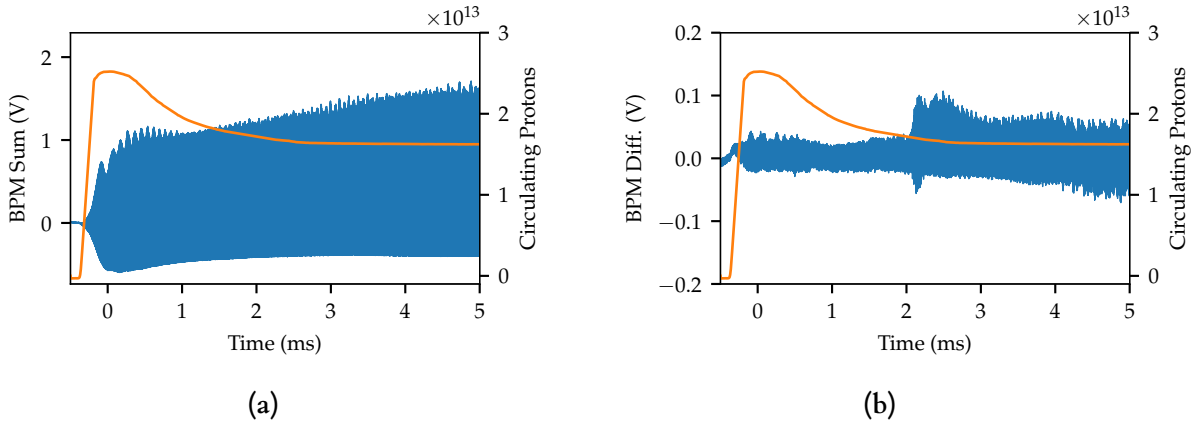


Figure 6.18: BPM sum (a) and difference (b) signals during the RCS experiment with only fundamental cavities active between 0 and 4 ms. Intensity monitor signals are overlaid to show the number of circulating protons.

6.4.2 Experimental Results

Figure 6.18 shows a BPM sum and difference signal through the relevant part of the RCS cycle. An intensity monitor signal also shows the total number of protons circulating, which were shared between two bunches. The falling intensity monitor signal from ~ 0.5 ms is indicative of beam-losses, which are typically characterised as "trapping losses" at this time, and are caused by non-adiabatic capture of the injected beam [217]. In this experiment, losses in the first half of the RCS cycle were $\sim 30\,\%$ compared to operational values of $< 5\,\%$, because re-optimisation of the machine was not possible during the experiment. Even with this reduced intensity, an instability was observed around 2 ms, so the measurement was still a good representation of an operational cycle.

Rapid growth of the BPM difference signal can be seen from around 2 ms. To verify that this was associated with a coherent instability, a third-order Butterworth band-pass filter was applied to the BPM difference signal in post processing. An 80-300 kHz passband was chosen to select the baseband frequency associated with coherent oscillations. Figure 6.19 shows the filtered difference signal close to 2 ms. The initially growing envelope confirms that the observed growth in the BPM difference signal at $\sim$ 2 ms was associated with a coherent oscillation.

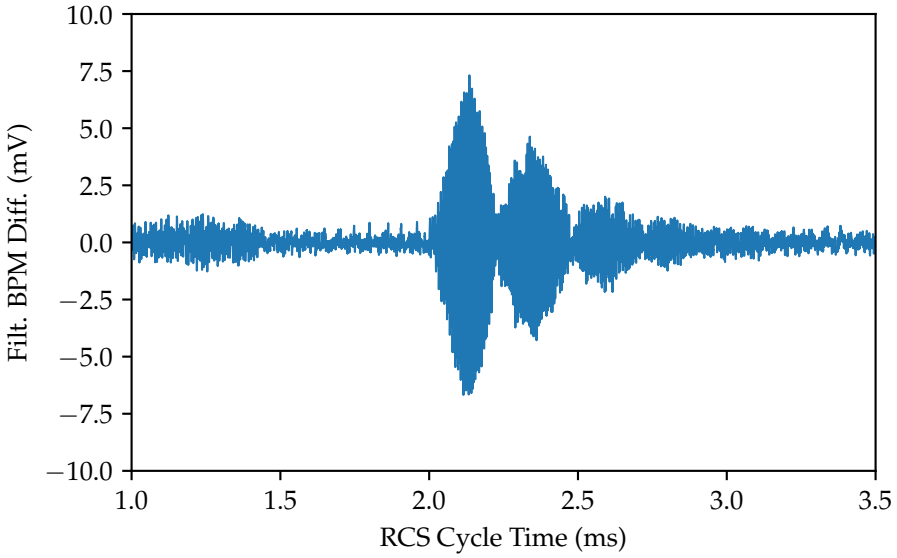


Figure 6.19: Difference signal from a vertical BPM, bandpass filtered around the expected baseband frequency.

As well as showing an initially growing oscillation amplitude, Figure 6.19 also shows a beating structure with a period of $\sim 0.25\,\mathrm{ms}$. One explanation for this structure is that several modes were simultaneously unstable. In that case, the BPM difference signal would be a superposition of all the unstable mode distributions. Nodes in the baseband envelope would occur when this superposition resulted in a small average coherent offset. To investigate this possibility, and see more details of the dynamics, the unfiltered difference signal was observed during the growing and damping phases. In each plot of Figure 6.20, the BPM difference signal of a single bunch has been overlaid over twenty sequential turns. The centre of the 20-turn window progresses throughout the plot, so that time-evolution of the instability can be understood.

The first peak in the filtered difference signal occurs around $2.13\,\mathrm{ms}$, which is seen to coincide with a coherent oscillation of the bunch with no visible nodes; it is qualitatively similar to the distribution of an azimuthal mode-0 instability. Coherent oscillations can still be seen around the minima of the envelope around $2.23\,\mathrm{ms}$, but there is a rapid oscillation along the bunch. At $2.29\,\mathrm{ms}$, the dominant coherent oscillation occurs at

the head of the bunch, but by $2.36\,\mathrm{ms}$ the central portion of the bunch has the largest amplitude. This behaviour is consistent with multiple modes being simultaneously unstable, one with a maxima close to the centre of the bunch, and the other with a maxima towards the head.

It is concluded that the observed growth in the BPM difference signal is associated with at least one coherent instability, but multiple coherent modes are thought to be simultaneously unstable. This would explain the observed beating envelope, but makes measurements of individual mode growth rates impossible. Conclusions are therefore limited to the qualitative observation that instability developed from around $2\,\mathrm{ms}$ into the RCS cycle, and that the oscillation amplitude grew on time scales on the order of $100\,\mu\mathrm{s}$.

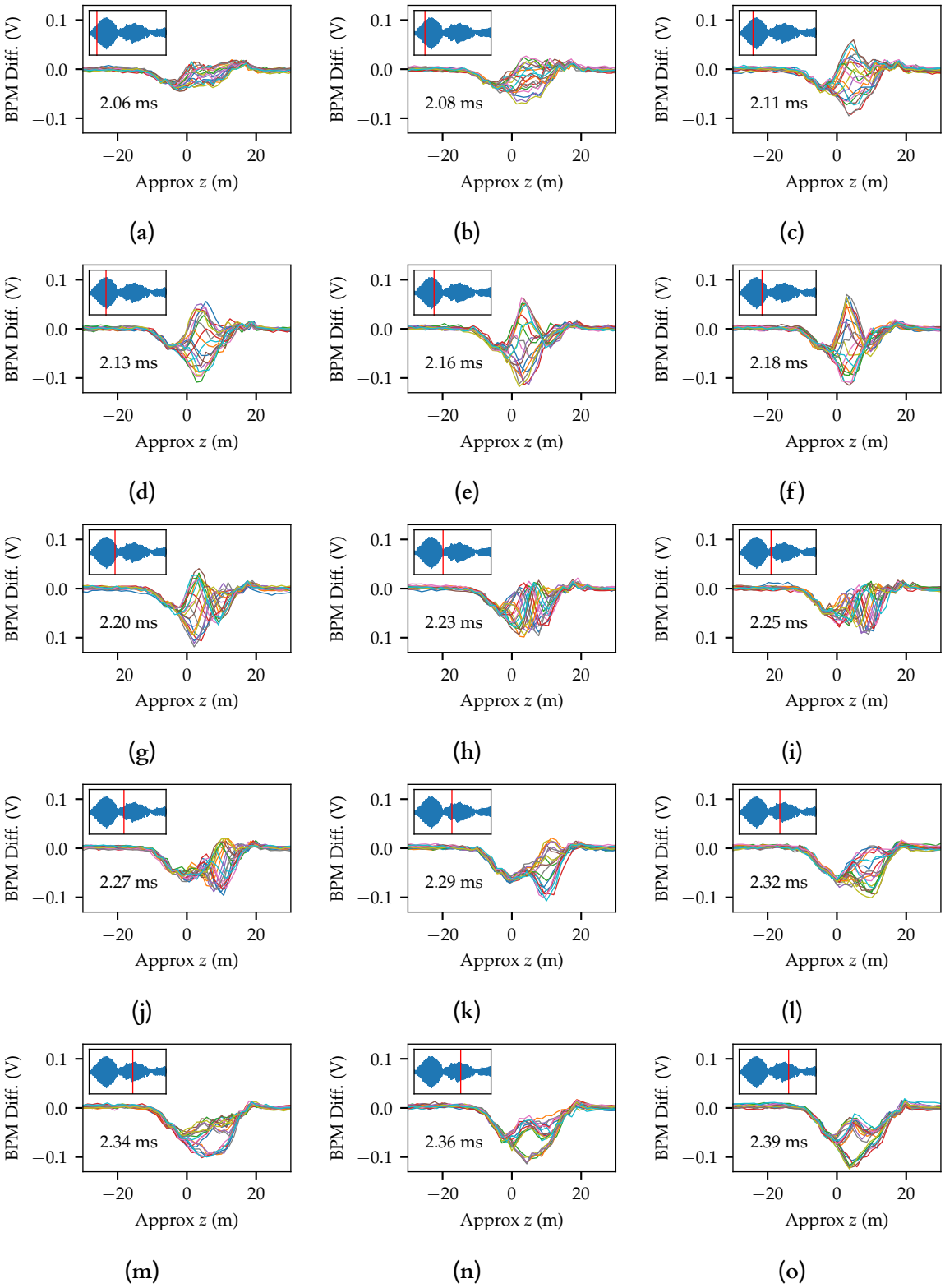


Figure 6.20: Unfiltered BPM difference signal from a single bunch, overlaid over twenty turns. This shows the distribution of the coherent dipole moment along the bunch. Inset plot shows the filtered BPM difference signal in blue with the central time of the twenty-turn window marked approximately with a red line. This time is also printed on the bottom-left of the plot.

6.4.3 PyTMCI Input Parameters

PyTMCI will now be used to investigate the RCS experiment. Even with the second-harmonic cavities disabled, an experiment carried out in RCS-mode still violates some assumptions made the analytical treatment behind PyTMCI. Revolution frequency, betatron tune, synchrotron tune and phase-space distributions are examples of parameters that are assumed to be constant by the theory, but will in reality change with time. In the quasi-stationary approximation made here, inputs to PyTMCI will be based on beam parameters as measured at a point in time. The input parameters will now be discussed and the results presented.

6.4.3.1 Longitudinal Distribution

As for the BSRM experiment, an unperturbed longitudinal distribution will be derived from BPM sum signals close to $2\,\mathrm{ms}$ into the RCS cycle. A centre of the distribution was defined as containing $50\,\%$ of the integrated sum signal and the distribution was divided into two halves about this point. To satisfy the assumption of azimuthal symmetry and remove noise, an average of the two sides was calculated, and the line charge for a full bunch formed by mirroring the result. This was repeated for sum signals acquired over three turns, a mean of these three distributions was found, and smoothing was applied to further reduce noise. Figure 6.21 shows an example measured BPM sum signal and the result of these processing steps. To obtain the unperturbed beam distribution as a function of radial distance in longitudinal phase space, $g_0(r)$, filtered back-projection tomography was used to compute a distribution, which is shown in Figure 6.22 with the Laguerre series representation used by PyTMCI. To demonstrate its validity, the line charge density was reconstructed from the tomography results and is overlaid in Figure 6.21.

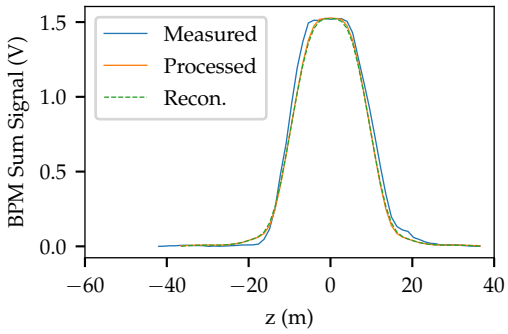


Figure 6.21: Line charge density from a BPM sum signal for one turn. The processed distribution for the tomography is overlaid with a reconstruction from the tomographic result.

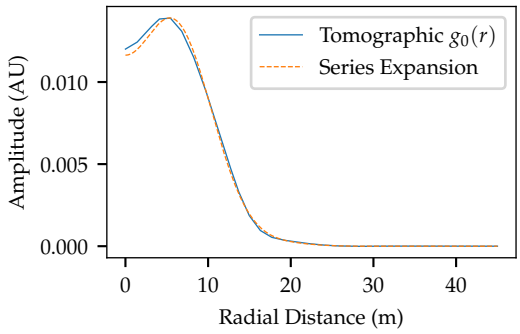


Figure 6.22: Unperturbed longitudinal distribution, $g_0(r)$, computed with tomography from the processed result in Figure 6.21. Series expansion used by PyTMCI is overlaid.

6.4.3.2 Synchrotron Tune

The synchrotron tune is given by Equation (6.1). Many of the required parameters are the same as those required for the BSRM experiment, although the RCS experiment also requires a synchronous phase. To obtain this quantity, it was assumed that the energy gained per turn was

$$E_{1\text{-turn}} = qV_{\text{rf}}N_{\text{gap}} \sin(\phi_s) \,. \tag{6.2}$$

$E_{1\text{-turn}}$ was estimated at time steps through the RCS cycle using the beam's measured revolution frequency to compute changes in kinetic energy. For each time step, ϕ_s was found from the average change in kinetic energy per turn and average V_{rf}. Figure 6.23 shows the computed kinetic energy versus time and the inferred synchrotron tune versus time through the RCS cycle. To predict a synchrotron tune as a function of time for calculations, linear interpolation was used between the plotted points.

6.4.3.3 Betatron Frequency

As explained in Section 6.2.2, the betatron frequency was interpreted as the frequency associated with the most unstable coherent mode, which will have the largest sideband amplitude. Sidebands were first identified from the spectrogram of a BPM difference

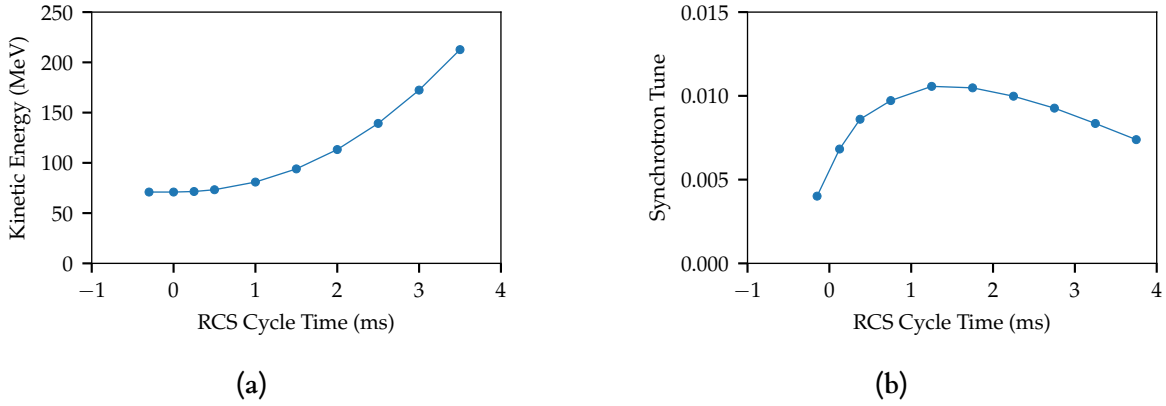


Figure 6.23: Kinetic energy computed from the measured revolution frequency (a), and the synchrotron tune (b) computed from Equation (6.1) by inferring a synchronous phase from the average energy gain per turn.

signal shown in Figure 6.24. As well as a baseband peak, sidebands can be seen around both revolution and RF harmonics. These are easily identified as their frequencies change with the revolution frequency and ramp rapidly from around 2 ms into the RCS cycle. The betatron tune will be computed from the frequency of one sideband.

Whilst any sideband can be used in principle, the straight horizontal lines below ~ 4 MHz are associated with non-beam induced noise and could be a source of systematic error. For this reason, the lower sideband around the third RF harmonic, which has a frequency of nearly 4 MHz at 0 ms will be used.

To compute the sideband frequency, BPM difference data was split into 100 µs segments. Changes in beam parameters were anticipated to be small over this period. A bandpass filter was applied to each of the time segments to suppress other narrowband signals, such as the nearby RF harmonic. Filtered data was then processed with the NAFF algorithm, and the dominant harmonic taken as the sideband frequency. Final values were taken from the dataset with the best signal-to-noise ratio on the sideband amplitude; pulse-to-pulse variations of tune were expected to be small. The sideband frequencies are plotted as points on the spectrogram and are seen to follow the sideband until the beam stabilises from ~ 3 ms.

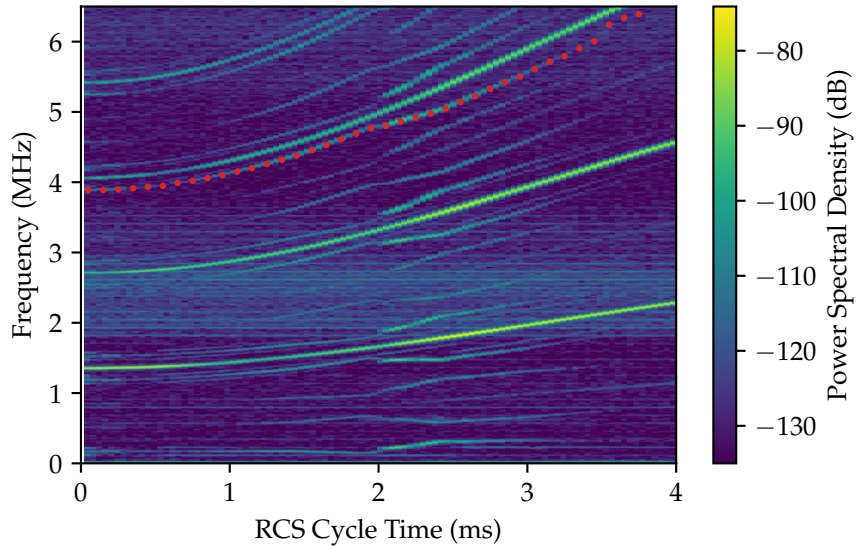


Figure 6.24: Spectrogram of a BPM difference signal during RCS experiment.

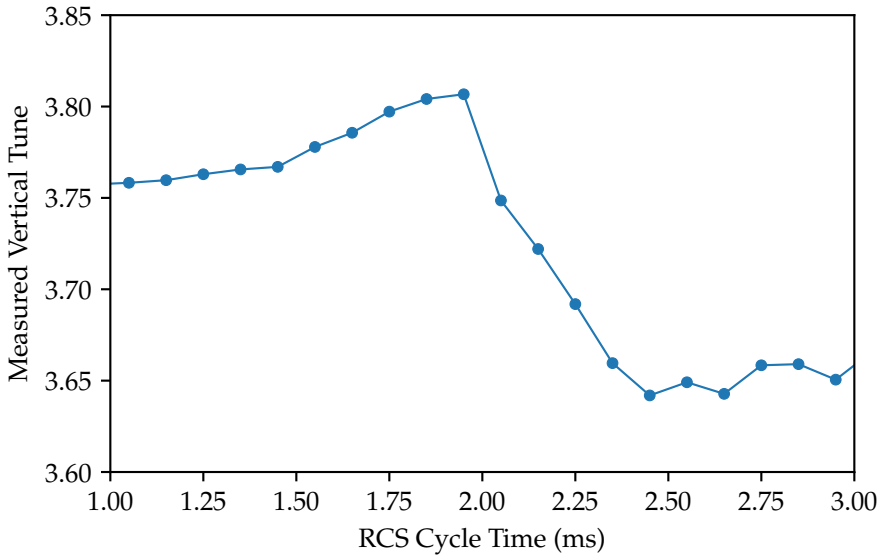


Figure 6.25: Measured vertical tunes versus cycle time for RCS experiment.

A fractional vertical tune was computed from the separation of the sideband from its revolution harmonic [218], and the total tune shown in Figure 6.25 computed by assuming the integer part to be its nominal value. Linear interpolation of the measured tune was used as an input to PyTMCI.

6.4.3.4 Bunch Intensity

The intensity-monitor signal in Figure 6.18 shows a falling intensity for the first $\approx$ $2.5\,\mathrm{ms}$ of the RCS cycle. The associated beam-losses began before the large-amplitude coherent motion between 2.0 and $2.25\,\mathrm{ms}$. This suggests that beam-losses which began before $2.0\,\mathrm{ms}$ were not associated with coherent instabilities. Since the rate of intensity change is comparatively slow at $2\,\mathrm{ms}$, a constant intensity will be taken from that time. This gives the number of protons-per-bunch as 8.5×10^{12}.

6.4.3.5 Number of Radial and Azimuthal Modes

To ensure sufficient accuracy of PyTMCI solutions, the number of radial and azimuthal modes was chosen by observing convergence using the impedance model of Chapter 5 with no uncertainties specified. Calculations were performed using quasi-stationary parameters taken throughout the unstable time period between 1.8 and $2.4\,\mathrm{ms}$. Growth rate versus RCS cycle time is shown in Figure 6.26 for a number of settings. The maximum number of modes was increased until the peak growth rate varied by less than $10\,\%$ between subsequent runs. This was achieved with 10 radial modes and 20 azimuthal modes, which are the maximum values currently available in PyTMCI. These values will be used in all subsequent calculations.

The maximum number of harmonics at which to sample the impedance model was also increased until the peak growth rate converged. Growth rate versus baseband frequency is shown in Figure 6.27 for several numbers of harmonics. In this case, there was less than $1\,\%$ difference between results with 1001 and 21 harmonics. Since the number of harmonics did not significantly affect computation time, 1001 harmonics were used for all computations.

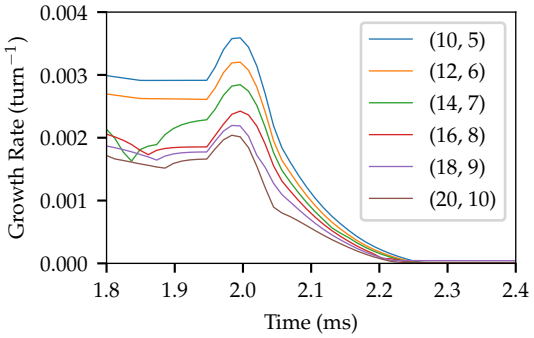


Figure 6.26: Growth rate of the most unstable mode versus RCS cycle time. Legend shows the number of azimuthal and radial modes respectively used in each calculation.

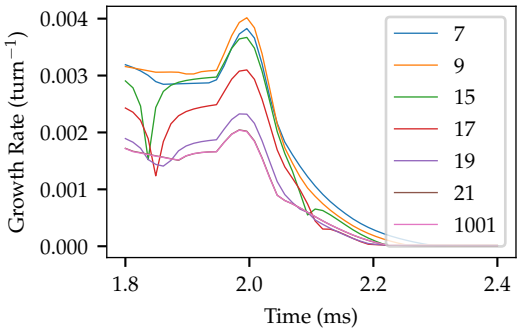


Figure 6.27: Growth rate of the most unstable mode versus RCS cycle time. Legend shows the number of harmonics used in each calculation.

6.4.4 Comparison of PyTMCI and Experimental Results

6.4.4.1 Instability Growth Rates

Figure 6.28 shows the predicted growth rate versus time through the RCS cycle. The mean growth rate is computed from a repeat of 100 PyTMCI calculations per time setting, and error bars represent the standard deviation. As was also done for the BSRM experiment, uncertainties on the RF screen resonators were included by evaluating the resonator impedance with parameters that were sampled from a randomly generated normal distribution derived from Table 5.8. Other sources of uncertainty were considered negligible compared to those on the RF screen resonators. A peak in growth rate is predicted to occur at around 2 ms, having a growth rate of $(1.9 \pm 0.3) \times 10^{-3}\text{turn}^{-1}$, corresponding to a characteristic growth time of (0.6 ± 0.1) ms. This peak is narrow, so that by 2.2 ms, the growth rate has fallen to 5 % of its maximum value.

6.4.4.2 Instability Distribution

Using parameters from the most unstable time point, 1.98 ms, ($\beta = 0.45$, $Q_V = 3.79$, $\nu_s = 0.01$) the longitudinal distribution of the dipole moment, $g_1(r, \phi)$, of the most unstable mode was computed to within a constant scaling parameter. This distribution

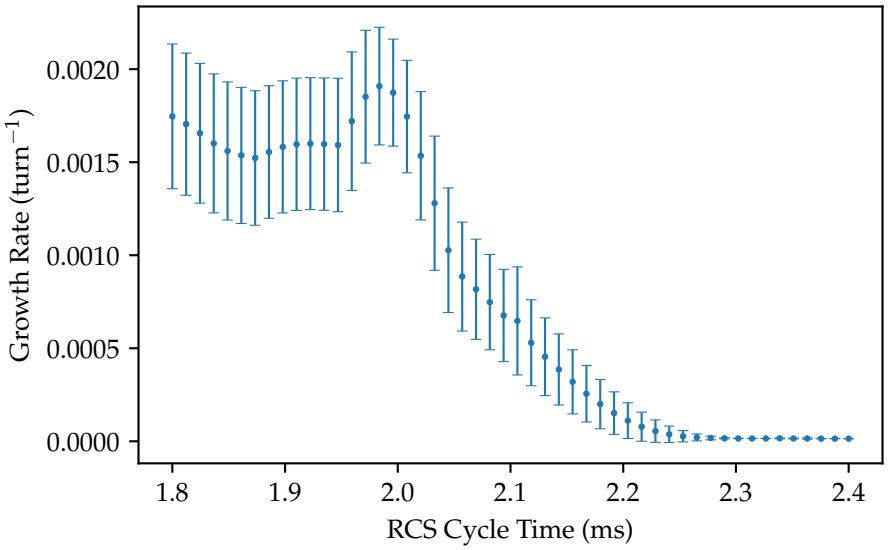
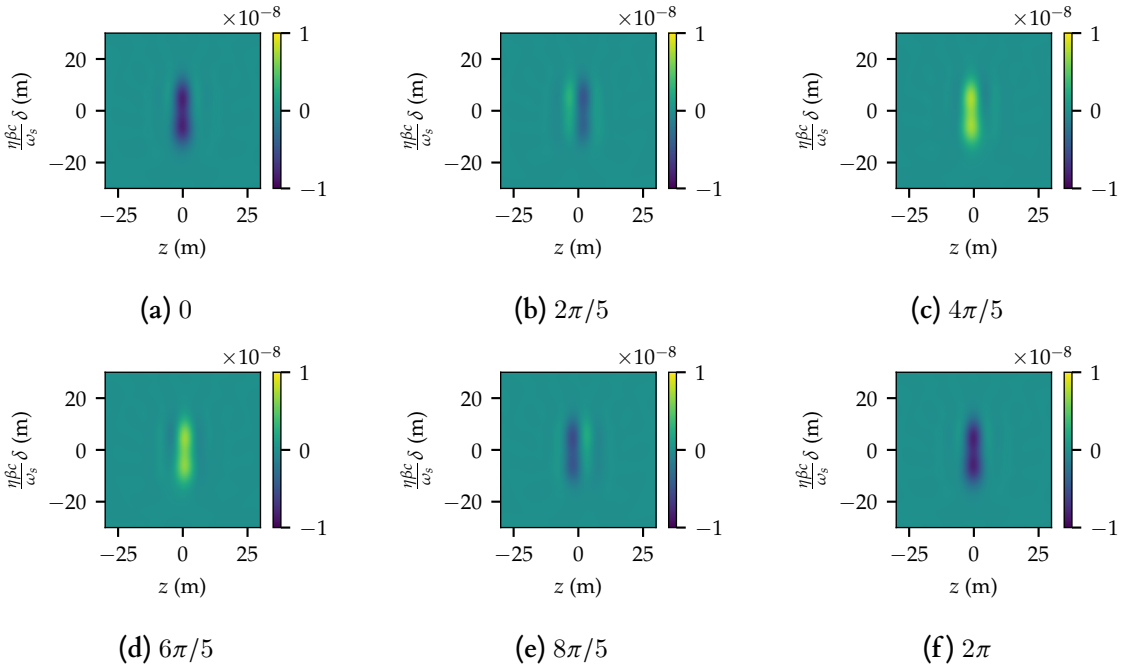


Figure 6.28: Growth rate computed by PyTMCI versus RCS cycle time. Points indicate the mean of 100 repeat calculations and error bars are the standard deviation.

and its evolution through a single period is shown in Figure 6.29, whilst its projection accumulated over 20-turns is shown in Figure 6.30. Although the projection may resemble a head-tail mode, it can be seen from the phase-space distribution that the coherent offset is not described by a rotation as would be expected for a decoupled head-tail mode, suggesting that some form of mode coupling is taking place. Instead, the coherent offset travels along the bunch, from tail-to-head, with a peak amplitude near the centre of the bunch.

The first node in Figure 6.30 occurs at $|z| < 5.5\,\mathrm{m}$, despite the projected line density of the unperturbed distribution having RMS of $7.5\,\mathrm{m}$. Since the amplitude of this central lobe is almost an order-of-magnitude larger than the surrounding lobes, it could be claimed that less than 1σ of the bunch is predicted to oscillate with significant amplitude. This behaviour was also observed experimentally in Figure 6.20, where it can clearly be seen that an oscillation is superimposed on top of only part of a non-oscillating offset. The distribution of this mode, with a single large-amplitude peak near the centre of the bunch, was also qualitatively similar to that seen during the RCS experiment.



(a) 0 (b) $2\pi/5$ (c) $4\pi/5$

(d) $6\pi/5$ (e) $8\pi/5$ (f) 2π

Figure 6.29: Longitudinal dipole distribution in longitudinal phase space, $g_1(r, \phi)$, for the most unstable mode of the most unstable time point. Plots show an advancing phase as indicated by captions. Colours indicate a quantity proportional to vertical dipole moment in arbitrary units.

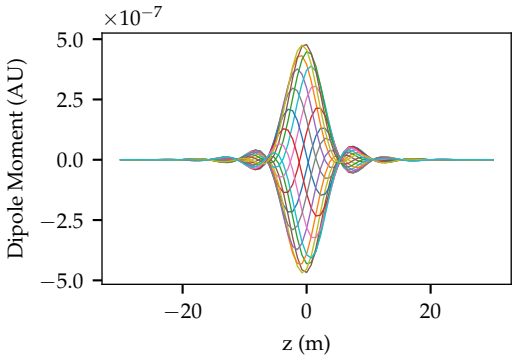


Figure 6.30: Each line shows the dipole moment from Figure 6.29 projected onto the z axis for a single turn, with twenty turns overlaid. Line colours assist with identification of a single turn.

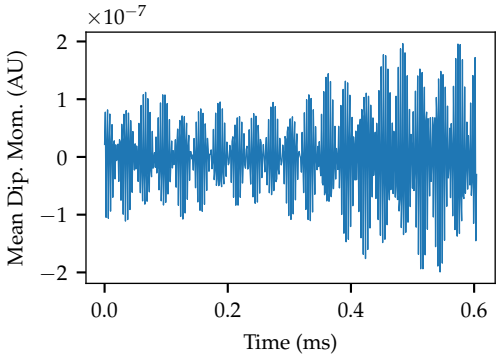


Figure 6.31: Mean dipole moment per-turn, plotted for 500 turns, with multiple modes initially allowed to grow for 300 turns before plotting. Shows a beating structure.

As with the BSRM experiment, several modes are predicted to be simultaneously unstable. Two modes are predicted to have a characteristic growth times of $< 1.1\,\mathrm{ms}$, and since coherent oscillations were observed for $< 1\,\mathrm{ms}$, a single mode may not have dominated the observed longitudinal distributions in Figure 6.20. To draw comparisons between the observed and predicted longitudinal structures, it is necessary to include more than a single mode in the calculated distributions. This could potentially explain the observed beating structure. Figure 6.31 shows the mean dipole moment of each turn, computed by PyTMCI from the three most unstable modes. Whilst the observed beat period does not matched that observed on ISIS, a beating envelope is clear.

Figure 6.32 shows the time evolution of the predicted vertical dipole moment along the bunch, computed from the sum of the same three most unstable modes. Thirty subsequent turns are overlaid on each plot, with mode amplitudes initially allowed to grow over 300 turns. Time evolution of the distribution can be understood by comparing subsequent plots. From turn 360, the largest amplitude lobe occurs in the tail of the bunch, whilst no large-amplitude lobes can be seen from turn 480. From turn 570, the largest amplitude lobe can be seen near the centre of the bunch. It is therefore observed that when the amplitudes of several modes grow simultaneously, nodes and lobes in the coherent offset can be seen to oscillate along the bunch. This general behaviour was observed experimentally in Figure 6.20, although its exact features will depend on the relative frequencies of the unstable modes, their growth rates and associated dipole distributions.

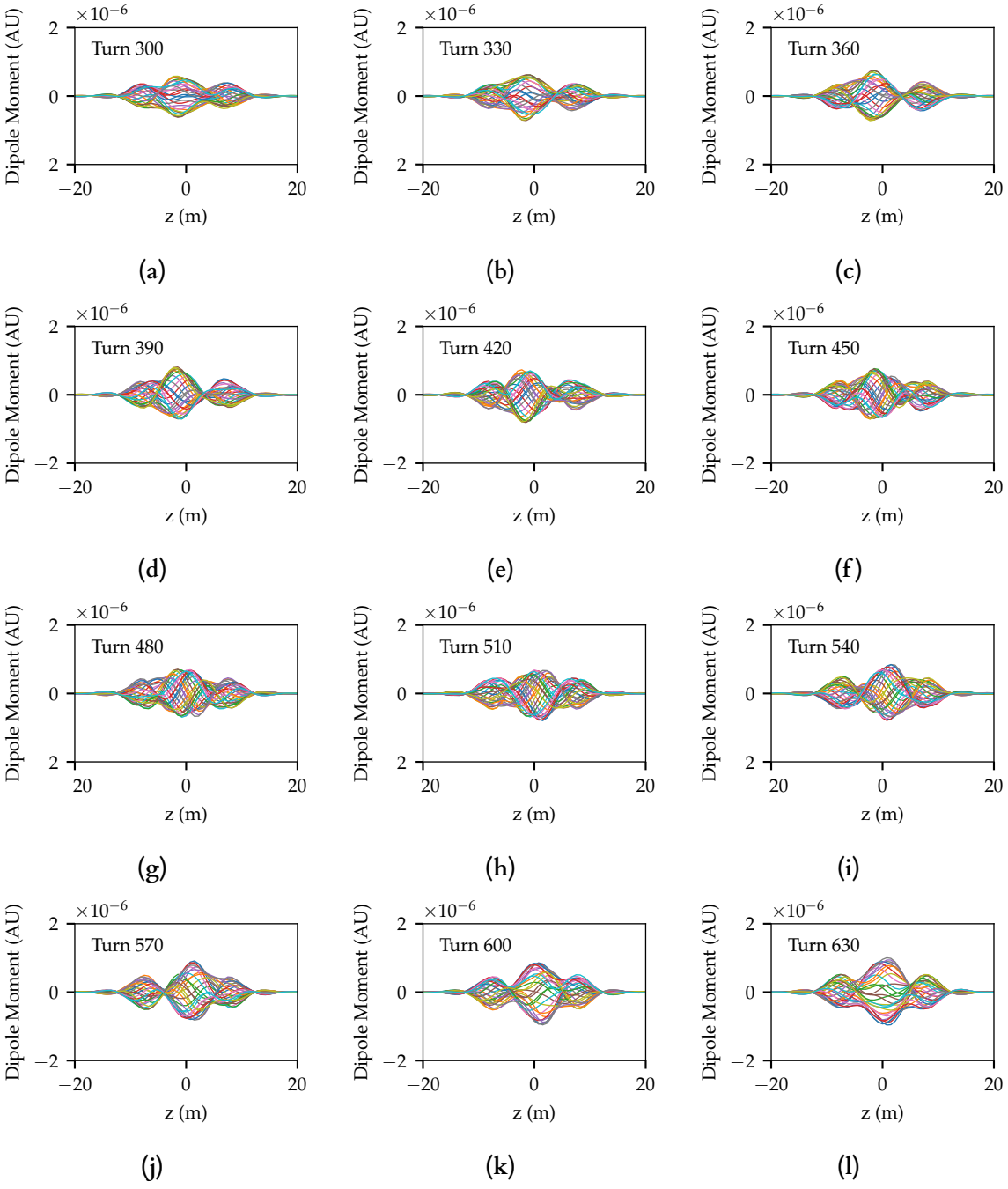


Figure 6.32: Sum of the vertical dipole moment along a bunch for the three most unstable modes, computed by PyTMCI at the RCS cycle time predicted to have the largest growth rate. Each line represents the distribution on a single turn, 30 consecutive turns are overlaid and colours are to distinguish each turn. Evolution of the distribution in time can be understood by looking at subsequent plots; the inset text indicates the turn number of the first plotted line.

6.4.5 PyTMCI Predictions for Higher Intensity

ISIS typically accelerates $\sim 1.2 \times 10^{13}$ protons-per-bunch, whilst the bunch intensity in this RCS experiment was reduced to 8.5×10^{12}. To understand how predictions for this experiment might relate to an operational scenario, mode frequencies have been computed as a function of bunch intensity with other input parameters taken as those from the RCS experiment at 2 ms ($\beta = 0.45$, $Q_V = 3.78$, $\nu_s = 0.01$). Figure 6.33 shows the derived quantity of the head-tail mode frequency, Ω. The imaginary part of this quantity is proportional to the instability growth rate, so that a positive imaginary part indicates a mode with a growing amplitude. It can be seen that above $\sim 1 \times 10^{13}$ ppb, the growth rate of two unstable modes rises rapidly. With operational intensities the characteristic growth time of these modes is predicted to be ~ 0.36 ms. This is within the 0.2-0.6 ms growth time range that is typical [80].

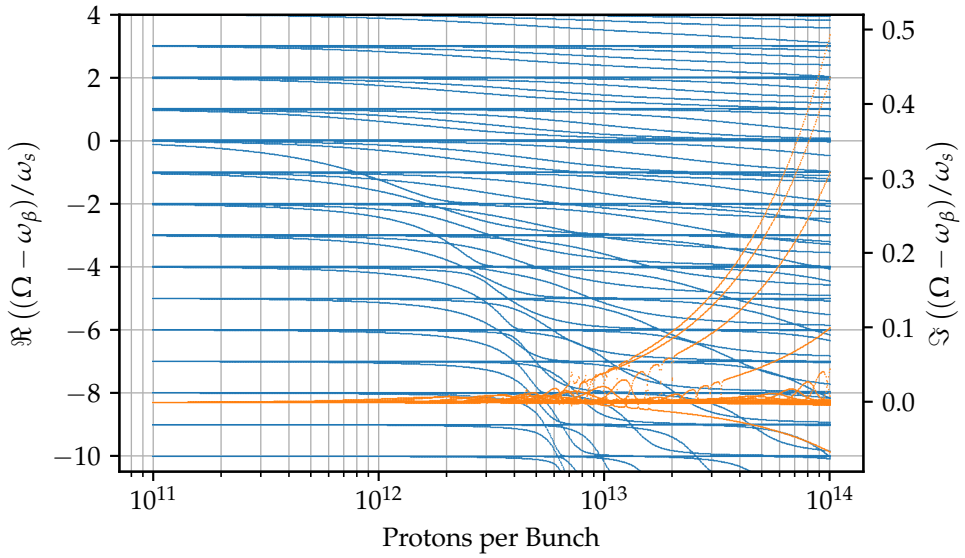


Figure 6.33: Normalised coherent mode frequencies versus protons-per-bunch. Normalised oscillation frequency is in blue, and normalised growth rates in orange.

6.4.6 Discussion of RCS Results

Since changes to many beam parameters cannot be neglected in an RCS, quantitative predictions aren't possible with the theory outlined in Chapter 4. Nevertheless, to investigate whether the impedance model outlined in Chapter 5 could partially explain the observed coherent instabilities, a quasi-stationary approach was taken by performing PyTMCI calculations with fixed beam parameters taken from different times through the RCS cycle. Order-of-magnitude agreement is likely to be the limit of what can be achieved with this approach, and a dedicated RCS theory or sophisticated tracking simulations would be required for more accurate predictions. Despite treating this dynamic scenario with a quasi-stationary model, some features of the experimental observations were reproduced, which has allowed a qualitative physical interpretation of the experimental results.

Figure 6.28 shows that the predicted growth rate will peak $\sim 2\,\mathrm{ms}$ into the RCS cycle, which was reproduced in the RCS experiment, and is routinely seen during operations. This key result is the first time that a peak in growth rate has been predicted to occur at $2\,\mathrm{ms}$ through the ISIS RCS cycle. The impedance model developed in Chapter 5 now offers a physical interpretation of this behaviour. By overlaying the real part of the impedance with the lowest frequency betatron sideband through the RCS cycle as in Figure 6.34, it can be seen that the sideband remains on the side of the $\sim 200\,\mathrm{kHz}$ peak until around $2\,\mathrm{ms}$, after which it crosses over the maximum. Because this new impedance model was derived from equipment properties, we can now attribute the instability to the source of this peak, which are primarily the singlet and module-13 RF screens.

The rapid change of the sideband frequency at this time in the RCS cycle is due to the tune-ramp, which was introduced to reduce beam-losses associated with the instability. The impedance model now offers a physical explanation for why this approach was effective. Ramping the tune down reduces the time where the sideband remains on the $\sim 200\,\mathrm{kHz}$ peak, and moves it over to higher frequencies where the impedance falls off

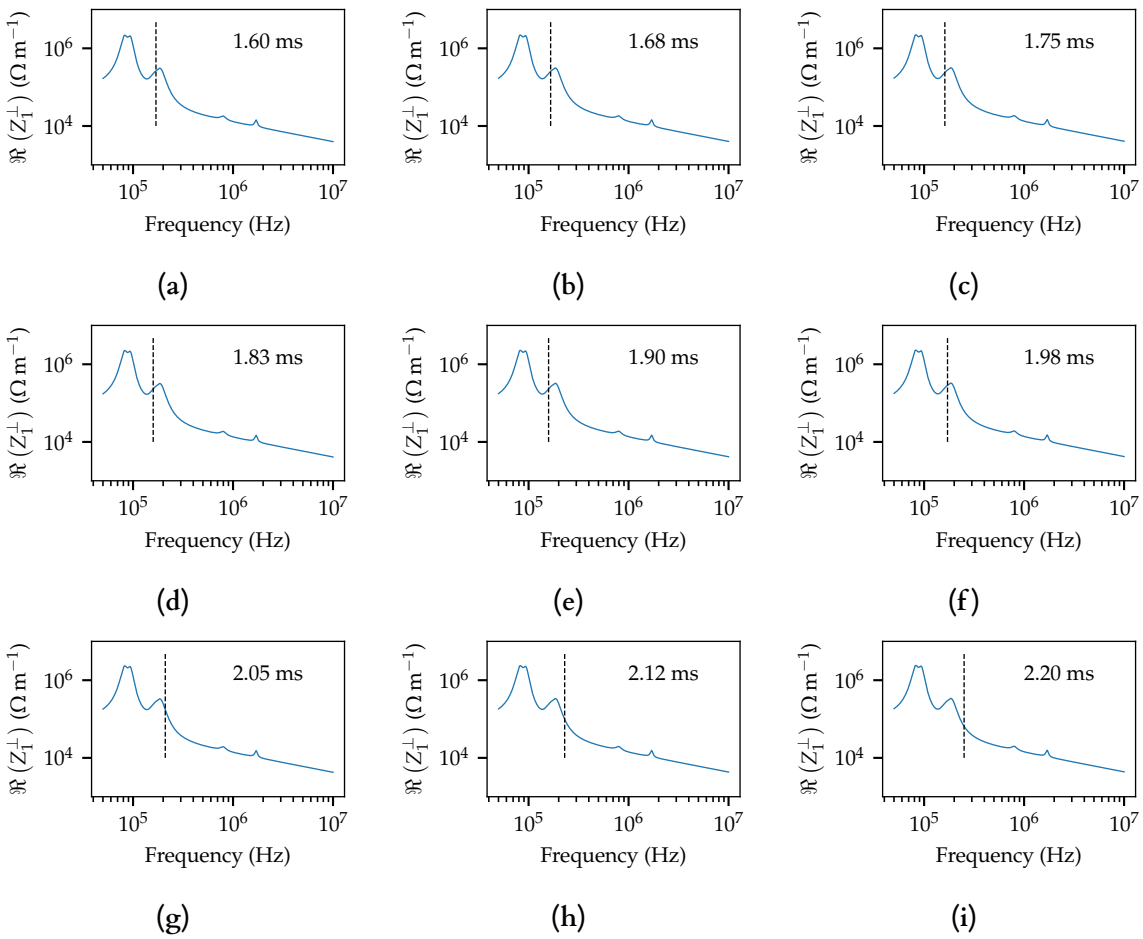


Figure 6.34: Sum of the separate impedance contributions from Chapter 5, overlaid with a vertical line indicating the measured baseband frequency at different time points throughout the RCS experiment.

rapidly. Figure 6.28 shows that by $\sim 2.2\,\mathrm{ms}$, growth rates are predicted to fall by an order of magnitude compared to the peak value.

Although an instability was observed at $2\,\mathrm{ms}$, it did not grow for a sufficient time to measure a growth rate, so no quantitative comparisons can be drawn with Figure 6.28. Nevertheless, comparisons can be drawn with growth times that are typically observed in operations, which are in the range of 0.2-$0.6\,\mathrm{ms}$ [80]. The fastest growing mode predicted by PyTMCI for this experiment was consistent with this range, but at the top end. To investigate the possibility that this lower growth rate was due to the reduced

intensity, growth rates were computed at $2\,\mathrm{ms}$ as a function of beam intensity in Figure 6.33. This predicted instability growth rates that are consistent with the observed range at operational intensities, despite neglecting direct space-charge. This is the first time that analytical predictions based on a rigorously derived impedance model have achieved this level of accuracy for the $2\,\mathrm{ms}$ instability on ISIS.

Beating of the filtered BPM difference signal in Figure 6.19, could be explained if more than one mode was simultaneously unstable during the RCS experiment. Beating of a beam's coherent offset has previously been reported in machines with multiple unstable modes [219], and was also predicted by PyTMCI in Figure 6.31. Interference between these unstable modes could explain why the location of the peak in the dipole-moment distribution was seen to oscillate between the centre and the head of the bunch in Figure 6.20, and similar behaviour was also observed in the PyTMCI results of Figure 6.32.

Previous studies have noted that only part of the ISIS bunch is seen to oscillate during an instability [80], and Figure 6.20 shows that this was also the case during this experiment. Simplified versions of the theory outlined in Chapter 4 predict that whole bunches will oscillate, but this is not required by the more general version of the theory applied here. For the dipole moment distribution of the most unstable mode, PyTMCI has predicted that the large-amplitude central lobe will be fully contained within $\pm \sim 5.5\,\mathrm{m}$, whilst the standard deviation of the unperturbed line charge density input was $\sim 7.5\,\mathrm{m}$. PyTMCI has therefore predicted that only part of the bunch will oscillate with a large amplitude. Furthermore, Figure 6.29 shows a dipole moment distribution which is not a decoupled head-tail mode, and whilst a classification of the instability is beyond the scope of this thesis, PyTMCI is predicting mode coupling. Whilst earlier studies have posited that ISIS may suffer from a transverse-mode coupling instability (TMCI), this is the first analytical prediction that coupling between azimuthal modes are significant on ISIS.

6.5 Summary and Conclusion

This chapter compared the predictions of PyTMCI with experimental results from ISIS in BSRM and in RCS mode with single harmonic RF. Section 6.2.1 introduced a number of assumptions to make this comparison, which included: assuming instability mode frequencies, adopting a quasi-stationary model and neglecting direct space-charge.

In the BSRM experiment, the validity of this last assumption was improved by reducing the intensity to produce a space-charge parameter of $\sim 3-5$. A key result of this experiment was Figure 6.11, where PyTMCI predicted the instability growth rate to within an order of magnitude, and its functional dependence with betatron tune. The impedance model from Chapter 5, allowed Figure 6.14 to offer a new understanding of this behaviour, and has identified RF screens in the ISIS dipoles and doublets as being primarily responsible for the $85\,\mathrm{kHz}$ peak in growth rate.

A second experiment was performed in RCS mode to apply PyTMCI and the new impedance model to the instability which limits ISIS performance. Whilst neglecting direct space-charge is understood to be a systematic limitation in this case, important new results were obtained. A key result was Figure 6.28, where PyTMCI predicted a peak in instability growth rate at $2\,\mathrm{ms}$ through the RCS cycle, which agrees with operational experience. Section 6.4.5 showed that for a full intensity beam, PyTMCI predictions of growth rate match observations to within an order of magnitude. Figure 6.34 offers a physical interpretation of why the growth rate peaks, as the baseband betatron sideband crosses the $200\,\mathrm{kHz}$ impedance peak at that time. The impedance model of Chapter 5 identifies the source of that peak as RF screens in module-13 and the singlet quadrupoles.

The second thesis objective is considered to have been achieved. Although tracking with direct space-charge is likely to make more accurate predictions, the theory outlined in Chapter 4 can make partially accurate predictions for ISIS provided the assumptions of Section 6.2 are made. The new knowledge obtained from these studies will now go on to inform mitigation approaches in Chapter 7.

It sounds plausible enough tonight, but wait until tomorrow.
Wait for the common sense of the morning.

— H.G. Wells, "The Time Machine"

7 Instability Mitigation on ISIS

7.1 Introduction

It has been demonstrated that the impedance model introduced in Chapter 5 can be used to reproduce many features of the coherent vertical instabilities observed on ISIS. Although this model is largely based on finite element simulations, some bench impedance measurements have proven largely consistent with the simulations when some small resistive elements were included. The evidence presented in this thesis strongly indicates that the RF-screens are the main drivers of the 2 ms instability and the source of the ~ 85 kHz resonator impedance.

It is unclear whether a fundamental redesign of the screens is possible, given that all high-intensity RCSs since ISIS have adopted similar structures [208, 55], but such a redesign will not be discussed here because it would probably be prohibitively expensive and operationally intrusive. The aim of this chapter is therefore to review less intrusive, less expensive modifications that might reduce the growth rate of the 2 ms instability. One such possible modification is to move their resonant frequencies.

7.2 Impedance Optimisation on ISIS

The theory of Chapter 4 used the transverse impedance, sampled at $(p\omega_0 + \omega_\beta + l\omega_s)$, where p and l are integers, to compute elements of the interaction matrix. If the resonant frequencies were moved far from these samples, then their contribution to the sums in Equation (4.45) could be reduced, improving beam stability. On ISIS, the lowest frequency sample is close to the vertical baseband betatron sideband, which is $\sim 90\,\text{kHz}$ at injection but then increases as the beam accelerates, as shown in Figure 7.1. If the resonant frequencies of the RF screens were moved to below $90\,\text{kHz}$ then their impedances would not contribute to the sums at any time through the RCS cycle.

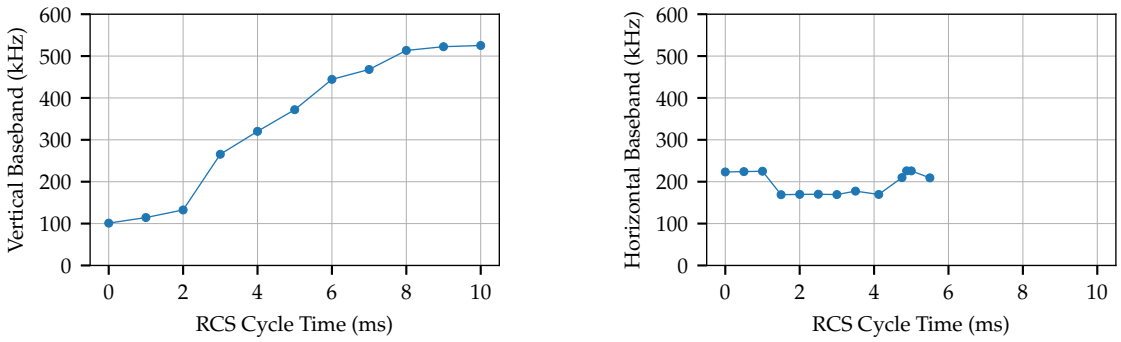


Figure 7.1: Measured baseband frequencies during an RCS cycle. These were used to compute the tunes in Figure 2.9 [85].

7.3 Impedance Optimisation with Capacitors

If the RF screens act like a resonating RLC circuit, then their resonant frequency would be given by $1/\sqrt{2\pi LC}$ [144]. Whilst the inductance, L, in this equation is likely associated with the geometry of the screen, the capacitance, C, is expected to be primarily associated with the lumped capacitors. It follows that the resonant frequency could be changed by changing the capacitor values.

To verify this, a series of low-frequency CST simulations of the singlet quadrupole RF screen have been performed with different capacitors. In each case, the resonant frequency was found by fitting the resonator impedance to the computed transverse impedance. Figure 7.2 shows the resonant frequency for each simulated capacitor value, which approximately follows a $1/\sqrt{C}$ relationship; the discrepancy for larger capacitances could be because resistive-wall contributions were not subtracted. This figure confirm that the frequency can be moved by changing the capacitors and that they roughly follow $\propto 1/\sqrt{C}$, which will be tested experimentally in the next section.

7.3.1 Experimental Verification

This result was verified experimentally on the singlet RF screen by exchanging the 0.1 µF capacitors with 1 µF, and performing a three-turn probe coil measurement as described in Section 5.3.4.1. The resonant frequency would be expected to reduce from ~ 190 kHz to ~ 60 kHz if it followed $1/\sqrt{C}$. Both frequencies are indicated on the measured real part of the impedance in Figure 7.3. The measured peak is closer to 75 kHz, indicating that there are other sources of capacitance which define the resonant frequency, but that the general approach works. The real part of the impedance at this peak reduced to around 10 kΩ m^{-1}, around 1/3 of the original peak.

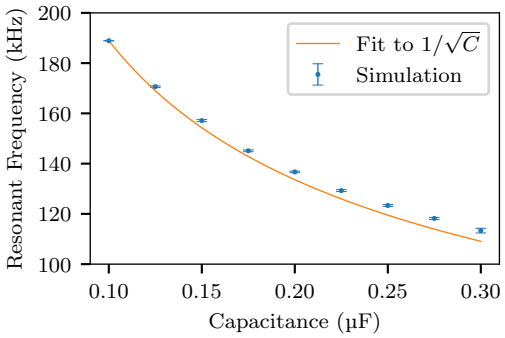


Figure 7.2: Resonant frequencies of the singlet quadrupole RF screen with different capacitor values.

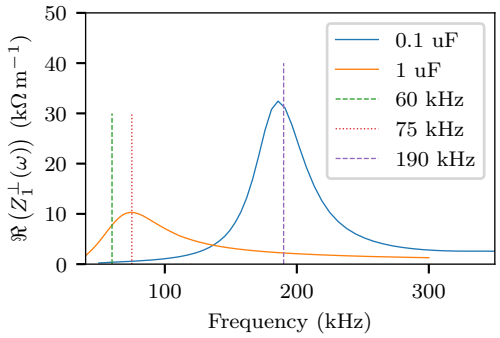


Figure 7.3: Measured Re $(Z_1^{\perp}(\omega))$ of the singlet quadrupole RF screen with original 0.1 µF and 1 µF capacitors. Vertical lines indicate key frequencies.

7.4 Instability Predictions with Optimised Impedance

Following from the assumption that the $1/\sqrt{C}$ relationship observed in the previous section applies for all RF screens, PyTMCI has been used to estimate the impact of reducing all RF screen resonant frequencies by a factor of $\sqrt{10} \approx 3$. Growth rates were computed between 1.8 and $2.4\,\mathrm{ms}$ through the RCS cycle, with parameters were taken from the RCS experiment of Section 6.4.

In this case, the convergence criteria of $< 10\,\%$ change in peak growth rate between calculations with different numbers of azimuthal and radial modes was not achieved. In-part this was because all calculated growth rates were between 2 and 5 orders of magnitude lower than the peak in Figure 6.28, making convergence more numerically challenging. Using the maximum numbers of azimuthal and radial modes currently available (20 and 10 respectively), produces the growth rates throughout the RCS cycle shown in Figure 7.4. The numerical quantities shown would predict a characteristic growth time that is longer than an RCS cycle, which would be effectively a full mitigation for ISIS operations. Whilst full convergence has not been achieved, the prediction of order-of-magnitude reductions in growth rate is expected to remain valid.

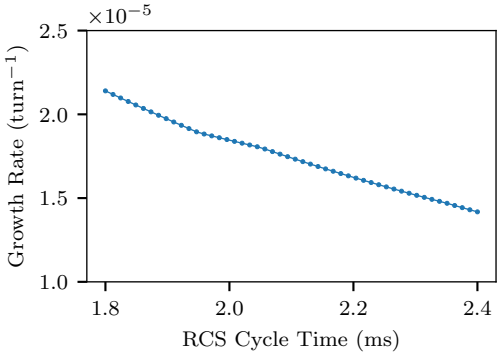


Figure 7.4: Growth rates calculated with PyTMCI for the RCS experiment described in Section 6.4, but with the resonant frequencies of the RF screens reduced by a factor of $\sqrt{10}$. Computed using the maximum number of azimuthal and radial modes currently available.

7.5 Summary and Conclusion

It is suggested that the $2\,\mathrm{ms}$ head-tail instability on ISIS might be completely mitigated if capacitors in all the RF screens were changed to reduce their resonant frequencies by a factor of ~ 3. While the resonant frequency does not exactly follow $1/\sqrt{C}$, it is suggested that increasing all capacitances by a factor of ten would achieve this; especially given the reduction in peak amplitude observed in Figure 7.3. Verification of these predictions is beyond the scope of this thesis, but initial changes to capacitors have now been made on ISIS, with promising early results [220]. Their effect on beam stability will continue to be investigated in future studies.

Although the third thesis objective has been achieved, only one mitigation method has been discussed here. The results presented in this thesis have allowed the onset of the instability to be understood in terms of the impedance model of Chapter 5, which opens up new possibilities for improving beam stability. For example, it is now possible that the vertical tune programme could be optimised through the RCS cycle to minimise the sampled impedance. Although the tune is constrained by other factors, an optimised program could offer a simple and cheap approach to improving beam instability. Developing such a program will also be a focus of future studies.

Well, here at last, dear friends, on the shores of the Sea comes the end of our fellowship in Middle-earth. Go in peace! I will not say: do not weep; for not all tears are an evil.

— J.R.R Tolkien, "The Return of the King"

8 Conclusion

8.1 Summary and Conclusions

Introduction and Thesis Objectives

Every short-pulse spallation neutron source operating today is either based on a high intensity RCS or accumulator ring. The average beam power of these facilities is up to three orders of magnitude greater than those built in the 1970's and 80's, and even higher powers are expected in the future. Without efforts to mitigate coherent beam instabilities, growth rates are likely to increase with intensity, which could limit performance.

At least four high-intensity facilities currently operating have reported coherent instabilities. Chapter 1 suggested that if the models of these machines are otherwise complete and accurate, then this would imply there were either impedance sources yet to be identified, or that the theory of coherent instabilities was not making sufficiently accurate predictions. Understanding instabilities at existing facilities was proposed as a potential solution, and attention was turned to the 2 ms vertical instability at ISIS. The objectives of the thesis were then set out as: generating an impedance model for ISIS, understanding whether the accepted theory of coherent transverse instabilities makes accurate predictions for ISIS and identifying ways of improving beam stability on ISIS.

New Tools and Methodologies for Determining Impedances

To build the foundations required to achieve these objectives, Chapters 3 reviewed the analytical treatments of wake fields and impedances. Earlier studies had identified a low-frequency resonator impedance on ISIS [80], so evaluating low-frequency impedances became a focus. To address the issue of low-frequency EM fields penetrating conductors, RWAL was developed in Section 3.4 to compute the transverse impedance of multi-layer cylindrical structures. For more complex structures, a technique was developed in Section 3.3.2 to find the transverse impedance from low-frequency CST simulations. These tools were used extensively in later chapters.

New Tools for Understanding Coherent Instabilities

Chapter 4 used the impedance concept to describe coherent beam stability. Earlier applications of instability theory on ISIS had made a number of assumptions that are not present in the general theory. To address this, a new Vlasov solver, PyTMCI [119] was developed to apply the most general version of the theory to ISIS. Benchmarks of PyTMCI demonstrated excellent agreement with tracking simulations in Section 4.2.

The ISIS LF Driving Impedance Model

To apply PyTMCI to ISIS, it was necessary to develop a new vertical driving impedance model with a focus on low frequencies, which was built up in Chapter 5. A series of resonator impedances were identified on the RF screens that are used inside all AC magnets at ISIS. Bench measurements were described in Section 5.3.4 which confirmed the existence of these resonances on two types of RF screens. Measured quality factors and amplitudes differed from simulation, but could be partially reproduced by including small resistive elements in the CST model. Resonator impedances from these simulations were summarised in Table 5.8.

Impedance contributions of other equipment were also described in Chapter 5, including resistive-wall and indirect space-charge. Bench measurements of the ISIS extraction kickers were presented in Section 5.5, but it was found that their terminating resistors suppress resonant impedances on their feeder cables. The RF screens were found to dominate the real part of the overall impedance model in Figure 5.69, which is the most detailed model ever developed for ISIS. Crucially, the RF screens contribute large peaks at $\sim$ 85 and $\sim$ 200 kHz.

Predictions and Experimental Comparisons on ISIS

In Chapter 6, the newly developed impedance model was used as an input to PyTMCI, and its predictions compared with experiments. In BSRM, instability growth rates were measured as a function of vertical tune [80]. The peak predicted growth rate in Figure 6.11 occurred around the same frequency as observed, and its amplitude was the same order of magnitude as the experimentally observed value. This discrepancy was thought to be associated with the simplified analytical model, but the general agreement between theory and experiment was considered to be excellent. Although the distribution of the dipole moment along the bunch was not well predicted, PyTMCI did predict that relatively small changes in tune would produce very different distributions, which was observed experimentally.

A second experiment, carried out in RCS mode but with the second harmonic cavities disabled, was more challenging to compare with PyTMCI because the baseband betatron sideband displayed a beating amplitude. Nevertheless, in Figure 6.28 PyTMCI predicted a peak in growth rate at $\sim$ 2 ms, with a characteristic time at the top end of observations during routine operations [80]. When differences in intensity were accounted for, the predicted growth time was within the typically observed range. The predicted dipole moment distribution along the bunch showed some similarity with observation, most notably that only part of the bunch is predicted to oscillate.

In both BSRM and RCS experiments, order-of-magnitude levels of agreement in the instability growth rates were observed with PyTMCI, suggesting that the widely accepted theory of coherent transverse instabilities is at least partially applicable to ISIS. The impedance model of Chapter 5 has allowed the RF screens to be identified as the cause of the 2 ms instability, and it has identified the dipole and doublet RF screens as being responsible for the 85 kHz narrowband impedance found in earlier studies [80].

New Methods for Impedance Optimisation

The RF screens have been identified as major impedance sources on ISIS. Chapter 7 proposed and verified a method of optimising the impedance of the RF screens by changing a set of lumped capacitors. PyTMCI calculations suggested that the 2 ms instability growth rate could be reduced by orders of magnitude if all capacitors were exchanged.

Wider Impact of this Study

Since publishing the initial results for ISIS [64], resonances on similar structures at other facilities are now thought to drive instabilities [221]. With RCSs being considered for future facilities [48, 222], identifying these resonator impedances, which have been omitted from impedance models for 40 years, was an important achievement.

The targeted methodology adopted by this study allowed the RF screen impedances to be identified without characterising the impedance of all structures in ISIS. Instead, the nature of the driving impedance was understood from coasting beam impedance measurements [80], and equipment that could produce such impedances were investigated directly. The general problem was also greatly simplified by the decision not to consider direct space-charge. This meant that fast analytical calculations could be performed in-place of time-consuming tracking simulations. Whilst this no-doubt limited the accuracy of some predictions, it allowed the study to focus on the important point: finding and mitigating the source of a performance limit. This methodology can now serve as a roadmap for many future studies.

Key achievements and Contributions

- Developed technique to calculate $Z_1^{\perp}(\omega)$ for low-frequencies with CST, Section 3.3.2.
- New semi-analytical impedance calculation code, RWAL, Section 3.4.
- New Vlasov solver for coherent instabilities, PyTMCI, Section 4.1.5.
- Identified large, low-frequency resonator impedances on RF screens, Section 5.3.
- New vertical driving impedance model for ISIS RCS, Section 5.7.
- First prediction of 85 kHz peak in growth rate for ISIS in BSRM with an impedance model derived from equipment properties, Figure 6.11.
- First prediction of growth rate peak 2 ms through ISIS RCS cycle with an impedance model derived from equipment properties, Figure 6.28.
- Identified equipment responsible for these instabilities, Sections 6.3.5 and 6.4.6, now identified as instability driver at other facilities [221].
- First predictions of growth rates accurate to within an order of magnitude on ISIS, with a rigorously derived impedance model, Sections 6.3.4.1 and 6.4.4.1.
- First analytical predictions of mode coupling on ISIS, Sections 6.3.4.2 and 6.4.4.2.
- New RF screen impedance optimisation approach with capacitors, Chapter 7.

8.2 Future Work

The impedance mitigation approach described in Chapter 7 is now being trialled on some RF screens at ISIS. Beam based impedance measurements are being employed to monitor the impact of capacitor changes, and further changes could be made if beam stability is improved. Even without these changes, the impedance model of Chapter 5 will allow an optimised vertical tune programme to be developed, which could improve beam stability without any mechanical interventions.

More generally, the ISIS RCS now has a high intensity proton beam and a well defined resonator impedance, making it an excellent testing ground for studies into the exciting topic of coherent instabilities with strong direct space charge.

Appendices

A

ISIS Design Stage Impedance Reduction

The ISIS synchrotron was designed approximately a decade after the concept of beam coupling impedance was developed [91]. The widely accepted theory of coherent transverse instability had been developed more recently [98]. At that time, the impedance of key accelerator components would not have been accurately determined, and tools were more limited than today. The designers of ISIS nevertheless anticipated beam instabilities, explicitly stating:

> In the SNS [1] synchrotron, the maximum intensity achievable will probably be determined by the collective phenomena of coherent instabilities. [68]

Efforts to prevent instabilities extended to the design of individual systems such as the extraction kicker magnets. It was recognised that their transverse coupling impedance could be significant because they resembled similar devices at the Proton Synchrotron Booster (PSB), where large narrowband impedances had been measured [98]. The feeder cables of the ISIS kickers were therefore terminated with matched resistors [199], despite the associated increase in required power.

Some numerical tools for computing impedances were available, and the designers of ISIS made full use of these. For example, it was recognised that without a conducting vacuum vessel inside the main magnets, the beam's EM fields would be exposed to the pole faces of the laminated magnets. To prevent this, a series of conducting RF screens were envisaged to shield the magnets, whilst limiting the induced 50 Hz Eddy currents [184]. To understand whether these screens should be placed inside or outside the

[1] ISIS was originally known as the Spallation Neutron Source, SNS.

ceramic vessels, a set of two-layer, cylindrical resistive-wall impedance calculations were made with the LUWAT code [223]; the output is shown in Figure A.1. Case A, which consisted of a ceramic layer surrounded by a semi-infinite conductor had a larger imaginary impedance than Case B which only consisted of a conductor. Resonant impedances at frequencies exceeding 1 GHz were also predicted in Case A. On this basis, and with some other practical considerations, it was decided that conducting RF screens would be installed inside the ceramic vacuum vessels, despite the mechanical complexity.

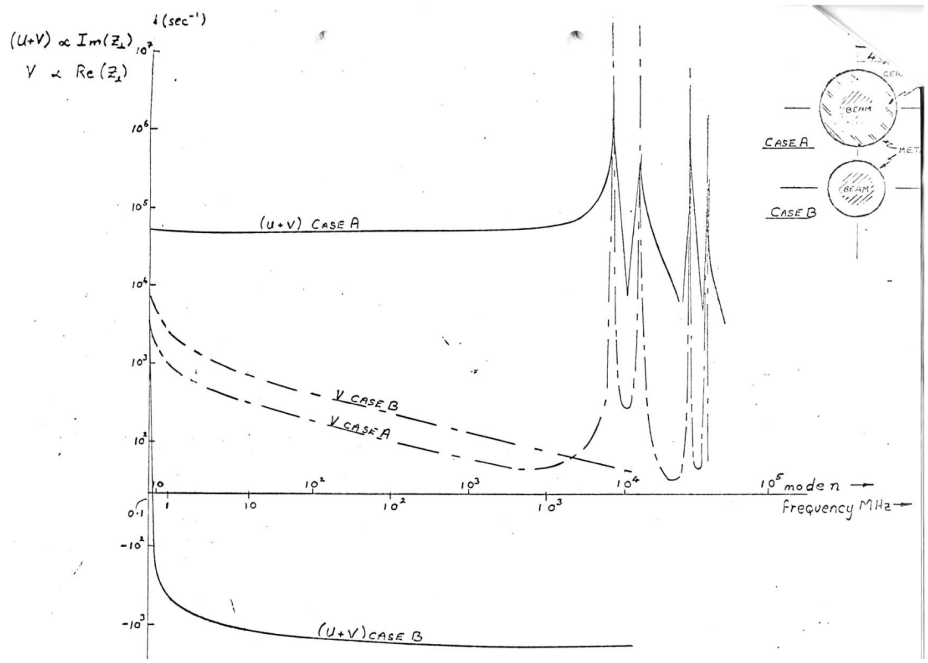


Figure A.1: Plots of quantities proportional to $Z_1^{\perp}$ computed by the LUWAT code, used to justify aspects of the RF-screen geometry at ISIS [184].

The designers of ISIS demonstrated great foresight in their efforts to minimise the beam coupling impedance, but lacked the tools to properly characterise it, which have since become widely available. Despite their efforts, beam instabilities were measured during commissioning [39], including a vertical head-tail instability that appeared around 2 ms through the RCS cycle. Operators at the time found solutions to mitigate the effects of these instabilities, and with these ISIS was able to achieve its design intensity [62].

B
Fourier Conventions

The forward and inverse Fourier transforms between z and ω are defined here as

$$\hat{f}(\omega) = \hat{\mathcal{F}}\left(f(z)\right) \quad = \int_{-\infty}^{\infty} f(z) e^{-i\omega\frac{z}{\beta c}}\,\mathrm{d}z, \tag{B.1}$$

$$f(z) = \hat{\mathcal{F}}^{-1}\left(\hat{f}(\omega)\right) = \frac{1}{2\pi\beta c}\int_{-\infty}^{\infty} \hat{f}(\omega) e^{i\omega\frac{z}{\beta c}}\,\mathrm{d}\omega, \tag{B.2}$$

where a hat distinguishes it from the transforms defined in Equations (3.36) and (3.37). Whilst those follow a common convention [134], the z-ω convention is less common, so some theorems will now be derived.

Shift Theorem

The function $\rho(z)$ has a transform $\hat{\rho}(\omega)$.

$$\begin{aligned}
\hat{\mathcal{F}}\left(\rho(z-a)\right) &= \int_{-\infty}^{\infty} \rho(z-a) e^{-i\omega\frac{z}{\beta c}}\,\mathrm{d}z, \\
&= \int_{-\infty}^{\infty} \rho(z-a) e^{-i\omega\frac{z-a}{\beta c}} e^{-i\omega\frac{a}{\beta c}}\,\mathrm{d}z, \\
&= e^{-i\omega\frac{a}{\beta c}} \int_{-\infty}^{\infty} \rho(z-a) e^{-i\omega\frac{z-a}{\beta c}}\,\mathrm{d}(z-a), \\
&= e^{-i\omega\frac{a}{\beta c}} \hat{\rho}(\omega)
\end{aligned}$$

Convolution Theorem

The convolution of functions $f(z)$ and $g(z)$ is defined as

$$f(z) * g(z) = \int_{-\infty}^{\infty} f(u) g(z-u)\,\mathrm{d}u,$$

and its transform is

$$\hat{\mathcal{F}}\left(f * g\right) = \int_{-\infty}^{\infty} e^{-i\omega\frac{z}{\beta c}} \left[\int_{-\infty}^{\infty} f(u)g(z-u)\,\mathrm{d}u\right] \mathrm{d}z.$$

Swapping the order of integration gives

$$\hat{\mathcal{F}}\left(f * g\right) = \int_{-\infty}^{\infty} f(u) \left[\int_{-\infty}^{\infty} g(z-u)e^{-i\omega\frac{z}{\beta c}}\,\mathrm{d}z\right] \mathrm{d}u.$$

Using the shift theorem, the integral inside the square brackets is written down and brought out of the integral

$$\hat{\mathcal{F}}\left(f * g\right) = \hat{g}(\omega) \int_{-\infty}^{\infty} f(u)e^{-i\omega\frac{u}{\beta c}}\,\mathrm{d}u.$$

The remaining integral is seen to be the Fourier transform of f, so the conclusion is

$$\hat{\mathcal{F}}\left(f * g\right) = \hat{g}(\omega)\hat{f}(\omega). \tag{B.3}$$

Poisson Summation

Define the time domain function

$$f(z) = \sum_{n=-\infty}^{\infty} \delta(z - nC),$$

where δ is the Dirac delta function and C is interpreted as the machine circumference. This is clearly a periodic function and can be expressed as a Fourier series

$$f(z) = \sum_{k=-\infty}^{\infty} s_k e^{2\pi ikz/C}$$

with the definition

$$s_k = \frac{1}{C}\int_{-C/2}^{C/2} \sum_{k=-\infty}^{\infty} \delta(z - kC)e^{-2\pi ikz/C}\,\mathrm{d}z = \frac{1}{C},$$

giving

$$f(z) = \frac{1}{C}\sum_{k=-\infty}^{\infty} e^{2\pi ikz/C}. \tag{B.4}$$

Taking the Fourier transform of this gives

$$\begin{aligned}\hat{f}(\omega) &= \frac{1}{C}\int_{z=-\infty}^{\infty}\sum_{n=-\infty}^{\infty} e^{2\pi i n z/C} e^{-i\omega\frac{z}{\beta c}}\,\mathrm{d}z,\\ &= \frac{1}{C}\sum_{n=-\infty}^{\infty}\int_{z=-\infty}^{\infty} e^{2\pi i n z/C} e^{-i\omega\frac{z}{\beta c}}\,\mathrm{d}z,\\ &= \frac{1}{C}\sum_{n=-\infty}^{\infty}\int_{-\infty}^{\infty} e^{-i(\omega-\frac{2\pi\beta c}{C})z/c}\,\mathrm{d}z,\end{aligned}$$

and substituting the Fourier representation of a Dirac delta function,

$$\hat{f}(\omega) = \frac{2\pi\beta c}{C}\sum_{n=-\infty}^{\infty}\delta\left(\omega - \frac{2\pi\beta c}{C}n\right). \tag{B.5}$$

The Fourier transform can also be taken directly from the original definition of $f(z)$

$$\hat{f}(\omega) = \sum_n \int_{z=-\infty}^{\infty}\delta(z-nC)e^{-i\omega\frac{z}{\beta c}}\,\mathrm{d}z = \sum_n e^{-i\omega\frac{nC}{\beta c}}, \tag{B.6}$$

which can be equated with the solution from the Fourier series to give

$$\sum_{n=-\infty}^{\infty} e^{-i\omega\frac{nC}{\beta c}} = \frac{2\pi\beta c}{C}\sum_{n=-\infty}^{\infty}\delta\left(\omega - \frac{2\pi\beta c}{C}n\right). \tag{B.7}$$

C

Fourier Conventions for Impedance

There are several definitions for impedance and so different formulas for the same impedance. For example, one reference defines the space-charge impedance as [135]

$$\frac{1}{L}Z_1^{\perp} = -i\frac{Z_0}{2\pi\beta\gamma^2}\left(\frac{1}{a^2} - \frac{1}{b^2}\right), \tag{C.1}$$

whilst the equivalent impedance in a different reference is (with $\beta \approx 1$) [89]

$$\frac{1}{L}Z_1^{\perp} = i\frac{Z_0}{2\pi\gamma^2}\left(\frac{1}{a^2} - \frac{1}{b^2}\right). \tag{C.2}$$

The source of this apparent inconsistency is the Fourier transform convention in defining the impedance from the wake function. The first formula uses the definition

$$Z_1^{\perp} = -\frac{i}{\beta c}\int_{z=-\infty}^{\infty} W_1^{\perp}(z)e^{i\frac{\omega}{\beta c}z}\,\mathrm{d}z, \tag{C.3}$$

and the second, which is the definition used in this thesis, uses

$$Z_1^{\perp} = \frac{i}{\beta c}\int_{z=-\infty}^{\infty} W_1^{\perp}(z)e^{-i\frac{\omega}{\beta c}z}\,\mathrm{d}z. \tag{C.4}$$

These definitions lead to different formulas to express the impedance in terms of the Fourier transform of the Lorentz force. The first author specifies this as

$$Z_1^{\perp}(\omega) = \frac{i}{q_1 d_1}\int_{s=-\infty}^{\infty}\left(\tilde{E}_x(\omega) - v\tilde{B}_y(\omega)\right)e^{i\omega\frac{s}{\beta c}}\,\mathrm{d}s, \tag{C.5}$$

and an equivalent for the second definition will now be derived. The witness particle is assumed to experience the wake force due to a source particle when it reaches the

location that the wake was generated; at a time $-\frac{z}{\beta c}$ after the source particle passes it. For the horizontal impedance

$$Z_1^{\perp}(\omega) = i\int_{z=-\infty}^{\infty} W_1^{\perp}(z)e^{-i\frac{\omega}{\beta c}z}\,\frac{\mathrm{d}z}{\beta c}, \tag{C.6}$$

$$= \frac{-i}{eq_1d_1}\int_{z=-\infty}^{\infty}\left[\int_{s=-L/2}^{L/2} F_{\perp}\left(x,y,s;t-\frac{z}{v}\right)\,\mathrm{d}s\right]_{\substack{x=x_2=0\\ y=y_2=0\\ x_1=d_1\\ y_1=0}} e^{-i\frac{\omega}{\beta c}z}\,\frac{\mathrm{d}z}{\beta c}, \tag{C.7}$$

z is defined to be positive in the direction of the source particle's velocity, so that in the $\beta \to 1$ limit, a witness particle that experiences a wake force always has $z < 0$. Assuming the Fourier transform exists, the order of the integrals can be exchanged

$$Z_1^{\perp}(\omega) = \frac{-i}{q_1d_1}\int_{s=-L/2}^{L/2}\mathrm{d}s\int_{z=-\infty}^{\infty}\left(E_x\left(x,y,s;t-\frac{z}{v}\right)-\beta cB_y\left(x,y,s;t-\frac{z}{v}\right)\right)e^{-i\frac{\omega}{\beta c}z}\,\frac{\mathrm{d}z}{\beta c}, \tag{C.8}$$

$$= \frac{-i}{q_1d_1}\int_{s_1=-L/2}^{L/2} e^{-i\omega\frac{s}{v}}\,\mathrm{d}s\int_{u=-\infty}^{\infty}\left(E_x\left(x,y,s;u\right)-\beta cB_y\left(x,y,s;u\right)\right)e^{i\omega u}\,\mathrm{d}u, \tag{C.9}$$

where the substitution $u = t - \frac{z}{\beta c} = \frac{s}{\beta c} - \frac{z}{\beta c}$ was made.

The second integral is a Fourier transform, but it does not follow the time-frequency definition in Equation (3.36) [134]. Since the time-domain electric and magnetic fields are real quantities, the two Fourier transforms are related by a complex conjugate, giving

$$Z_1^{\perp}(\omega) = \frac{-i}{q_1d_1}\left[\int_{s=-L/2}^{L/2}\left(\tilde{E}_x^{*}\left(x,y,s;\omega\right)-v\tilde{B}_y^{*}\left(x,y,s;\omega\right)\right)e^{-i\omega\frac{s}{v}}\,\mathrm{d}s\right]_{\substack{x=x_2=0\\ y=y_2=0\\ x_1=d_1\\ y_1=0}}. \tag{C.10}$$

This is the same form as Equation (3.38), and it can be seen by eye that this is the complex conjugate of the first authors definition.

It is common to categorise impedances as "inductive" or "capacitive". These categories are defined by the sign of $\mathrm{Im}\left(Z_1^{\perp}\right)$, which will differ for these two definitions. Whilst both authors agree that the thick resistive-wall impedance is inductive, the first author defines this to imply that $\mathrm{Im}\left(Z_1^{\perp}\right) > 0$ for $\omega > 0$, and the second that $\mathrm{Im}\left(Z_1^{\perp}\right) < 0$ in that region, which is the definition used in this thesis.

D
Special Hankel Transform

The integral to be solved is

$$\int_0^\infty x^{\nu+1} e^{-\alpha x^2} L_m^{(\nu-\sigma)}(\alpha x^2) L_n^{(\sigma+\beta)}(\alpha x^2) J_\nu(xy)\,\mathrm{d}x, \tag{D.1}$$

where β is a positive integer and all other quantities are as defined in the related tabulated integral [182]. To evaluate this integral, apply the relationship [181]

$$L_n^{(\sigma+\beta)}(\alpha x^2) = \sum_{r_1=0}^{n} L_{r_1}^{\sigma+\beta-1}(\alpha x^2), \tag{D.2}$$

repeatedly to give

$$L_n^{(\sigma+\beta)}(\alpha x^2) = \sum_{r_1=0}^{n} L_{r_1}^{\sigma+\beta-1}(\alpha x^2) = \sum_{r_1=0}^{n}\sum_{r_2=0}^{r_1} L_{r_2}^{(\sigma+\beta-2)}(\alpha x^2), \tag{D.3}$$

$$= \sum_{r_1=0}^{n}\sum_{r_2=0}^{r_1}\sum_{r_3=0}^{r_2} \cdots \sum_{r_\beta=0}^{r_{\beta-1}} L_{r_\beta}^{(\sigma)}(\alpha x^2). \tag{D.4}$$

Substituting this into the integral gives

$$\sum_{r_1=0}^{n}\sum_{r_2=0}^{r_1}\sum_{r_3=0}^{r_2} \cdots \sum_{r_\beta=0}^{r_{\beta-1}} \int_0^\infty x^{\nu+1} e^{-\alpha x^2} L_m^{(\nu-\sigma)}(\alpha x^2) L_{r_\beta}^{(\sigma)}(\alpha x^2) J_\nu(xy)\,\mathrm{d}x, \tag{D.5}$$

which is a sum of tabulated integrals [182]. It is thus shown that

$$\int_0^\infty x^{\nu+1} e^{-\alpha x^2} L_m^{(\nu-\sigma)}(\alpha x^2) L_n^{(\sigma+\beta)}(\alpha x^2) J_\nu(xy)\,\mathrm{d}x, = \tag{D.6}$$

$$\sum_{r_1=0}^{n}\sum_{r_2=0}^{r_1}\sum_{r_3=0}^{r_2} \cdots \sum_{r_\beta=0}^{r_{\beta-1}} \frac{(-1)^{m+r_\beta}}{2\alpha} \left(\frac{y}{2\alpha}\right)^\nu L_m^{(\sigma-m+r_\beta)}\left(\frac{y^2}{4\alpha}\right) L_{r_\beta}^{(\nu-\sigma+m-r_\beta)}\left(\frac{y^2}{4\alpha}\right). \tag{D.7}$$

For the case of $\beta = 1$ the RHS becomes

$$\sum_{r_1=0}^{n} \frac{(-1)^{m+r_1}}{2\alpha} \left(\frac{y}{2\alpha}\right)^\nu \exp\left(-\frac{y^2}{4a}\right) L_m^{(\sigma-m+r_1)}\left(\frac{y^2}{4\alpha}\right) L_{r_1}^{(\nu-\sigma+m-r_1)}\left(\frac{y^2}{4\alpha}\right). \tag{D.8}$$

E
Laguerre Series Coefficients

The normalisation of $f_0(q)$ and $g_0(r)$, are chosen such that

$$\int_{z=-\infty}^{\infty}\int_{\delta=-\infty}^{\infty} g_0(r)\,\mathrm{d}z\mathrm{d}\delta = N. \tag{E.1}$$

If $\hat{g}_0(r)$ is introduced such that $g_0(r) = \frac{N\eta c}{2\pi\omega_s}\hat{g}_0(r)$ then the Laguerre series for the unperturbed longitudinal distribution and its normalisation integral becomes

$$\hat{g}_0(r) = e^{-ar^2}\sum_{k'=0}^{\infty} G_{k'}L_{k'}^{(0)}(ar^2), \tag{E.2}$$

$$\int_0^{\infty} r\hat{g}_0(r)\,\mathrm{d}r = 1, \tag{E.3}$$

multiplying both sides by $L_k^{(0)}(ar^2)$, integrating over (ar^2) from 0 to ∞ and exchanging the summation and integral gives [181]

$$G_k = \int_0^{\infty} \hat{g}_0(r)L_k^{(0)}(ar^2)\,\mathrm{d}(ar^2). \tag{E.4}$$

For certain distributions explicit expressions can be derived, for the example of a Gaussian $\hat{g}_0(r) = \frac{1}{\sigma^2}e^{-\frac{r^2}{2\sigma^2}}$.

The variable a can be chosen arbitrarily, although optimum values can improve convergence. For Gaussian distributions, values on the order of $\frac{1}{\sigma_z^2}$ have been used throughout these studies.

F

Eddy Current Conductivity Measurements

To measure the conductivity of a good conductor with an Eddy current probe, a sample is placed adjacent to a probe wire which is fed with a time-varying current. Eddy currents induced in the sample produce a quantifiable effect on the impedance of probe. Analytical solutions for the impedance can be found for simple arrangements of probe coils and samples [224]. In this appendix, the impedance of a probe coil wrapped around a two-layer, infinitely long cylindrical conducting sample will be derived from a published Green's function [224], and it will make use of the notation from this reference.

The infinitely long cylindrical sample is assumed to be composed of two concentric, conducting layers, with radii a and b, as indicated by regions I and II in Figure F.1. A probe coil with a rectangular cross-section is also concentric to the sample and has inner and outer radii of r_1 and r_2, which are both larger than b, and forms region III-IV. The conductivity in regions I and II are σ_1 and σ_2, and the relative magnetic permeabilities in these regions are here assumed to be 1. Regions III and IV are assumed to be empty space.

A magnetoquasistatic approach is taken, and it is assumed that current flows uniformly inside the coil's cross-section. From the superposition principal, the vector potential can be written as in Equation 96 of [224] with

$$A(r,z) = \frac{1}{(r_2 - r_1)(z_2 - z_1)} \int_{r_1}^{r_2} \int_{z_1}^{z_2} A'(r,z,r_0,z_0)\, \mathrm{d}r_0 \mathrm{d}z_0 \tag{F.1}$$

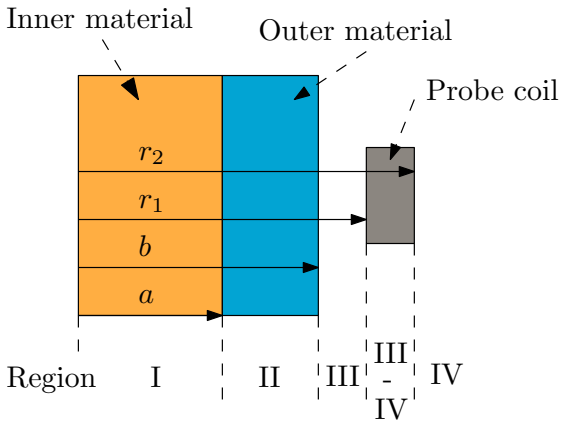


Figure F.1: Schematic of the wire conductivity measurement geometry.

where $A(r,z)$ is the vector potential of the probe coil and $A'(r,z,r_0,z_0)$ is the vector potential produced by a current density

$$i_0(r_0,z_0) = I\delta(r-r_0)\delta(z-z_0), \tag{F.2}$$

where I is the current in a single probe loop winding. $A'(r,z,r_0,z_0)$ is obtained from separation of variables and field-matching, and solutions are available in Equations 90-93 of [224]. Substituting these give the vector potentials in regions III and IV as

$$A^{(3)}(r,z) = \frac{\mu_0 I}{\pi(r_2-r_1)(z_2-z_1)} \int_{\alpha=0}^{\infty} \left[\frac{1}{\alpha^3} B_k(r_1,r_2) \left[I_1(\alpha r) + \Gamma K_1(\alpha r) \right] \times \right. \tag{F.3}$$
$$\left. (\sin(\alpha(z-l_1)) - \sin(\alpha(z-l_2))) \right] \mathrm{d}\alpha,$$

$$A^{(4)}(r,z) = \frac{\mu_0 I}{\pi(r_2-r_1)(z_2-z_1)} \int_{\alpha=0}^{\infty} \left[\frac{1}{\alpha^3} K_1(\alpha r) \left[B_i(r_1,r_2) + \Gamma B_k(r_1,r_2) \right] \times \right. \tag{F.4}$$
$$\left. (\sin(\alpha(z-l_1)) - \sin(\alpha(z-l_2))) \right] \mathrm{d}\alpha,$$

where I_1 and K_1 are modified Bessel functions of the first and second kinds and α is a separation variable with the dimensions of length,

$$\alpha_1 = \sqrt{\alpha^2 + j\omega\mu_0\sigma_1}, \tag{F.5}$$

$$\alpha_2 = \sqrt{\alpha^2 + j\omega\mu_0\sigma_2}. \tag{F.6}$$

The following functions were also defined to simplify the expressions

$$B_k(r_1, r_2) = \int_{\alpha r_1}^{\alpha r_2} xK_1(x)\,\mathrm{d}x, \tag{F.7}$$

$$B_i(r_1, r_2) = \int_{\alpha r_1}^{\alpha r_2} xI_1(x)\,\mathrm{d}x, \tag{F.8}$$

$$\begin{aligned}\Gamma(\alpha) = &-\frac{K_1(\alpha_2 b)}{bDK_1(\alpha b)}\left[\alpha_1 I_1(\alpha_2 a)I_0(\alpha_1 a) - \alpha_2 I_1(\alpha_1 a)I_0(\alpha_2 a)\right] \\ &+\frac{I_1(\alpha_2 b)}{bDK_1(\alpha b)}\left[\alpha_1 K_1(\alpha_2 a)I_0(\alpha_1 a) + \alpha_2 I_1(\alpha_1 a)K_0(\alpha_2 a)\right] + \frac{I_1(\alpha b)}{K_1(\alpha b)}.\end{aligned} \tag{F.9}$$

To compute the vector potential in the region III–IV, special treatment is required. $A^{(3)}(r, z)$ must be used between r_1 and r and $A^{(4)}(r, z)$ from r to r_2. Substituting r_2 for r in Equation (F.4) and r_1 for r in Equation (F.5), then summing the resulting equations gives the vector potential $A^{(3,4)}(r, z)$ which is the quantity required to calculate the coil resistance.

With this newly derived expression for $A^{(3,4)}(r, z)$, Equation 112 of [224] can be used to find the impedance of a probe coil of n turns and length $l = z_2 - z_1$

$$\begin{aligned}Z(\omega) &= \frac{j2\pi\omega n^2}{I(z_2 - z_1)^2(r_2 - r_1)^2}\int_{z=l_1}^{l_2}\int_{r=r_1}^{r_2} rA^{(3,4)}(r, z)\,\mathrm{d}r\mathrm{d}z, \\ &= \frac{-j4\omega n^2\mu_0}{l^2(r_2 - r_1)^2}\int_{\alpha=0}^{\infty}\frac{\cos(\alpha l) - 1}{\alpha^4}\int_{r=r_1}^{r_2} r\,\big(B_k(r_1, r)\left[I_1(\alpha r) + \Gamma K_1(\alpha r)\right] \\ &\qquad + K_1(\alpha r)\left[B_i(r, r_2) + \Gamma B_k(r, r_2)\right]\big)\,\mathrm{d}r\,\mathrm{d}\alpha.\end{aligned} \tag{F.10}$$

The real part of this expression has been evaluated numerically with Romberg integration [225, 226]. To evaluate the improper integral numerically, the limits on α were truncated on both sides. This approach was adopted because Figure F.2 shows that for typical conductors, the integrand approaches a constant as $\alpha \to 0$ and drops off rapidly for larger values. The integration limits were therefore adjusted until adequate convergence was achieved.

Benchmarking of this method was performed against a finite element solution in CST. A sample wire with $\sigma_1 = \sigma_2 = 1.4\times10^6\,\mathrm{S\,m^{-1}}$ was simulated, along with probe coil

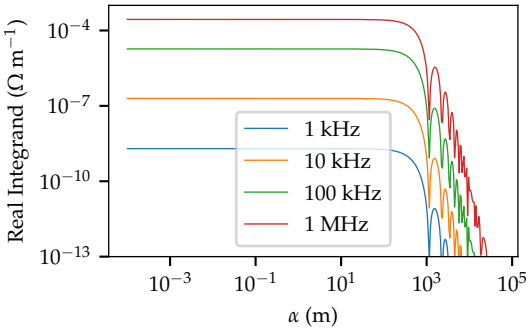


Figure F.2: Real part of the integrand from Equation (F.10).

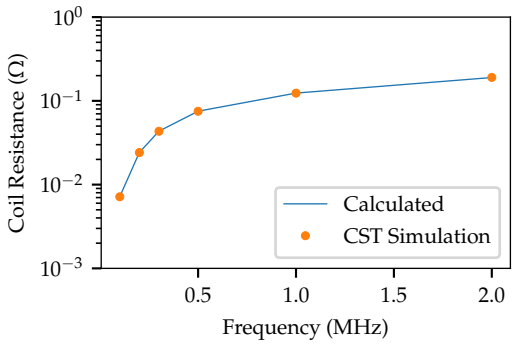


Figure F.3: Overlay of resistances calculated from a numerical evaluation of Equation (F.10) and a CST Low Frequency simulation.

and sample properties listed in listed in Table F.1; a has no meaning for a single-material sample. The coil resistance is plotted in Figure F.3 for several different frequencies. Good agreement between the numerical integral and the finite element solution were found over the full frequency range.

Table F.1: Parameters used for finite-element benchmark of AC probe coil conductivity measurement technique.

Parameter	Value
b	1.710 mm
r_1	1.225 mm
r_2	1.710 mm
l	5.500 mm
No. Turns	9

References

[1] R. C. Kilbride et al. “The Nanoscale Structure and Stability of Organic Photovoltaic Blends Processed with Solvent Additives”. In: *Small* 20.33 (Aug. 2024), p. 2311109. ISSN: 1613-6810, 1613-6829. DOI: 10.1002/smll.202311109.

[2] L. A. Clifton et al. “An Accurate In Vitro Model of the *E. coli* Envelope”. In: *Angew Chem Int Ed* 54.41 (Oct. 5, 2015), pp. 11952–11955. ISSN: 1433-7851, 1521-3773. DOI: 10.1002/anie.201504287.

[3] M. Gaifullin et al. “Influence of mechanical stress on electron transport properties of second-generation high-temperature superconducting tapes”. In: *Low Temperature Physics* 49.8 (Aug. 1, 2023), pp. 994–997. ISSN: 1063-777X, 1090-6517. DOI: 10.1063/10.0020169.

[4] L. Romero-Resendiz et al. “Exceptional strength–ductility combination of heterostructured stainless steel for cryogenic applications”. In: *Scripta Materialia* 258 (Mar. 2025), p. 116527. ISSN: 13596462. DOI: 10.1016/j.scriptamat.2024.116527.

[5] B. Narasimham et al. “Scaling Trends and the Effect of Process Variations on the Soft Error Rate of advanced FinFET SRAMs”. In: *2023 IEEE International Reliability Physics Symposium (IRPS)*. Monterey, CA, USA: IEEE, Mar. 2023. DOI: 10.1109/IRPS48203.2023.10118025.

[6] L. W. Alvarez. “The Production of Collimated Beams of Monochromatic Neutrons in the Temperature Range 300°-10°K”. In: *Phys. Rev.* 54.8 (Oct. 15, 1938), pp. 609–617. ISSN: 0031-899X. DOI: 10.1103/PhysRev.54.609.

[7] L. W. Alvarez. *Alvarez: Adventures Of A Physicist*. Reprint edition. New York: Basic Books, May 30, 1989. 320 pp. ISBN: 978-0-465-00116-3.

[8] O. Frisch. *What Little I Remember*. Cambridge University Press, 1980. ISBN: 978-0-521-28010-5.

[9] I. Švajger et al. “Evaluation of reactor pulse experiments”. In: *Nuclear Engineering and Technology* (Nov. 15, 2023). ISSN: 1738-5733. DOI: 10.1016/j.net.2023.11.021.

[10] T. P. McLaughlin et al. *A Review of Criticality Accidents 2000 Revision*. LA-13638. Los Alamos National Lab. (LANL), Los Alamos, NM (United States), May 1, 2000. DOI: 10.2172/758324.

[11] T. F. Wimett and J. D. Orndoff. *Applications of GODIVA-II Neutron Pulses*. Los Alamos, Oct. 31, 1958. URL: https://www.osti.gov/biblio/4305660.

[12] J. D. Cockcroft. “High-Energy Electron Accelerators as Pulsed Neutron Sources”. In: *Nature* 163.4153 (1949), pp. 869–869. DOI: 10.1038/163869a0.

[13] D. J. S. Findlay. *History of the Harwell 136 MeV electron linear accelerator - a brief personal view*. ISIS-DJSF-24-09-A. Sept. 20, 2024. URL: https://www.chilton-computing.org.uk/harwell/pdfs/history-harwell-136mev-electron-linac.pdf.

[14] C. G. Windsor and R. N. Sinclair. *A Discussion Paper for the Exploitation of the New Harwell LINAC for Condensed Matter Studies*. 1975. URL: https://neutronsources.org/media/1975%5C_exploitation%5C_of%5C_the%5C_new%5C_harwell%5C_linac.pdf.

[15] M. Kawai, S. Ikeda, and T. Ino. "KENS-II, its History from Design to Removal". In: *Materials Science Forum* (2021). DOI: 10.4028/www.scientific.net/MSF.1024.13.

[16] B. S. Brown and J. Carpenter. "Status of IPNS". In: ICANS-XIV. June 1998.

[17] H. Hotchi et al. "1 MW J-PARC RCS Beam Operation and Further Beyond". In: HB2021 (2022). ISSN: 2673-5571. DOI: 10.18429/JACOW-HB2021-MOIPI1.

[18] J. Galambos. "Operations Experience of SNS at 1.4MW and Upgrade Plans for Doubling the Beam Power". In: *Proceedings of the 10th Int. Particle Accelerator Conf.* IPAC2019 (2019). DOI: 10.18429/JACOW-IPAC2019-FRXPLM1.

[19] L. Huang. Private Correspondence. Mar. 2024.

[20] ISIS-II Working Group. *ISIS-II Roadmap*. URL: https://www.isis.stfc.ac.uk/Pages/ISIS-II%5C%20Roadmap.pdf.

[21] M. Champion et al. "Completion of the proton power upgrade project at the Spallation Neutron Source". In: (July 1, 2024). Ed. by F. Pilat et al., 1691–1694 pages, 0.97 MB. ISSN: 2673-5490. DOI: 10.18429/JACOW-IPAC2024-TUPS27.

[22] G. P. Lawrence. "Performance of the Los Alamos Proton Storage Ring". In: *Proc. PAC'87*. Vol. 870316. Washington, DC, USA, 1987, p. 825. URL: https://proceedings.jacow.org/p87/PDF/PAC1987%5C_0825.PDF.

[23] M. A. DiStravolo. *The Manuel Lujan, Jr. Neutron Scattering Center, LANSCE experiment reports: 1990 Run Cycle*. Report. Los Alamos National Laboratory, Jan. 10, 1991. DOI: 10.2172/5005223.

[24] R. J. Macek. *Progress on the PSR/LANSCE upgrade*. LA-UR–95-3566; CONF-9510212–5. Los Alamos National Lab., NM (United States), Dec. 1, 1995. URL: https://www.osti.gov/biblio/135539.

[25] J. M. Carpenter et al. "The Argonne Pulsed Neutron Source Program". In: Conference on Diffraction Profile Analysis. Poland, Aug. 1979. URL: https://powder.ornl.gov/%5C_downloads/971ba8a8a68b7e382a87c36749ea375d/report%5C_argonne%5C_pulsed%5C_neutrons.pdf.

[26] J. M. Carpenter et al. "Pulsed spallation neutron sources". In: *Physics Today* (1979). ISSN: 0031-9228, 1945-0699. DOI: 10.1063/1.2995314.

[27] Y. Ishikawa and N. Watanabe. *KEK Neutron Source and Neutron Scattering Research Facility*. KEK-78-19. 1978. URL: https://inis.iaea.org/records/csjmc-kgb73.

[28] Y. Ishikawa. "Present Status – The KENS Facility". In: Fourth Meeting of the International Collaboration on Advanced Neutron Sources. Oct. 1980, p. 181. URL: http://www.neutronresearch.com/parch/1980/01/198001000890.pdf.

[29] H. Seto and S. Ikeda. "The 50th Anniversary of KEK and the 40th Anniversary of KENS". In: *Neutron News* 33.2 (June 17, 2022), pp. 5–6. ISSN: 1044-8632. DOI: 10.1080/10448632.2022.2050629.

[30] H. Ikeda. "Status Report of KENS". In: ICANS XIV. 1998. URL: http://www.neutronresearch.com/parch/1998/01/199801000460.pdf.

[31] T. Kawakubo et al. *The First Test Experiment of H- Charge-Exchange Injection in the KEK Booster*. KEK 84-6. June 1984. URL: https://inis.iaea.org/records/vydv5-gcb21/files/17013051.pdf.

[32] F. Maekawa et al. "First neutron production utilizing J-PARC pulsed spallation neutron source JSNS and neutronic performance demonstrated". In: *NIMA* 620.2 (Aug. 11, 2010), pp. 159–165. ISSN: 0168-9002. DOI: 10.1016/j.nima.2010.04.020.

[33] C. Westfall. *How Argonne's Intense Pulsed Neutron Source came to life and gained its niche : the view from an ecosystem perspective.* Argonne, IL: Argonne National Laboratory (ANL), Feb. 25, 2008. DOI: 10.2172/924693.

[34] R. G. Teller. *Intense Pulsed Neutron Source Home Page*. Jan. 2008. URL: https://web.archive.org/web/20190315214422/http://www.neutron.anl.gov/ipns/.

[35] J. M. Carpenter et al. "Status of the Intense Pulsed Neutron Source". In: ICANSVIII. July 1985. URL: https://www.osti.gov/servlets/purl/5225071-C0kdIJ/.

[36] C. Potts et al. *Recent performance of the Intense Pulsed Neutron Source accelerator system*. CONF-870302-220. Argonne National Lab., IL (USA), Mar. 1, 1987. URL: https://www.osti.gov/biblio/6179006.

[37] L. C. W. Hobbis. *A Pulsed Neutron Facility for Condensed Matter Research*. RL-77-064/c. 1977.

[38] J. Thomason. "The ISIS Spallation Neutron and Muon Source–The first thirty-three years". In: *NIMA* 917 (Feb. 2019), pp. 61–67. ISSN: 01689002. DOI: 10.1016/j.nima.2018.11.129.

[39] C. W. Planner. "Progress to operating at 100-microA on ISIS". In: *1988 DPF Summer Study on High-energy Physics in the 1990s (Snowmass 88)*. 1988, pp. 422–424.

[40] J. W. G. Thomason. "Upgrades to ISIS for the New Second Target Station". In: *Proc. EPAC'08*. 2008.

[41] T. Wangler and P. W. Lisowski. *The LANSCE National User Facility*. 28. Los Alamos National Lab, 2003.

[42] F. A. Morse. "Status of the Commissioning of the Los Alamos Neutron Scattering Center". In: ICANS-VIII. July 1985. URL: https://epubs.stfc.ac.uk/work/42064.

[43] *LANSCE History*. URL: https://lansce.lanl.gov/about/history.php.

[44] S. J. Russell et al. "Update on the status of the Los Alamos Neutron Science Center Accelerator Modernization". In: *Proc. LINAC'24*. Chicago, IL, USA, 2024. DOI: 10.18429/JACoW-LINAC2024-MOPB095.

[45] M. Arai and F. Maekawa. "Japan Spallation Neutron Source (JSNS) of J-PARC". In: *Nuclear Physics News* (Dec. 2009). DOI: 10.1080/10506890903405316.

[46] J. Wei et al. "China Spallation Neutron Source: Design, R&D, and outlook". In: *NIMA* (2009). DOI: 10.1016/j.nima.2008.11.017.

[47] L. Huang et al. "Pulsed octupole magnet for beam instability mitigation in Rapid Cycling Synchrotron". In: (2025). DOI: 10.12074/202502.00148.

[48] D. W. Posthuma de Boer. "ISIS-II Update". In: Annual Meeting of Particle Accelerator Society of Japan. Funabashi, Japan, Aug. 2023. URL: https://www.pasj.jp/web%5C_publish/pasj2023/proceedings/PDF/WEOB/WEOB3.pdf.

[49] K. Johns et al. "Design and structural assessment of the Spallation Neutron Source 2.0 MW target". In: *NIMA* (Dec. 2021). DOI: 10.1016/j.nima.2021.165799.

[50] H. Liu and S. Wang. "Longitudinal beam dynamic design of 500 kW beam power upgrade for CSNS-II RCS". In: *Radiat Detect Technol Methods* 6.3 (Sept. 1, 2022), pp. 339–348. ISSN: 2509-9949. DOI: 10.1007/s41605-022-00325-5.

[51] Engineering Strategy Working Group and Neutron Landscape Group. *Neutron scattering facilities in Europe Present status and future perspectives*. 2016. ISBN: 978-88-901562-5-0. URL: https://www.esfri.eu/esfri-scripta-vol1-neutron-scattering-facilities-europe-present-status-and-future-perspectives.

[52] M. A. Plum. "Beam Loss Mechanisms in High Intensity Linacs". In: *Proc. HB'12*. Beijing, 2012. URL: https://accelconf.web.cern.ch/HB2012/papers/MOI1C03.pdf.

[53] T. Wang et al. "Recent study of beam stability in the PSR". In: International Conference on Particle Accelerators. Washington, DC, USA: IEEE, 1993. DOI: 10.1109/PAC.1993.309631.

[54] R. J. Macek and J. S. Kolski. "Understanding Beam Losses in High Intensity Proton Accumulator Rings". In: *Proc. HB'14*. East-Lansing, MI, USA, 2014.

[55] H. Dong et al. "The vacuum system of the China spallation neutron source". In: *Vacuum* 154 (Aug. 2018). DOI: 10.1016/j.vacuum.2018.04.046.

[56] High-intensity Proton Accelerator Project Team. *Accelerator technical design report for high-intensity proton accelerator facility project, J-PARC*. 2003. URL: https://cds.cern.ch/record/747209.

[57] P. Saha et al. "Dynamic Variation of Chromaticity for Beam Instability Mitigation in the 3-GeV RCS of J-PARC". In: *Proc. IPAC'19*. Australia: JACoW Publishing, 2019. DOI: 10.18429/JACOW-IPAC2019-MOPGW037.

[58] L. Huang et al. "Intense Beam Issues in CSNS Accelerator Beam Commissioning". In: *Proc. HB'23*. Geneva, Switzerland, 2023. DOI: 10.18429/JACoW-HB2023-MOA1I3.

[59] Y. H. Chin. "Impedance and Beam Instability Issues at J-PARC Rings". In: *Proc. HB'08*. USA, 2008. URL: https://proceedings.jacow.org/HB2008/papers/wga01.pdf.

[60] Y. Shobuda et al. "Measurement scheme of kicker impedances via beam-induced voltages of coaxial cables". In: *NIMA* (June 2013). DOI: 10.1016/j.nima.2013.02.037.

[61] Z. Xie et al. "Transverse beam stability measurement and analysis for the SNS accumulator ring". In: *NIMA* 788 (July 11, 2015), pp. 161–167. ISSN: 0168-9002. DOI: 10.1016/j.nima.2015.03.038.

[62] M. Harold et al. "Diagnostics and commissioning progress on ISIS". In: *Proc. EPAC'88*. World Scientific Pub Co, 1988. ISBN: 978-9971-5-0642-1.

[63] R. E. Williamson. "Beam Loss Mitigation for High Intensity Operation at ISIS". June 2020. URL: https://indico.gsi.de/event/10458/contributions/45031/.

[64] D. W. Posthuma de Boer et al. "Development of an Impedance Model for the ISIS Synchrotron and Predictions for the Head-Tail Instability". In: *Proc. HB'23*. Geneva, Switzerland, Oct. 2023. DOI: 10.18429/JACoW-HB2023-TUC4I2.

[65] A. L. Robinson. "First Neutrons from Rutherford Lab's SNS". In: *Science* 227.4690 (Mar. 1985), pp. 1021–1024. DOI: 10.1126/science.227.4690.1021.

[66] D. A. Gray. "First neutrons from new machine". In: 25.2 (Mar. 1985), pp. 57–59. ISSN: 0304-288X. URL: https://inis.iaea.org/records/0szrb-x5553.

[67] P. Dobson. "ISIS Neutron & Muon Source, Facility Diagram". In: (July 3, 2026). DOI: 10.5281/zenodo.21157242.

[68] B. Boardman. *ISIS - Description of Accelerator and Target*. RL-82-006. 1982.

[69] R. E. Williamson et al. "High-Intensity Studies on the ISIS RCS and Their Impact on the Design of ISIS-II". In: *Proc. HB'23*. Apr. 2024. DOI: 10.18429/JACoW-HB2023-THA1I2.

[70] S. R. Lawrie. "Understanding the Plasma and Improving Extraction of the ISIS Penning H- Ion Source". DPhil Thesis. University of Oxford, 2017. URL: https://ora.ox.ac.uk/objects/uuid:1648761a-57b1-4d6f-8281-9d1c36ccd46a.

[71] A. Letchford et al. "Testing, Installation, Commissioning and First Operation of the ISIS RFQ Pre-Injector Upgrade". In: *Proc. PAC'05*. May 2005, pp. 695–697. DOI: 10.1109/PAC.2005.1590531.

[72] D. C. Plostinar, C. Prior, and G. Rees. "Modelling the ISIS 70 MeV Linac". In: *Proc. IPAC'12*. New Orleans, Louisiana, USA, 2012.

[73] M. R. Harold. "The design, manufacture and testing of the ISIS fast-cycling magnets". In: kaon pds magnet design workshop. 1989. URL: http://inis.iaea.org/Search/search.aspx?orig%5C_q=RN:25028686.

[74] M. R. Harold. *ISIS Octupoles - Control and Measurements*. IADM/MAG/2/92. 1992.

[75] M. R. Harold. *ISIS Sextupoles - Control and Measurements*. IADM/MAG/1/92. 1992.

[76] E. Ahmadi et al. "Beam dynamics studies on the ISIS RCS with a new assessment of non-linear driving terms and motion". In: *Proc. HB'25*. Huizhou, China, Oct. 2025. DOI: 10.18429/JACoW-HB2025-WEIDB01.

[77] J. R. J. Bennett and R. J. Elsey. "Glass Jointed Alumina Vacuum Chambers". In: *IEEE Transactions on Nuclear Science* 28.3 (June 1981), pp. 3336–3338. ISSN: 1558-1578. DOI: 10.1109/TNS.1981.4332098.

[78] B. Jones, D. J. Adams, and C. M. Warsop. "Injection Optimisation on the ISIS Synchrotron". In: *Proc. EPAC'08*. 2008.

[79] B. Jones, D. J. Adams, and H. V. Smith. "Initial Experience with Carbon Stripping Foils at ISIS". In: IPAC. 2016.

[80] R. E. Williamson. "Studies of Beam Instabilities and Associated Beam-Loss on a High-Intensity Proton Synchrotron". DPhil Thesis. University of Oxford, 2023. URL: https://ora.ox.ac.uk/objects/uuid:fdedfe67-9e52-479e-b965-ad12fcac7149.

[81] I. S. K. Gardner. "Ferrite dominated cavities". In: *CERN Accelerator School: RF Engineering for Particle Accelerators*. 1992. DOI: 10.5170/CERN-1992-003.349.

[82] A. Seville et al. "First Results from the use of Dual Harmonic Acceleration on the ISIS Synchrotron". In: *Proc. PAC'05*. Knoxville, TN, USA: IEEE, 2005. DOI: 10.1109/PAC.2005.1590941.

[83] S. J. Payne et al. "Beam Diagnostics at ISIS". In: *Proc. HB'08*. Nashville, Tennessee, USA, 2008. URL: https://proceedings.jacow.org/HB2008/papers/wgf10.pdf.

[84] R. E. Williamson, B. Jones, and C. M. Warsop. "Development of Physics Models of the ISIS Head-Tail Instability". In: *Proc. HB'16*. Sweden, July 2016. URL: http://accelconf.web.cern.ch/AccelConf/hb2016/papers/mopr031.pdf.

[85] R. E. Williamson. Private Correspondence.

[86] G. H. Rees. "Interpretation of the Higher Mode, Head-Tail Motion Observed on ISIS". In: *Part. Accel.* 39 (1992), pp. 159–167. URL: http://cds.cern.ch/record/1108258/files/p159.pdf.

[87] A. Pertica et al. "Optimisation of the ISIS Proton Synchrotron Experimental Damping System". In: IBIC. 2019. DOI: 10.18429/JACOW-IBIC2019-MOPP031.

[88] V. Kornilov and R. E. Williamson. "Thresholds of the Head-Tail Instability in Bunches with Space Charge". In: *Proc. HB'14*. 2014. URL: http://accelconf.web.cern.ch/AccelConf/HB2014/.

[89] A. W. Chao. *Physics of Collective Beam Instabilities in High Energy Accelerators*. 1st ed. John Wiley & Sons, 1993. ISBN: 978-0-471-55184-3. URL: http://www.slac.stanford.edu/%5C%7Eachao/wileybook.html.

[90] V. K. Neil and A. M. Sessler. "Longitudinal Resistive Instabilities of Intense Coasting Beams in Particle Accelerators". In: *Review of Scientific Instruments* 36.4 (Apr. 1, 1965), pp. 429–436. ISSN: 0034-6748. DOI: 10.1063/1.1719594.

[91] V. G. Vaccaro. *Longitudinal instability of a coasting beam above transition, due to the action of lumped discontinuities*. Geneva, 1966. URL: https://cds.cern.ch/record/1216806.

[92] C. D. Curtis, A. Galonsky, and R. H. Hilden. *Beam Experiments with the MURA 50 MeV FFAG Accelerator*. CONF-114-8, 4660777. Sept. 9, 1963, CONF–114–8, 4660777. DOI: 10.2172/4660777.

[93] M. Q. Barton et al. *A summary of the Cosmotron Experiments on the Coherent Vertical Instability*. BNL-7674. Brookhaven National Lab., Upton, N.Y., Nov. 26, 1963. URL: https://www.osti.gov/biblio/4101995.

[94] R. L. Martin. "Performance Characteristics of the ZGS". In: *IEEE Trans. Nucl. Sci.* 14.3 (1967), pp. 740–742. ISSN: 0018-9499. DOI: 10.1109/TNS.1967.4324648.

[95] I. S. K. Gardner, M. Harold, and G. Rees. "The Resistive Wall Instability and Damping System in Nimrod". In: *Nuclear Science, IEEE Transactions on* 14 (July 1, 1967), pp. 653–659. DOI: 10.1109/TNS.1967.4324634.

[96] D. Möhl. *Equipment responsible for transverse beam instability in the PS*. Geneva: CERN, 1974. URL: https://cds.cern.ch/record/2830993.

[97] E. Keil. *The Intersecting Storage Rings*. 1972. DOI: 10.5170/CERN-1972-014.

[98] F. Sacherer. *Methods for computing bunched-beam instabilities*. CERN-SI-Int-BR-72-5. Geneva: CERN, 1972. URL: https://cds.cern.ch/record/2291670.

[99] B. W. Zotter. *Transverse oscillations of a relativistic particle beam in a laminated vacuum chamber*. CERN 69-15. June 1969. DOI: 10.5170/CERN-1969-015,10.5170/CERN-1969-015.

[100] R. L. Gluckstern, J. van Zeijts, and B. Zotter. "Coupling impedance of beam pipes of general cross section". In: *Phys. Rev. E* 47.1 (Jan. 1, 1993), pp. 656–663. DOI: 10.1103/PhysRevE.47.656.

[101] K. Yokoya. "Resistive wall impedance of beam pipes of general cross section". In: *Part. Accel.* 41 (1993), pp. 221–248. URL: https://cds.cern.ch/record/248630.

[102] G. Nassibian and F. Sacherer. "Methods for measuring transverse coupling impedances in circular accelerators". In: *Nuclear Instruments and Methods* (1979). DOI: https://doi.org/10.1016/0029-554X(79)90323-9.

[103] D. Davino and H. Hahn. "Improved analytical model of the transverse coupling impedance of ferrite kicker magnets". In: *Physical Review Special Topics - Accelerators and Beams* (Jan. 9, 2003). DOI: 10.1103/PhysRevSTAB.6.012001.

[104] C. Zannini et al. *Electromagnetic simulations of simple models of ferrite loaded kickers*. CERN-BE-Note-2010-006. June 14, 2010. URL: https://cds.cern.ch/record/1271720.

[105] Y. Shobuda, Y. Irie, and T. Toyama. "Analytical approach to evaluate coupling impedances of traveling kicker magnets". In: *NIMA* 691 (Nov. 1, 2012), pp. 135–151. ISSN: 0168-9002. DOI: 10.1016/j.nima.2012.06.066.

[106] K.-Y. Ng. *Coupling Impedances of Laminated Magnets*. FERMILABFN-0744. Apr. 2004. URL: https://lss.fnal.gov/archive/test-fn/0000/fermilab-fn-0744.pdf.

[107] A. Macridin. "Coupling impedance and wake functions for laminated structures with an application to the Fermilab Booster". In: *Phys. Rev. ST Accel. Beams* 14.6 (2011). DOI: 10.1103/PhysRevSTAB.14.061003.

[108] T. Weiland. "Comment on wake field computation in time domain". In: *Nuclear Instruments and Methods in Physics Research* 216.1 (Oct. 15, 1983), pp. 31–34. ISSN: 0167-5087. DOI: 10.1016/0167-5087(83)90327-7.

[109] U. Niedermayer. "Determination of Beam Coupling Impedance in the Frequency Domain". PhD thesis. Darmstadt: Technische Universität, 2016. URL: http://tuprints.ulb.tu-darmstadt.de/5157.

[110] A. Burov and V. Lebedev. "Transverse Resistive Wall Impedance for Multilayer Round Chambers". In: *Proc. EPAC'02*. Paris, France, 2002. URL: https://proceedings.jacow.org/e02/PAPERS/WEPRI021.pdf.

[111] A. Burov and V. Lebedev. "Transverse Resistive Wall Impedance for Multi-Layer Flat Chambers". In: *Proc. EPAC'02*. Paris, France, 2002. URL: https://proceedings.jacow.org/e02/PAPERS/WEPRI022.pdf.

[112] N. Mounet, E. Métral, and G. Switzerland. "Impedances of two dimensional multilayer cylindrical and flat chambers in the non-ultrarelativistic case". In: *Proc. HB'10*. Morschach, Switzerland, Jan. 1, 2010. URL: https://accelconf.web.cern.ch/HB2010/papers/tuo1c02.pdf.

[113] M. Sands and J. R. Rees. *A Bench Measurement of the Energy Loss of a Stored Beam to a Cavity*. SLAC-TN-05-051, 878797. Aug. 8, 1974. DOI: 10.2172/878797.

[114] H. Hahn. "Interpretation of coupling impedance bench measurements". In: *Physical Review Special Topics - Accelerators and Beams* 7.1 (Jan. 5, 2004). ISSN: 1098-4402. DOI: 10.1103/PhysRevSTAB.7.012001.

[115] A. Mostacci, F. Caspers, and U. Iriso. "Bench measurements of low frequency transverse impedance". In: *Proc. PAC'03*. May 2003. DOI: 10.1109/PAC.2003.1288675.

[116] E. Chapochnikova. "Beam-Based Impedance Measurements". In: *CERN Yellow Reports: School Proceedings* (July 25, 2017). DOI: 10.23730/CYRSP-2017-003.107.

[117] E. Métral. "Intrabunch motion". In: *Phys. Rev. Accel. Beams* 24.1 (Jan. 22, 2021), p. 014401. DOI: 10.1103/PhysRevAccelBeams.24.014401.

[118] A. Burov. "Nested head-tail Vlasov solver". In: *Phys. Rev. ST Accel. Beams* 17.2 (2014), p. 021007. DOI: 10.1103/PhysRevSTAB.17.021007.

[119] D. W. Posthuma de Boer. *PyTMCI*. Sept. 7, 2023. URL: https://github.com/stfc/PyTMCI.

[120] N. Mounet. *DELPHI: an Analytic Vlasov Solver for Impedance-Driven Modes*. 2014. URL: https://cds.cern.ch/record/1954277.

[121] D. Amorim et al. "Improvement of the Analytic Vlasov Solver DELPHI". In: *Proc. IPAC'17*. May 2017. DOI: 10.18429/JACoW-IPAC2017-THPAB005.

[122] A. Oeftiger. *PyCOMPLETE/PyHEADTAIL*. Dec. 18, 2024. URL: https://github.com/PyCOMPLETE/PyHEADTAIL.

[123] N. Mounet and E. Métral. *Electromagnetic fields created by a macroparticle in an infinitely long and axisymmetric multilayer beam pipe*. CERN-BE-2009-039. Nov. 2009. URL: https://cds.cern.ch/record/1228293.

[124] S. Heifets, A. Wagner, and B. Zotter. *Generalized impedances and wakes in asymmetric structures*. SLAC/AP110. 1998. URL: http://inspirehep.net/record/466605/files/slac-ap-110.pdf.

[125] A. Burov and V. Danilov. "Suppression of Transverse Bunch Instabilities by Asymmetries in the Chamber Geometry". In: *Physical Review Letters* (1999). DOI: 10.1103/PhysRevLett.82.2286.

[126] E. Métral et al. *Kicker Impedance Measurements for the Future Multi-turn Extraction of the CERN Proton Synchrotron*. CERN-AB-2006-051. 2006. URL: https://cds.cern.ch/record/971884/.

[127] B. Salvant et al. "Quadrupolar Transverse Impedance of Simple Models of Kickers". In: (2010). URL: https://cds.cern.ch/record/1271348.

[128] I. Zagorodnov. "Impedances of anisotropic round and rectangular chambers". In: *Phys. Rev. Accel. Beams* 21.6 (2018). DOI: 10.1103/PhysRevAccelBeams.21.064601.

[129] N. Mounet et al. "Closed Form Formulas of the Indirect Space Charge Wake Function for Axisymmetric Structures". In: *Proc. HB21*. JACoW Publishing, Geneva, Switzerland, 2022. ISBN: 978-3-95450-225-7. DOI: 10.18429/JACOW-HB2021-MOP10.

[130] E. de la Fuente et al. "A generalized tool to compute wake potential and impedance from electromagnetic time domain simulations". In: *Proc. IPAC'23*. Ed. by R. Assmann et al. Geneva, Sept. 2023. DOI: 10.18429/JACOW-IPAC2023-WEPL170.

[131] C. Antuono. "Methods to evaluate the beam coupling impedance of accelerators: a novel technique for bench measurements and beam-based measurements at the Proton Synchrotron Booster". In: (Jan. 30, 2025). URL: https://tesidottorato.depositolegale.it/handle/20.500.14242/190523.

[132] N. Mounet. "The LHC Transverse Coupled-Bunch Instability". PhD thesis. Ecole Polytechnique, Lausanne, 2012. DOI: 10.5075/epfl-thesis-5305.

[133] M. Cohen-Solal. "Design, test, and calibration of an electrostatic beam position monitor". In: *Physical Review Special Topics - Accelerators and Beams* 13.3 (Mar. 16, 2010). ISSN: 1098-4402. DOI: 10.1103/PhysRevSTAB.13.032801.

[134] R. N. Bracewell. *The Fourier Transform & Its Applications*. 3rd edition. Boston: McGraw-Hill Higher Education, July 1999. 624 pp. ISBN: 978-0-07-303938-1.

[135] R. Gluckstern. *Analytic Methods for Calculating Coupling Impedances*. CERN-2000-011. CERN, 2000. DOI: 10.5170/CERN-2000-011.

[136] M. Abramowitz and I. A. Stegun, eds. *Handbook of Mathematical Functions: with Formulas, Graphs, and Mathematical Tables*. New York, NY: Dover Publications, June 1, 1965. 1072 pp. ISBN: 978-0-486-61272-0.

[137] L. Vos. *The Transverse Impedance of a Cylindrical Pipe with Arbitrary Surface Impedance*. CERN-AB-2003-005 ABP. 2003. URL: http://cds.cern.ch/record/604828/files/ab-2003-005.pdf.

[138] K. Y. Ng. *Physics Of Intensity Dependent Beam Instabilities*. Hackensack, N.J: World Scientific Publishing Co Pte Ltd, Jan. 3, 2006. 800 pp. ISBN: 978-981-256-342-2.

[139] M. Blaskiewicz and W. Weng. *Transverse Instability with Large Space Charge Tune Shift*. BNL–104796-2014-IR, 1151287. Sept. 8, 1993, BNL–104796–2014–IR, 1151287. DOI: 10.2172/1151287.

[140] W. K. H. Panofsky and W. A. Wenzel. "Some Considerations Concerning the Transverse Deflection of Charged Particles in Radio-Frequency Fields". In: *Rev. Sci. Instrum.* (Nov. 1, 1956). DOI: 10.1063/1.1715427.

[141] H. Tsutsui. *On single wire technique for transverse coupling impedance measurement*. SL-Note-2002-034-AP. CERN, 2002. URL: https://cds.cern.ch/record/702715.

[142] T. Kroyer, F. Caspers, and E. Gaxiola. *Longitudinal and Transverse Wire Measurements for the Evaluation of Impedance Reduction Measures on the MKE Extraction Kickers*. 2007. URL: https://cds.cern.ch/record/1035461.

[143] E. Ergenlik. "Longitudinal and Transverse Impedance Measurements and Simulations for ThomX". PhD thesis. Université Paris-Saclay, Feb. 28, 2022. URL: https://theses.hal.science/tel-03865535.

[144] D. M. Pozar. *Microwave Engineering*. 4th Edition edition. Hoboken, NJ: John Wiley & Sons, Dec. 23, 2011. 752 pp. ISBN: 978-0-470-63155-3.

[145] V. G. Vaccaro. *Coupling Impedance Measurements*. INFN/TC-94/023. Nov. 14, 1994. URL: https://cds.cern.ch/record/276443.

[146] L. S. Walling et al. "Transmission-line impedance measurements for an advanced hadron facility". In: *NIMA* (Sept. 1989). DOI: 10.1016/0168-9002(89)91474-5.

[147] L. Eyges. *Classical Electromagnetic Field*. 1st edition. Addison-Wesley Educational Publishers Inc, Dec. 1, 1972. 413 pp. ISBN: 978-0-201-01891-2.

[148] L.-S. Huang et al. "Impedance measurements of the extraction kicker system for the rapid cycling synchrotron of China Spallation Neutron Source". In: *Chinese Physics C* 40.4 (2016), p. 047002. DOI: 10.1088/1674-1137/40/4/047002.

[149] U. Niedermayer, L. Eidam, and O. Boine-Frankenheim. "Analytic modeling, simulation and interpretation of broadband beam coupling impedance bench measurements". In: *NIMA* (2015). DOI: 10.1016/j.nima.2014.12.053.

[150] V. I. Kaminskii, S. V. Matsievskiy, and V. I. Rashikov. "Modernized Program for the Vacuum Chamber Coupling Impedance Calculation BeamImpedance2Dx". In: *Phys. Atom. Nuclei* (Dec. 2022). DOI: 10.1134/S1063778822100222.

[151] A. Meurer et al. "SymPy: symbolic computing in Python". In: *PeerJ Comput. Sci.* 3 (Jan. 2, 2017), e103. ISSN: 2376-5992. DOI: 10.7717/peerj-cs.103.

[152] The MPMath Development Team. *mpmath - Python library for arbitrary-precision floating-point arithmetic*. URL: https://mpmath.org/.

[153] B. W. Zotter. *New Results on the Impedance of Resistive Metal Walls of Finite Thickness*. CERN-AB-2005-043. 2005. URL: https://cds.cern.ch/record/877819.

[154] M. Migliorati et al. "Resistive wall impedance in elliptical multilayer vacuum chambers". In: *Phys. Rev. Accel. Beams* 22.12 (Dec. 12, 2019), p. 121001. DOI: 10.1103/PhysRevAccelBeams.22.121001.

[155] K. L. F. Bane and M. Sands. "The Short-Range Resistive Wall Wakefields". In: *AIP Conference Proceedings*. Micro bunches workshop. Vol. 367. Upton, New York (USA): AIP, 1996, pp. 131–149. DOI: 10.1063/1.50300.

[156] E. Métral. *Transverse resistive-wall impedance from very low to very high frequencies*. Geneva, 2005. URL: https://cds.cern.ch/record/895805.

[157] S. Joly et al. "Update of the Transverse Proton Synchrotron Impedance Model". In: *Proc. IPAC'21*. 2021. DOI: 10.18429/JACoW-IPAC2021-WEPAB224.

[158] J. Gareyte. "Experimental observations of electron beam instabilities in storage rings". In: *NIMA* 239.1 (Aug. 15, 1985), pp. 72–82. ISSN: 0168-9002. DOI: 10.1016/0168-9002(85)90701-6.

[159] L. J. Laslett, V. K. Neil, and A. M. Sessler. *Transverse Resistive Instabilities of Intense Coasting Beams in Particle Accelerators*. UCRL-11090. California Univ., Berkeley, CA (US). Lawrence Radiation Lab., Oct. 25, 1963. DOI: 10.2172/4036646.

[160] E. D. Courant and A. M. Sessler. "Transverse Coherent Resistive Instabilities of Azimuthally Bunched Beams in Particle Accelerators". In: *Rev. Sci. Instrum.* (Nov. 1966). DOI: 10.1063/1.1720048.

[161] C. Pellegrini. "On a new instability in electron-positron storage rings (The head-tail effect)". In: *Nuovo Cimento A (1965-1970)* 64.2 (Nov. 1, 1969), pp. 447–473. ISSN: 1826-9869. DOI: 10.1007/BF02754905.

[162] M. Sands. *The Head-Tail Effect: An Instability Mechanism in Storage Rings*. SLAC-TN-69-8. Mar. 28, 1969.

[163] M. Sands. *The Head-Tail Effect II: From a Resistive-Wall Wake*. SLAC TN-69-10. Apr. 24, 1969. URL: https://www.slac.stanford.edu/pubs/slactns/tn01/slac-tn-69-010.pdf.

[164] F. J. Sacherer. *Transverse bunched-beam instabilities*. Nov. 1, 1976. URL: https://cds.cern.ch/record/322533.

[165] J. Gareyte and F. J. Sacherer. *Head-tail type instabilities in the CERN PS and Booster*. CERN-MPS-DL-74-4. 1974. URL: https://cds.cern.ch/record/322647.

[166] C. Zannini et al. "Understanding of the CERN-SPS Horizontal Instability with Multiple Bunches". In: *Proc. of HB21*. 2022. DOI: 10.18429/JACoW-HB2021-MOP12.

[167] Y. Chin. *Transverse mode coupling instabilities in the SPS*. CERN-SPS-85-2-DI-MST. 1985. URL: https://cds.cern.ch/record/157995.

[168] E. Métral and M. Migliorati. "Longitudinal and transverse mode coupling instability: Vlasov solvers and tracking codes". In: *Physical Review Accelerators and Beams* 23 (July 6, 2020). DOI: 10.1103/PhysRevAccelBeams.23.071001.

[169] Y. Chin, K. Satoh, and K. Yokoya. "Instability of a Bunched Beam With Synchrotron Frequency Spread". In: *Part. Accel.* 13 (1983), pp. 45–66.

[170] Y. Chin. "Transverse Mode Coupling Instability in a Double RF System". In: *Particle Accelerators* 45 (Feb. 1, 1993). ISSN: 0031-2460. URL: https://www.osti.gov/biblio/1001637.

[171] S. V. Furuseth and X. Buffat. "Vlasov description of the beam response to noise in the presence of wakefields in high-energy synchrotrons: beam transfer function, diffusion, and loss of Landau damping". In: *Eur. Phys. J. Plus* (Apr. 2022). DOI: 10.1140/epjp/s13360-022-02645-3.

[172] N. Mounet. "Landau damping in the transverse plane". In: *Proceedings of the ICFA mini-Workshop on Mitigation of Coherent Beam Instabilities in Particle Accelerators*. MCBI2019. Zermatt, Switzerland, 2020. DOI: 10.23732/CYRCP-2020-009.45.

[173] M. Blaskiewicz. "Fast head-tail instability with space charge". In: *Phys. Rev. ST Accel. Beams* (1998). DOI: 10.1103/PhysRevSTAB.1.044201.

[174] A. Burov. "Head-tail modes for strong space charge". In: *Phys. Rev. ST Accel. Beams* 12.4 (Apr. 30, 2009). DOI: 10.1103/physrevstab.12.044202.

[175] V. Balbekov. "Transverse modes and instabilities of a bunched beam with space charge and resistive wall impedance". In: *Phys. Rev. ST Accel. Beams* 15.5 (May 21, 2012). ISSN: 1098-4402. DOI: 10.1103/physrevstab.15.054403.

[176] A. Burov. "Convective instabilities of bunched beams with space charge". In: *Phys. Rev. Accel. Beams* (2019). DOI: 10.1103/PhysRevAccelBeams.22.034202.

[177] X. Buffat et al. "Description of beam instabilities in synchrotrons with wakefields and space charge forces using the circulant matrix model". In: *Phys. Rev. Accel. Beams* (June 2021). DOI: 10.1103/PhysRevAccelBeams.24.060101.

[178] E. Métral. "Space charge in the GALACTIC Vlasov solver". In: *Proc. IPAC'25*. Taipei, Taiwan, 2025. DOI: 10.18429/JACoW-IPAC25-WEPM094.

[179] D. Amorim et al. "Transverse coherent direct space charge: comparison between several approaches". In: *Proc. IPAC'25*. Taipei, Taiwan, 2025. DOI: 10.18429/JACoW-IPAC25-WEPM095.

[180] A. Wolski. *Beam Dynamics In High Energy Particle Accelerators: Second Edition*. World Scientific Publishing Co Pte Ltd, 2023. ISBN: 978-981-12-7332-2.

[181] I. S. Gradshteyn and I. M. Ryzhik. *Table of Integrals, Series, and Products*. Ed. by A. Jeffrey and D. Zwillinger. Amsterdam: Academic Press, 2009. 1216 pp. ISBN: 978-0-12-373637-6.

[182] K. Kölbig and H. Scherb. "On a Hankel transform integral containing an exponential function and two Laguerre polynomials". In: *Journal of Computational and Applied Mathematics* 71.2 (July 1996). DOI: 10.1016/0377-0427(95)00224-3.

[183] T. Uesugi et al. "Beam stacking experiment at a fixed field alternating gradient accelerator". In: *Phys. Rev. Accel. Beams* 28.1 (Jan. 16, 2025), p. 012803. DOI: 10.1103/PhysRevAccelBeams.28.012803.

[184] C. W. Planner. *Some Considerations in the Design of an RF Shield for ISIS*. Internal Report SNS/phi/N8/79. Rutherford Appleton Laboratory, 1979.

[185] T.-S. F. Wang, S. S. Kurennoy, and R. L. Gluckstern. "Space-charge impedance of rf-shielding wires with external ceramic and conducting pipes". In: *Phys. Rev. ST Accel. Beams* 4.10 (Oct. 2001). DOI: 10.1103/PhysRevSTAB.4.104201.

[186] ISIS Image Archive. *Science and Technology Facilities Council Digital Media Library*. Webpage http://images.stfc.ac.uk.

[187] J. Bennett, R. Elsey, and T. Parry. "The performance of the vacuum system of the 800 MeV proton synchrotron, ISIS". In: *Vacuum* (May 1, 1993). ISSN: 0042-207X. DOI: 10.1016/0042-207X(93)90078-O.

[188] I. S. K. Gardner. "The Relevance Of ISIS Experience To The Design Of Future High intensity synchrotrons". In: *Part. Accel.* PAC. Vol. 31. 1990, pp. 227–234. URL: http://cds.cern.ch/record/1108185/.

[189] CCLRC, ISIS Design Division. *SI-5100-121-01, Issue X*. ISIS Engineering Drawing Database. Aug. 2004.

[190] D. R. Lide, ed. *CRC Handbook of Chemistry and Physics 79th Edition: 79th edition 1998-1999*. 79th edition. Boca Raton, Fla.: CRC Press, May 28, 1998. 2496 pp. ISBN: 978-0-8493-0479-8.

[191] C. Ridders. "A new algorithm for computing a single root of a real continuous function". In: *IEEE Transactions on Circuits and Systems* 26.11 (Nov. 1979), pp. 979–980. ISSN: 1558-1276. DOI: 10.1109/TCS.1979.1084580.

[192] R. Vila et al. "Dielectric spectroscopy of alumina ceramics over a wide frequency range". In: *Journal of Nuclear Materials* (Mar. 1998). DOI: 10.1016/S0022-3115(97)00308-5.

[193] I. Rodriguez. Private Correspondence.

[194] Y. Tokpanov, V. A. Lebedev, and W. Pellico. "Measurements of Magnetic Permeability of Soft Steel at High Frequencies". In: *Proc. IPAC'12*. 2012.

[195] B. Pine and C. Warsop. "High Order Image Terms and Harmonic Closed Orbits at the ISIS Synchrotron". In: *Proc. IPAC'18*. JACoW, June 2018. DOI: 10.18429/JACoW-IPAC2018-TUPAL056.

[196] L. Huang et al. "The Ferrite Loaded Cavity Impedance Simulation". In: *Proc. IPAC'21*. Vol. IPAC2021. 2021. DOI: 10.18429/JACOW-IPAC2021-TUPAB261.

[197] S. Lucyszyn. "Microwave Characterization of Nickel". In: *Piers Online* 4 (Jan. 1, 2008), pp. 686–690. DOI: 10.2529/PIERS080119215655.

[198] R. Timsit. "High Speed Electronic Connector Design: A Review of Electrical and Electromagnetic Properties of Passive Contact Elements – Part 1". In: *IEICE Transactions on Electronics* E91-C (2008). DOI: 10.1093/ietele/e91-c.8.1178.

[199] E. G. Sandels. *Notes on the Design of the SNS Extraction Kicker Magnets*. Internal Report SNS/MAG/N2/83. Rutherford Appleton Laboratory, Sept. 1983.

[200] M. Martin et al. "Multiphysics Finite Element Analysis of Wire and Ribbon Bonds Under Pulse Power Loads". In: *IET Power Electronics* 18.1 (2025), e70112. ISSN: 1755-4543. DOI: 10.1049/pel2.70112.

[201] E. Koukovini-Platia et al. "Source of horizontal instability at the CERN Proton Synchrotron Booster". In: *Phys. Rev. Accel. Beams* 22.12 (Dec. 31, 2019), p. 124201. DOI: 10.1103/PhysRevAccelBeams.22.124201.

[202] Y. Shobuda et al. "Demonstration of a kicker impedance reduction scheme with diode stack and resistors by operating the 3-GeV rapid cycling synchrotron of the Japan Proton Accelerator Research Complex". In: *Phys. Rev. Accel. Beams* 26.5 (May 31, 2023), p. 053501. DOI: 10.1103/PhysRevAccelBeams.26.053501.

[203] H. Hahn. *Impedance Measurements of the SNS Extraction Kicker System*. BNL–105704-2014-IR, 1157313. 2004. DOI: 10.2172/1157313.

[204] M. E. Brinson and S. Jahn. "Qucs: A GPL software package for circuit simulation, compact device modelling and circuit macromodelling from DC to RF and beyond". In: *International Journal of Numerical Modelling: Electronic Networks, Devices and Fields* 22.4 (2009), pp. 297–319. ISSN: 1099-1204. DOI: 10.1002/jnm.702.

[205] B. Salvant et al. "Building the Impedance Model of a Real Machine". In: *Proc. IPAC'19*. Melbourne, Australia, 2019. DOI: 10 . 18429 / JACoW - IPAC2019 - WEYPLS1.

[206] P. Saha et al. "Simulation, measurement, and mitigation of beam instability caused by the kicker impedance in the 3-GeV rapid cycling synchrotron at the Japan Proton Accelerator Research Complex". In: *Phys. Rev. Accel. Beams* 21.2 (Feb. 14, 2018), p. 024203. DOI: 10.1103/PhysRevAccelBeams.21.024203.

[207] J. Berg. *Coherent modes for multiple non-rigid bunches in a storage ring*. SLAC–478, 219364. Mar. 1, 1996, SLAC–478, 219364. DOI: 10.2172/219364.

[208] M. Kinsho et al. "Development of Alumina Ceramics Vacuum Chamber for J-PARC". In: *Shinku* 49.12 (2006), pp. 728–733. DOI: 10.3131/jvsj.49.728.

[209] V. Kornilov and O. Boine-Frankenheim. "Instability mitigation using octupoles in bunches with space-charge". In: *JACoW* IPAC2023 (2023), WEPA015. DOI: 10.18429/JACoW-IPAC2023-WEPA015.

[210] C. Prior. "Studies of Dual Harmonic Acceleration in ISIS". In: *Proc. of ICANS XII*. ICANS XII. 1993. URL: http://neutronresearch.com/parch/1993/01/199301030110.pdf.

[211] J. Xu, L. Qin, and H. Xu. "Vlasov solver for transverse mode coupling instability of double-rf system under arbitrary settings". In: *Phys. Rev. Accel. Beams* 28.11 (Nov. 24, 2025), p. 114401. DOI: 10.1103/x4gh-6c78.

[212] C. M. Warsop et al. "High Intensity Loss Mechanisms on the ISIS Rapid Cycling Synchrotron". In: *Proc. HB'14*. East-Lansing, USA, 2014. URL: https://accelconf.web.cern.ch/HB2014/papers/tuo3lr03.pdf.

[213] D. Amorim et al. "Simulations and measurements of the transverse mode coupling instability in the LHC". In: *Phys. Rev. Accel. Beams* 26.12 (Dec. 26, 2023), p. 124401. DOI: 10.1103/PhysRevAccelBeams.26.124401.

[214] J. Laskar. "The chaotic motion of the solar system: A numerical estimate of the size of the chaotic zones". In: *Icarus* 88.2 (Dec. 1, 1990), pp. 266–291. ISSN: 0019-1035. DOI: 10.1016/0019-1035(90)90084-M.

[215] H. Wiedemann. *Particle Accelerator Physics*. Graduate Texts in Physics. Cham: Springer International Publishing, 2015. DOI: 10.1007/978-3-319-18317-6.

[216] G. H. Rees. "Aspects of beam stability at ISIS". In: *AIP Conference Proceedings* 496.1 (Dec. 3, 1999), pp. 17–21. ISSN: 0094-243X. DOI: 10.1063/1.1301871.

[217] D. Adams et al. "Operational Experience and Future Plans at ISIS". In: *Proc. HB'16*. Sweden, 2016. DOI: 10.18429/JACOW-HB2016-TUPM3Y01.

[218] R. Bartolini et al. "Tune evaluation in simulations and experiments". In: *Part. Accel.* 52.3 (1996), pp. 147–177. URL: https://cds.cern.ch/record/292773.

[219] D. Quatraro et al. "Coherent Tune Shift and Instabilities Measurements at the CERN Proton Synchrotron Booster". In: *Proc. Pac'09*. Canada, 2009.

[220] D. W. Posthuma de Boer, C. M. Warsop, and R. E. Williamson. "Low-frequency transverse resonator impedances on the ISIS proton synchrotron". In: *Proc. HB'25* (China). JACoW, Oct. 2025. URL: https://meow.elettra.eu/83/doi/jacow-hb2025-thcbc02.

[221] L. Huang et al. "Source of instability in the rapid cycling synchrotron of the China spallation neutron source". In: *Eur. Phys. J. Plus* 140.1 (Jan. 26, 2025), p. 71. ISSN: 2190-5444. DOI: 10.1140/epjp/s13360-025-05997-8.

[222] A. Chance et al. "Parameter ranges for a chain of rapid cycling synchrotrons for a muon collider complex". In: IPAC23. JACoW Publishing, 2023. DOI: 10.18429/JACOW-IPAC2023-MOPL162.

[223] S. Kheifets and B. Zotter. *Impedances and Wakes in High Energy Particle Accelerators and Storage Rings*. Singapore ; River Edge, NJ: World Scientific Publishing Co Pte Ltd, Apr. 1, 1998. 428 pp. ISBN: 978-981-02-2626-8.

[224] C. V. Dodd and W. E. Deeds. *Analytical Solutions to Eddy Current Probe Coil Problems*. ORNL-TM-1987. Oak Ridge, Jan. 1967. DOI: 10.2172/4499902.

[225] W. H. Press. *Numerical Recipes 3rd Edition: The Art of Scientific Computing*. Cambridge University Press, Sept. 6, 2007. 1195 pp. ISBN: 978-0-521-88068-8.

[226] A. L. Garcia. *Numerical Methods for Physics*. Second, Revised. CreateSpace Independent Publishing Platform, July 12, 2017. 350 pp. ISBN: 978-1-5488-6549-8.